Development of Functional Nanoparticles for Biosensing and Antibacterial Applications

Lorico Delos Santos Lapitan Jr.

Submitted in accordance with the requirements for the degree of
Doctor of Philosophy

The University of Leeds
School of Chemistry

September 2018

The candidate confirms that the work submitted is his own, except where work which has formed part of jointly-authored publications has been included. The contribution of the candidate and the other authors to this work has been explicitly indicated below. The candidate confirms that appropriate credit has been given within the thesis where reference has been made to the work of others.

Chapter 1 is based on work from the following publication

Lorico Lapitan Jr., Yuan Guo, and Dejian Zhou, (2015). Nano-enabled bioanalytical approaches to ultrasensitive detection of low abundance single nucleotide polymorphisms. *Analyst*, *140*(12), 3872-3887.

Lorico Lapitan Jr. (candidate): performed the literature search and wrote the manuscript.

Dejian Zhou and Yuan Guo, commented on the manuscript and suggested additional references and revised over-all form of the manuscript.

I. Acknowledgments

The Leeds International Scholarship (LIRS) – 2014 for the financial support that enabled me to pursue my PhD studies at University of Leeds.

Prof. Philipina A. Marcelo Ph.D., (Dean of the University of Santo Tomas- Faculty of Engineering) for supporting my application to take a leave of absence from the faculty while studying at Leeds University and to my colleagues at the UST Department of Chemical Engineering for their encouragement.

Prof. Dejian Zhou, Ph.D., my research supervisor, for his unwavering support, patience and scholarly advice throughout the entire duration of the research work. Thank you for believing in my capabilities and for advancing my skills and knowledge to become a good researcher.

Dr. Yuan Guo from the School of Chemistry, Dr. Algy Kazlauciunas from the School of Colour and Polymer Science, Dr. Oscar Cespedes from the School of Physics, Dr. Peiyi Wang and Dr. Christopher Randall from School of Biological Sciences for helping me carry out various experiments in my research project. Special thanks to Prof. Fiona Meldrum, Ph.D., my internal postgraduate examiner for her valuable suggestions in the refinement of the contents of my annual progress research reports.

Mark Vincent Dela Cerna for his valued comments and suggestions in my posters and reports. The members of the Zhou research group, Weili Wang, and Yifei Kong for sharing knowledge and experiences needed to carry out some experiments in the laboratory specially in my first year. I highly appreciate Emma Poole for her kind assistance in compiling my thesis chapters, tea time breaks, and for her help in sorting out matters in the group and laboratory. Special thanks to Alexandra Gummer and Wei Ng for their efforts in carrying out the antimicrobial research project.

To all the wonderful people I met in Leeds for making my PhD experience pleasant. I would like to personally thank my colleagues at the School of Chemistry: Maria Kwan, Joan Mayol Llanas, Cecilia Madzivire, and Charlene Jordan for boosting my

confidence, and providing a supportive and encouraging environment. I am also grateful for the Filipino community in Leeds for their hospitality and generosity.

Special thanks to Edward King, Gesner Las Casas Brito Filho, Joey Mark Diaz, and Lorivell Fox for their kindness and love. I would also like to extend my gratitude Jace Cabanes, Kari Medala, Ronald Adalla, Kerwin Matula, Kevin Dacre, Teofanis Tsizme, Mario Fu, Earvin Cabahug and Mustafa Akarsu for their support and creating an enjoyable environment through different activities that helped me maintain good mental health.

My supportive family, thank you for the love and for always being around whenever I needed help and guidance. I am thankful to my sister, **RACHEL LAARNI LAPITAN**, for her constant encouragement during the low moments of my research, for reminding me of my prioritise and plan for my future, and for spending some time with me in Leeds. I am in deep sorrow that I lost you and I miss you beyond measure!

II. Abstract

This thesis is composed of two parts: Part 1 reports the design and synthesis of magnetic nanoparticle-DNA conjugates for DNA and ECOR-I detection. Part 2 reports the studies on the synthesis of Ag nanomaterials and evaluation of their antimicrobial properties.

Part I

The ability of ultrasensitive detection of specific genes and discrimination of disease related single nucleotide polymorphisms (SNPs) is important for biomedical research and clinical disease diagnosis. Herein, we report an ultrasensitive approach for label-free detection and discrimination of full-match target-DNA from its cancer related SNPs by combining magnetic nanoparticle (MNP) capture and poly-enzyme nanobead signal amplification. It uses a MNP linked capture-DNA and a biotinylated signal-DNA to sandwich the target followed by ligation to offer high SNP discrimination: only the perfect-match target-DNA yields a MNP covalently linked biotinylated signal-DNA for subsequent binding to a neutravidin-horseradish peroxidase conjugate (NAV-HRP) and signal amplification. The use of polymer nanobeads each tagged with thousands of copies of HRPs greatly improves the signal amplification power, allowing for detection of 10 aM target-DNA with a large dynamic range of 5 orders of magnitude (0.01-1000 fM). Moreover, this sensor also offers excellent signal discrimination between the perfect-match gene and its cancer-related SNPs and can positively detect 1 fM perfect-match target-DNA in the presence of 100 fold excess of co-existing SNPs. Furthermore, it works robustly in clinical relevant media (e.g. 10% human serum) and gives almost identical SNP discrimination as that in clean buffers. This ultrasensitive SNP sensor appears to have excellent potential for rapid detection and diagnosis of genetic diseases.

This study also reports the design of a MNP-DNA_{ss}-HRP nanoprobe for the label-free detection of DNA and ECOR-I. The Fe_3O_4 MNP were prepared by thermal decomposition and coated with silica by the reverse micelle method yielding core-shell nanoparticles. These silica coated MNP were modified with amino groups for further conjugation with DNA. In Design-1, the capture DNA contain DBCO and biotin group at the 5’ and 3’ end respectively. The capture DNA was linked to the amino modified MNP through copper free click chemistry approach. The NAV-HRP was

linked to the DNA strands through biotin-strepatividin interaction. The MNP-DNA conjugates were further incubated with NHS-PEG$_{\sim 17}$-OCH_3 to cap unreacted amines. In Design-2, the capture DNA also contain DBCO group at 5' end but a thiol (-SH) group at 3' end. The capture DNA strand was linked to MNP and the unreacted surface amines were blocked following the same strategy for Design-1. Incubation with maleimide-HRP led to the covalent linking of the enzyme to the DNA strands. The MNP-DNA_{ss}-HRP nanoprobes and target DNA are hybridized and the resulting double strand DNA contains specific sequence that is recognized and cleaved by ECOR-I. This releases thousands of HRP enzyme to the solution which in turn can catalyse a colourimetric reaction. Using Design-2, the optimal incubation temperature was 30 °C and 1 hour incubation time with ECOR-I. This approach can detect 10 $U \cdot mL^{-1}$ of ECOR-I and 1 nm of target DNA.

Part 2

Silver nanomaterials have been widely utilized for antimicrobial applications. Silver nanoparticles (Ag NPs) have been used in many biomedical and environmental applications for many years. Interestingly, silver nanoclusters (Ag NCs) have emerged as a new class of silver nanomaterials and currently being investigated for its antibacterial properties. In this study, we report the antibacterial properties of Ag NPs and NCs that were synthesized using the same protocol and capped with the same dihydrolipoic acid (DHLA) based ligands against *S. aureus* and *E. coli*. These ligands were DHLA-EG_n-NH_2 (n=3,12), DHLA-PEG_n-OCH_3 (n ~17, 23) and DHLA-zwitterion. The Ag NC-DHLA and Ag NC-PEG$_{\sim 23}$-OCH_3 inhibited *S. aureus* and *E. coli* with MIC results of 128, 64 and 64, 128 $\mu g \cdot mL^{-1}$ respectively. The Ag NPs were observed to be more effective antimicrobial agents as revealed by MIC results. The 5.7 nm Ag NP-zwitterion is the most potent antibacterial agent among all the Ag NPs tested with an MIC of 8 $\mu g \cdot mL^{-1}$ for both bacterial strains. This study demonstrated, for the first time, that the antibacterial properties of silver nanomaterials differ significantly when coated with different ligands. Moreover, surface coating and charge are most likely the key factors that control the antimicrobial efficacy of Ag NCs and NPs.

III. Table of Contents

IV. List of Tables

V. List of Schemes

VI. List of Figures

VII. List of Abbreviations

APTES	(3-aminopropyl)triethoxysilane
ABNC	Active but not culturable
Ag NPs	Silver nanoparticles
aM	Attomolar
Au NPs	Gold nanoparticles
avidin-HRP	Avidin-Horse Raddis Peroxidase
Bbc-Au NP	Gold nanoaprticles tagged with biobarcode dnas
BEAM	Beads, Emulsion, Amplification, and Magnetics
BSA	Bovine serum albumin
CCLR	Enzyme-free click chemical ligation reaction
DBCO	Dibenzocyclooctyne
DCC	Dicyclohexylcarbodiimide
Dhs	Hydrodynamic diameter (nm)
DHLA	Dihydrolipoic acid
DLS	Dynamic light scattering
DMAP	Dimethylaminopyridine
DNA_{ds}	Double stranded DNA
DNA_{ss}	Single stranded DNA
dNTPs	Deoxyribonucleotide triphosphate
ELISA	Enzyme linked immunosorbent assay
fM	Femtomolar
FRET	Förster (fluorescent) resonance energy transfer
FT-IR	Fourier transform- infrared spectrocopy
GMR	Giant magnetoresistive
Gox	Glucose oxidase
GSH	Glutathione (tripeptide Glu-Cys-Gly)
HAADF	High annular dark field
HABA	(4'-hydroxyazobenzene-2-carboxylic acid)
HCR	Hybridization chain reaction
HIV	Human immunodeficieny virus
HOMO-LUMO	Highest occupied molecular orbital- lowest unnocupied molecular orbital
HRP	Horseradish peroxidase
^{1}H-NMR	Proton numclear magentic resosnance spectroscopy
ICP-MS	Inducitvely coupled plasma - Mass spectrometry

IGEPAL CO 250	Polyoxyethylene (9) nonylphenylether
LCR	Ligation chain reaction
LOD	Limit of detection
LSPR	Localized surface plasmon resosnance
MNBs	Magnetic beads
MNP	Magnetic nanoparticle
MNP -NH_2	Amine –modified magnetic nanoparticle
MNP -NH_2 -350	Silica–modified magnetic nanoparticle treated with 350 ml of APTES
MNP -NH_2- 500	Silica–modified magnetic nanoparticle treated with 500 ml of APTES
MNP -NH_2- 750	Silica–modified magnetic nanoparticle treated with 750 ml of APTES
MNP -NH_2-1000	Silica–modified magnetic nanoparticle treated with 1000 ml of APTES
MNP-SiO_2	Silica modified magnetic nanoparticle
MS	Mass spectrometry
MW	Molecular weight
NAV	Neutravidin
NAv-HRP	Neutravidin- horse raddish proxidase
NHS	N-hydorxyssuccinamide
PB	Polymer bead
PBS	Phosphate-buffered saline PBS
PCR	Polymerase chain reaction
PDDA	Poly(diallyldimethyl) ammonium chloride
PMAO	Poly-(maleicanhydride-*alt*-1-octadecene
PMAO-PEG	Amphiphilic polymer containing polyethylene glycol-azide units
PPh3	Triphenylphosphine
QD	Quantum dots
qRT-PCR	Quantitative reverse transcription polymerase chain reaction
QY	Quantum yield
RCA	Rolling circle amplification
RNA	Ribonucleic acid
SERS	Surface enhanced Raman spectroscopy

$SM(EG)_{12}$ Maleimide	(succinimidyl-[(N-maleimidopropionamido)-dodecaethyleneglycol] ester)
SNPs	Single-nucleotide polymorphism
SPR	Surface palsmon resonance
SPR	Surface plasmon resonance
SPRI	Surface plasmon resosnance imaging
TA	Thiocitc acid
TEM	Transmission electron microscopy
TEOS	Tetraethyl orthosilicate
THF	Tetrahydrofuran
THMP	Triple-helix magnetic probe
UV	Ultraviolet
UV-Vis	Ultraviolet-visible
v/v	Volume by volume concentration
VSM	Vibrating sample magnetometer
WOT	Without target, control expriment
WS2-AB	Tungsten disulphide/acetylene black
WT	Wild type
zM	Zeptomolar

VIII. Glossary

Allelic - Pertaining to allele which is a possible forms of a gene. An allele can be dominant or recessive.

Codon- A sequence of three DNA or RNA nucleotides that corresponds with a specific amino acid or stop signal during protein synthesis.

KRAS- First identified as oncogene in **K**irsten **RA**t **S**arcoma virus. A gene that acts as a switch (on/off) in cell signaling. The normal gene control cellular proliferation but mutation can cause cells to continuously proliferate leading into cancer.

Multiplexing- The ability to detect several targets simultaneously in clinical diagnostics.

Mutation- Permanent alteration of the nucleotide sequence of the genome of an organism.

Nicked- A single-stranded cut or break in a DNA molecule. A single-stranded break in a double stranded DNA at which one or more nucleotide are missing or there is a break in the phosphodiester bond between two adjacent nucleotides on one strand of the DNA duplex.

Plasmonic- The study of the interaction between electromagnetic field and free electrons in a metal nanoparticles. The free electrons in the metal nanoparticle surface can be excited by the electric component of light to have collective oscillations.

Polymorphism- A DNA sequence variation that is common in the population.

Somatic- Refers to the cells in the body in contrast to the germ line cells (sperm and egg).

Somatic mutation- An alteration in DNA that occurs after conception. These alterations can (but do not always) cause cancer or other diseases

Streptavidin - tetrameric protein purified from the bacterium *streptomyces avidinii* that have an extraordinarily high affinity for biotin (K_d on the order of $\approx 10^{-14}$ mol/L).

Via - refers to "*by means of*..."

Chapter 1

Nano-enabled Bioanalytical Approaches to Ultrasensitive Detection of Low Abundant Single Nucleotide Polymorphisms

1.1 Introduction

The completion of the human genome project in 2003[1] has led to several important discoveries relating to structure of the human genome: it is characterized by variations in DNA nucleotide sequences of one or more bases in genes of the same population.[2, 3] These variations in DNA impart certain phenotypic traits that distinguish an organism from another. If such variations occur in greater than one percent of the human population, they are collectively referred to as polymorphisms. On the other hand, variations occurring in less than one percent of the population are often termed as “mutations” which are associated with a detrimental phenotype such as those linked with various cases of cancer.[3] The most common sequence variation occurring in the human genome is the stable substitution of a single nucleotide, also known as single nucleotide polymorphisms (SNPs). More than 10 million SNPs are estimated to distribute across the whole human genome at an frequency of at least one nucleotide every 1000 base pairs with apparent regional differences.[4, 5] While most SNPs do not alter the metabolic function and expression levels of a gene, some do result in differences in predisposition to certain heritable diseases,[6-8] response to drugs (pharmacogenetics),[9, 10] and perception of pain. [11] Several studies have shown that SNPs are closely associated with many types of cancer and presupposes the risk of cancer progression.[12-15] For instance, it was observed that single point mutations in the KRAS gene at codons 12, 13, and 61 are associated with the development of certain pancreatic[14] and lung cancers.[15] Moreover, numerous detrimental and inheritable diseases such as diabetes,[7] vascular diseases,[16] some forms of neurodegenerative and mental illness[17, 18] have also been linked to SNPs. On the other hand, microRNAs (miRNAs) which are 17–24 base short RNA molecules, play important roles in numerous cellular processes such as differentiation, cellular growth, and apoptosis. Point mutations in miRNAs have been

associated with several forms of cancers, affecting the cancer risk and treatment efficacy in some non-small cell lung cancer patients.[19, 20] These are just a few examples which highlight the association of SNPs to human diseases and treatment responses, and demonstrate the tremendous value of SNPs in biomedical research. Indeed, SNPs are considered as an important class of biomarkers that could allow scientists and medical practitioners to better understand certain diseases, develop novel non-invasive diagnostics tools and ultimately allow for a more personalized approach to disease treatment and therapies.

The most established techniques for point mutation detections in DNA have largely relied on the amplification power of the polymerase chain reaction (PCR) coupled with quantitative fluorescence detection and/or DNA sequencing techniques such as pyro-/next generation sequencing of the amplified product. Although highly sensitive and widely used, such methods can sometimes introduce errors during the PCR amplification process which is sensitive to contaminations and amplification bias, and hence may affect diagnostic accuracy[21, 22]. PCR is also often regarded as labour-intensive and time-consuming, making it unsuitable for rapid, point-of-care diagnostics. Moreover, it also requires an expensive thermal cycler and thereby the cost per analysis might be high for developing countries. These limitations have largely hampered the wide use of PCR for rapid, on-site diagnostics. In the case of point mutation detections involving miRNAs, the real-time quantitative reverse transcription polymerase chain reaction (qRT-PCR) is often the method of choice due to its high sensitivity. However, it also suffers several drawbacks which include complex analytical processes, requiring reverse transcription and multiple primer design and fluorophore labelled reporters, and the need of precise temperature control. [23] Unsurprisingly, many of the recent developments have focused on developing PCR-free alternatives in SNP biosensing. The reliable detection of low abundance specific SNPs without PCR pre-amplification represents an extremely challenging, albeit exciting research area of the bioanalytical science.

Recently, the BEAMing Digital PCR method shown in **Figure 1-1** named after its principal components (*i.e.* Beads, Emulsion, Amplification and Magnetics) was developed for detecting genetic variations[24]. In this method, biotinylated oligonucleotide primers are bound to streptavidin coated magnetic microbeads .

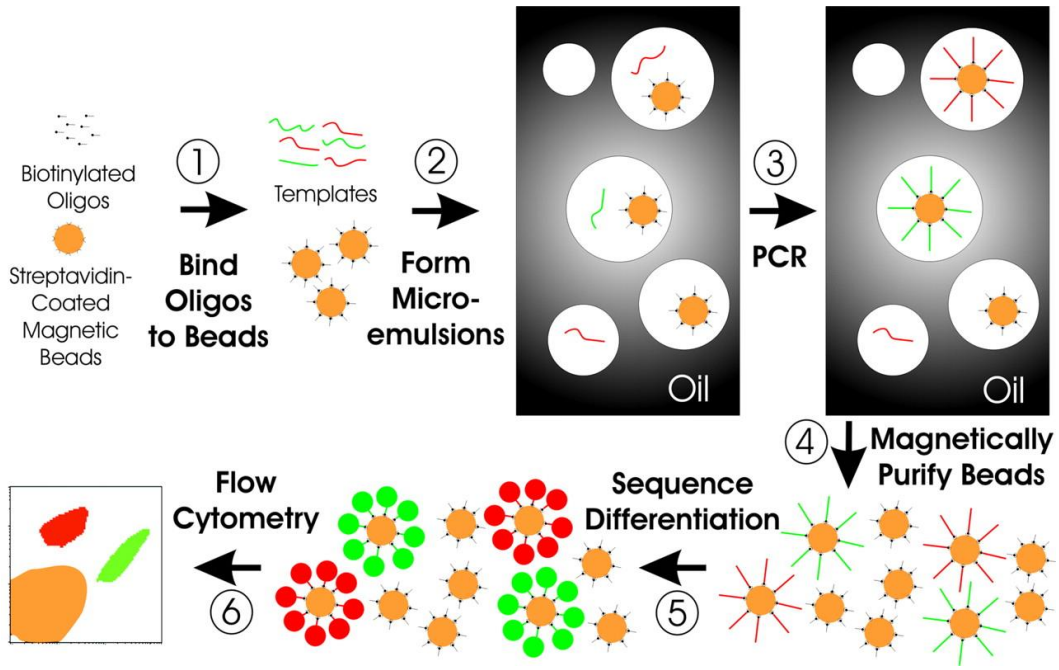

Figure 1-1. Schematic illustration of the processes in BEAMing. Step 1: streptavidin coated magnetic bead are bound to the biotinylated oligonucleotide. Step 2: Formation of microemulsions containing all the components for PCR and oligonucleotide bound magnetic beads, Step 3: Emulsion based PCR thermal cycling. Step 4: Emulsions are broken and magnetic beads are collected by a magnet and purified, Step 5: After denaturation, the magnetic beads are incubated with fluorescent-tagged probes specific for wild-type or for a specific point mutation to hybridize to the amplified DNA on MNP. Step 6: Flow cytometry of the beads to detect the fluorescent tag and quantify the beads containing mutated DNA. Reprinted from reference [24]

In the next step, an aqueous mixture containing all the components for conventional PCR and primer-bound magnetic beads are stirred together with an oil/detergent mixture to create micro emulsions, ensuring each emulsion containing no more than one bead and one target DNA. These micro emulsions are temperature-cycled for a defined period of time which produce amplified DNA strands conjugated to the microbeads and emulsions are subsequently broken. The magnetic microbeads are separated from the rest of the mixture using a magnet. After denaturation, the beads are incubated again with oligonucleotides that can distinguish between the

sequences of the different kinds of templates. Fluorescently labelled DNA are used to label the bound probes via hybridisation. This step renders the beads containing PCR product as either red or green after appropriate laser excitation. Finally, the red and green beads are analysed using flow cytometry where the proportion mutation can be quantified. This method allows the identification and quantification of allelic variations. Moreover, the DNA sample can be recovered from the flow cytometer for subsequent analysis. BEAming is extremely sensitive (detection down to 0.01% mutation level) but this method is expensive and involves a number of complex steps [25].

Over the past few years, enormous efforts have been directed towards the development of novel, ultrasensitive PCR-free SNP assays and a number of techniques have been developed [22, 26-29]. The detection and quantification of known SNPs are primarily based on the specificity of target hybridization [30, 31] and enzyme discriminations, such as specific enzymatic cleavage, [32] and single base primer extension [33, 34]. Of particular interest in the early stages of PCR-free SNP biosensing development has been based on using water-soluble, cationic conjugated polymers (CCPs) as fluorescence transducers. For example, the Leclerc group [35, 36] has pioneered and developed DNA detection based on the electrostatic attraction between a cationic polythiophene and DNA. The colour and fluorescence changes of the polymer in the presence of single stranded and double-stranded DNAs were used as the basis for biosensing. They have reported the first detection of SNPs directly from clinical samples without the need of DNA pre-amplification with an impressive detection limit of 3 zeptomolar. The Bazan and Jaeger groups have also detected specific DNA sequences via CCP sensitised Förster resonance energy transfer (FRET) to dye-labelled probes. [37, 38] The electrostatic attraction between the cationic CCPs and the anionic DNAs leads to short distance donor (CCP)–acceptor (DNA dye-label), hence strong FRET. [39] A substantive review of such work has already been provided by Swager et al. [40] and hence this will not be main topic here.

Recently, the use of various nanomaterials has provided the capability of ultra-sensitivity and high specificity in SNP detection. Nanomaterials have been well-studied primarily because of their unique, size dependent physical and chemical properties. In terms of biosensing applications, such useful properties include the extremely large surface area, tuneable surface chemical composition that allow easy and controlled immobilization of stable bioreceptors for efficient transduction of target binding into strong readout signals. These properties are advantageous for achieving

ultrasensitivities, allowing easy integration into miniaturized devices ushering an era of next generation cost-effective SNP diagnostics. Nanomaterials such as metallic nanoparticles (NPs),[41-46],[47] quantum dots (QDs), [48-51] magnetic nanoparticles (MNPs),[51-56] and carbon based nanomaterials [57] have been combined with biomolecules such as enzymes, oligonucleotides and DNAzymes to develop sensors for detection and quantification of cancer-specific SNPs. Such nanomaterial-based SNP assays have been coupled with a number of different readout strategies, including colorimetry, fluorimetry, surface enhanced Raman spectroscopy (SERS), electrochemical and electrochemiluminescence etc. For example, Boudreau and colleagues recently reported the use of FRET-based CCP transducers by combining them with highly fluorescent core–shell nanoparticles. The Ag nanoparticle core was used to amplify the optical signal generated upon target recognition. This plasmonic enhancement resulted to the direct detection of unamplified target nucleic acid at femtomolar concentration regime. [58-60] **Table** 1-1 summarizes some of the recently developed ultrasensitive SNP assays using different nanomaterials coupled with different probe and/or signal amplification strategies.

The sensitivities and specificities of these assays are already comparable to, or even surpass those of many PCR based techniques, demonstrating the high suitability of nanomaterials for ultrasensitive SNP detection. Despite significant developments, it is important to consider some other burgeoning challenges in clinical diagnosis, particularly in the quantification of extremely low abundant SNPs in an overwhelming background of wild-type genes in clinical settings. Moreover, the ability of simultaneous detection of multiple biomarker targets is also important for high diagnostic accuracy because *"no tumour marker identified to date is sufficiently sensitive or specific to be used on its own to screen for cancer"*.[61] The practical importance of these relies on the fact that most cancer cases are only diagnosed in the late stage and when the chances of patient survival are already slim. As a result, early diagnosis is of paramount importance for improving the survival and prognosis of cancer patients. All these necessitate the development of ultrasensitive assays with multiplexing capability that can detect the extremely low concentrations of cancer-specific SNPs in clinically media.

Table 1-1: Comparison of the sensing performance of some ultrasensitive nanomaterial based SNP detection assays. PCR: polymerase chain reaction, LCR: ligation chain reaction.

First Author ref.	Nanomaterial Platform	Amplification strategy	Transducer / Analytical Tool	LOD
PCR Based Pre amplification				
Y. Zhao [62]	Au NPs + Ag NPs	PCR	Circular Dichroism	17 zM
F. Patolsky [54]	Magnetic NP	PCR	Chemiluminescence	8.6 aM
PCR-free Amplification				
W. Shen [30]	Au NP	LCR	Colorimetric	20 aM
D. Kato [63]	Au NPs and Magnetic NP	LCR	Colorimetric	50 zM
J. Ji [49]	CdTe QD's	Target recycling + RCA	Electrochemical	11aM
S. Bi [53]	Magnetic NP	RCA + DNAzyme	Colorimetric	71 aM
Y.P. Zeng [64]	QD	Primer generation + RCA	Fluorometric	50. 9 aM
J.W. Nam [65]	Au NPs and MNP's	Bio-bar-code + Ag amplification	Scannometric	30 aM
J. Hu [66]	CdS QD's	CdS QD loaded in SiO_2 particles	H_2S Generation + Atomic Fluorescence Microscopy	0.8 aM
C. Ding[67]	Au NP's and CuS NP's	CuS NP loaded in Au NP	Electrochemical	19 aM
R. D'Agata [68]	Au NP's	Short DNA modified Au NP	Surface Plasmon Resonance Imaging	2.6 aM
J. Zhou [69]	QD's	QD's entrapped in a liposome	Single Particle Counting	1-2.5 aM

A survey of literature shows that three main approaches have been widely employed to improve the assay detection limits that we group into three main categories: target, probe, and signal amplification. Among these, target amplification is mainly achieved *via* enzyme-mediated replication of target nucleic acid sequences, leading to *ca.* 10^8–10^9 fold amplification of target concentration to make it high enough to be readily detected by traditional approaches such as gel electrophoresis [22]. An excellent example here is the well-established PCR. More recently, isothermal target (DNA) amplification strategies have also been developed and displayed sensitivities

comparable to that of the PCR [26-29, 70]. These methods do not need a thermal cycler, making them cost effective, simple to use and potentially suitable for point-of-care diagnostics [71]. In contrast, probe amplification does not change the copy number of the target (DNA), instead the probe sequence which is complementary to the target is amplified and detected. Signal amplification is to amplify the analytical signal generated by each labelled or unlabelled target so as to increase the assay sensitivity.

In this chapter, some of the most recent advances in the field of nanomaterial-based SNP detection will be discussed, with a particular focus on those techniques capable of detecting and quantifying extremely low target concentrations, down to the attomolar regimes or below. Given the high specificity, the hybridization-based method remains one of the most popular methods for nanomaterial based SNP assays. In general, the ultra-sensitivity of these assays has been achieved through one of the following five different strategies, (i) nanoparticle assisted PCR target amplification, (ii) nanoparticle assisted probe amplification, (iii) target recycling coupled with probe and/or signal amplification, (iv) tandem amplification coupled with signal catalytic cascades, and (v) nanomaterial enhanced signal amplification. Each of these classes will be discussed with a focus on the assay sensitivity and comment on their applicability to real biological matrices. Moreover, a critical categorization of such approaches on the basis of different amplification strategies is proposed.

1.2 Nanoparticle assisted PCR target amplification strategy

An essential first step in this approach is to pre-amplify the extremely low abundant SNP target into sufficiently high number of copies so that it can be readily detected by conventional methods. Given its extremely powerful exponential amplification power, it is unsurprising that PCR-based SNP biosensing assays have high sensitivities. [72] In particular, the incorporation of plasmonic nanomaterials such as Au and Ag nanoparticles has been recently combined with PCR pre-amplification of the target DNA, leading to unprecedented sensitivities. For example, Kotov and colleagues have reported an unexpected chirality of bridged metallic nanoparticle dimers and have exploited this in ultrasensitive biosensing. They have prepared different sized Au and Ag NPs and functionalized them with specific antibodies so that they can sandwich bind the specific target protein (e.g. prostate specific antigen PSA, a prostate cancer marker) and assemble into hetero-nanoparticle dimers. These biomolecule bridged NP heterodimers are chiral, leading to an observable

change in circular dichroism (CD) spectra over 350–600 nm region. The authors found that this assay was extremely sensitive, capable to detecting PSA down to the sub-aM level with an extremely impressive detection limit (DL) of 1.5×10^{-20} M and a linear dynamic range of ~3 orders of magnitude. Such a highly impressive sensitivity has been attributed to plasmonic enhancement of intrinsic chirality of biomolecules, strong optical coupling of photons with twisted NP heterodimers, and bisignate nature of the CD spectra. [73, 74] This assay has been recently modified to suit the detection of ultralow concentrations of DNA [62] by applying a PCR amplification of the dsDNA with primers linked to Au NPs (25 nm Au NP-linked forward primer and 10 nm Au NP-linked reverse primer) in the presence of *Taq* polymerase and dNTPs as shown in **Figure 1-2**. The DNA-bridged Au NP heterodimers displayed circular dichroism (CD) bands at 260 and 525 nm, attributed to the chiral secondary structures of duplex DNA and the chiral NP dimers, respectively. These dimers displayed unexpected chirality due to the ellipsoidal shape of the NPs and a scissor-like configuration with two long NP axes forming a dihedral angle of 10°. Coating of the Au NP dimers with Ag or Au are found to affect their chiro-plasmonic activity: as the thickness of the Ag shell increased, the intensity of the CD bands also increased and shifted from 525 to 418 nm. In the case of Au coating, increasing the Au shell thickness resulted in a colour change of the dispersion from pink to purple and the CD bands exhibited a 61 nm red shift.

More importantly, Au coating of DNA bridged Au NP dimers gave fairly narrow spectra with high optical anisotropy. Optimization of assay parameters such as specific design of primers and number of PCR cycles has yielded ultrasensitive DNA assay with a linear dynamic range spanning 7 orders of magnitude (from 160 zM to 1.6 pM) and an extremely low DL of 17 zM. Currently, this method reported the highest sensitivity for DNA detection using nanomaterials based sensing platforms, and hence appears to have good potential for genetic based early diagnostic applications. Despite such great sensitivity, the applicability of this assay towards the detection and discrimination of specific SNP's in complex media such as the wild-type DNA background has yet to be demonstrated. Moreover, given the fact that this assay requires PCR pre-amplification, it is less well-suited to applications that require rapid results such as the point-of-care diagnostics.

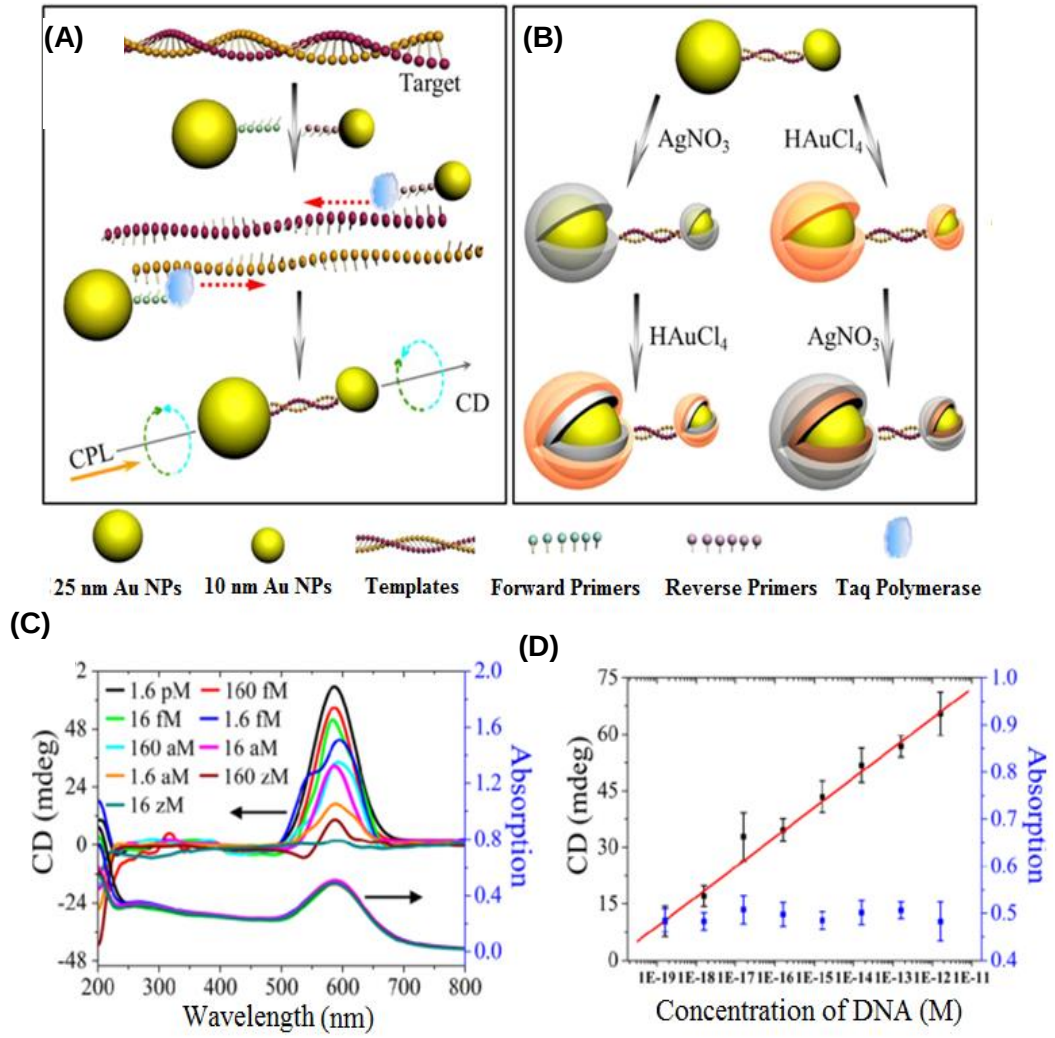

Figure 1-2. Chiroplasmonic core–shell DNA-bridged nanoparticle heterodimers. (A) Schematic illustration of the PCR based assembly of Au nanoparticle dimers. (B) Deposition of Au and Ag on the DNA-bridged Au nanoparticle dimers leading to single and multiple core–shell heterodimers. (C) CD and UV–vis spectra of Au coated heterodimers with DNA concentrations varying from 16 zM to 1.6 pM. (D) Calibration curve relating the intensity of CD bands of Au coated heterodimers and the concentration of DNA. Reprinted from reference 62.

1.3 Nanoparticle assisted probe amplification strategy

Rolling circle amplification (RCA) [75-77] and ligase chain reaction (LCR) [78-80] are two of the most extensively used probe amplification strategies in SNP detections. Recently, nanomaterials have been combined with these probe amplification assays, leading

to further improvements in detection limits. These assays typically use a complementary oligonucleotide capture probe chemically linked to an Au nanoparticle, a quantum dot, or a magnetic nanoparticle to directly interact with their specific analytes, thereby amplifying molecular recognition events such as DNA hybridization. In addition, magnetic nanoparticles have been further used for target capture, enrichment and separation which can further enhance the assay sensitivity. Unlike PCR which requires thermal cycles, RCA is an isothermal probe amplification strategy using a single-stranded DNA as a padlock probe as shown in **Figure 1-3.** The 5′-(phosphate modified) and 3′-terminal fragments of the padlock probe are specifically designed to be complementary to the target DNA. Hybridisation of the target to the padlock probe then brings its 5′- and 3′-terminus close to each other, forming a nicked circle which can be covalently ligated together by a DNA ligase if the padlock and target sequences are fully-matched, forming a circularized padlock probe. The circularised padlock probe is then amplified by a ϕ29 polymerase in the presence of dNTP's, producing a greatly elongated single-stranded DNA containing numerous copies of repeat tandem sequence units complementary to the circular padlock probe. However, the presence of a single-base mismatch at the nicked target/padlock duplex probe can prevent the specific ligation and formation of the circular padlock probe, and therefore no RCA amplification (**Figure 1-3 (B)**). The stringent requirement of full sequence complementary between the padlock and target to form the ligated circular padlock probe allows the RCA strategy to have excellent specificity for SNP detection.[44, 81] In summary, RCA has two fold benefits, first, is the simple reaction mechanism which requires only a single primer and a productive enzyme. Second, the reaction is carried out in isothermal conditions, thus, requiring simple laboratory equipment. Incubation temperature in RCA are usually carried out as low as 23 °C to 30 °C followed by enzyme inactivation at 65 °C.[44,81]

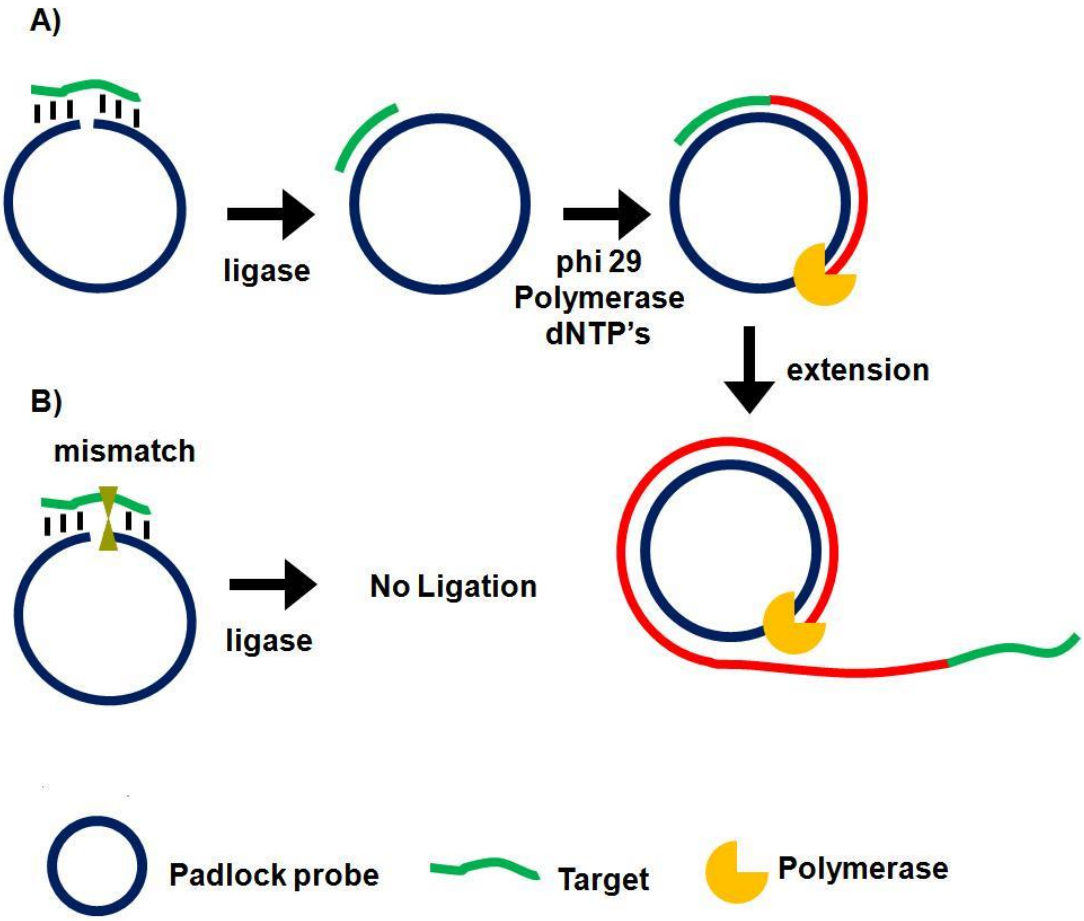

Figure 1-3. Schematic principle of the rolling cycle amplification and SNP discrimination. (A) Hybridization of the perfect-match target DNA to circular padlock probe leads to covalent ligation, producing a target DNA hybridized circular probe where in the presence of phi29 polymerase and dNTP's, the target serves as primer to initiate the circular extension of long single-stranded DNA with repeat sequence complementary to the padlock probe. (B) The presence of a single base mismatch between the target DNA to the padlock probe leads to no ligation and hence no amplification.

Similar to PCR, the ligase chain reaction (LCR) also requires multiple thermal cycles to achieve specific ligation of two short DNA probes catalysed by a DNA ligase into a single strand templated by a full-match DNA target. [26-29] In a typical SNP assay, LCR uses two pairs of probes each containing two short complementary oligonucleotides, but the overall sequence is complementary to the target DNA sequence as shown in **Figure 1-4**.

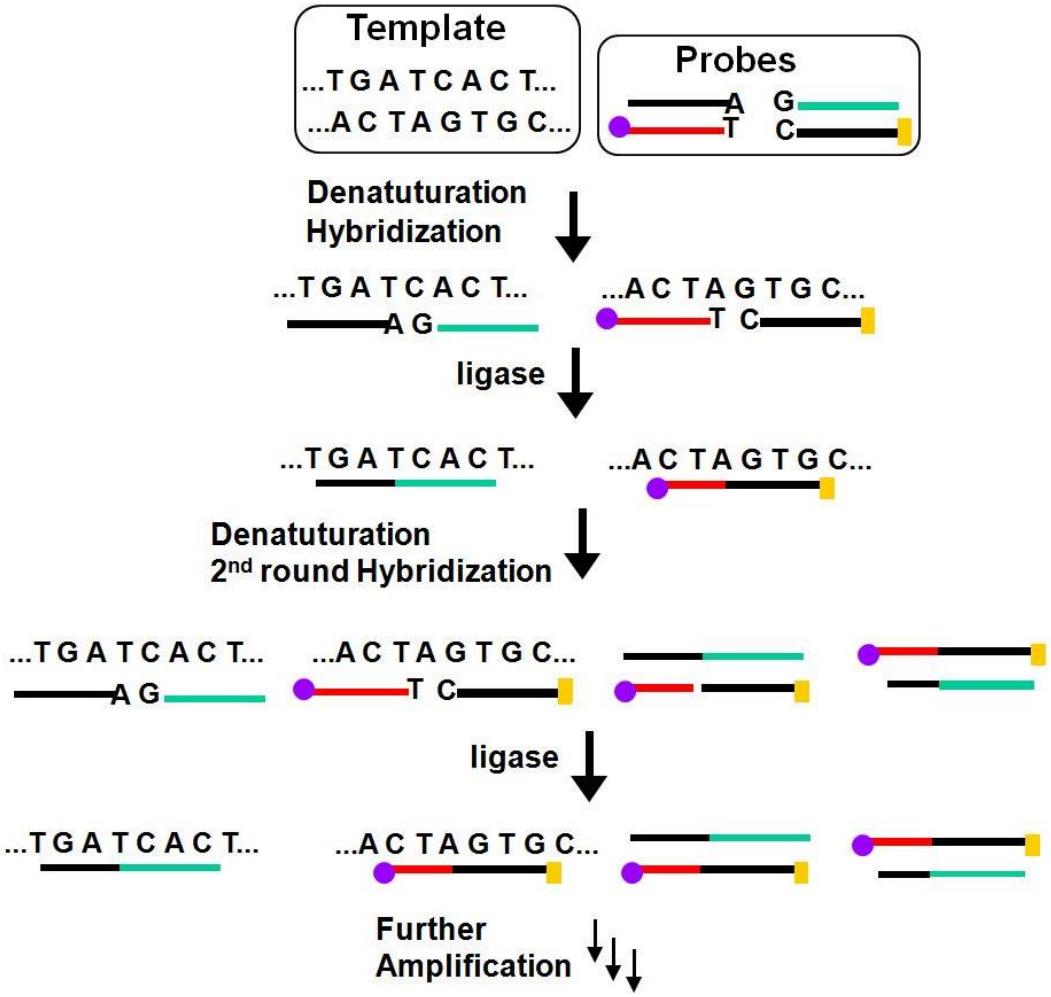

Figure 1-4. Schematic principle of the ligase chain reaction (LCR) based DNA amplification strategy. Each of the two DNA strands in the duplex target serves as a template to ligate its respective two short DNA strands, leading to doubling of the ligated product in each cycle and hence an exponential amplification of the target DNA. The amplified target sequences can then be detected by using their specific and tags.

After thermal denaturation followed by annealing, a pair of the probes are hybridized to one of the denatured target DNA strand. They are subsequently ligated by a DNA ligase if the probes and target sequences are fully complementary at the nick site. On the other hand, the presence of single base mismatch at the nick site can prevent specific ligation, allowing for the LCR to have high SNP selectivity. After the first ligation round, each ligated product can then function as a new template to ligate further probes in the following thermal cycles. Repeating the thermal cycles thus

leads to an exponential increase of the ligated probes. Ligation reactions have better single-base mismatch discriminatory ability than primer extension methods, making LCR more specific for SNP detection than PCR based methods. [26]

A particularly attractive SNP assay has been the colorimetric sensing using Au NPs because of their extremely strong surface plasmon resonance (SPR) absorption at ~520 nm ($\varepsilon > 10^9$ M^{-1} cm^{-1} for a 20 nm Au NP, 4–5 orders of magnitudes stronger than typical organic dyes), making it strongly coloured even at sub-nM concentrations. Moreover, its SPR band is also sensitive to aggregation, isolated Au NPs appear red but aggregated ones are blue or purple. The resulting colour change is distinct and clearly visible by the naked eye.[29] Here specific DNA targets that can induce the aggregation of Au NPs have been used to detect SNPs, taking the full advantage of the very sharp melting transition for the sandwich duplex formed between the target DNA and a pair of probe DNA (with sequence complementary to each half of the DNA target) modified Au NPs. The sharp melting transition means a single-base mismatch between the target and probes can be distinguished due to their slightly different thermal stability. This leads to distinct colour changes at elevated temperatures that can be exploited for SNP detection. [82, 83] Combined with various amplification strategies, such assays have achieved pretty low detection limits, down to the femtomolar region. More recently, LCR has been combined with Au NP for ultrasensitive colorimetric SNP detection by the Gao group. [42] The assay involves the real time ligation of oligonucleotide coated Au NPs templated by the complementary SNP target as shown in **Figure 1-5 (A)**.

In each LCR cycle, there is an increasing amount of Au NPs being ligated that are subsequently used to template the ligation of further Au NPs, leading to an exponential increase in the amount of covalently linked Au NPs. Since the SPR band of Au NPs is sensitive to NP assembly, this resulted in a colour change that can be directly monitored by UV-vis as shown in **Figure 1-5 (B).** This assay has an impressive linear dynamic range of 6 orders of magnitude and is capable of detecting specific DNA targets down to 20 aM. This assay also has high selectivity: it can specifically detect the wild-type (WT) KRAS gene in the presence of large excesses of genomic DNAs even at 1:100 000 (KRAS: genomic DNA) base pair ratios when readings were taken at 90°C. At this temperature, all non-chemically ligated DNA–Au NP conjugates were dislodged, leaving only the covalently ligated Au NPs in the solution. Thus, the incorporation of ligation allowed for easy elimination of interferences from coexisting DNA, giving a greatly reduced background.

(A)

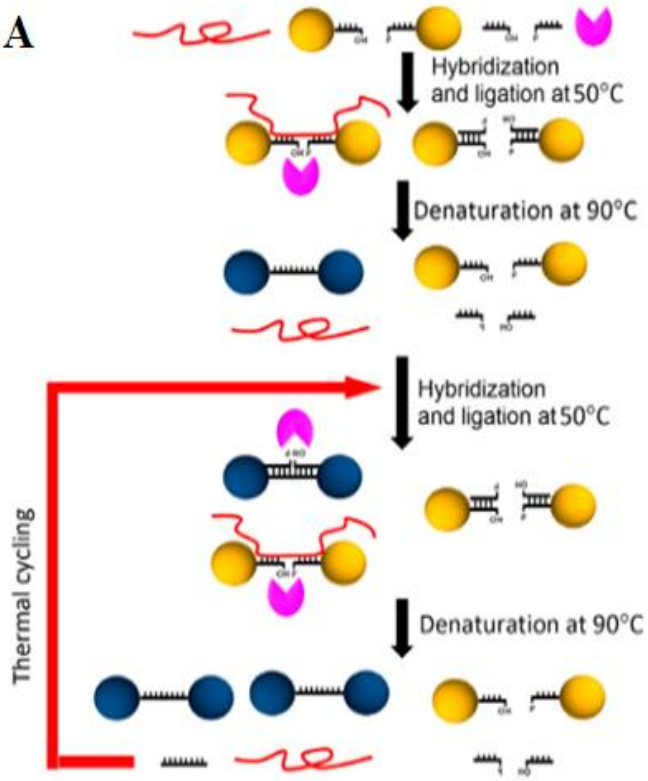

(B)

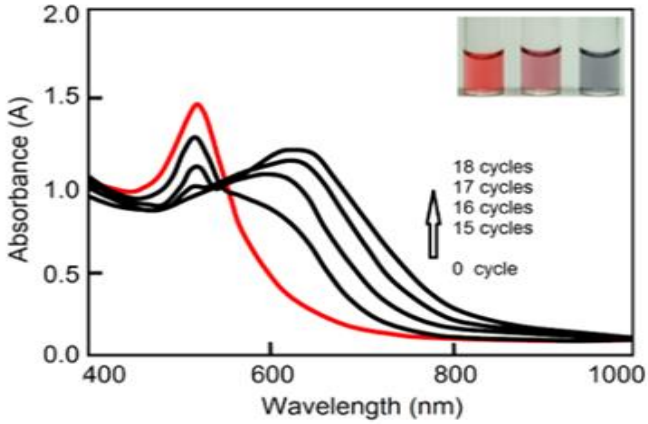

Figure 1-5. (A) Schematic illustration of the real-time Au NP mediated LCR assay. (B) UV–Vis spectra of the solution containing 100 fM target DNA and 10 nM CP-coated Au NPs (CP refers to the trithiolated capture probes) during the LCR process. Inset: colour of solution after addition of 0, 5, and 50 nM (left to right) target DNA to 10 nM CP coated Au NPs. Reprinted from reference [42]

This assay has been further employed to detect the WT-KRAS in the presence of KRAS single point mutants, yielding an impressive SNP selectivity factor of 2000. This assay can be used as an efficient approach for detecting specific mutant DNAs by simply redesigning the sequences of capture probes and signal probes, and thus has great potential for ultrasensitive detection of various disease-related SNPs.

Despite such great promises, the relatively long assay time and the requirement of multiple thermal cycles may limit its use in rapid, point-of-care applications. Although the LCR strategy appears to be a highly attractive alternative to PCR amplification, an apparent weakness has been its low amplification efficiency when being combined with nanomaterials. This is due to the restricted accessibility of the ligases to the ligation site in oligonucleotide modified Au NPs. In an attempt to overcome the limitations of conventional LCR, a process called enzyme-free click chemical ligation reaction (CCLR) that involves Au NP and magnetic bead was developed by Kato and colleagues [63] as shown in **Figure 1-6 (A)**. Unlike the earlier cross-linked Au NP systems, this assay does not require the use of ligases to carry out LCR or the formation of large assemblies. The CCLR method uses an azide-containing DNA modified Au NP and a dibenzocyclooctyne-containing biotin-DNA probe. Sandwich hybridization of the target DNA (RNA) with the azide-DNA modified Au NP and biotin-DNA lead to enzyme-free covalent ligation *via* the copper free click chemistry, producing biotin-ligated Au NPs. Repeating the thermal cycles lead to the biotin-ligated Au NPs being exponentially amplified, which are then captured by using streptavidin-modified magnetic beads. After magnetic separation, the strong absorption of the Au NP can be used to detect and quantify the target DNA (RNA). Using this assay strategy, a DNA sequence associated with the hepatitis A virus Vall 7 polyprotein gene (HAV) has been detected at a concentration as low as 50 zM with a linear dynamic range of 3 orders of magnitude as shown in **Figure 1-6 (B)**, which is highly impressive. However, it should be noted that the absolute signal difference throughout the whole dynamic range was relatively small, being only ~30% (e.g. increased from ~1.0 to 1.3), which can significantly limit its diagnosis accuracy.

The rather small signal difference is likely due to the non-specific nature of the copper-free click reaction: the azide and DBCO-modified DNA probes can react with each other to form covalent linkage even in the absence of a template DNA target, albeit at a slower rate, which is a drawback of this assay design. Nevertheless, this method can discriminate specific single point mutations, with the G-, T-, and C-Mutant signals being 17, 0, and 0% of that of the full-match control, respectively. This result

shows that this essay has an excellent SNP discrimination, although a more useful demonstration of the SNP specificity would be the ability to detect low specific target SNPs in a background of wide-type genes under clinical relevant media [63].

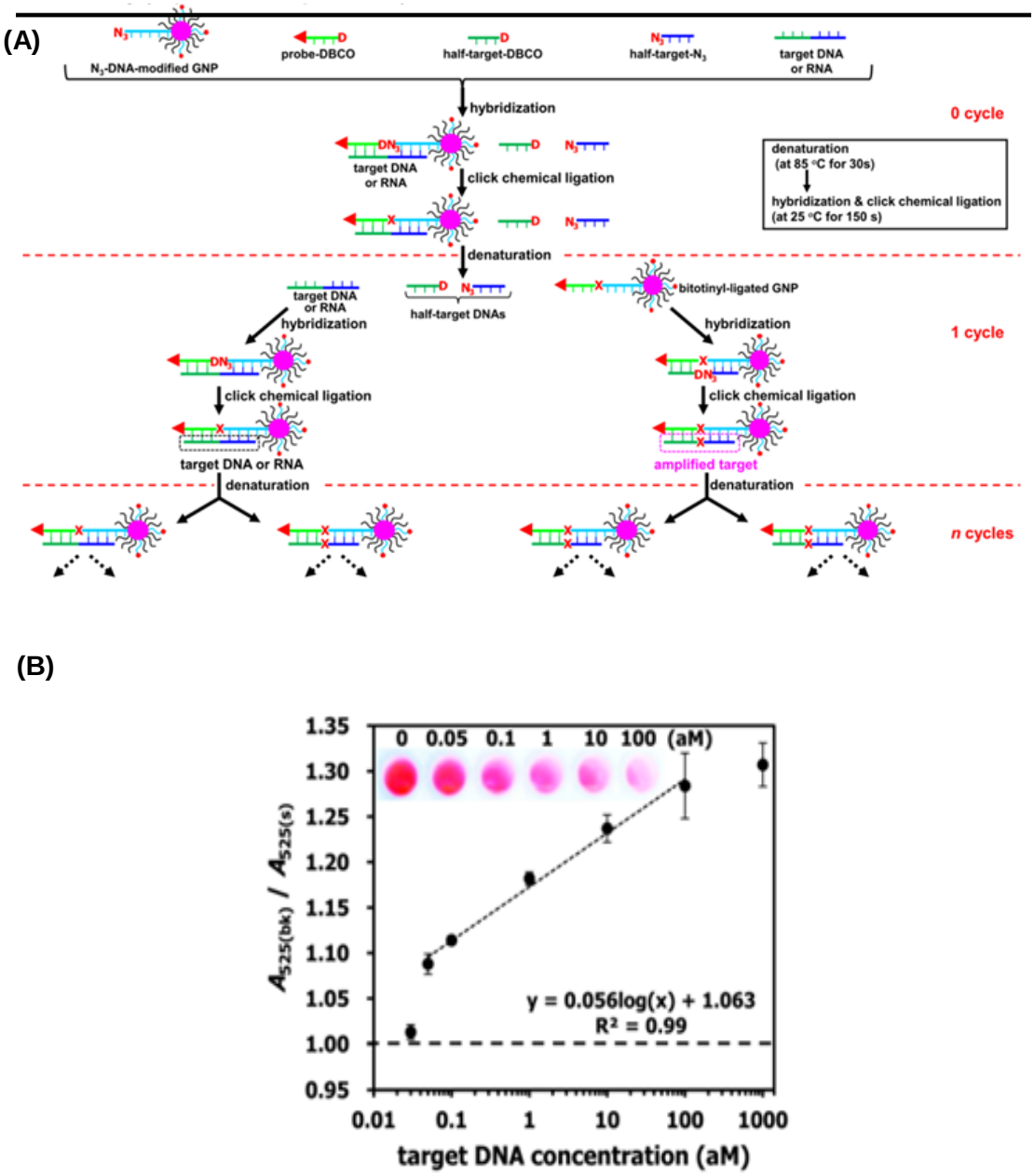

Figure 1-6. (A) Schematic illustration of Enzyme Free Click Chemical Ligation on Au nanoparticles involves the hybridization of the target DNA with an azide-modified Au NP (N3-AuNP), dibenzocyclooctyne-modified probe (DBCO-probe). (B) A plot of the A525(bk)/A525(s) ratio at different target DNA concentrations using 40 thermal cycles. Inset shows a photograph of the supernatants at different target DNA concentrations. Reprinted from reference [63].

Hybridization chain reaction (HCR) is a new DNA assembly technique which based on a chain reaction of recognition and hybridization events between two sets of DNA hairpin molecules [84]. More importantly, this technique offers an enzyme-free alternative for the rapid detection of specific DNA sequences thereby making it simple and cost-effective for DNA biosensor technology [85, 86]. **Figure 1-7** shows the basic reactions taking place in HCR. A single-stranded DNA initiator is added to a stable mixture of two DNA hairpins, it opens a hairpin of one species, exposing a new single-stranded region that opens a hairpin of the other species.

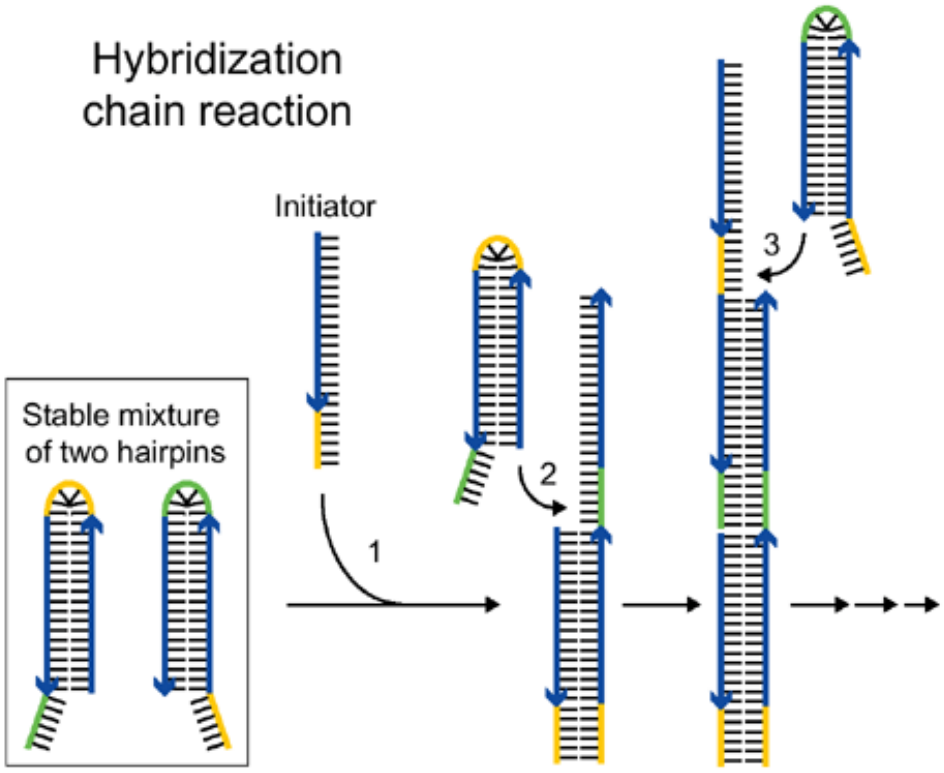

Figure 1-7. Schematic representation of HCR. In Hybridization chain reaction the addition of an initiator strand of DNA to the stable mixture of two hairpin species triggers a chain reaction of hybridization events between the hairpins. Reprinted from reference [84].

This process, in turn, exposes a single-stranded region identical to the original initiator. The resulting chain reaction leads to the formation of a nicked double helix that grows until the hairpin supply is exhausted. However, unlike PCR, HCR is a linear amplification technique, although research is underway to develop non-linear HCR techniques [87-89] which could lead to the possibility of attaining a PCR-like level of sensitivity. Recently, Shuai and colleagues [90] developed an ultrasensitive

DNA biosensor by combining tungsten disulphide/acetylene black (WS_2-AB) nanocomposite coupled with HCR. **Figure 1-8** shows the design principle of the DNA biosensor. In their work, tungsten disulphide/acetylene black (WS_2–AB) composite nanosheets were synthesized by a hydrothermal method. The electrochemical DNA biosensor was fabricated based on the Au nanoparticles (Au NPs) and a WS_2–AB composite modified glassy carbon electrode (GCE) to form the Au NPs/WS_2–AB/GCE. The ssDNA probe was linked to the modified electrode *via* an Au–S bond. In the presence of target DNA, the probe DNA can hybridize with target DNA on the electrode. After that, an auxiliary DNA (sequence complementarity to target DNA) hybridizes with target DNA and the two species of DNA hairpins biotin-H_1 and biotin-H_2 are opened by the recognition probe, and hybridized one by one. The nicked double helices from hybridization chain reaction were used to immobilize Neutravidin-horseradish peroxidase *via* the strong biotin–avidin interaction, converting each target DNA into multiple copies of HRP for signal-amplification through the catalytic reaction of the H_2O_2 + hydroquinone system. As a 2D layered nanostructure, the as-prepared WS_2–AB displayed a large effective surface area. This allowed more biomolecules (capture DNA) to be immobilized at the electrode surface, which reduced the distance for electron transfer and ion diffusion paths between the capture DNA and nanomaterials. As a result, the electron transfer to the electrodes became easier. Under optimal conditions, the as-prepared biosensor showed a good linear relationship between the current value and logarithm of the target DNA concentration ranging from 0.001 pM - 100 pM with an LOD as low as 0.12 fM. Moreover, the fabricated biosensor exhibits good selectivity to differentiate the single base mismatched DNA sequence. However, the need to design multiple DNA probes and multiple steps may limit its potential for cost-effective and rapid DNA detection.

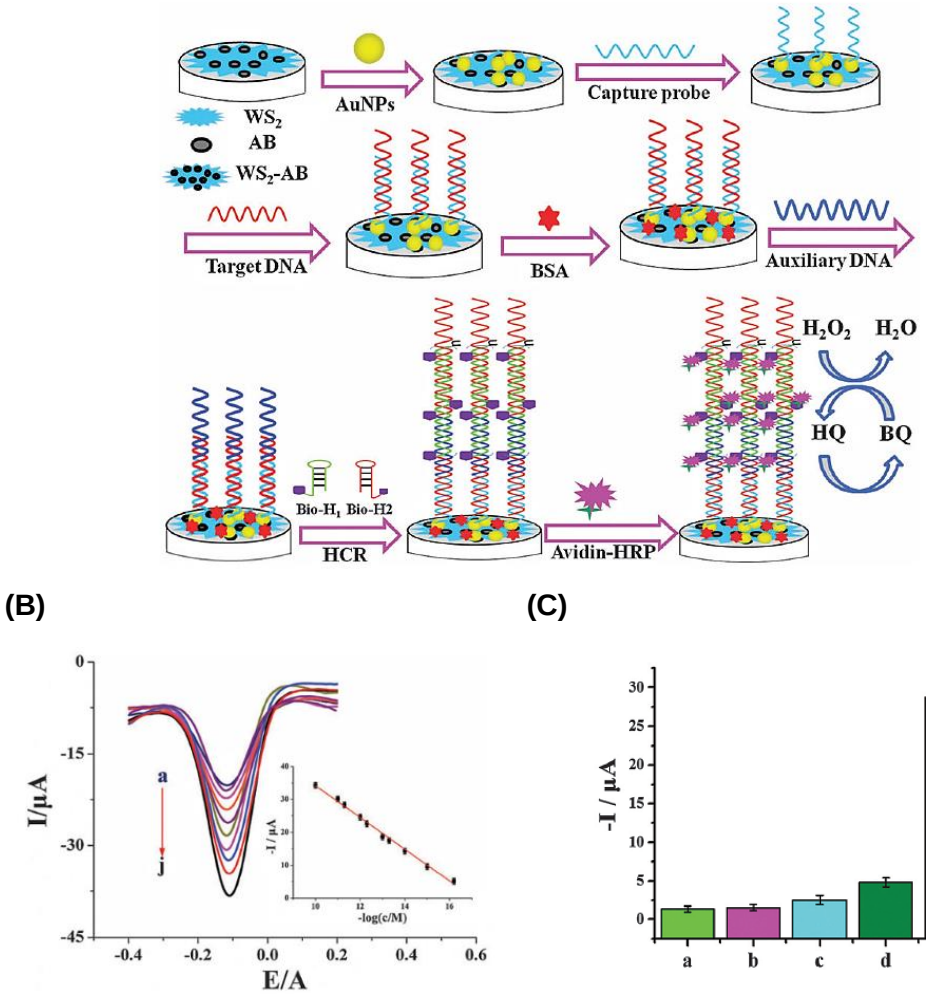

Figure 1-8. (A) Schematic illustration of the working principle of DNA detection based on the hybridization chain reaction. (B) DPV curves responding to different target DNA concentrations (from a to j): 0, 1.0 x 10^{-15}, 1.0 x 10^{-14}, 5.0 x 10^{-14}, 1.0 x 10^{-13}, 5.0 x 10^{-13}, 1.0 x 10^{-12}, 5.0 x 10^{-12}, 1.0 x 10^{-11}, 1.0 x 10^{-10} M, respectively. Inset: the relationship between the peak current and the negative logarithm of the target DNA concentration, and (C) The specificity of the HCR-based DNA sensor hybridized to different target sequences: blank (PBS 7.0) (a), 1.0 x 10^{-11} M non-complementary sequence (b), 1.0 x 10^{-11} M three-based mismatch sequence (c), 1.0 x 10^{-11} one-base mismatch sequence (d) and 1.0 x 10^{-11} M complementary sequence (e). Reprinted from reference [90].

1.4 Target recycling coupled with probe and/or signal amplification

Target recycling is another useful strategy to amplify low copy number SNPs. In this strategy, the target DNA is cycled in a number of hybridization events, each time producing one or several copies of the complementary probe, depending on the approaches used. However, the linear amplification nature of target recycling has largely limited its detection limit to the fM regime only [56, 91]. More recently, target recycling has been combined with other probe amplification strategies to further improve detection limits. A significantly higher sensitivity has been achieved by Ji and colleagues [49] who have designed a template enhanced hybridization process (TEHP) coupled with rolling cycle amplification. This assay uses a biotinylated molecular beacon [MB] bound to a streptavidin coated plate as the template. Hybridization of the target DNA and an assistant DNA to the loop region of the MB forms a “Y” shaped junction as shown in **Figure 1-9 (A)**. This configuration provided a specific nucleotide sequence that can be nicked by a suitable endonuclease. Once released, the target DNA and assistant DNA initiate another round of hybridization and strand scission cycle. The numerous MB fragments left in the plate then served as primers for the RCA process to produce thousands of repeat oligonucleotide sequences. These repeated sequences then are hybridized to an oligonucleotide functionalized CdTe QD and separated. The QDs are then dissolved by an acid, releasing greatly amplified Cd^{2+} ions that are detected by square wave voltammetry. The combination of TEHP and RCA coupled with the use of QD signal tags has offered an enormous amplification of the DNA target, allowing for greatly increased assay sensitivity. An impressive sensitivity of 11 aM has been attained together with a wide dynamic range of 6 orders of magnitude as shown in **Figure 1-9 (B)** and **(C)**. This assay was also able to discriminate the perfect complementary DNA target against various mismatch targets with a discrimination ratio of 3.8, 5.7 and 6.6 fold for the single-base, three-base mismatch and non-complementary oligonucleotides, respectively. Despite a high sensitivity, its SNP discrimination ratio is relatively moderate compared to other SNP assays, which may limit its potential for applications in real clinical samples where the presence of large background genomic DNAs and/or wild-type genes may strongly interfere the specific SNP detection.

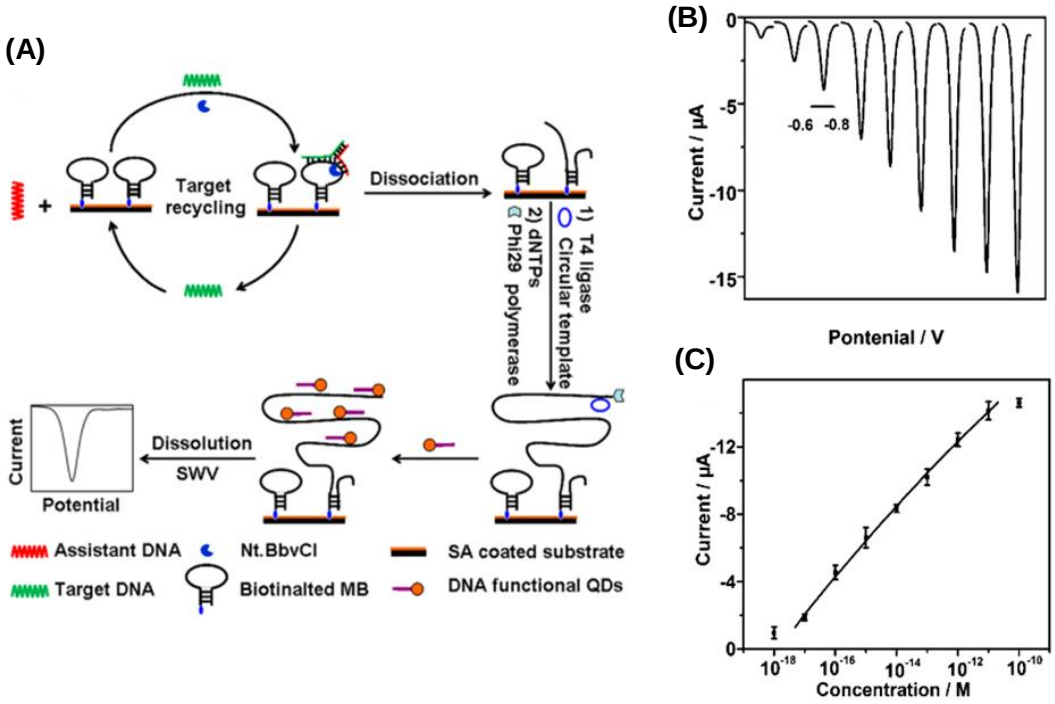

Figure 1-9 (A) Schematic illustration of the TEHP amplification strategy for DNA detection, (B) stripping voltammetric curves of cadmium ions corresponding to (left to right) 10^{-18}, 10^{-17}, 10^{-16}, 10^{-15}, 10^{-14}, 10^{-13}, 10^{-12}, 10^{-11}, and 10^{-10} M of target DNA. (C) The corresponding analytical quantitative dynamic range. Reprinted from reference[49].

1.5 Tandem amplification schemes and signal catalytic cascades

In order to achieve detections in even lower concentration regimes, several researchers have reported the use of tandem amplification schemes.[44, 64, 81] The combination of two amplification strategies has been deemed necessary to further improve the sensitivity and specificity of SNP detection. Moreover, this strategy can overcome the low amplification efficiency of a single amplification strategy. For example, the colorimetric detection of SNPs using a combination of RCA and nicking endonuclease-assisted nanoparticle amplification strategy was developed by Xu and colleagues. [44] In this assay, ligation was performed when the target DNA was hybridized with the padlock probe, leading to a circularized template. Subsequent RCA reaction in the presence of dNTPs led to the formation of a long single strand DNA. Nicking reactions at many of the repeated sites along the RCA elongated

single-stranded DNA occurred simultaneously. Upon completion of the strand scission cycles, the addition of a specific oligonucleotide modified Au NP provided a simple, colorimetric detection of target DNA down to 1 pM.

The sensitivity of ligation assays can be further improved when being coupled to another probe amplification scheme. For example, the combination of LCR and RCA in detecting SNPs has been recently demonstrated by Cheng and colleagues, [79] who have demonstrated the sensitive detection of 1 fM of unlabelled target DNA under the optimised assay conditions. Further improvements of assay sensitivity have been achieved by incorporation of DNAzymes (catalytic nucleic acids) based catalytic cascades signal amplification. In this regard, Zhang and colleagues [53] have designed a new RCA amplification approach where the presence of the target KRAS SNP triggers the ligation of the padlock probe. Subsequently, multiple other circular templates were interlocked to the padlock probe by means of complementary sequence forming an ABABAB-type DNA copolymer as shown in **Figure 1-10 (A)**. The inter-locked circular primers containing the HRP-mimicking DNAzymes subsequently underwent another round of RCA, producing long, single-strand DNA products each containing thousands of copies of the repeated DNAzyme sequences acting catalytic units. The incorporation of numerous such catalytic units thereby greatly enhanced the chemiluminescence signal in the presence of luminol and H_2O_2, leading to an impressive detection limit of 71 aM for the target SNP. This assay also provided excellent performance in quantitative analysis in human blood serum with a linear dynamic range of 2 orders of magnitude with good signal linearity from 0.1–10 fM as shown in **Figure 1-10 (B)** and **(C)**. The excellent sensitivity of this assay lies on the inherent capacity to generate great amplification as a consequence of the high turnover reaction of DNAzymes. This assay was also highly specific, and can detect 1 fM specific mutant target in the presence of 10 pM wild-type gene background, representing a SNP detection capability of 1 in 10 000 (SNP versus wild-type target) level, which was among the best reported in literature. Hence, combining high sensitivity and specificity, this assay appears to have excellent potential for SNP based disease diagnostics by specific detection of the low abundant mutated target in clinical laboratory settings. This assay, however, is relatively complex and requires multiple amplification cycles, making it less well-suited for rapid, point-of-care applications.

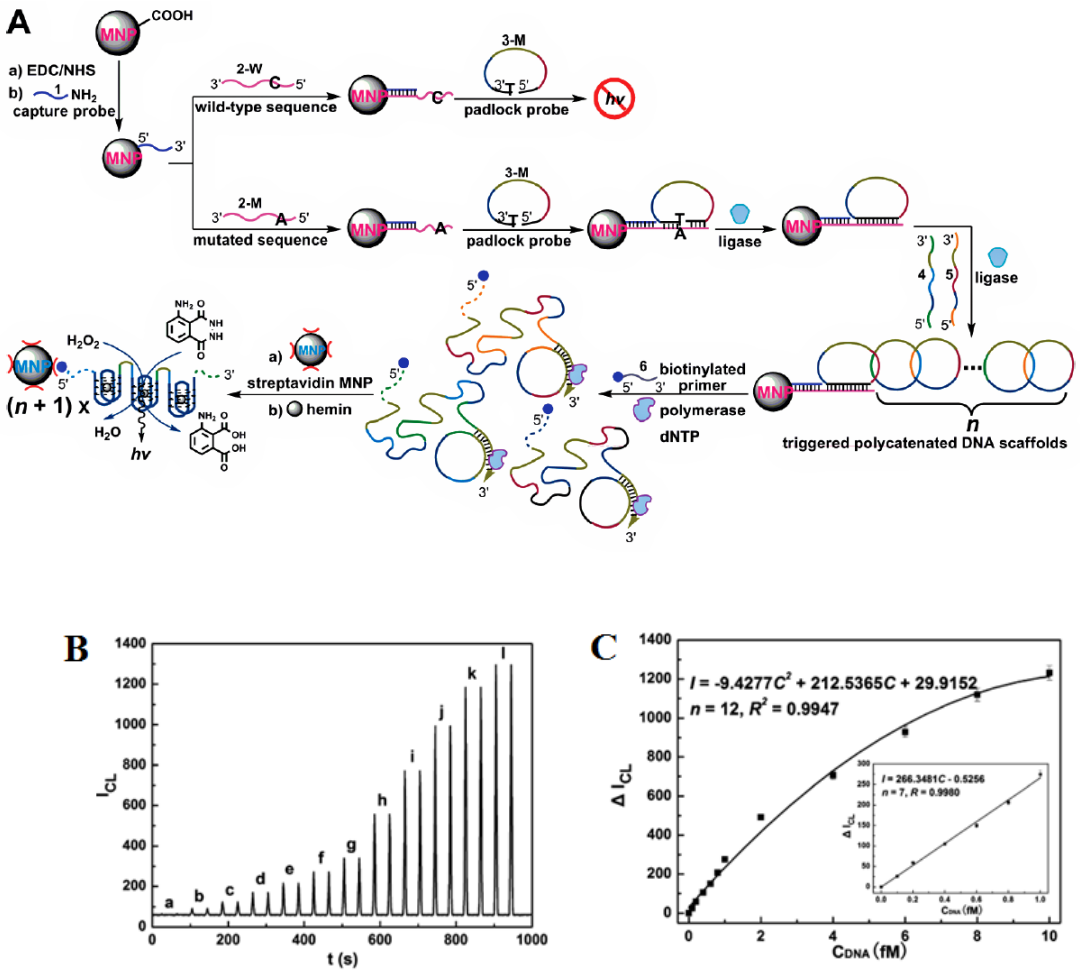

Figure 1-10. (A) Schematic representation of interlocked DNA scaffold mediated RCA reaction and DNAzyme amplification assay for the detection of G12C mutation in the KRAS gene. (B) Chemiluminescence signals for the HRP-mimicking DNAzyme-catalyzed luminol-H_2O_2 system corresponding to different concentrations of single-base mutant target DNA: (a) 0; (b) 0.1; (c) 0.2; (d) 0.4; (e) 0.6; (f) 0.8; (g) 1.0; (h) 2.0; (i) 4.0; (j) 6.0; (k) 8.0; (l) 10.0 fM, and (C) The corresponding calibration curve of peak height versus the concentration of target DNA. Reprinted from reference [53].

Recently, the Zhang group developed an ultrasensitive miRNA assay based on primer generation-mediated rolling circle amplification [PG-RCA]. This assay was used to analyse the point mutation of mir-196a2 [T→C] in the lung tissue samples of non-small cell lung cancer patients. [64] In this assay, the presence of target mir-196a2T circularizes the padlock probe and the mir-196a2T further functioned as a primer to initiate the next round of RCA reaction in the presence of Vent (exo-) polymerase. This resulted in a long single-stranded RCA product containing numerous restriction sites for *Nb.BsmI*. The RCA product was then nicked by *Nb.BsmI*, generating a large number of new primers that was further used to initiate a new RCA reaction. The amplified DNA products were subsequently hybridized with a biotin/Cy5-labeled capture probes to form a double-stranded DNA. This DNA duplex contains a recognition site for the *Nt.BstNBI* nicking enzyme, and after the nicking reaction the capture probe was cleaved, separating Cy5 and biotin. This also resulted in the release of the amplified DNA product which can repeatedly hybridize with new biotin/Cy5-labeled to initiate the next rounds of cleavage. In a similar strategy, mir-196a2C was detected using the designed mir-196a2C padlock probes. In the absence of the mir-96a2T, more Cy5/biotin capture probes were cleaved, leading to smaller amounts of the intact capture probes to bind to the streptavidin-coated QD. Consequently, this reduced the FRET between the QD donor and Cy5 acceptors, resulting in decreased Cy5 counts being detected in the single particle FRET detection measurement. On the other hand, the mir-196a2T-specific linear padlock probe cannot be circularized in the absence of mir-196a2T. Under these conditions, RCA amplification and cleaving reactions will happen. Hence, the biotin/Cy5-labeled capture probe remains intact which can bind to the QD surface via specific streptavidin–biotin interactions, resulting in strong QD sensitised Cy5 FRET signal. With the integration of the PG-RCA reaction and nicking enzyme-driven recycling amplification, this QD-based miRNA nanosensor exhibited an impressive detection limit of 50.9 aM and a large dynamic range of 7 orders of magnitude from 0.1 fM to 1 nM for the specific microRNA target. Moreover, this assay can even distinguish variant frequencies down to as low as 0.001% in the mixtures of mir-196a2C and mir196a2T. Importantly, this QD-based miRNA nanosensor can be used to analyse the point mutation of mir-196a2 in the lung tissues of NSCLC patients, holding great potentials for clinical diagnosis in the clinical laboratory settings. Its complex signal amplification and assay procedures together with a relatively complex single-particle counting readout method may, however, limit its use in applications that require rapid results.

1.6 Nanomaterial assisted signal amplification

In signal amplification, nanomaterials are often functionalised with biomolecules for target-specific recognitions and/or carrying high loads of signal moieties, catalysts, optical emitters, and electronic conductors. Biofunctionalised nanomaterials can amplify the signal transduction events due to their capability of direct interaction with their target, allowing for detection of biomolecules down to the single-molecule level [92]. Signal amplification can eliminate some requirements of the target/probe amplification schemes such as the need of enzymes and thermal cycles (*ca.* PCR). As a result, this can simplify experimental protocols, reduce the assay cost, and provide amenability to miniaturisation. Hence, the use of biofunctionalised nanomaterials for signal amplification has been very attractive in the development of simple, ultrasensitive DNA assays without the need of target and probe amplifications. The following section presents some ultrasensitive detection of SNPs achieved through use nanomaterials for signal amplification.

1.6.1 Nanoparticle bio-barcode amplification

An excellent example of the earlier developments here is the Bio-barcode assay developed by the Mirkin group. [65] It uses a short DNA modified Au NP tagged with hundreds of copies of the biobarcode DNAs (Bbc-Au NP) as signal probe, and another DNA modified magnetic microparticle (Oligo-MMP) as capture probe as shown in **Figure 1-11**. The two DNAs are complementary to each half of the target DNA, so that they can sandwich bind to the target DNA, forming a Bbc-Au NP/DNA target/Oligo-MMP hybrid structure. After magnetic separation and washing to remove any unbound species, thermal denaturation of the hybrid releases the bio barcode DNAs, converting each capture DNA target into hundreds of copies of barcode DNAs. These are then detected by a sensitive scanometric assay coupled with silver amplification to achieve ultrasensitivity. [93] This assay provides an impressive label-free detection of target DNA down to 500 zM, comparable to many PCR based methods. [65] It can also discriminate the perfect match DNA from the SNP target. Although its relatively modest discrimination ratio, ~3:1, may limit its capability of detecting low abundant SNP targets in wild-type gene background.

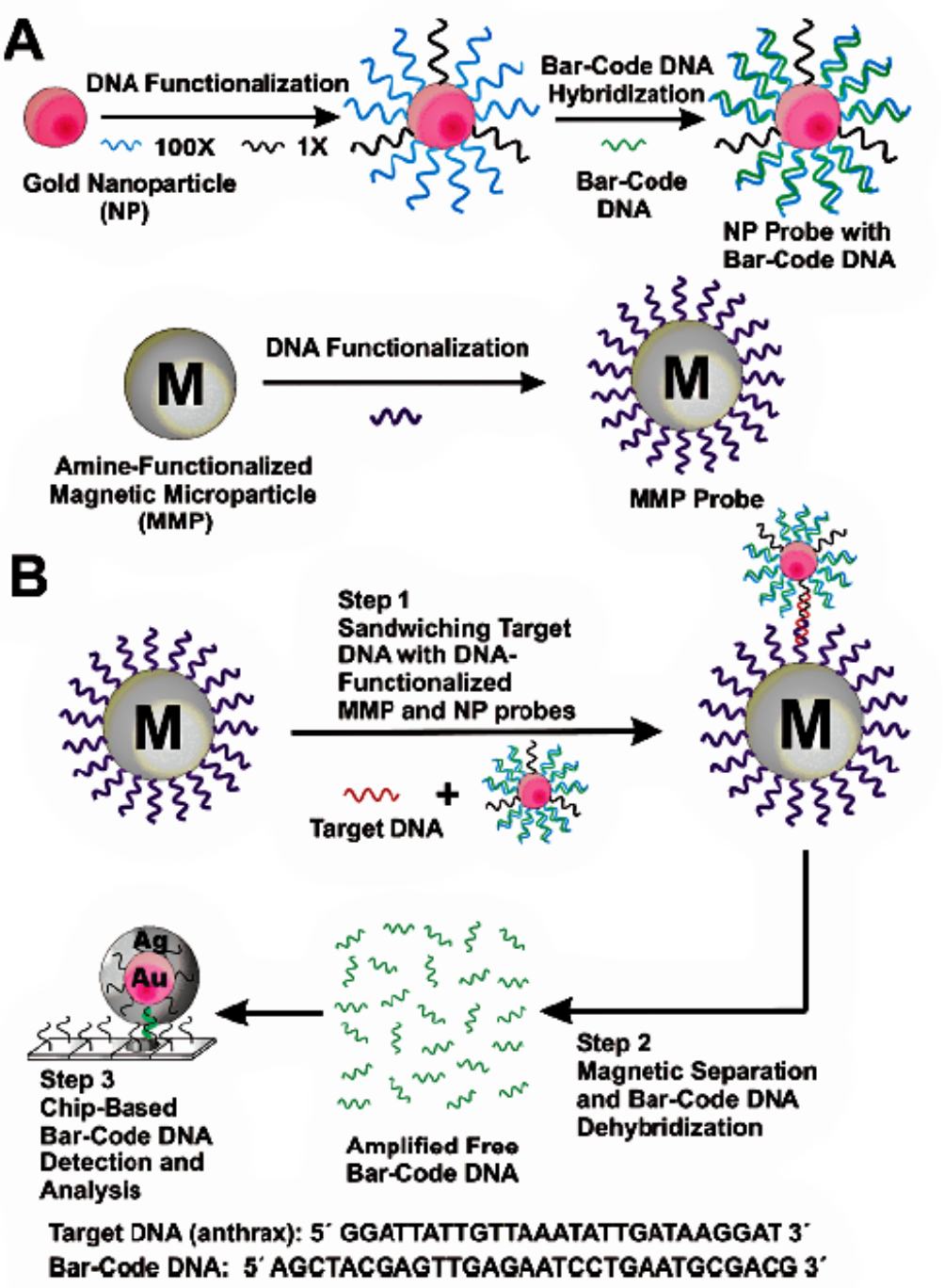

Figure 1-11. Schematic illustration of the DNA-Bio-bar-code based ultrasensitive assay for DNA detection. (A) The preparation of the DNA modified Au NP and magnetic microparticle probes. (B) Schematics of the nanoparticle-based PCR-free DNA amplification and detection scheme. Reprinted from reference [65].

1.6.2 Signal amplification using labelled and enriched nanoparticle probes

Metallic nanoparticles can be employed as scaffold for loading not only the capture but also signal molecules. These labelled nanoparticles present an important signal amplification strategy as they can directly enhance the readout signal for each target and probe recognition while retaining a high binding specificity. An interesting ultrasensitive biosensor was demonstrated by Taylor and colleagues [94] by developing a metallic core-shell nanoparticle signal amplifier which they termed “ultrabright SERS nanorattle”. These ultrabright SERS nanorattles are composed of an Au core and a shell with resonance Raman reporters loaded in the gap space between the core and the shell as shown in **Figure 1-12 (A)**. These metallic core-shell “nanorattles” greatly enhanced the signal readout using surface enhanced Raman scattering (SERS) as compared to the conventional Raman reporters (Au or Ag NP) coated with Raman reporter tags. The fabrication of the “nanorattle” signal amplifier and the biosensing principle are shown in **Figure 1-12 (B)**. The biosensing approach is based on the hybridization of the target DNA to the magnetic bead (MB) modified with DNA capture probe and nanorattle modified with DNA forming a MB-DNA-Nanorattle sandwich. A permanent magnet is then used to concentrate the “MB-DNA-Nanorattle sandwich” onto a small spot for SERS measurement. The nanorattle’s intense SERS brightness can be attributed to two factors. First, with a nanometre size gap between the nanorattle’s core and shell which could be loaded with a greater number of Raman reporters than monolayer coated Au NPs. Second, the E field enhancement in the gap space of the nanorattle was estimated to be several times higher than that on Au NP surface. Using this method and under optimal conditions, a specific DNA sequence of the malaria parasite *Plasmodium falciparum* was detection with a detection limit of approximately 100 attomoles (30 µL reaction volume). The biosensor could also discriminate SNP of wild type malaria DNA and mutant malaria DNA (SNP discrimination ratio ~ 8:1) [94].

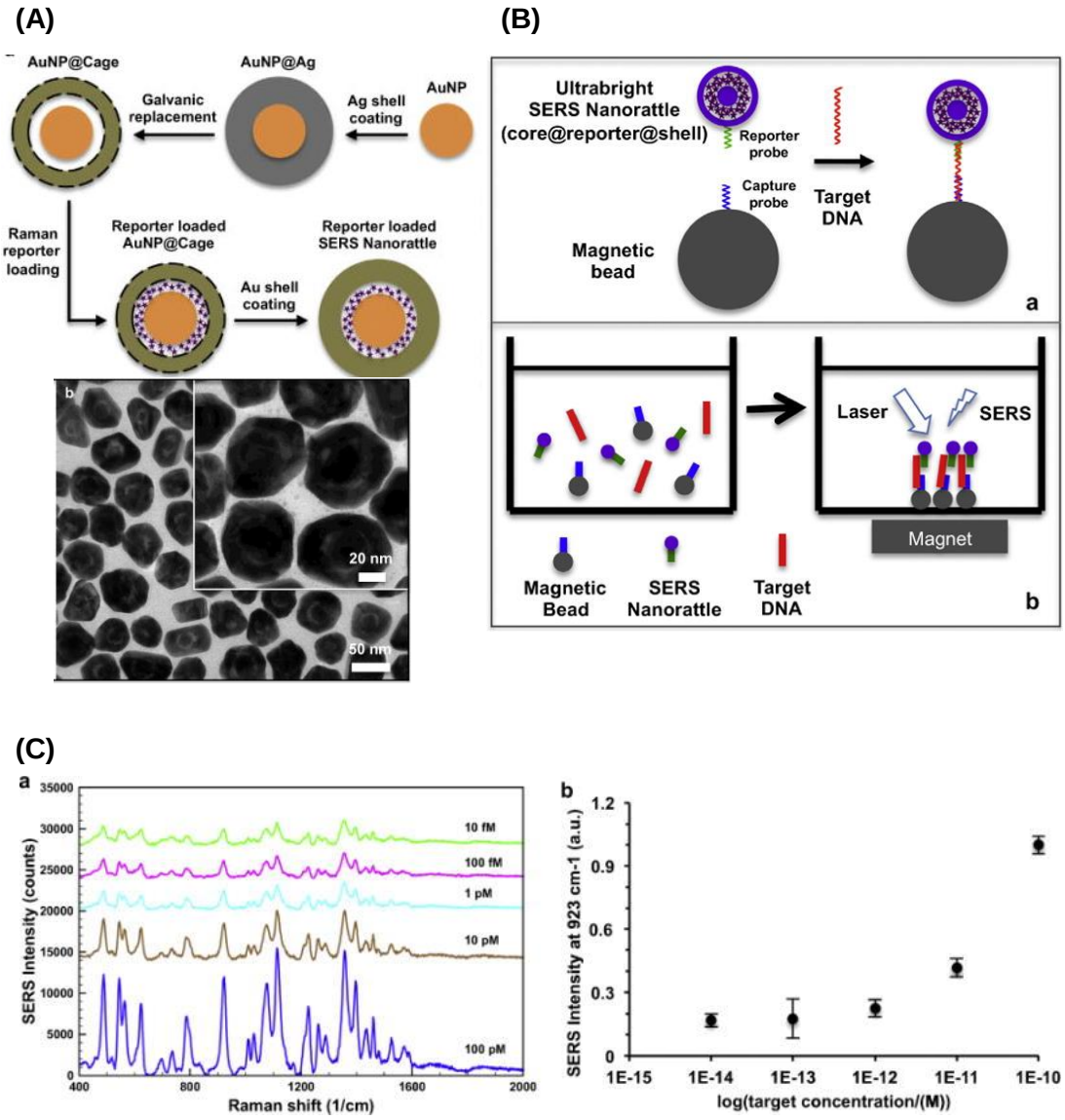

Figure 1-12. (A) SERS nanorattle synthesis process and TEM image of nanorattles with core-gap-shell structure (inset: higher magnification TEM image). Raman reporters were loaded into the gap space between the core and the shell. The nanorattle-based DNA detection method using sandwich hybridization of (1) magnetic bead that are loaded with capture probes, (2) target sequence, and (3) ultrabright SERS nanorattles that are loaded with reporter probes. (b) A magnet is applied to concentrate the hybridization sandwiches at a detection spot for SERS measurements. (C) SERS spectra at different concentrations of wild type target *P. falciparum* gene *PF3D71343700* (vertically shifted for clarity). (b) SERS intensities at 923 cm^{-1} (normalized) vs. log(target concentration/(M)). Error bars represent standard deviations (*n* = 3). Reprinted from reference [94].

Over the past few years, silica particles have been used as another platform for carrying signal tags due to their large surface areas, well-known surface chemistries and good biocompatibility. Wu and colleagues have reported a labelling-based signal amplification strategy for ultrasensitive detection of target DNA using QD assembled SiO_2 microspheres. [66] This method is used as an indirect method for ultrasensitive detection of HIV DNA using hydride generation atomic fluorescence spectrophotometry [HG-AFS]. This assay involves the use of sandwich hybridization between the target DNA, biotin-capture probe and streptavidin tagged QD-SiO_2 assembly, converting each captured DNA target into thousands of SiO_2 tagged QDs. After acid dissolution of the QDs, the resulting Cd^{2+} ions were detected by HG-AFS, giving a highly impressive detection limit of 0.8 aM for the target DNA and a dynamic range of 3 orders of magnitude (from 1 aM to 1 fM). The outstanding sensitivity suggests that the HG-AFS method is suitable for the ultrasensitive biosensing.

An ultrasensitive chemiluminescent method using Au NP based signal amplification has recently been developed by Zhang and colleagues. [67] Using the Watson–Crick base pairing, a guanine monomer modified Au NP probe is coupled to the cytosine mutated DNA duplex in the presence of DNA polymerase I. Each guanine modified Au NP probe is also linked to 77 CuS NPs which act as signal generator. After acid dissolution of the CuS NPs, the released Cu^{2+} ions are coordinated to cyanides to form $[Cu(CN)_4]^{2-}$ complexes which are then reacted with luminol to give rise to chemiluminescence signal for target DNA quantification. A further improvement in the signal sensitivity is achieved by incorporating a pre-concentration of Cu^{2+} ions by anodic stripping voltammetry (ASV). These have enabled this assay to achieve a low detection limit of 19 aM for one base mutant DNA and a linear range of 80 aM to 10 fM.

Zhang and colleagues [95] have recently demonstrated a simple electrochemical DNA biosensor based on CdSe QDs as signal amplifier combined with *MspI* restriction endonuclease. The design concept of the biosensor is shown in **Figure 1-13.**

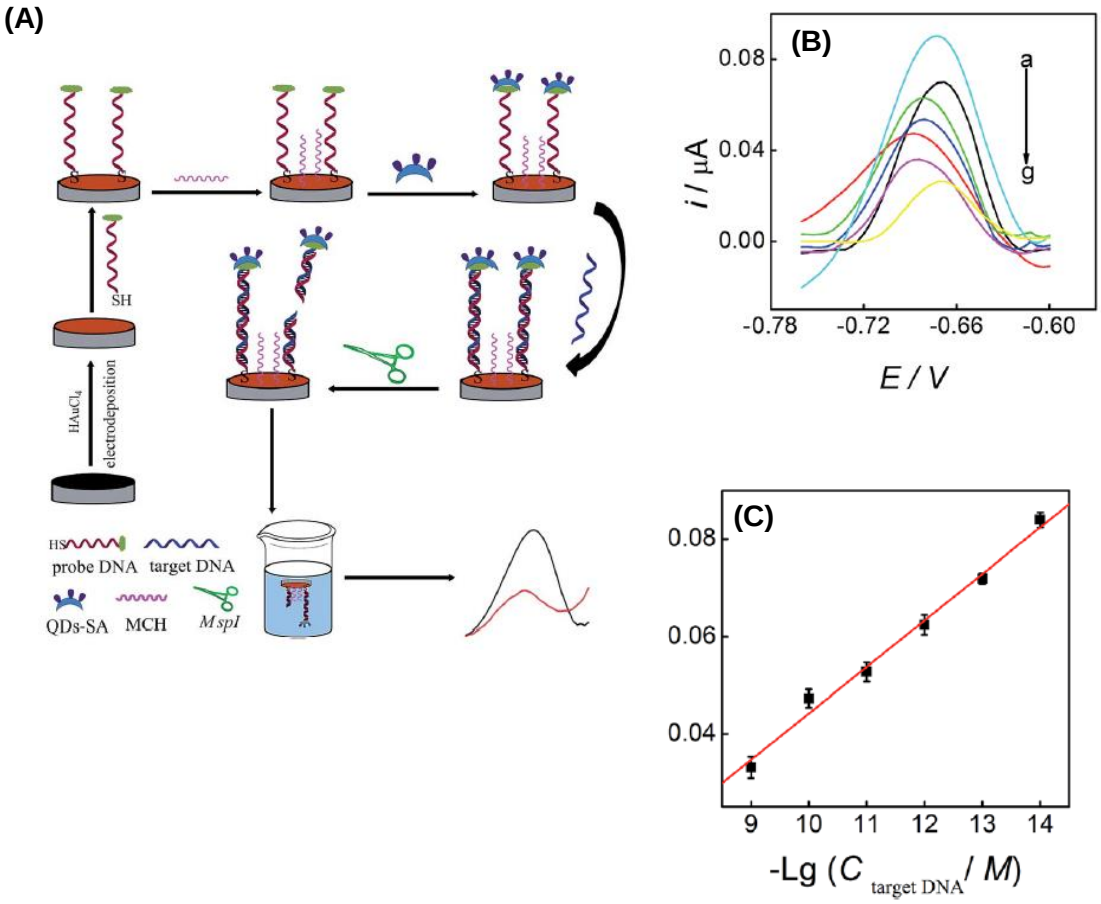

Figure 1-13. (A) Schematic diagram of the biosensor approach (B) SWV of the *MspI*/target DNA/CdSe QDs–SA/MCH/probe DNA/AuNPs modified glass carbon electrode in the presence of different concentrations of target DNA (0, 10^{-14}, 10^{-13}, 10^{-12},10^{-11}, 10^{-10} and 10^{-9} M from top to bottom) in 0.1 M HAc–NaAc buffer solution (pH 4.6). (C) The linear relationship between the currents (i) and the negative logarithm of target DNA concentrations. Reprinted from reference [95].

The biosensor is glassy carbon electrode modified with Au NPs . The electrode is labelled with biotin-DNA-SH probes and bound to CdSe QD–streptavidin (SA) *via* the specific biotin-streptavidin interaction. After hybridization to the complimentary target DNA probe, the *MspI* endonuclease recognize the specific sequence in the ds DNA and cleaves the dsDNA-CdSe QDs from the electrode. This results to a decrease in the electrochemical signal. The concentrations of target DNA could be simultaneously detected by the signal of metal markers. Using mycobacterium tuberculosis (*Mtb*) DNA as a model, under the optimal conditions, the proposed biosensor could detect *Mtb* DNA down to 8.7 f M with a linear range of 5 orders of

magnitude spanning from 1.0 x 10^{-14} to 1.0 x 10^{-9} M. Furthermore, the biosensor was also shown to be able to discriminate single nucleotide mismatch from target DNA.

The labelling of the target DNA with a large number of signal generators coupled with sensitive electrochemiluminescence SNP detection was demonstrated by the Willner group[54]. In this assay, a mutant DNA with one base mismatch (C→G mutation) was hybridised to a complementary DNA modified magnetic NP. It was then treated with a DNA polymerase in the presence of biotin-dCTP and other dNTPs. This was followed by multiple thermal cycles of dissociation, annealing and labelling, resulting in poly-labelling of the magnetic NPs with biotins. After magnetic separation and treatment with avidin-horseradish peroxidase (Avidin-HRP), the resulting avidin-HRP functionalised magnetic NPs and napthoquinone NPs were deposited on an electrode guided by an external magnetic field. Applying an electric potential reduces napthoquinone to hydroquinone, which simultaneously reduces O_2 to H_2O_2, triggering the HRP catalysed oxidation of luminol and yielding a chemiluminescence signal. Under optimized conditions, this assay has reported an impressive sensitivity of 8.3 aM for the M13φ DNA (50 copies in 10 μL sample) and 10 aM for a mutant DNA. Despite showing impressive sensitivities, none of the above ultrasensitive assays have reported the simultaneous detection of multiple targets. Further developments on the multiplexing capability of an SNP assay are highly desirable for improving the diagnostic accuracy.

Recently, Gambari and colleagues [68] have reported the direct detection of SNPs in non-amplified human genomic DNA carrying the mutated β°39-globin gene sequence by surface plasmon resonance imaging (SPRI). This gene is involved in the hereditary blood disorder diseases known as β-thalassemia. The detection is achieved by using Au NP conjugated with multiple copies of DNA β°39, an 11-mer oligonucleotide. Prior to analysis, the surfaces of 6 microfluidic channels are modified with PNA-N and PNA-M probes whose nucleic acid sequences are complementary to the normal and mutant genes respectively as shown in **Figure 1-14**. The samples are directly fluxed into these channels to allow the direct hybridisation between each of the samples (e.g. normal βN/βN; homozygous β°39/β°39 and heterozygous β°39/βN) on PNA functionalized surfaces. The SPRI responses between the samples and the two different PNA probes are used as controls. Subsequently, the conjugated Au NPs are fluxed into the microchannels and captured by specific hybridization between their surface DNA β°39 strands and exposed target DNA sequence not involved in binding to the PNA probes, allowing for greatly enhanced SPRI signal.

This assay has achieved the sensitive detection of genomic DNAs down to 2.6 aM (5 pg μL^{-1}) without PCR amplification. It can also discriminate between the normal, homozygous β°39/β°39, and heterozygous β°39/βN sequences, albeit with a relatively modest discrimination ratio.

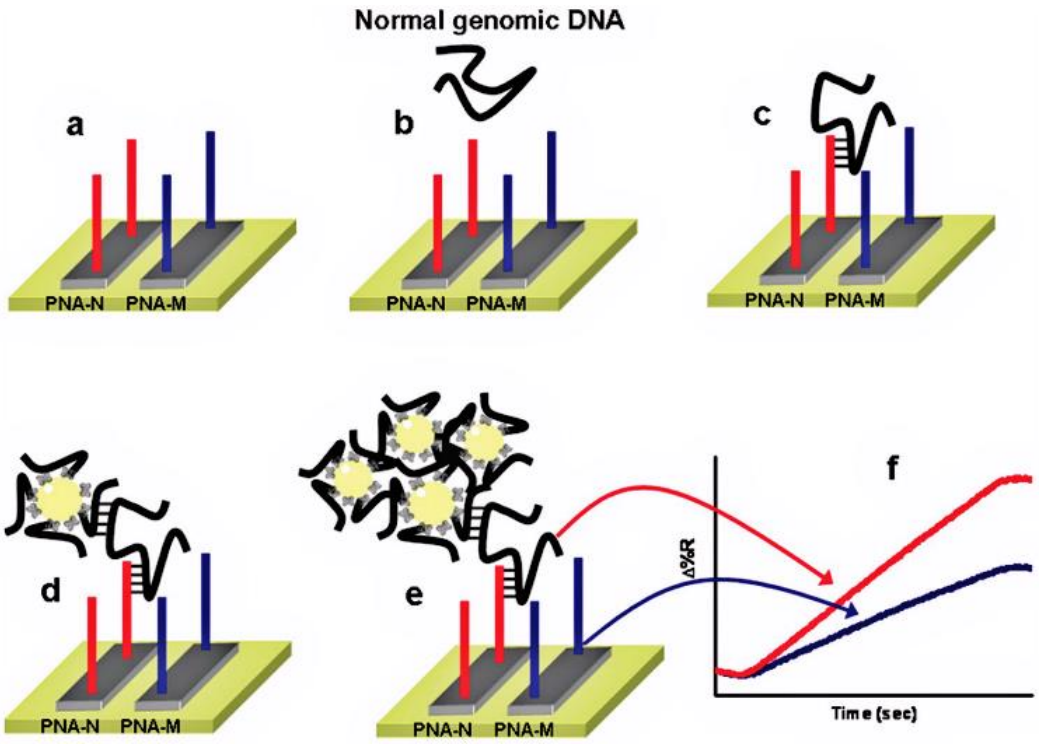

Figure 1-14. Schematic illustration of the nanoparticle-enhanced SPRI strategy used to detect the normal βN/βN, heterozygous β°39/β°N, and homozygous β°39/β°39 genomic DNAs. The PNA-N and PNA-M recognize specifically the normal β-globin and the mutated β°39-globin genomic sequences, respectively. Reprinted from reference [68].

1.6.3 Signal amplification using functionalized nanocontainers

The use of nanomaterials with hollow structures for encapsulation of signalling elements is another attractive strategy for ultrasensitive biosensing. Lin and colleagues [51] have used a similar base-pairing mechanism to target DNA point mutations using a novel signal amplification strategy. It uses DNA polymerase I (Klenow fragment) to couple a guanine modified NP probe to the mutation site of a duplex DNA. The signal enhancement is achieved by incorporating Cd^{2+} ions inside an engineered protein with a hollow cage of interior cavity diameter of 8 nm. This NP probe is also modified with guanine nucleotide to specifically pair with cytosine point mutation in the DNA duplex. As a result, hybridization of the mutant DNA (cytosine point mutation) and the biotin-labelled DNA probe forms a stable duplex DNA structure which is then captured by avidin-modified magnetic NPs. The Cd^{2+} ions released from the nanoparticle cavity is then detected electrochemically by square wave voltammetry. This assay is sensitive, allowing for detection of 21.5 attomol mutant DNA and can detect SNPs down to frequencies as low as 1%.

Recently, Zhang and colleagues [69] has developed a new approach using QD-based SNP detection without the need for target or probe amplification. This assay uses a reporter probe modified-liposome (liposome–QD-reporter probe; L@QD complex) serving as a “nano-container” for encapsulation of hundreds of QDs. The presence of the target DNA (T-DNA) and capture probe modified magnetic bead (CP-MB) lead to sandwich hybridization, forming a liposome–QD-reporter probe/T-DNA/CP-MB hybrid structure which is then separated magnetically. The subsequent disruption of liposome–QD complexes results in release of the encapsulated QDs, which are sensitively detected by single-particle counting as shown in **Figure 1-15**.

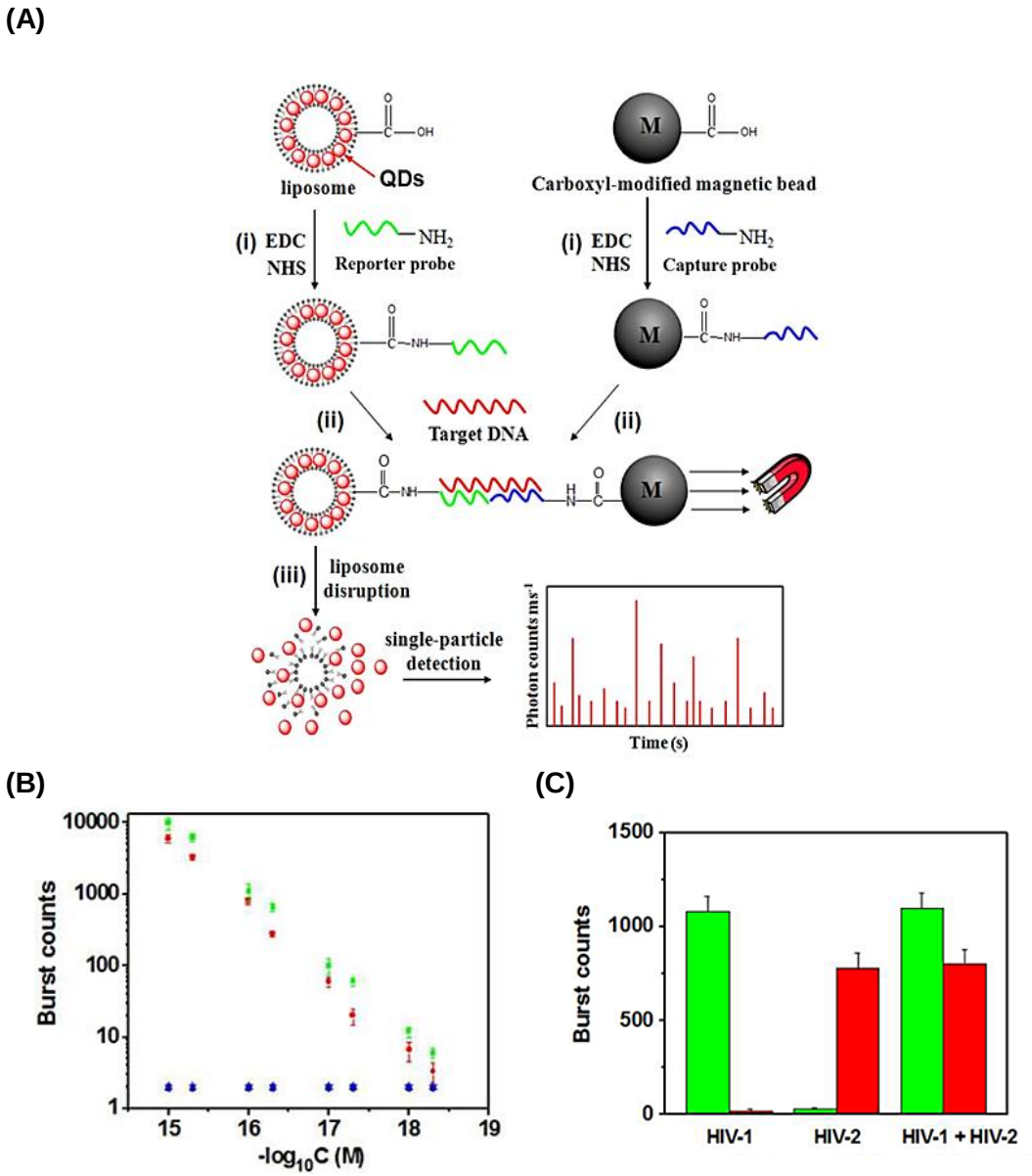

Figure 1-15. (A) Schematic illustration for Liposome–QD complexes (L@QD complex) based ultrasensitive detection of attomolar DNA using single-particle detection techniques. The assay involves the sandwich type hybridization of the target DNA to L@QD complex-tagged reporter probes and capture probe modified-magnetic bead. Liposome disruption leads to the release of QD's for single particle detection. (B) A plot of burst counts from the released QDs as a function of the concentrations of HIV-1 (green) and HIV-2 (red). There was no change in the burst counts in the control groups with non-complementary DNA (black and blue), and (C) Simultaneous detection of HIV-1 (green) and HIV-2 (red). The error bars corresponds to standard deviation of three replicates. Reprinted from reference [69].

An advantage of this approach is that each pair of reporter/ capture probes can be encoded with a different coloured QD, allowing for easy detection of multiple DNA targets simultaneously. As shown in as shown in **Figure 1-15**, the presence of HIV-1 only produces fluorescence bursts from the green QDs but not the red QDs. In contrasts, the presence of HIV-2 only produces red QD fluorescence, but not green QD, and thus indicating high assay specificity. Multiplexing has been achieved by encapsulating red and green QDs into the respective reporter probe 1 and reporter probe 2 tagged liposomes, whereupon specific sandwich hybridization leads to the formation of specific magnetic bead-liposome complexes. After magnetic separation, the use of two different coloured liposome–QD complexes has enabled the simultaneous detection of the HIV-1 and HIV-2 genes as shown in **Figure 1-15 (B)** and **(C)**.

The great target amplification (each captured DNA targeted is converted into several hundreds of QDs) coupled with sensitive single-particle counting method has enabled this assay to be ultrasensitive, with detection limits down to 1 and 2.5 aM for HIV-1 and for HIV-2, respectively. With the judicious design of capture and signal probes, this assay may provide an ultrasensitive approach for simultaneous detection of multiple DNA targets. However, this assay is unlikely to be able to provide high enough SNP discrimination ratio useful for detection of specific low abundant SNPs in wild-type gene background because of the small stability difference of the sandwich DNAs for the wild-type and SNP DNAs formed with the reporter/capture probes. Its single particle counting readout strategy may also limit its application in resources poor environment.

Instead of QDs being encapsulated inside liposomes, fluorescent dye molecules can offer better alternative because of much simpler signal detection read outs leading to more cost-effective biosensors. An interesting work here was reported by Li and colleagues [96] wherein they developed a biosensor for p53 gene. The biosensor is based on coupling a triple-helix magnetic probe (THMP) to a fluorescent liposome hybridization assembly The design concept of the biosensor is shown in **Figure 1-16.** The sensing platform consist of the triple-helix DNA immobilized on a streptavidin-magnetic beads (MNBs).

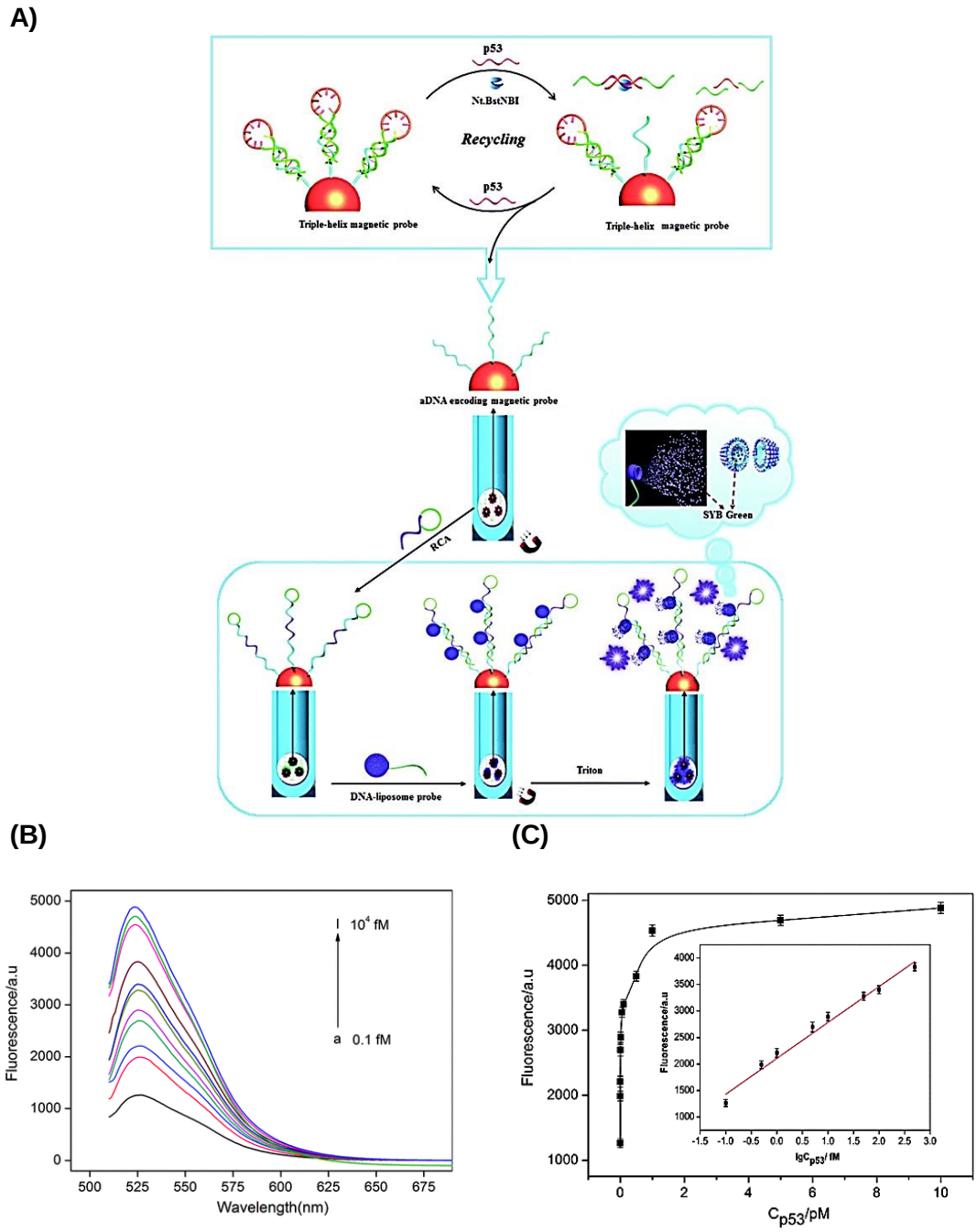

Figure 1-16. (A) Schematic illustration of the THMP coupled with the hybridization assembly of fluorescent liposomes for p53 gene detection. (B) Fluorescence emission spectra obtained in the proposed sensing strategy for p53 genes at varying concentrations and (C) linear relationship between the fluorescence intensity and the concentration of p53 genes. The error bars represent the standard deviation of three repetitive measurements. Reprinted from reference 96.

In the presence of p53, the loop portion of the THMP is unfolded, thus forming a double-stranded DNA and subsequently releasing the aDNA-MNB probes. The nicking endonuclease (*Nt·BstNBI*) specifically recognized the specific asymmetric sequence 5′- GAGTC-3′ in this duplex, thereby cleaving the fourth base from its 3′ end. In this way, the loop portion of the THMP is cleaved into two and liberates p53 gene for another round of enzyme cleavage cycle. The aDNA-MNB probes were separated to trigger the subsequent RCA process producing long DNA strands. After interaction with the long single DNA strands, multiple fluorescent dye-encapsulated liposome probes were appended on the DNA strands to form a duplex structure. After hydrolysis of the fluorescent liposomes, a dramatically enhanced fluorescence signal was obtained. In the absence of p53, the THMP remained intact and blocked the aDNA-MNB probe release and fluorescent liposome assembly, thus yielding a very low background signal. The significant enhancement of sensitivity of the developed biosensor are due to the following factors (i) integrates p53 gene-triggered enzyme cleavage recycling for primary target amplification, (ii) fluorescent liposome hybridization assembly initiated by RCA for secondary signal amplification, and (iii) magnetic isolation for background signal elimination. Under optimal conditions, this biosensor approach reported a detection limit of 0.07 fM. Moreover, the biosensor showed a remarkable selectivity for p53 against single-base mismatches due to ability of the THMP to specifically detect the involved targets and the precise site-specific endonuclease cleavage.

1.6.4 Signal amplification using enzyme catalysed crystal growth

Stevens and colleagues have recently developed a novel plasmonic nanosensor that works on a principle of inverse sensitivity signal-generation mechanism [97, 98] where an amplified signal is observed when less target molecules are present. The inverse sensitivity procedure is achieved using glucose oxidase (GOx) which catalyses the generation of hydrogen peroxide to tailor the plasmonic response of the gold nanosensors. Depending on the concentration, GOx can control the in situ rate of nucleation of nascent Ag nanocrystals or Ag coating on Au nanostars, resulting in variations of the localized surface plasmon resonance (LSPR). At low GOx concentration, a low supply of H_2O_2 favours the deposition of a homogeneous silver coating on the Au nanostars, leading to blueshift of the LSPR band. Whereas a high GOx concentration favours the nucleation of silver nanocrystals instead of depositing on Au nanostars, leading to less LSPR shifts as shown in **Figure 1-17 (A)**. This

principle is used to develop a plasmonic ELISA using a GOx conjugated antibody in a typical sandwich immune-binding format.

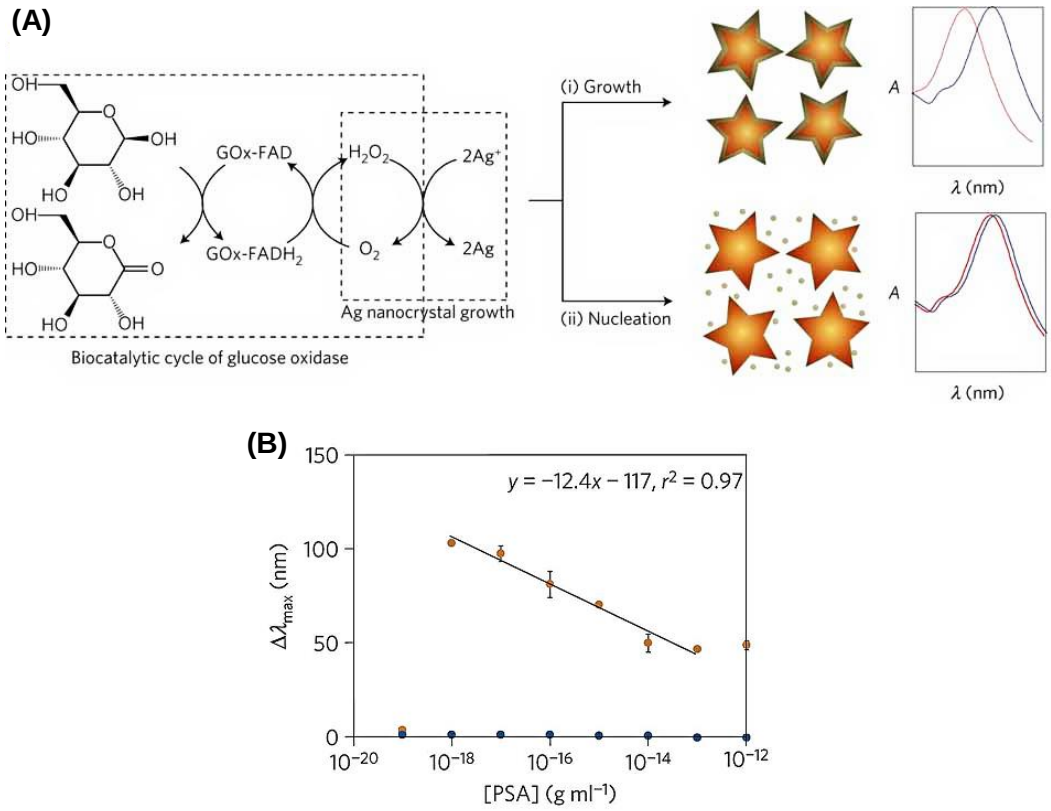

Figure 1-17 (A) Schematic illustration of the proposed signal-generation mechanism by means of enzyme-guided crystal growth for the plasmonic ELISA assay. (B) Immunoassay for the ultrasensitive detection of PSA with GOx-labelled antibodies and of PSA (red) and BSA (green) spiked into whole serum. Reprinted from reference [98].

The concentration of GOx is directly related to the target concentration. Prostate specific antigen (PSA) and HIV-1 capsid antigen p24 are used as model protein targets in whole serum conditions. This assay has demonstrated an extremely impressive sensitivity of 40 zM [99] and 1 aM [97] for PSA and HIV-1 capsid antigen, respectively. Moreover, the assay results can be directly visualised by the naked eye, and therefore offers a simple, highly attractive alternative to the costly nucleic acid based HIV infection diagnosis test. In principle, it can be adapted for the detection of any analyte with a suitable antibody, making it a versatile tool for ultrasensitive diagnostics. Despite of great simplicity and ultrasensitivity, the plasmonic ELISA

however, has a rather small absolute signal change, making it difficult to quantify the exact target concentration.

1.7 Summary

Significant advances have been made over the past few years in the development of PCR-free assays suitable for specific and ultrasensitive detection of SNPs. The incorporation of various biofunctionalised nanomaterials coupled with novel amplification strategies have permitted the detection of extremely low concentrations of SNPs, down to the aM–zM range. Such levels of sensitivity have already compared very favourably with many PCR based methods. The amplification strategies may be classified as one of the following categories:

(i) Nanoparticle assisted target PCR amplification.
(ii) Nanoparticle assisted probe amplification.
(iii) Target recycling coupled with probe and/or signal amplification.
(iv) Tandem amplification schemes and signal catalytic cascades.
(v) Nanomaterial enhanced signal amplification.

In general, the sensitivity of a nanomaterial-based SNP assay can be greatly enhanced by combining target, probe and signal amplification schemes. Most of the recent target and probe amplification schemes have exploited the great catalytic power and specificity of enzymes to achieve ultra-sensitivity and specificity. Of particular interest here is the use of DNAzymes that can undergo the so-called enzymatic cascade reactions, where the activation of multiple enzymes by a target DNA can result in ultra-sensitivity, comparable many PCR based assays. Another widely used strategy is the use of restriction enzymes that specifically recognise the restriction sites to degrade the reporter probe, allowing for target recycling. These autocatalytic strategies have resulted in unmatched sensitivities while still maintaining high specificity. However, a limitation here is that restriction enzymes can only recognize a specific sequence and therefore are not suitable for universal SNP detection. Several ingenious ways in the design of nanomaterials for signal amplification strategies have also been developed, including the use of multiple tagging and enrichment of nanoparticle probes with signal moieties to enable ultra-sensitivity. Some of these strategies also hold great promises for multiplexed detection, an important property for high diagnostic accuracy. Despite significant

advances, several limitations still need to be resolved before they can be translated into clinical diagnostic assays. For example, although a number of assays have reported aM, even zM sensitivity, most of which were still at the proof-of-concept stage and were carried out under clean buffers. They have not yet been tested in clinically related media, such as blood, serum, saliva and urine. Furthermore, most assays have reported a rather limited SNP discrimination ratio (<10 fold), making them potentially unsuitable for detection of low abundant disease related SNPs in the background of wild-type gene/genomic DNA because of the strong interference from the background DNAs. Moreover, the lack of the multiplexing capability could pose a significant limiting factor for the real clinical potential. The stability of the biofunctionalised nanomaterials is another important issue for such nano-enabled SNP biosensors. In this regard, the fundamental understanding of the biomolecule-nanomaterial interactions is imperative to alleviate problems of high background signals due to non-specific adsorptions in serum and/or other complex clinical samples.

The use of biofunctionalised nanomaterials together with novel amplification strategies has transcended barriers to the attainment of extremely low detection limits of disease-related SNPs. This ultimately ushers the way for more practical concerns such as the realistic applications of the technology in clinical settings. Even more challenging is the development of a robust, portable, point-of-care diagnostic system that can specifically detect the ultralow level of disease-related SNPs rapidly and conveniently on the site of the patient and in places such as the doctor's office, school clinic and in patients' residence. [82] These also call for improving the assays' amenability towards automation and miniaturization because most current assays still require the use of expensive and complex instrumentation and complex procedures, limiting their potential in rapid diagnosis. Electro-chemical signal transduction can provide an option for the miniaturization and automation but these methods are prone to false positives.(26) The recent advances in microfluidics [100, 101] may be able to address sample throughput and automation challenges in SNP assays. If all of these challenges were met, the automation of these ultrasensitive assays may lead to the integration of sample processing, quantification and signal measurement in an all-in-one device in real clinical setting. This would greatly facilitate the rapid, accurate disease diagnosis and prognosis. In view of this, these are still crucial challenges that need to be addressed, and more efforts will be needed to improve the analytical sensing performance and portability of SNP assays.

1.8 Aim of the project

The overall project objective is to develop a rapid, ultrasensitive sensing technology that can specifically detect the tiny amount of cancer gene mutants in the background of overwhelming wide type genes for early cancer diagnosis and prognosis. The biosensor that is currently being developed is a simple and sensitive fluorimetric magnetic nanoparticle-enzyme based DNA sandwich assay that is suitable for label free quantitation of DNA targets down to the low attomolar level. The sensing approach is based on the use of a specific pair of DNA probes, with one covalently conjugated to the MNP for target capture (*i.e.* capture-DNA). The other (*i.e.* signal-DNA) is modified with biotin for linking to a neutravidin conjugated enzyme for signal amplification. Each capture DNA and signal-DNA is complimentary to each half of their DNA target, allowing for the specific sandwich hybridization of the target DNA. Ligation using *Taq* enzyme enables the MNP conjugated capture-DNA to be covalently linked to the signal-DNA, ensuring that the signal DNA (together with its attached biotin group) will not detach from the MNP during the subsequent washing steps (without ligation, the double-stranded DNA sandwich structure may dissociate during washing steps). After washing to remove any unbound species, excess neutravidin-enzyme conjugates are added to bind to the MNP surface biotins, converting each captured target DNA into an active enzyme for powerful enzymatic signal amplification. This DNA biosensor is expected to be robust and effective in discriminating between wild type DNA targets and cancer specific SNPs because the ligation is highly specific, a single base mismatch at the nicked double-stranded site can prevent covalent ligation.

Enzymatic signal amplification can offer higher sensitivity than dye labelled affinity reagents because each enzyme can turn over tens to hundreds copies of a fluorogenic substrate per second, leading to greatly amplified signals as compared for methods using dye labelled affinity reagents. Enzyme labelling works through the use of an enzyme conjugated to a target specific affinity reagent (*e.g.* neutravidin). Previously, the Zhou group has shown that by converting each captured DNA target into a single horseradish peroxidase (HRP) enzyme for signal amplification as shown in **Figure 1-18**, fM levels of target DNA can be detected in 40 min [52].

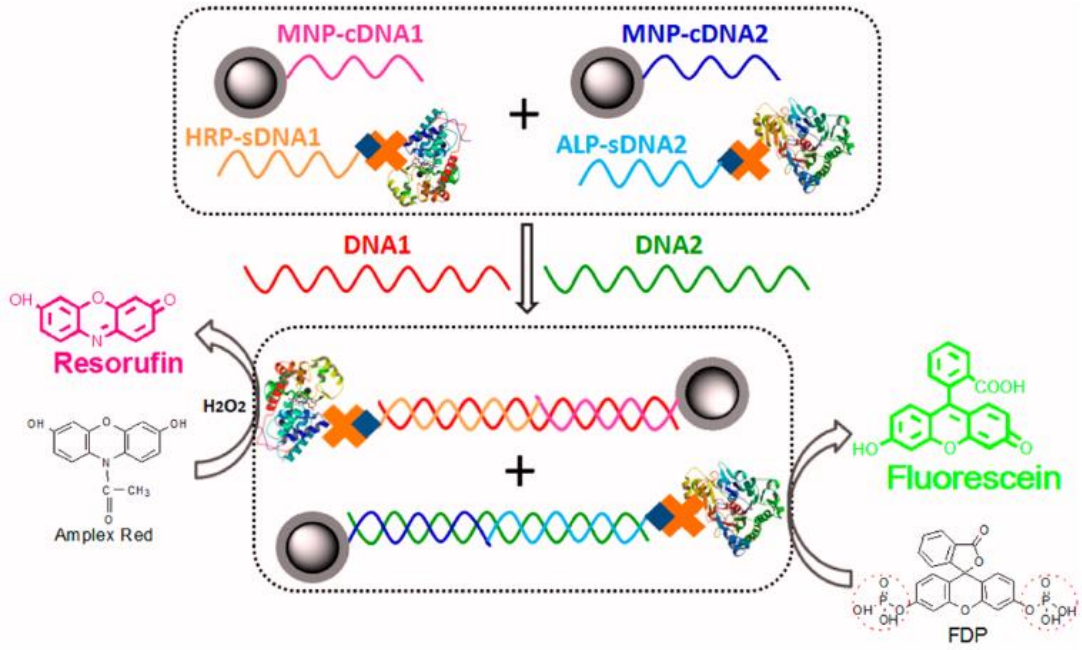

Figure 1-18. Principle of the MNP–Enzyme Sandwich Assay for Simultaneous Detection of Two DNA Targets Using Two Sets of Unique MNP–cDNA and sDNA–Enzyme Probe. The cDNA and sDNA probes are complementary to each half of their DNA targets for specific sandwich hybridization, linking HRP (with T-DNA1) or ALP (with T-DNA2) to the MNP. Therefore, HRP/ALP-amplified enzyme products, resorufin (λ_{max} = 571 nm) and fluorescein (λ_{max} = 485 nm), are used to quantitate T-DNA1/T-DNA2, respectively. Reprinted from reference [52].

This project aims to build upon such results and further improve the sensitivity of the assay by developing a novel signal amplification strategy with greater amplification power: the development poly neutravidin-horseradish peroxidise (NAv-HRP) tagged polymer bead (PB-HRP_m). The amino modified polymer bead is first biotinylated by *N*-hydroxysuccinimide-Biotin in a bicarbonate buffer (pH= 8.3) and linked to NAV-HRP enzyme *via* the strong "biotin-neutravidin" interaction. Biotin is a small ligand molecule (molecular mass of ~250 Da) that specifically binds to a larger cationic glycoprotein, avidin (isoelectric point (pI) ~ 10.5 and molecular mass ~67 kDa) with high affinity (binding constant, $K_d \approx 10^{-15}$)[102]. The biotin-avidin interaction is the strongest known non-covalent biochemical bond[103]. Streptavidin is a non-glycosylated protein with a near-neutral isoelectric point (pI ~ 5-6 and molecular mass ~60 kDa). The biotin-binding properties of non-glycosylated avidin (*i.e.* streptavidin)

have been reported to be equivalent to those obtained for the native (glycosylated) avidin molecule [104]. Similar to avidin, streptavidin binds to biotin at four binding sites, two binding sites on each of two opposing faces of the molecule, with an extremely high binding constant ($K_D \sim 10^{-13}$ M) [105, 106]. The binding affinity of Neutravidin® (pI ~6.3, and molecular mass 60 kDA) [107] is similar to avidin and streptavidin but NAV exhibits the lowest non-specific binding (based on Thermo Pierce ®product description).

In this biosensing assay, the polymer bead detector can bind with the MNP-ligated DNA ensemble through the biotin-neutravidin interaction. The HRP in the presence of H_2O_2 is capable of converting a non-fluorescent substrate amplex red into a strong-fluorescent product (*i.e.* resorufin). The rate of fluorescence production is linearly proportional to the number of HRPs conjugated on the MNPs, which implies the concentration of the target DNA in the solution.

In order to achieve this biosensing strategy, uniform and stable magnetic nanoparticles must be prepared. In our earlier work (results not included in this thesis), we prepared amino modified silica coated magnetic nanoparticles. The amino modified silica surface were first modified with a heterobifunctional linker (*i.e.* NHS-PEG-Maleimide). The NHS (*i.e. N*-hydroxysuccinimide) moiety reacts with surface amines and the maleimide groups react with the thiol modified DNA (capture probe) and thiolated zwitterion ligand. The zwitterion ligand was previously shown to resist non-specific adsorption of proteins [108] and was used to passivate the surface of the nanoparticle. Moreover, the surface was further blocked by bovine serum albumin (BSA). Initial results show low background signals due to the reduction of non-specific adsorption by the zwitterion ligand and BSA. However, this biosensing procedure was not very reproducible due to the inconsistency of achieving high DNA loading (capture DNA efficiency was only ~ 38 - 40 %), and differences in capture DNA loading per mg of MNPs were also observed in different batches of MNPs even though the conjugation were done using the same protocol. These problems affected the reproducibility of the biosensing data and lead to re-design the biosensor platform. More importantly, these observations suggest an important aspect in designing nanoparticles probes for biosensing applications - that is to consider the surface chemistry of the nanoparticles to ensure a low background and obtain reproducible conjugation efficiency of the capture probes (*i.e.* DNA). Moreover, experimental optimizations must be done in order to ensure the low background

signal possible. This can be done by optimizing biosensing parameters such as effect of washing conditions, effect of DNA loading (nmol·mg^{-1} MNP), and effect of signal DNA concentration. Furthermore, signal amplification as discussed earlier will be developed in order to attain the attomolar sensitivity.

Chapter 2

Preparation, Surface Functionalization, and Bioconjugation of Iron (II) Oxide - Silica Core Shell Magnetic Nanoparticles for Biosensing Applications

2.2 Introduction

Magnetic nanoparticles (MNP) are among the most promising nanomaterials developed for biomedical applications so far. Among Iron oxide nanoparticles (IONPs), magnetite (Fe_3O_4) and maghemite (γ-Fe_2O_3) have attracted research attention for use in medical and biosensing applications because of their non-toxicity and excellent biocompatibility [109, 110]. The distinctive properties of MNP offers many exciting opportunities in biology and medicine. First, the size of MNPs can be easily tuned and optimized from a few to hundreds of nanometres to match the interest or purpose of the study. Second, their superparamagnetic property makes them easily manipulated by an external magnetic force, allowing for easy sample retrieval from the matrix and for further re-use. Indeed, the “action at a distance” provides a tremendous advantage for a plethora of applications (*e.g.* bacterial detection [111], protein purification [112], removal of toxins [113]). Third, the magnetic moment of MNPs can enhance the magnetic relaxation signal of nearby protons, allowing MNPs to act as important MRI contrast agents [114]. Fourth, the MNPs can transform electromagnetic energy from an external high-frequency field into heat, providing promising applications in magnetic hyperthermia treatment of cancerous tumours [115]. Similar to any other nanomaterials, the nanometre size of MNPs imparts a large surface to volume ratio and a high surface energy, making them to aggregate and/or oxidise readily in the absence of proper surface coating. This can adversely affect their intrinsic magnetic properties and applications. In this regard, MNPs are often capped with a protective coating to improve their stability and water-dispersibility, and more importantly, to introduce reactive functional groups to facilitate further conjugation to biomolecules. There are several different types of coatings already reported in the literature such as silica, amphiphilic polymer micelles, and polymeric ligands [116-119].

This chapter will present a brief overview of the properties of MNPs, the synthesis of iron (III) oxide (Fe_3O_4) nanoparticles using co-precipitation and thermal decomposition methods, silica coating and amino modification, and the synthesis of heterobifunctional ligands to improve the water dispersion of silica coated MNPs. These water dispersible MNPs are then used for biosensing applications.

2.2.1 Physical Property of Magnetic Nanoparticles

MNPs consist of elements such as iron, nickel, and cobalt or their chemical compounds and show some response to an applied magnetic field [120]. Magnetic effects is a consequence of the movement of particles with charge and mass. Specifically, the origin of magnetic moments in individual atoms is governed by two electronic movements: orbital movement which is the movement of electrons around the nucleus and spin movement which originates from the movement of electrons around its own axis [117]. In general, materials can be classified into three categories depending on their response to an external magnetic field as shown in **Figure 2-1** [121]: diamagnetic (no net moment and produce a weak magnetic field in the direction opposite to an applied magnetic field), paramagnetic (zero net moment, produce a weak magnetic field in the direction of the applied magnetic field), and ferromagnetic (have net moment, all its magnetic moments can align in one direction creating a high magnetic moment) materials [121].

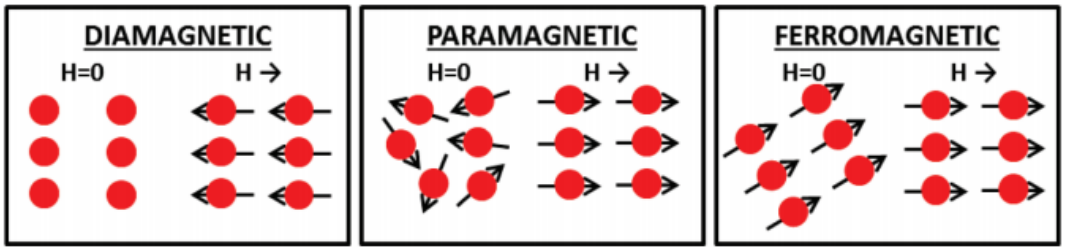

Figure 2-1. Schematic representation of diamagnetic, paramagnetic, and ferromagnetic materials microscopic structures at rest and in the presence of a magnetic field (H). Figure reprinted from reference [121]

Bulk ferromagnetic materials contain smaller regions called magnetic domains whose atoms spins are all pointing in the same direction giving a net magnetization [109, 117]. Each magnetic domains are separated by domain walls and the overall magnetization is the sum total of all the different magnetizations of all domains. The formation of magnetic domains results from a balance of several energy terms: the exchange energy which

aligns all magnetic moments in the same direction, magnetocrystalline anisotropy energy which orients magnetic moments along specific directions, and the magnetostatic energy which eliminates the magnetization in the material [110]. When the size of a ferromagnetic material is reduced below a critical value, it becomes single domain wherein the electron spins rotate in the same direction [109]. The MNP coercivity which is the magnetic field required to bring the magnetization back to zero is critically size dependent. MNPs show a maximum coercivity at the transition from multi-domain to single domain [109]. As the size of the particle is reduced to the single domain limit, the coercivity reaches the maximum, further reducing the MNP size leads to decreased coercivity and finally reaches zero, where the MNPs become superparamagnetic as shown in **Figure 2-2** [110].

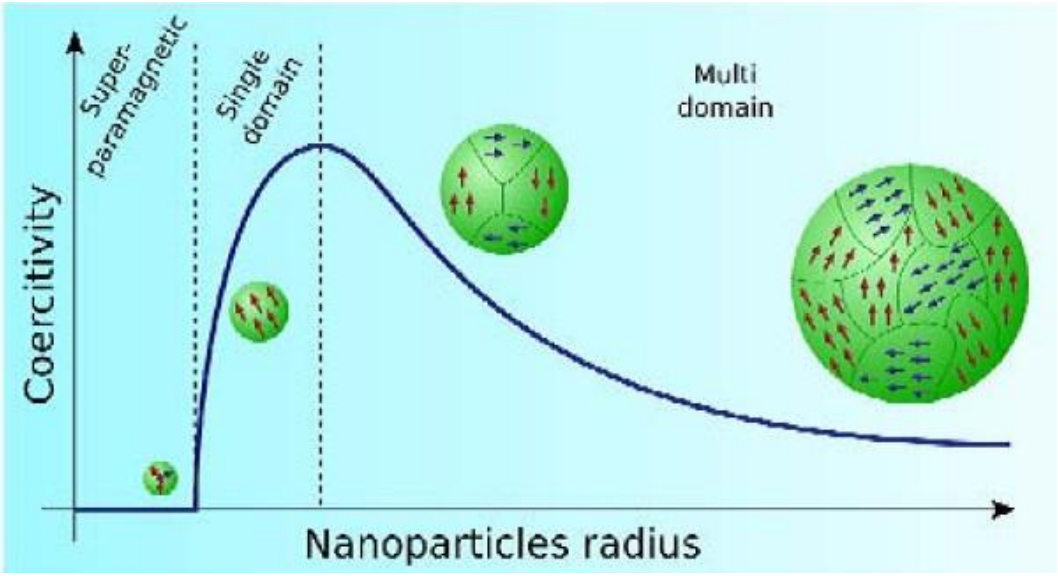

Figure 2-2. Schematic illustration of the coercivity-size relations of small particles. Reprinted from reference [110]

The interaction of ferromagnetic materials on an applied field is best described by a magnetization curve, which is characterized by two main parameters: remanence (residual magnetism) and coercivity (H_c) (coercive force) as shown in **Figure 2-3 (b-d)**.

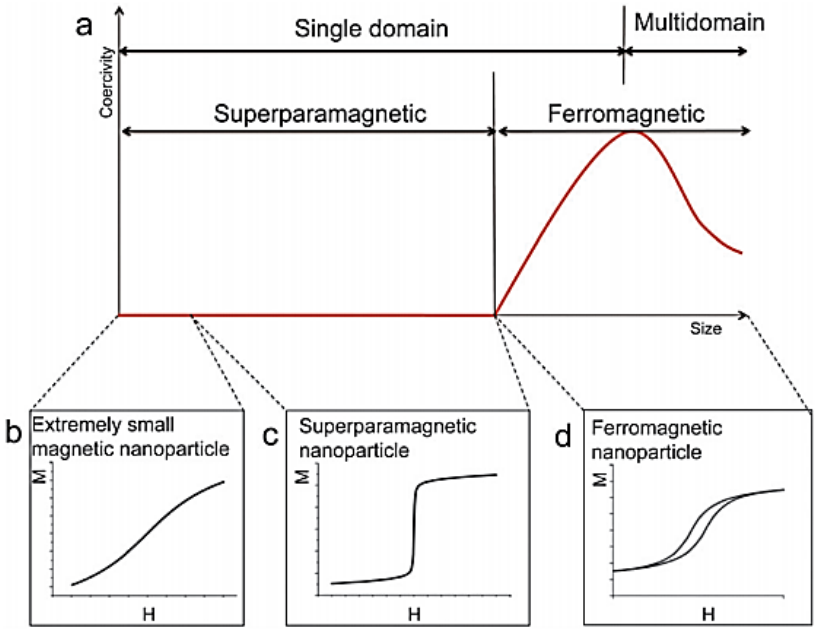

Figure 2-3. Schematic illustration of the relationship between coercivity, nanoparticle size and their corresponding magnetization curves. Figure reprinted from reference [109]

Extremely small MNPs exhibit an almost linear relationship between the magnetization (M) and magnetic field (H). The magnetization is not saturated until very high magnetic field is applied as shown in **Figure 2-3(b)**. MNPs with bigger sizes but still in the single domain range exhibit a superparamagnetic property. When a magnetic field is applied, MNPs in the superparamagnetic state display a fast response to the changes of the magnetic field without remnant (residual) magnetization and coercivity as shown **Figure 2-3 (c)**. Further increase of the particle size leads to a ferromagnetic behaviour which displays appreciable remanence and coercivity in the magnetization curve.

2.2.2 Overview of the Project

The ability to detect ultralow concentrations of biochemical molecules such as nucleic acids and enzymes by using simple and inexpensive assays is highly desirable in clinical diagnostics and biomedical research. Polymerase chain reaction (PCR) coupled with gel electrophoresis or molecular fluorophore assays is still considered as the golden standard among nucleic acid detection techniques because it offers high sensitivity of

detection. However, PCR methods suffer from complex handling procedures, high cost, easy contamination, and lack of portability. On the other hand, the enzyme linked immune absorbent assay (ELISA) is a method of choice for detection of peptides, proteins, antibodies and hormones because it offers high sensitivity and specificity [122, 123]. There are different types of ELISA assays but the major steps include the immobilization or capture of the antigen onto a solid surface followed by binding to an enzyme-linked detection antibody . The detection step is accomplished by incubating a substrate to produce a measurable coloured product. The high sensitivity of ELISA comes from the enzymatic amplification which can catalyse a chromogenic reaction at a high rate. Moreover, the high specificity is due to the selectivity of the antigen-antibody recognition. However, ELSIA also suffers from several drawbacks such as the labelling of antibodies for each specific ELISA system can be very time-consuming and expensive [124]. Furthermore, there is no flexibility in choice of antibody label from one experiment to another [122].

MNPs have been utilized in various applications involving the sensitive detection of DNA and protein targets. Motivated by the attractive features of MNPs such as target capture and ease of retrieval from the sample matrix, a colourimetric biosensor for the detection of a cancer related DNA target and endonuclease is designed. Endonucleases are a class of enzymes known as “molecular scissors” because they can specifically cleave the phosphodiester bond within the DNA at defined positions [125]. Endonucleases are deemed important targets in antimicrobial and antiviral drug discoveries [126, 127]. The biosensor platform is based on a biofunctionalized magnetic nanoparticle. The MNP probe contains a capture DNA that is linked to a horse radish peroxidase (HRP). Specifically, 2 designs of the MNP-DNA_{ss}-HRP (ss stands for single strand DNA) probe were prepared. Both types of capture-DNAs contained a DBCO moiety at the 5′ end, the 3′ end was modified with a biotin or a thiol group for design 1 or 2 respectively. The attachment of HRP were carried out using two different methods because of the difference in the functional groups at the of the 3′ end of the DNA. The first manner of HRP linking termed as Design-1 involves the non-covalent interaction of NAV-HRP to the biotin group of MNP-DNA_{ss}-Biotin probes. **Scheme 2-1** shows the schematic illustration for the preparation of MNP probe Design-1.

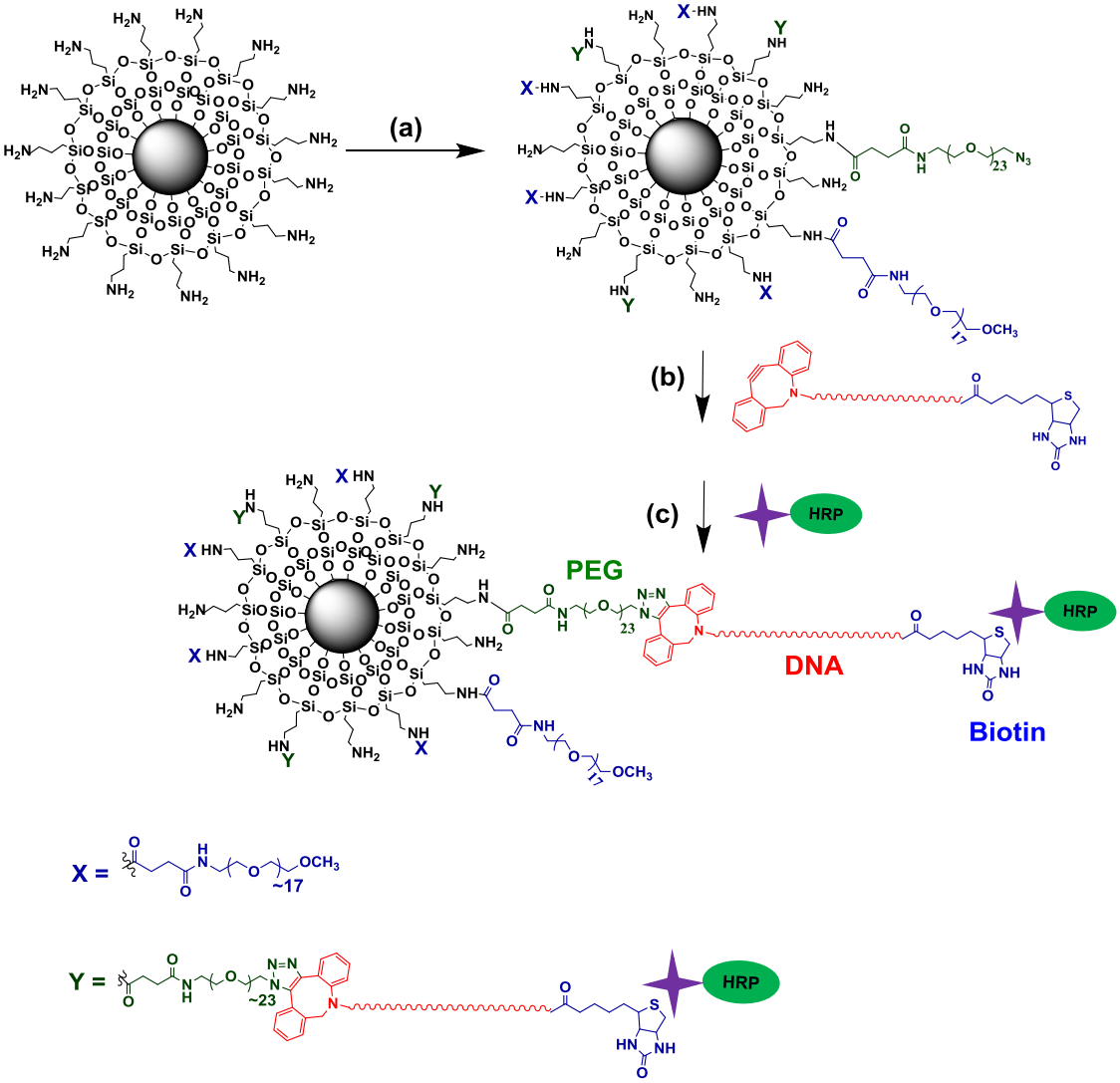

Scheme 2-1. Schematic illustration for the preparation of MNP-DNA$_{ss}$-HRP Design-1. The reaction conditions are (a) 1% NHS-PEG$_{\sim 23}$-N$_3$, 99 %, NHS-PEG$_{\sim 17}$-OCH$_3$; (b) DBCO-DNA-Biotin, PBS; (c) Neutravidin–HRP, PBS. The X and Y in the MNP denotes PEG$_{\sim 23}$-DNA-HRP and PEG$_{\sim 17}$-OCH$_3$ respectively.

Scheme 2-2 shows the schematic route to prepare MNP-DNA$_{ss}$-HRP Design-2 by covalently linking the maleimide modified HRP to the thiol modified DNA strand on the MNP surface. This was accomplished by reacting HRP with a heterobifunctional linker (*i.e.* NHS-PEG$_{12}$-Maleimide) where the NHS ester reacted with the terminal amino groups of HRP at pH 7.4 to introduce maleimide groups. Thereafter, the maleimide modified HRP reacted with the MNP-DNA$_{ss}$-SH to form covalent conjugation. The amounts of the MNP linked HRP molecules were determined spectrophotometrically.

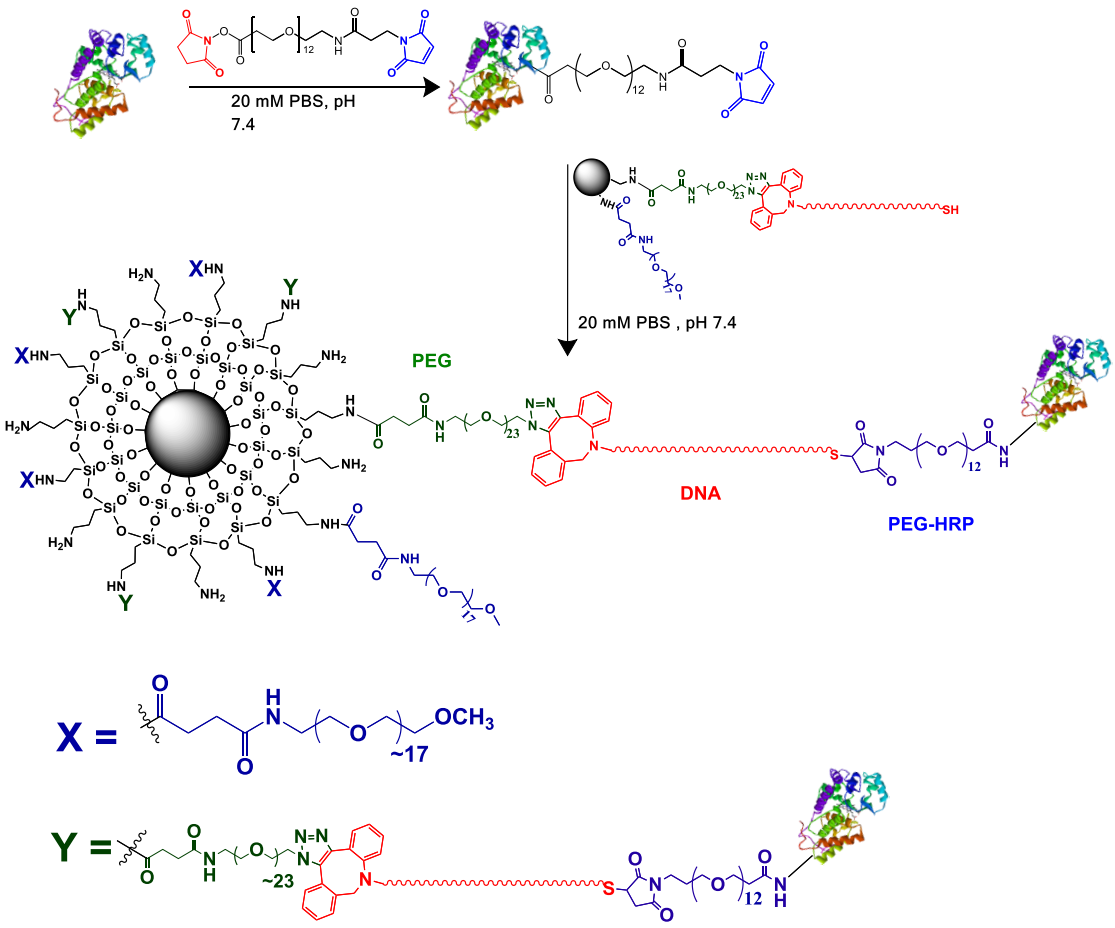

Scheme 2-2. Schematic illustration for the preparation of MNP-DNA$_{ss}$-HRP Design-2 probes. The X and Y denote PEG$_{\sim 23}$-DNA-HRP and PEG$_{\sim 17}$-OCH$_3$ respectively.

To test the feasibility of the biosensor, the ECOR-I is used as a model endonuclease enzyme. The enzyme cuts specifically the phosphodiester bond of the duplex DNA [128, 129]. The biosensor is further used for DNA detection by incubating the MNP-DNA$_{ss}$-HRP probes with different concentrations of the target DNA. After hybridization, ECOR-I was used to cleave the ds DNA and the same colourimetric assay was used to correlate the absorbance and target DNA concentration. Overall, this biosensor design is simple, inexpensive, and can be easily used to detect either DNA or ECOR-I.

2.3 Materials and Methods

2.3.1 Instruments

Transmission electron microscopy (TEM) micrographs were taken on the Philips CM200 transmission electron microscope. The specimen for TEM study was prepared by depositing a drop of the MNP solution onto a carbon-coated TEM grid. Hydrodynamic size and zeta potential measurements were determined using Malvern® zetasizer-nano with BI-APD detector using a He-Ne laser at 633 nm (scattering angle: 90º, temperature, 25ºC). UV-vis absorption spectra were conducted using a UV-Vis Cary50 ® spectrophotometer, Agilent technologies, USA. XRD (X-ray diffraction) measurements were performed on Bruker XRD. The scan range (2θ) was from 10° to 90° at increments of 0.0332° with a scan speed of 0.5 second/step. pH adjustments were done using a Fischer brand Hydrus 300 pH meter at room temperature. Ultrapure water (resistance >18.2 MΩ·cm) was purified by ELGA Purelab classic UVF system, was used for all experiments. Proton NMR (^{1}H NMR) and Mass spectrometry (MS) data of the synthesized ligands were collected using BRUKER DPX400®, 400 MHz nuclear magnetic resonance spectrometer and high resolution BRUKER Maxis Impact ® mass spectrometer respectively. The magnetic property of Fe_3O_4 MNP were measured using the superconducting quantum interference device-vibrating sample magnetometer (SQUID-VSM) at the School of Physics, Leeds University.

2.3.2 Reagents

Iron (II) chloride tetrahydrate (>98%), Iron (III) chloride hexahydrate (> 98%), Iron (III) acetyl acetonate (> 99.9), IGEPAL CO-520, Oleylamine (technical grade 70%), Oleic acid (technical grade, 70%), 1,2-hexadecanediol (technical grade, 90%), Tetraethylorthsilicate (TEOS, 98%), and 3-(aminopropyl) triethoxysilane (APTES, >98%), succinic anhydride, N-hydroxysuccinimide (NHS, 98%), methane sulfonyl chloride (>99.7%), Sodium azide (NaN_3), triphenylphosphine (PPh_3, >98.5%) were purchased from Sigma Aldrich (UK). Trisodium citrate, ammonium hydroxide (35% v/v), ethanol, hydrogen peroxide (30% v/v), and ninhydrin (>98%) were purchased from Fischer Scientific.

2.3.3 DNA Probes and Biochemical Reagents

All DNA probes and target DNA strands were purchased commercially from IBA GmbH (Germany). They were all HPLC purified by the supplier and their sequences are summarized in **Table 2-1**. High fidelity (HF) ECOR-I (20,000 $U \cdot mL^{-1}$)and CutSmart ® buffer (50 mM Potassium acetate 20 mM Tris-acetate 10 mM Magnesium acetate 100 µg/ml BSA pH 7.9 at 25°C supplied as a 10X concentrated stock) were purchased from New England Biolabs. High activity Horse Radish Peroxidase (HRP), Neutravidin-HRP (NAV-HRP), and N(Hydroxysuccinamide)-PEG_{12}-Maleimide (NHS-PEG_{12}-Maelimide) were purchased from Thermo Scientific. 30Amplex red was purchased from Invitrogen Life Technologies (UK). 20 mM PBS buffer (150 mM NaCl, pH 7.4) and 1 M NaN_3 was made with ultra-pure MilliQ water (resistance > 18 $M\Omega.cm^{-1}$).

Table 2-1. DNA sequences used in this study.

DNA Name	Sequence (5′→3′)
DBCO-DNA-Biotin	DBCO-T_3 GAA TTC AAC ATC AGT CTG ATA GCT ATT-Biotin
DBCO-DNA-SH	DBCO-T_9 GAA TTC AAC ATC AGT CTG ATA AGC TA T_7-SH
Target DNA	AGA CTG ATG TTG AAT TCA AA

2.3.4 Synthesis Fe_3O_4 MNPs using co-precipitation method, silica coating and amino modification

2.3.4.1 Synthesis of Fe_3O_4 MNPs using co-precipitation method

The Fe_3O_4 MNPs were prepared using the co-precipitation method under a nitrogen atmosphere [130, 131]. Briefly, 5 mmol of $FeCl_2$ and 10 mmol of $FeCl_3$ were dissolved in 50.0 mL of deoxygenated water at pH 5.0. The solution was bubbled with nitrogen and 25.00 mL of NH_4OH (35% v/v) was added dropwise until the solution reached pH 11.0. The solution was heated to 80 ^oC for 30 minutes and then was raised to 90 ^oC for the next 2 hours. A 50.0 mL of 0.20 M trisodium citrate was added and was allowed to react with the Fe_3O_4 magnetic particles for another 30 minutes at the same temperature. The Fe_3O_4 MNPS which appeared as black precipitates were centrifuged at 4 500 rpm for 5 minutes and were washed with acetone once. The citrate capped Fe_3O_4 MNPs were re-dispersed in ultrapure water to a total volume of 30.0 mL.

2.3.4.2 Silica coating of Fe_3O_4 MNPs

Different amounts of as-prepared Fe_3O_4 MNPs and volumes of tetraethylorthsilicate (TEOS) were used to coat the Fe_3O_4 nanoparticles with silica. Specifically, 1.0 mL of 4.13, 8.3, 12.4, 16.5, and 20.7 mg mL^{-1} of Fe_3O_4 MNPs were dispersed in a mixed solution of 4.0 mL ultrapure water and 20.0 mL absolute ethanol. The dispersions were homogenized using an ultrasonicator for 15 minutes purged with nitrogen gas for 15 minutes. 0.430 mL of NH_4OH (35% v/v) and a known volume of tetraethylorthoslicate (TEOS) were added consecutively. The resulting solution was stirred at room temperature (*ca.* 15°C) under an N_2 atmosphere for 3 hours. The silica coated Fe_3O_4 MNPs (*i.e.* Fe_3O_4-SiO_2) were centrifuged at 4500 rpm for 5 minutes and washed with ultrapure water three times. The Fe_3O_4-SiO_2 nanoparticles were re-dispersed in water to a final volume of 1.0 mL. The concentration of the Fe_3O_4-SiO_2 suspension was estimated by comparing the suspensions weight with pure water of the same volume. It should be noted that the density difference of the Fe_3O_4/SiO_2 core/shell MNP in water was ignored.[52]

2.3.4.3 Pre-treatment of Fe_3O_4-SiO_2 with polydiallyldimethyl ammonium chloride (PDDA)

A 50.0 mg of the as-synthesized Fe_3O_4-SiO_2 MNPs was added dropwise to a solution containing 0.1 % v/v polydiallyldimethyl ammonium chloride solution under vigorous stirring and room temperature. After 1 hour, the PDDA coated MNPs were magnetically separated and were washed with water three times. The resulting PDDA modified MNPs were re-dispersed in water.

2.3.4.4 Amino modification of Fe_3O_4-SiO_2 MNPs

The amine functionalized F_3O_4-SiO_2 core-shell MNPs were synthesized under a N_2 atmosphere as follows: ~ 20.0 mg of the F_3O_4-SiO_2 (as-prepared and PDDA treated) were dispersed in 4.00 mL ultrapure water and 20.0 mL of absolute ethanol. Then 0.430 mL $NH_3 \cdot H_2O$ (35% v/v) and 3-aminopropyl-triethoxysilane (APTES) were consecutively added to the solution under vigorous stirring. The reaction was heated at 65°C for 3 hours and then cooled to room temperature (20°C). The amine modified MNPs (MNP-NH_2) were separated by centrifugation (5 minutes, 7000 rpm), washed with ultrapure water three times and re-dispersed in 1.00 mL of ultrapure water.

2.3.5 Synthesis of Fe_3O_4 MNPs via thermal decomposition method, silica coating, and amino modification

2.3.5.1 Synthesis of Fe_3O_4 MNPs *via* thermal decomposition

The high temperature synthesis of the iron oxide MNPs was done under a nitrogen atmosphere [132, 133]. A 0.71 g iron (III) acetylacetonate (2 mmol), 2.58 g hexadecanediol (10 mmol), 2 mL oleylamine (6 mmol), and 2.0 mL oleic acid (6 mmol), were magnetically stirred in 20.0 mL benzyl ether. The solution was heated to 200 ^oC for 2 hours and then heated to reflux (300 ^oC) for another 1 hour. The solution gradually turned black when the temperature reached 300 ^oC, indicating the formation of the iron oxide nanoparticles. The solution was cooled down slowly to room temperature. A 50.0 mL of ethanol was added to the mixture and the resulting suspension was centrifuged at 4 500 rpm for 5 minutes. 20.0 mL hexane containing 0.05 mL oleic acid and 0.05 mL oleylamine was added to the black coloured material and was sonicated for 5 minutes. The mixture was centrifuged at 4600 rpm for 5 minutes and the undispersed residue was discarded. 50.0

mL of ethanol was again added to the hexane solution containing the MNPs which was then centrifuged (4600 rpm, 5 minutes). The black coloured material was collected using a permanent magnet and dispersed finally in 10 mL hexane.

2.3.5.2 Seed mediated growth of Fe_3O_4 MNPs

Seed mediated growth was done to increase the particles size of the MNPs previously synthesized in section 2.3.5.1. Specifically, 50.0 mg of the as-prepared MNPs was added to a solution containing 0.71 iron (III) acetylacetonate (2mmol), 2.58 g hexadecanediol (10 mmol), 2 mL oleylamine (6 mmol), 2.0 mL oleic acid (6 mmol) in 20.0 mL benzyl ether. The mixture was heated for 1 hour at 100 ˚C to remove hexane. The mixture was heated at 200 ˚C for 1 hour and refluxed at 300 ˚C for another hour [132]. The black mixture was cooled down gradually to room temperature. The same steps were carried out to purify the MNPs as described in section 2.3.5.1

2.3.5.3 Silica coating of Fe_3O_4 using micro-emulsion method [134]

A solution containing 0.500 g of IGEPAL-CO 250 in 11.0 mL cyclohexane was prepared and sonicated for 10 minutes at room temperature. Approximately 1.3 mg of Fe_3O_4 MNPs (obtained after the first seed mediated growth) were dispersed in 1.00 mL cyclohexane, sonicated for 5 minutes, and then dispersed in the IGEPAL CO-250 mixture, sonicated again for 10 minutes, and stirred for 12 hours at room temperature. After which 0.100 mL of 28% v/v NH_4OH was added and the resulting solution was stirred for 1 hour. Subsequently, 0.300 mL of TEOS was added *via* equally fractionated drop of 0.075 mL per two hours. After that, acetone was added to precipitate the formed Fe_3O_4-SiO_2 core-shell nanoparticles. The nanoparticles were collected by centrifugation at 5000 rpm for 3 minutes, followed by washings with 10 mL of butanol: hexane mixture (1:1), 10 mL of isopropanol: hexane (1:1) mixture and 10 mL of ethanol: hexane (1:1) mixture. The nanoparticles were further washed three times with pure ethanol and finally dispersed in 10.0 mL ethanol [134]. The final concentration of Fe_3O_4-SiO_2 was determined to be 55 $mg \cdot mL^{-1.}$

2.3.5.4 Optimization of silica coating parameters: (i) Effect of amount of TEOS and (ii) Effect of amount of MNP

Optimization of synthesis parameters for Fe_3O_4 - SiO_2 was done by (i) changing the amount of TEOS and (ii) changing the amount of MNPs while all other reaction conditions and purification steps were kept constant. First, the amount of TEOS were varied as shown in **Table 2-2**. TEOS were added at an increment volume of 75 µL every three hours till the total volume was added to the reaction mixture.

Table 2-2. Different volumes of TEOS used in MNP coating.

Fe_3O_4 (mg)	IGEPAL CO-520 (g)	NH_3 (µL)	Total TEOS (µL)	No. TEOS addition
1.3	0.50	100	75	1 x
1.3	0.50	100	150	2 x
1.3	0.50	100	300	4 x
1.3	0.50	100	450	6 x

The weight of MNPs used the reaction was varied as shown in **Table 2-3**.

Table 2-3. Different amount of Fe_3O_4 nanoparticles used in the reaction mixture

Fe_3O_4 (mg)	IGEPAL CO-520 (g)	NH_3 (µL)	Total TEOS (µL)	No. TEOS addition
1.3	0.50	100	300	4 x
4.0	0.50	100	300	4 x
10.0	0.50	100	300	4 x

2.3.5.5 Amino modification of Fe_3O_4-SiO_2 MNPs

A ~ 20.0 mg of the as-prepared F_3O_4-SiO_2 MNPs were dispersed in 4.00 mL ultrapure water and 20.0 mL of absolute ethanol. Then 0.430 mL $NH_3 \cdot H_2O$ (35% v/v) and 3-(aminopropyl)triethoxysilane (APTES) were added to the solution under vigorous stirring. The reaction was heated at 65°C for 3 hours and cooled to room temperature

(20°C). The amine modified MNPs (MNP-NH_2) were separated by centrifugation (5 minutes, 6000 rpm), washed with ethanol three times and re-dispersed in 5.00 mL ethanol and kept in the fridge (4°C) until use. Further experiments were carried out by aliquoting 1.0 mL of the MNP-NH_2 in ethanol and washing the nanoparticles three times with pure water. The final MNP-NH_2 were dispersed in 1.0 mL of water.

2.3.6 Quantification of amine loading on the Fe_3O_4 MNPs

The amount of MNP surface amine (A_M, mol/g) was determined by a ninhydrin test. First, ninhydrin reagent was reacted with various concentrations of APTES to form coloured products and used as calibration standards [135]. The absorbance at 570 nm of the above samples was recorded to establish the calibration curve by plotting the absorbance versus the APTES concentration. A 1.0 mg of the amine-modified MNPs (weight of MNP-NH_2 beads, W_s) was added to the solution containing 1.00 mL of ninhydrin reagent. The mixture was heated at 65 °C for 30 minutes and then cooled to 30 °C in a dry bath incubator for another 30 minutes. The mixture was centrifuged (5 minutes, 14000 rpm) and the supernatant was collected and diluted to 1.5 mL with absolute ethanol. The supernatant volume was designated as V (L) and its absorbance at 570 nm was measured against blank reference (absence of MNP-NH_2) on a UV-Vis spectrophotometer. By using the calibration curve, the corresponding amine concentration (M, mol/L) was determined. The molar quantity of amine, (A_M, mol·g^{-1}) on the surface of MNP-NH_2 were calculated as follows:

$$\mathbf{A_M(mol/g)} = \frac{\mathbf{M\,V}}{\mathbf{W_s}} \qquad \textbf{Equation 2-1}$$

2.3.7 Synthesis of NHS-PEG-N_3 heterobifunctional linker ligand

Scheme 2-3 shows the synthetic procedures of NHS-PEG-N_3. The product of each step was confirmed by thin layer chromatograpl~23TLC), nuclear magnetic resonance (NMR) spectroscopy, and high resolution mass spectrometry (MS). The synthesis of amine-PEG_{23}-azide (MW ~1000, consisting an average of ~23 PEG units) was carried out as described by Mattoussi and colleagues [136] with some modifications. The amine-$PEG_{\sim 23}$-azide was further reacted with succinic anhydride to give a carboxylic acid-$PEG_{\sim 23}$-azide ligand (d), which was reacted with N-hydroxysuccinimide (NHS) to give an NHS ester activated bifunctional linker, NHS-$PEG_{\sim 23}$-Azide (e). The NHS ester readily reacts with the primary amine group to form covalently linked PEG-N_3 groups on the MNP surface to improve the MNP water dispersion stability and provide functional N_3 groups for efficient bioconjugation with DBCO-modified DNA via a copper-free click chemistry approach.

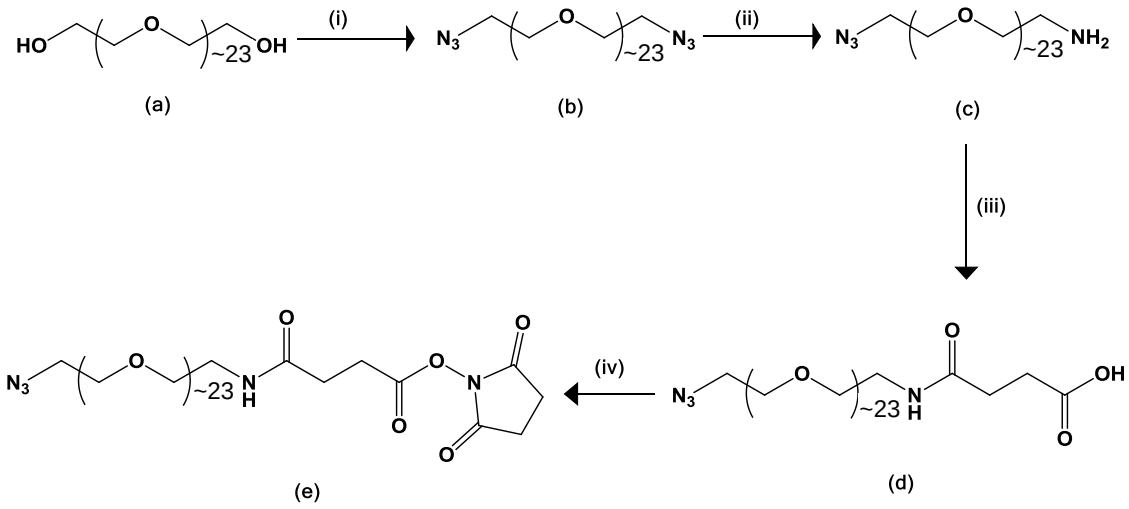

Scheme 2-3. Chemical structures and the synthetic route of NHS-$PEG_{\sim 23}$-N_3. (i) 1. MsCl, THF, Et_3N, 2. H_2O, $NaHCO_3$, NaN_3; (ii) 1. EtOAc/$CHCl_3$, 1M HCl, 2.PPh_3; (iii) Succinic anhydride, DCM. Et_3N; (iv) NHS, DCC/DMAP, dry DCM.

2.3.7.1 Synthesis of N_3-PEG_n-N_3 (n = ~23)

Poly(ethylene glycol) (average MW =1000, 37.0 g, 37 mmol) was dissolved in 150 mL of dry THF containing methane sulfonyl chloride (11.0 g, 92.5 mmol) in a 500 mL three neck round bottom flask equipped with an addition funnel, septa and magnetic stirrer. The mixture was stirred under a N_2 atmosphere and cooled to 0 ºC in an ice bath. Triethylamine (13 mL, 92.5 mmol) was added dropwise to the reaction mixture through the addition funnel over ~ 30 minutes. The reaction mixture was gradually warmed up to room temperature (~ 20 -25 ºC) and was stirred for 12 hours. The mixture turned cloudy white and was filtered to remove the white powdery material. The product was checked by TLC with MeOH: $CHCl_3$= 1:15 (vol/vol) as elution solvent, R_f (MsO-PEG_{23}-OMs) = 0.14, R_f (OH-PEG_{23}-OH) = 0.08, R_f (N_3-PEG_{23}-N_3) = 0.20. The filtrate was transferred to a round bottom flask and diluted with water (150 mL) and added with $NaHCO_3$ (3.73 g, 44.4 mmol). The resulting mixture was transferred to a separation funnel and extracted with $CHCl_3$ (60 mL x 3). The combined organic phase was evaporated to dryness on a rotary evaporator, yielding the desired product as a waxing solid (weight ~40 g). The above product (40 g), sodium azide (10 g, 154 mmol), THF (50 mL), H_2O (50 mL) and $NaHCO_3$ (0.5 g) were then added to a two-necked round bottom flask equipped with a distilling head connected with a round bottom flask as solvent trap placed in an ice bath. The reaction was heated to distill off the THF. After all the THF have been removed, the reaction mixture was refluxed overnight. After cooling to room temperature, the reaction mixture was transferred to a separatory funnel and was repeatedly extracted with $CHCl_3$ (100 mL x 5). The organic layers were combined and dried over anhydrous Na_2SO_4 (~50 g, for 30 minutes), filtered and concentrated in vacuum yielding a pale brown oil which solidifies into a waxy material at low temperature (~ 53 g). A ~ 1.50 g portion of the crude compound was purified by column chromatography using silica gel with 15:1 (vol/vol) $CHCl_3$:MeOH as the eluent. Each fraction was checked by TLC (R_f for N_3-PEG-N_3 = 0.24) and the fractions containing the pure product were combined. The solvent was removed by rotary evaporation to yield 0.852 g of the desired product (58% yield) as a waxing solid. The chemical structure of N_3-PEG-N_3 was confirmed by ^{1}H NMR as shown in **Figure 2-4**. N_3-PEG_{23}-N_3: ^{1}H NMR (400 MHz, $CDCl_3$ residue solvent peak δ= 7.27 ppm): 3.65-3.70 (m), 3.35-3.4 (t, 4H, *J* = 5.0 Hz).

(A)

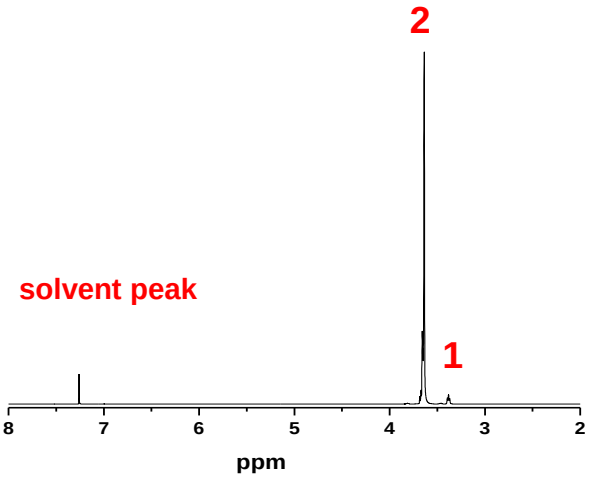

(B)

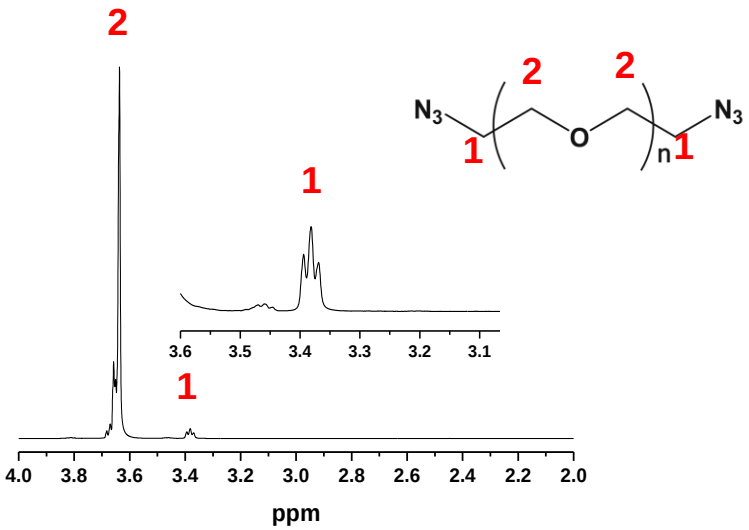

Figure 2-4. (A) ^{1}H NMR spectrum for N_3-PEG$_{\sim 23}$-N_3 (MW ~1000) in $CDCl_3$. (B) The enlarged regions showing proton assignment: the larger peaks at ~ 3.65 ppm are the CH_2 groups of the repeating PEG units. The 3.1 -3.6 ppm region was enlarged for clarity. The triplet peaks at ~3.4 ppm were the resonances of CH_2 groups of the terminal CH_2 connected to the azide group.

The chemical structure of N_3-PEG-N_3 was further characterized by mass spectrometry. The PEG (average MW ~ 1000) used is a mixture of different lengths of ethylene glycol chain. The general molecular formula for the N_3-PEG-N_3 can be written as $(CH_2)_2(C_2H_4O)_nN_6$:

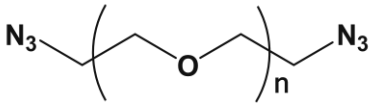

Where *n* corresponds to the number of the ethylene gylcol units (EG, MW = 44 g·mol^{-1}). The MW peaks reported in the mass spectra were determined as sodium ion abductions [MW+NH_4^+]. Therefore, the EG chain length of N_3-PEG-N_3 was estimated using the following formula:

$$\sim 130 + 44\,n$$ **Equation 2-2**

The mass spectra of N_3-PEG_n-N_3 and the assignment of the corresponding EG chain length for each molecular ion peak is shown in **Figure 2-5**.

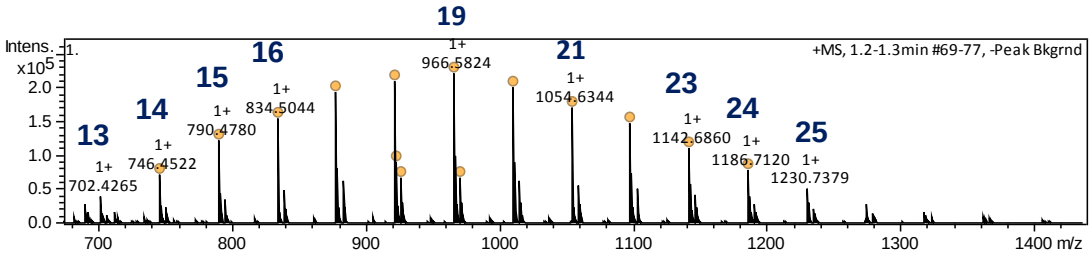

Figure 2-5. Typical mass spectra of N_3-PEG_n-N_3. The ion peaks are reported as (MW + NH_4^{1+}) and the corresponding ethylene glycol chain lengths (n) were assigned to each molecular ion peak.

The mass error in ppm was calculated using the formula [137]:

$$error\ (ppm) = \frac{m_i - m_a}{m_a}\ x\ 10^6 \qquad \textbf{Equation 2-3}$$

Where m_i and m_a refers to the measured accurate mass (experimentally observed m/z) and monoisotopic calculated exact mass (theoretical m/z) respectively. The m_a was determined by summing the masses of the individual isotopes for a given ion. The molecular formula for N_3-PEG_n-N_3 with 21 PEG units and ammonium ion is $C_{44}H_{92}N_7O_{21}$. Therefore, the measured accurate mass (from the mass spectra) and monoisotopic calculated exact mass are 1054.6344 and 1054.6351 respectively. The mass error in ppm = - 0.66. The same calculation can be carried out to calculate the mass error of an assignment with the other mass spectral peaks in **Figure 2-5 (C).**

2.3.7.2 Synthesis of N_3-PEG_n-NH_2 (n = ~23)

N_3-PEG-N_3 (4.5 g, 4.36 mmol) was dissolved in a mixture of 15 mL EtOAc and 15 mL $CHCl_3$ and 1.0 M HCl (10 mL, 10 mmol) in a 500 mL two necked round bottom flask equipped with an addition funnel, septa and magnetic stirrer. The solution was stirred under a N_2 atmosphere and cooled to 0 ºC in an ice bath. Then triphenylphosphine (TPP, 1.25 g, 4.76 mmol) dissolved in ethyl acetate (17.0 mL) was transferred to the addition funnel and added dropwise to the reaction mixture while maintaining the temperature at 0-5ºC. After the addition was complete, the reaction was gradually warmed up to room temperature (20-25 ºC) and was allowed to stir overnight (~12 hours) under a N_2 atmosphere. The biphasic mixture was transferred to a separatory funnel and the aqueous layer was collected and washed with EtOAc (100 mL x 2). The aqueous layer was transferred to a round bottom flask with a magnetic stirrer and placed in an ice bath. Potassium hydroxide (5.05 g, 90.0 mmol) was slowly added and the mixture was stirred until all solid KOH dissolved. The aqueous layer was transferred to a clean separatory funnel and was repeatedly extracted with EtOAc (100 mL x 5). The combined organic layers were dried over anhydrous Na_2SO_4 (~50 g, for 30 min), filtered and concentrated in vacuum yielding a pale colourless oil which solidifies into a waxy material at low temperature (~ 5.1 g). A ~1.5 g portion of the crude compound was purified by flash chromatography using silica gel with 5:1 (vol/vol) $CHCl_3$:MeOH as the eluent. Each fraction was checked by TLC (R_f for N_3-PEG-NH_2 = 0.28) and fractions containing the

pure desired compound were combined. After removal of the solvent, 0.875 g of the pure product was obtained (68% yield) and its ^{1}H NMR spectrum was shown in **Figure 2-6**. ^{1H} NMR spectrum for NH2-PEGn-N3 in CDCl3 (n = ~23). (B) The enlarged 2.6 -3.6 ppm region showing proton assignment. The residual methanol peak is observed at ~ 3.48 ppm. NH_2-$PEG_{\sim 23}$-N_3: ^{1}H NMR (400 MHz, δppm): 7.27 ($CDCl_3$ solvent peak); 3.65-3.70 ((m, -CH_2 in PEG repeat units, 4), 3.52 (m, -C**H**$_2$, 3), 3.40 (t, 2H, *J* = 4.8 Hz, -C**H**$_2$-N_3, 2), 2.89 (t, 2H, *J* = 5.0 Hz, -C**H**$_2$-NH_2, 1).

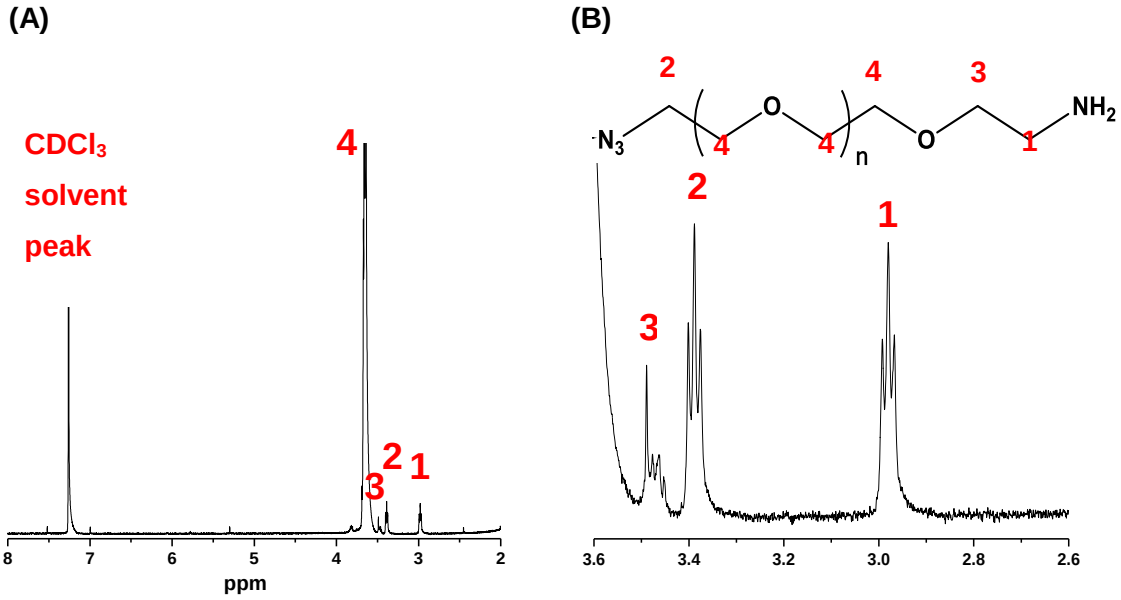

Figure 2-6. ^{1}H NMR spectrum for NH_2-PEG_n-N_3 in $CDCl_3$ (n = ~23). (B) The enlarged 2.6 -3.6 ppm region showing proton assignment. The residual methanol peak is observed at ~ 3.48 ppm.

The chemical structure of NH_2-PEG-N_3 linker was further characterized by MS. Assuming a mono azide reduction of the N_3-PEG-N_3 linker, the general molecular formula for the NH_2-PEG-N_3 must be $(CH_2)_2(C_2H_4O)_nH_2N_4$:

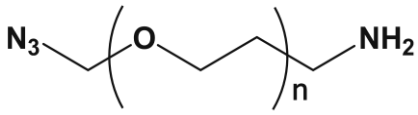

The MW peaks [MW + H^+] for NH_2-PEG_n-N_3 was estimated using the following formula:

$$\sim 87 + 44\, n$$ **Equation 2-4**

The mass spectra of NH_2-PEG-N_3 and the assignment of the corresponding EG chain length for each molecular ion peak is shown in **Figure 2-7**.

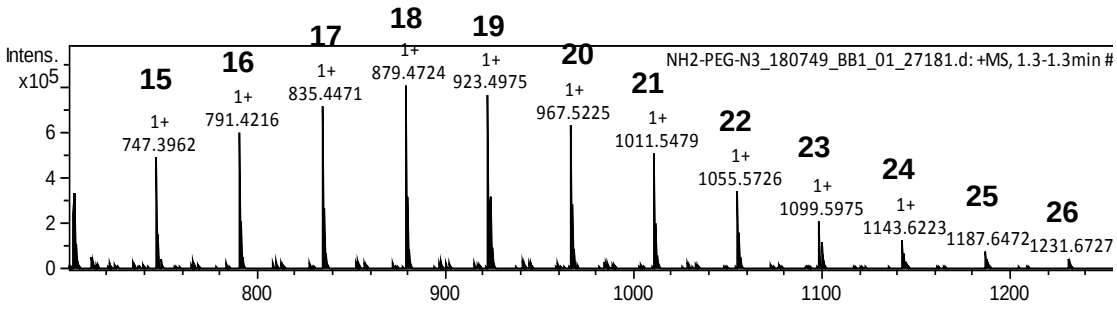

Figure 2-7. Typical mass spectra of NH_2-PEG_n-N_3. The ion peaks are reported as (MW + H^{1+}) and the corresponding ethylene glycol chain lengths were assigned to each molecular ion peak.

The molecular formula for N_3-PEG_n-NH_2 with 19 EG units and proton is $C_{40}H_{83}O_{19}N_4$. Therefore, the measured accurate mass (from the mass spectra) and monoisotopic calculated exact mass are 923.4975 and 923.5670 respectively. The mass error in ppm = -73.84. The same calculation can be carried out to calculate the mass error of an assignment with the other mass spectral peaks in **Figure 2-7 (C).**

2.3.7.3 Synthesis of carboxylic acid-PEG-N_3 ligand

NH_2-PEG-N_3 (1.23 g, 1.23 mmol) was transferred to a round bottom flask equipped with magnetic stirrer and 10.0 mL of dry DCM. Triethylamine (173 µL, 1.23 mmol) was added and the solution was stirred under a N_2 atmosphere for 30 minutes. Succinic anhydride (0.247 g, 2.47 mmol) was dissolved in 10 mL of dry DCM with the aid of sonication and was added dropwise to the reaction mixture at room temperature. The reaction was stirred overnight (~12 hours) under a N_2 atmosphere. After removal of the DCM solvent, the crude product was obtained a pale waxy material. The crude compound was purified by column chromatography using silica gel with 5:1 (vol/vol) $CHCl_3$:MeOH as the eluent. Each fraction collected was checked by TLC (R_f for N_3-PEG-NH_2 = 0.28; Rf for HOOC-PEG-N_3= 0.56) and the fractions containing the pure desired product were combined. After removal of the solvent, 1.271 g of the pure product was obtained (97 % yield). The ^{1}H NMR spectra of the purified compound is shown in **Figure 2-8**. HOOC-PEG_n-N_3: ^{1}H NMR (400 MHz, δ ppm): 7.27 ($CDCl_3$ solvent peak); 3.65-3.70 (m,-CH_2- in PEG repeat units, 4), 3.55 (m, 2H, -CH_2- in PEG unit, 3), 3.48-3.50 (t, 2H, *J* = 4.8 Hz, -CH_2-N_3, 2), 3.28-3.30 (m, 2H,-CH_2-NH-, 1), 2.70-2.75 (m, 2H, -NH-C(O)-CH_2-, 6), 2.53-2.60 (m, 2H,-CH_2-COOH-, 5).

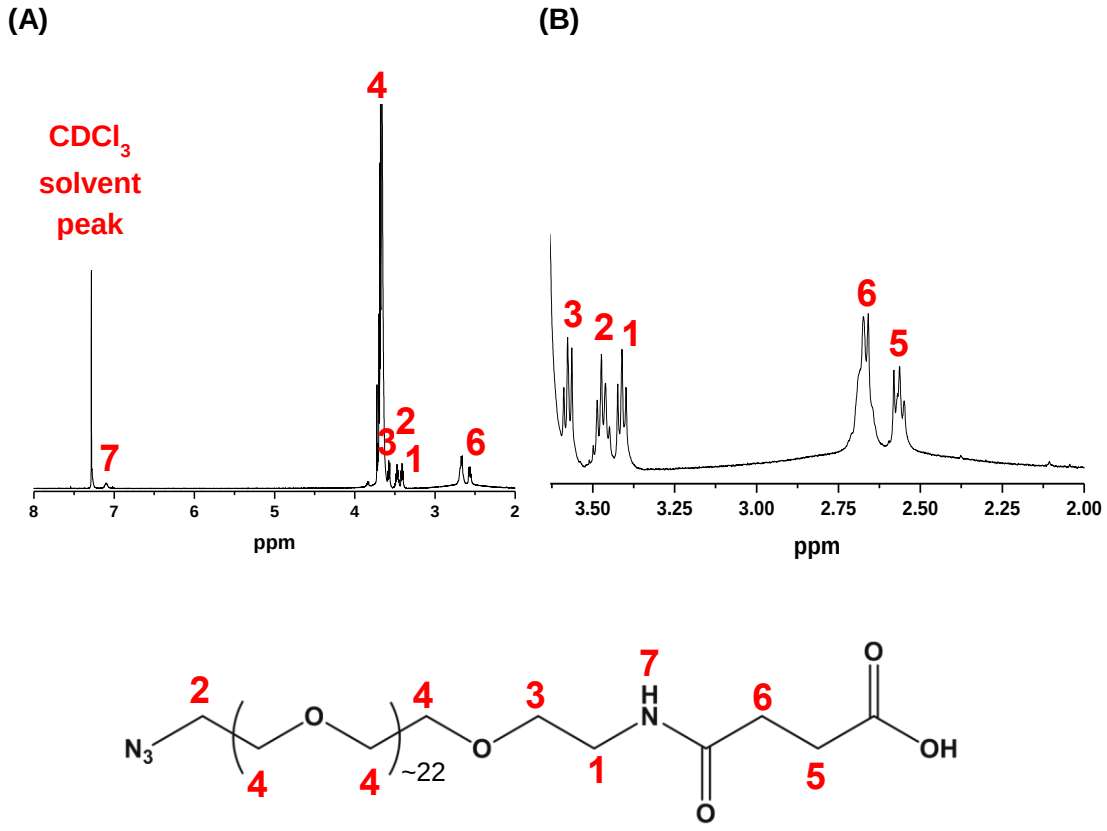

Figure 2-8. (A) ^{1}H NMR spectrum for HOOC-PEG$_n$-N$_3$ in CDCl$_3$ (n = ~23). (B) The enlarged 2.0-3.6 ppm region showing proton assignment.

The chemical structure of HOOC-PEG-N_3 linker was further characterized by MS. The general molecular formula of NH_2-PEG-N_3 is $C_4H_5O_3(C_2H_4O)_nC_2H_5N_4$:

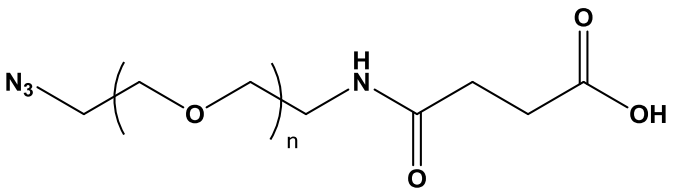

The MW peaks [MW + Na^+] for COOH-PEG$_n$-N_3 was estimated using the following formula:

$$\sim 209.16 + 44\,n$$ **Equation 2-5**

The mass spectra of NH_2-PEG-N_3 and the assignment of the corresponding EG chain length for each molecular ion peak is shown in **Figure 2-9**.

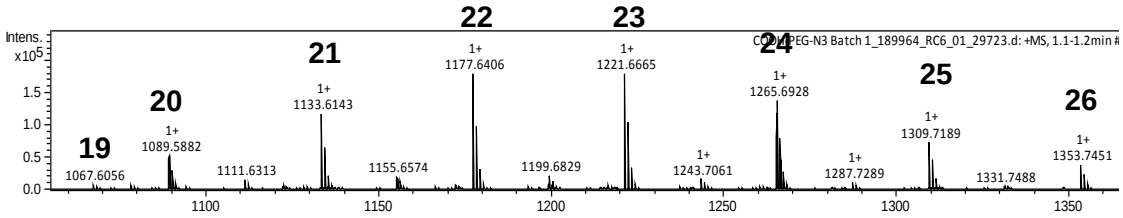

Figure 2-9. Typical mass spectra of HOOC-PEG-N_3. The ion peaks are reported as (MW + Na^{1+}) and the corresponding ethylene glycol chain lengths were assigned to each molecular ion peak.

The molecular formula for N_3-PEG_n-COOH with 23 EG units and sodium is $C_{52}H_{102}O_{26}N_4Na$. Therefore, the measured accurate mass (from the mass spectra) and monoisotopic calculated exact mass are 1221.6665 and 1221.6685 respectively. The mass error in ppm = -1.63. The same calculation can be carried out to calculate the mass error of an assignment with the other mass spectral peaks in **Figure 2-9 (C).**

2.3.7.4 Synthesis of NHS-PEG-N_3 ligand

HOOC-PEG–N_3 (0.76 g, 0.62 mmol), N-hydroxysuccinimide (0.143 g, 1.24 mmol), and 4-dimethylaminoyridine (0.076 g, 0.615 mmol) were dissolved in 10.0 mL of dry DCM in a 3-necked round bottom flask. The mixture was stirred under a N_2 atmosphere for 30 minutes and maintained at 0 ^oC using an ice bath. Dicyclohexyl-carbodiimide (0.225g, 1.24 mmol) dissolved in 10.0 mL of dry DCM was added dropwise to the mixture while keeping the temperature at 0 ^oC. After the addition, the reaction mixture was allowed to gradually warm up to room temperature and stirred for 48 hours. The crude compound was purified by column chromatography using silica gel with 5:1 (vol/vol) $CHCl_3$:MeOH as the eluent. Each fraction was checked by TLC (R_f for NHS-PEG-NH_2 = 0.66; R_f for COOH-PEG-N_3= 0.56) and the fractions containing the desired pure compound were combined. After removal of the solvent, 0.695 g of the pure product was obtained (91 %

yield). The ^{1}H NMR spectrum of the purified compound is shown in **Figure 2-10**. The product was dissolved in dry DMSO and stored in a freezer in aliquot till further use.

NHS-PEG$_n$-N$_3$: ^{1}H NMR (400 MHz, δ ppm): 7.27 ($CDCl_3$ solvent peak); 3.65-3.70 (m,-CH_2- in PEG repeat units, 4), 3.55 (m, -CH_2- in PEG unit, 3), 3.48-3.50 (m, 2H,-CH_2-N_3, 2), 3.30-3.42 (m, 2H,-CH_2-NH-,1), 2.90-3.00 (m, 2H, -CH_2-C(O)-,5) 2.78-2.82 (s, broad, 4H, -CH_2- succinimide ring, 8), 2.53-2.60 (m, 2H, NH-C(O)-CH_2-, 6).

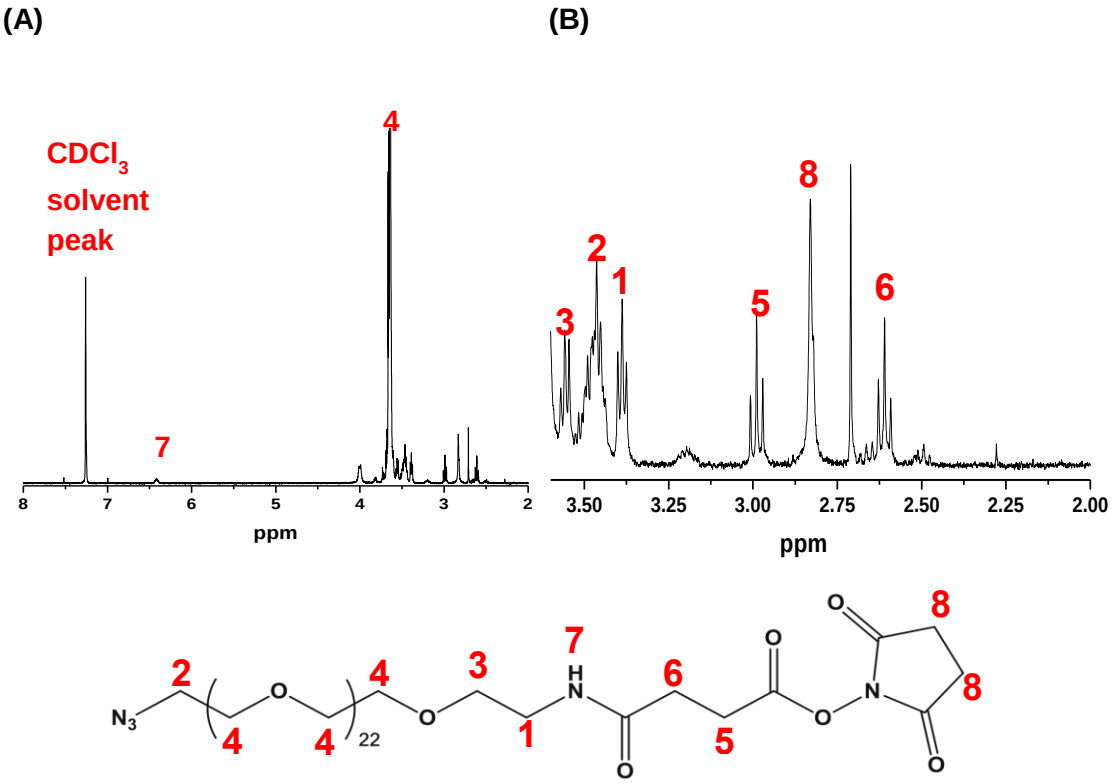

Figure 2-10. (A) ^{1}H NMR spectrum for NHS-PEG$_n$-N$_3$ in $CDCl_3$ (n = ~23). (B) The enlarged 2.0-3.6 ppm region showing proton assignment.

The chemical structure of NHS-PEG-N_3 linker was further characterized by MS. The general molecular formula for the NHS-PEG-N_3 must be $C_8H_8O_5N(C_2H_4O)_nC_2H_5N_4$:

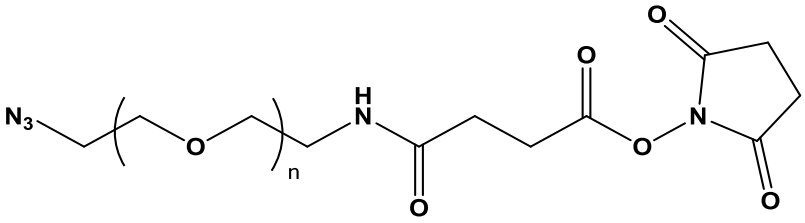

The MW peaks [MW + K^+, H^+] for NHS-PEG_n-N_3 was estimated using the following formula:

$$\sim 323.23 + 44n \qquad \textbf{Equation 2-6}$$

The mass spectra of NHS-PEG_n-N_3 and the assignment of the corresponding EG chain length for each molecular ion peak is shown in **Figure 2-11.**

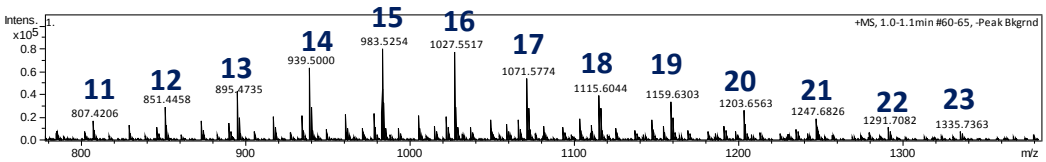

Figure 2-11. Typical mass spectra of NHS-PEG_n-N_3. The ion peaks are reported as (MW + K^+ + H^+) and the corresponding ethylene glycol chain lengths were assigned to each molecular ion peak.

2.3.8 Surface Functionalization of MNP-NH_2 and Preparation of MNP-DNA_{ss}-HRP Design-1 and Design-2

The MNP-NH_2 used in the succeeding experiments were the ones obtained from section 2.2.5.5. The amine content were determined using ninhydrin assay to be ~ 760 nmol·mg^{-1}. The MNPs were conjugated with 1% NHS-$PEG_{\sim 23}$-N_3 and 99% NHS-$PEG_{\sim 17}$-OCH_3. The amine content were determined for every new batch of MNP-NH_2 prepared and the amount of the PEG linkers were adjusted accordingly. The azide modified MNP were then modified with the DBCO modified capture-DNA strands via copper-free click chemistry. Zeta potential measurements were carried out after each functionalization step. The incorporation of PEG linkers and DNA molecules onto the MNPs would change the surface charge thus, implying the success of the functionalization steps.

2.3.8.1 Surface Functionalization with NHS-PEG$_{\sim 23}$-N$_3$ and blocking with NHS-PEG$_{\sim 17}$-OCH$_3$

An ~ 15 mg of MNP-NH_2 (contains ~ 1.14 x10^{-5} mol amine) was washed with dry DMF three times and dispersed in 500 µL dry DMF. A 0.1216 g of NHS-PEG-N_3 (0.094 mmol) was dissolved in 1000 µL dry DMF to yield a final concentration of ~ 94 mM. Then, ~1.5 µL of the NHS-PEG-N_3 solution was added to the MNP-NH_2 and incubated for ~72 hrs at room temperature, leading to MNP surface being functionalized with azide. Thereafter, the MNPs were washed again with dry DMF and added with 45 µL of 250 mM NHS-PEG$_{\sim 17}$-OCH_3 and incubated for another 72 hrs at room temperature to passivate unreacted surface amine. The MNPs were washed by ultrapure water five times and dispersed in 1.0 mL PBS (pH 7.4) and stored in the fridge till use.

2.3.8.2 Conjugation of DBCO- DNA-Biotin to azide modified MNP and linking with NAV-HRP

500 µL of the MNP-PEG$_{\sim 23}$-N_3 (~ 8 mg·mL^{-1}) and 50 µL of 85 µM DBCO-DNA-Biotin were mixed and incubated for 72 hrs. The MNPs were washed with ultrapure water three times and finally dispersed in PBS containing 1 mg·mL^{-1} BSA. This yielded a final MNP concentration of ~ 4 mg·mL^{-1} and the DNA loading per mg MNP was determined to be ~ 0.36 nmol·mg^{-1}. The conjugation of the NAV-HRP to MNP-PEG$_{\sim 23}$-DNA-Biotin was carried out in a 1:1 mol ratio of NAV-HRP to DNA-Biotin. A 200 µL aliquot of the MNP-PEG$_{\sim 23}$-Biotin was mixed with 28 µL of 10 µM NAV-HRP in an eppendorf tube and incubated overnight and subsequently washed 5 times with PBS. Finally, the MNP-DNA_{ss}-Biotin probe (Design 1) was dispersed in 1.0 mL PBS.

2.3.8.3 Conjugation of DBCO-DNA-SH to azide modified MNP

~ 15 mg of MNP-PEG-N_3 was washed with 1.0 mL ultrapure water and dispersed in 100 µL of pure water. A 100 µL of ~200 µM capture DNA-SH was added and incubated for 72 hrs at room temperature, leading to the DBCO-DNA-SH being covalently conjugated to the MNP surface *via* copper free click chemistry. The MNPs were subsequently washed three times with PBS. All the original and washing supernatants were collected for UV-Vis measurement at λ=260 nm to determine the amount of free-unbound DBCO-DNA-SH, allowing the estimation of the DBCO-DBA-SH conjugation efficiency. Finally, the MNP-DNA probes were treated with 1 mL PBS buffer containing 1 mg/mL BSA to

block MNP surface and reduce non-specific absorption of HRP in the subsequent steps. The MNP-DNA-SH were kept in the fridge till further use.

The amount of the DBCO-DNA-SH loading was determined by comparing the concentration of the DBCO-DNA-SH before and after conjugation. The conjugation efficiency was computed using Equation 2-7:

$$\boldsymbol{Conjugation\ efficieny_{DNA} = \frac{C_i - C_x}{C_i}\ x\ 100} \qquad \textbf{Equation 2-7}$$

where C_i is the intial concentration of the DBCO-DNA-SH and C_x is the remaining concentration of the DBCO-DNA-SH in solution after conjugation taken into account of the dilution factor. The absorbance of the DNA solutions were determined at λ=260 nm using nanodrop UV-Vis and the corresponding concentrations were calculated from the molar extinction coefficient (3.86 x 10^5 M^{-1} cm^{-1}). This conjugation protocol afforded a DNA loading of 0.64– 0.70 nmol·mg^{-1} with conjugation efficiency ranging from 35% - 72%.

2.3.8.4 TCEP treatment of MNP-DNA-SH

The MNP-DNA-SH obtained from section 2.3.8.3 were treated with TCEP to reduce any disulphide bonds and to allow the conjugation of the maleimide modified HRP via Michael addition. This reduction step was simultaneously carried out while labelling HRP with NHS-PEG_{12}-Maleimide linker as mentioned in section 2.3.8.5. Specifically, 1.0 mL of the MNP-DNA-SH was washed with once with PBS and dispersed in 200 µL PBS. This was added with 30 µL of 350 µM TCEP and incubated for 1 hr at room temperature. The MNP-DNA-$SH_{(reduced)}$ was washed once with 1.0 mL PBS to remove by-products from TCEP reduction.

2.3.8.5 HRP labelling with NHS-PEG_{12}-Maleimide

A 200 µL of 100 µM HRP (dissolved in PBS) was mixed with 10 µL of NHS-PEG_{12}-Maleimide (10 µg·mL^{-1}) and incubated for 1.5 hrs at room temperature. The maleimide labelled HRP was transferred to a centrifugal filter (MW cut off 10 kDa) and washed

twice with 1.0 mL PBS. The volume of the HRP was adjusted to 100 µL by adding PBS. Then, 80 µL of the labelled HRP was mixed with 100 µL MNP-DNA-SH and was incubated for 3 hrs at room temperature and was left in the fridge overnight. The remaining 20 µL portion of the labelled HRP was used to determine the HRP concentration. The MNP-DNA-HRP were separated from the unreacted HRP by centrifugation at 10,000 rpm for 5 min and the supernatant was collected for UV-Vis measurement. Thereafter, the MNP-DNA-HRP were purified by repeated 5 cycles of centrifugation and washing with 1.0 mL PBS containing 0.1 % Tween-20 and once with 1.0 mL PBS to remove any excess Tween-20. The final MNPs were dispersed in 1.0 mL PBS and kept in the fridge till further use.

The amount of the labelled HRP conjugated to the MNPs were determined by comparing the concentration of the labelled HRP before and after conjugation. The percent conjugation efficiency was computed using **Equation 2-8.**

$$\boldsymbol{Conjugation\ efficieny_{HRP}} = \frac{\boldsymbol{C_i - C_x}}{\boldsymbol{C_i}}\ \boldsymbol{x\ 100} \qquad \textbf{Equation 2-8}$$

where C_i was the initial HRP concentration and C_x was the free unconjugated HRP concentration in solution after conjugation, taken into account of the dilution factor. The absorbance of the HRP solutions were measured at λ= 403 nm on a nanodrop UV-Vis and the corresponding concentrations were calculated using the molar extinction coefficient (1.0 x10^5 M^{-1} cm^{-1}) [138]. This conjugation protocol afforded efficiencies from 14 – 27 %.

2.3.9 General Experimental for detection of ECOR-I and DNA

The general biosensing procedure was summarized in **Scheme 2-4.** Twice the amount of target DNA to that on the MNP beads was added to ensure efficient hybridisation. The capture-DNA loading used in the study ranged from 0.66 to 0.70 nmol·mg^{-1} MNP unless otherwise stated. The MNP probe Design-1 and Design-2 were incubated with the target DNA then with ECOR-I. The MNPs were magnetically separated from the solutions and a portion of the clear supernatant was used for colorimetric detection

reaction using amplex red and H_2O_2 with 1 hr incubation and then quenched by NaN_3. The absorbance of the solutions were determined by using UV-vis at λ=572 nm.

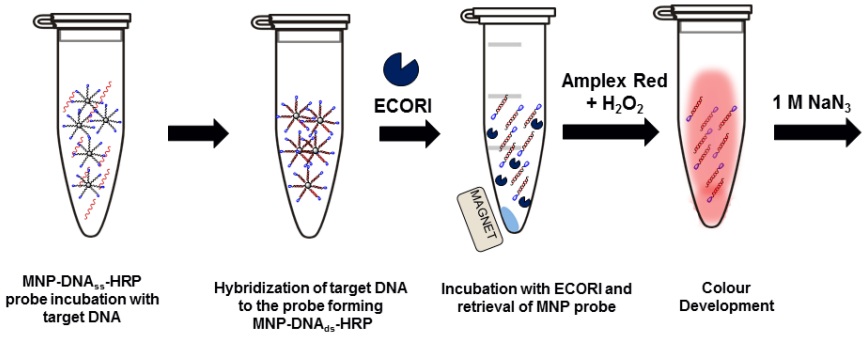

Scheme 2-4. Schematic illustration of the biosensing steps for the detection of ECOR-I and DNA.

2.3.9.1 Optimization of incubation temperature with ECOR-I

12 μL (~ 60 μg) MNP-DNA_{ss}-HRP in PBS was mixed with 10 μL of (5 μM) target DNA and incubated at room temperature for 1 hr. After that, 148 μL water, 20 μL Cutsmart® buffer and 10 μL of 200 $U{\cdot}mL^{-1}$ ECOR-I were added and incubated at different temperatures from 4˚C - 40˚C for 1 h. The final volume of the reaction was 200 μL with 10 $U{\cdot}mL^{-1}$of the ECOR-I. A control experiment was also carried out in which all reaction components were mixed except the target DNA. The experiment was conducted in triplicates. The MNPs were separated by centrifugation at 4000 rpm for 5 min. 150 μL of the clear supernatant were transferred to a clean Eppendorf tube and added with 750 μL PBS, 50 μL of 0.40 mM amplex red and 50 μL of 0.40 mM hydrogen peroxide and was incubated at room temperature for 1 hr. The chromogenic reaction was stopped by addition of 100 μL of 1.0 M NaN_3 to the samples and the absorbance was recorded using Cary UV-Vis 50 spectrophotometer.

2.3.9.2 Optimization of incubation time with ECOR-I

12 μL (~60 μg) MNP-DNA_{ss}-HRP in PBS was mixed with 10 μL of (5 μM) target DNA and incubated at room temperature for 1 hr. Then 148 μL water, 20 μL Cutsmart® buffer and 10 μL of 200 $U{\cdot}mL^{-1}$ ECOR-I were added and incubated at 30 ˚C for 1 and 2 hrs. The final volume of the reaction was 200 μL and the concertation of the ECOR-I was 10

$U \cdot mL^{-1}$. The same procedures mentioned in section 2.2.9.1 were followed in the succeeding steps.

2.3.9.3 Endonuclease Activity Assay with MNP-DNA_{ds}-HRP probes

5 μL (~ 60 μg) MNP-DNA_{ss}-HRP in PBS was mixed with target 10 μL of 5 μM target DNA and incubated at room temperature for 1hr. Then, 155 μL water, 20 μL Cutsmart® buffer and 10 μL ECOR-I were added and incubated at 30 ˚C for 1 h. The final volume of the reaction mixture was all 200 μL and the final ECOR-I concentration varied from $1x10^{-5}$ to 10 $U \cdot mL^{-1}$. All experiments were done in triplicates along with a control experiment (*i.e.* without target DNA, WOT). The same procedures mentioned in section 2.3.9.1 were followed in the succeeding steps.

2.3.9.4 DNA Detection with MNP-DNA_{ds}-HRP probes

5 μL (~ 60 μg) MNP-DNA_{ss}-HRP in PBS was were mixed with target 10 μL of target DNA and incubated at room temperature for 1hr. After that, 155 μL water, 20 μL Cutsmart® buffer and 10 μL of 10 $U \cdot mL^{-1}$ ECOR-I were and incubated at 30 ˚C for 1 h. The final volume of the reaction mixture was 200 μL. The final concentrations of DNA varied from 1×10^{3} to 1×10^{-3} pM. Each samples were done in triplicates along with a control experiment (WOT; without target DNA). The same procedures mentioned in section 2.3.9.1 were followed in the succeeding steps.

2.4 Results and Discussion

2.4.1 Synthesis of Fe_3O_4 nanoparticles using co-precipitation and preparation of SiO_2 capped Fe_3O_4 MNPs

Iron oxide MNPs were successfully synthesized as black precipitates by using the co-precipitation method. Co-precipitation is the simplest synthesis method for iron oxide MNPs. There are several chemical reaction steps known to take place in the Fe_3O_4 MNP formation, including the formation of some iron complexes as shown below [130]:

1. $Fe^{3+} + 3\ OH^- \rightarrow Fe(OH)_3$
2. $Fe(OH)_3 \rightarrow FeOOH + H_2O$
3. $Fe^{2+} + 2\ OH^- \rightarrow Fe(OH)_2$
4. $2\ FeOOH + Fe(OH)_2 \rightarrow Fe_3O_{4\ (MNP)} + 2H_2O$

Based on the above equations, the Fe^{2+} and Fe^{3+} molar ratio must be controlled to 1:2 to form the magnetite (Fe_3O_4) MNPs. Since the $Fe(OH)_2$ intermediate is susceptible to rapid oxidization by O_2 under basic conditions, the entire synthesis vesicle was protected by an atmosphere of N_2. The reaction was carried out under basic conditions (pH 11) by adding NH_4OH. The nature of the alkali precipitator has known to play an important role in the reaction. Several studies reported that the use of strong base NaOH abruptly increased the OH^- concentration in the solution, leading to rapid precipitation reaction and the formation of large Fe_3O_4 MNPs [131, 139]. In contrast, ammonia is a weaker base than NaOH, and hence the pH of the reaction media would be lower, leading to smaller particle sizes. Magnetite (Fe_3O_4) is also known to be susceptible to oxidation in air, although this happens much slower than $Fe(OH)_2$ does. Hence, purging with nitrogen was used during the reaction to prevent magnetite oxidization to maghemite (Fe_2O_3). **Figure 2-12 (A)** showed that the as synthesized Fe_3O_4 MNPs were homogeneously dispersed in an aqueous solution and remained stable up to 9 months without visible signs of precipitation. These Fe_3O_4 MNPs were found to adhere to the side wall of the Eppendorf tube when placed near a magnet within *ca.* 1 min of magnetic contact, leaving a clear supernatant solution as shown in **Figure 2-12 (B)**. The Fe_3O_4 MNP concentration was 4.3 $mg \cdot mL^{-1}$.

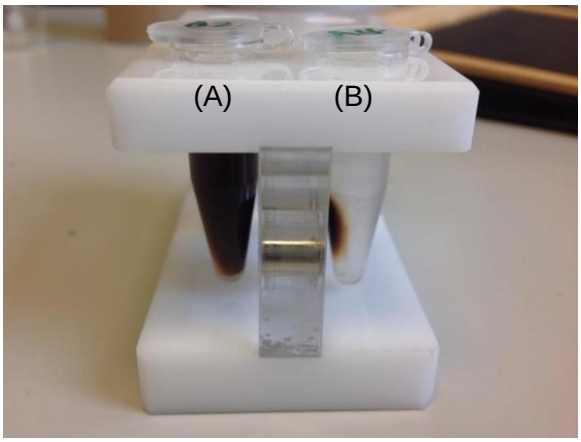

Figure 2-12. The as-synthesized Fe_3O_4 MNPs as, (A) a homogeneous dispersion just being placed in the magnet prior to photo taken, and (B) after magnetic retrieval for 1 min with an external magnet.

The MNPs were easily coated with amorphous silica *via* a sol–gel process because the iron-oxide surface has strong affinity for silica [140]. The silica surface is terminated by silanol (Si-OH) groups which can easily couple to organosilanes by the formation of Si-O-Si covalent bonds. Moreover, the silica coating can also protect the Fe_3O_4 MNPs from further oxidation and prevent direct interactions with biomolecules [140]. In this study, silica coating was achieved by reacting Fe_3O_4 MNPs with tetraethylorthosilcate (TEOS) in a sol-gel reaction [134, 141, 142] in the presence of water and NH_4OH catalyst. The hydrolysis and condensation reactions of TEOS can be illustrated by the following reactions:

(A)

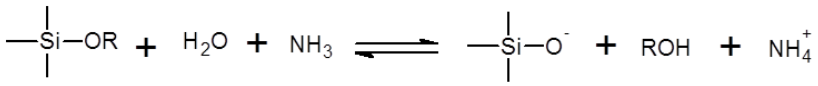

(B)

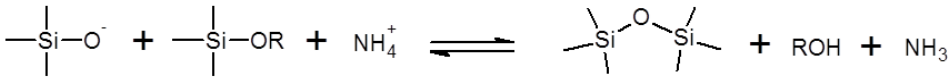

Scheme 2-5. (A) Hydrolysis, and (B) condensation reaction of TEOS

The hydrolysis of TEOS in a basic medium is associated with the formation of a supersaturated solution of silicic acid $[SiO_x(OH)_{4-2x}]_n$. Subsequent condensation of TEOS results in the formation of siloxane bonds (-Si-O-Si-) and the loss of the protonated NH_4^+ [143-145]. Sol-gel silica coating of iron oxide nanoparticles often leads to particle agglomeration and a significant increase of the overall particle size [140, 146-150]

which can be a disadvantage for some biomedical applications. In this view, a careful control on the amount of TEOS and Fe_3O_4 particles must be considered in order to achieve a homogeneously dispersed Fe_3O_4-SiO_2 in aqueous solution. Table 2-4 summarizes the observations when different amounts of Fe_3O_4 were treated with the same volume of TEOS.

Table 2-4. Parameters for synthesizing Fe_3O_4-SiO_2 core-shell MNPs using different amounts of Fe_3O_4 (MW = 231.5 g·mol^{-1}) and 0.100 mL (0.448 mmol) TEOS. The Hydrodynamic diameter (D_h) and zeta potential (ξ, mV) were determined.

Sample	Amount of Fe_3O_4 (mg)	mol TEOS : mol Fe_3O_4	Dispersion stability	D_h (nm)	Zeta potential (ξ, mV)
uncoated	4.30	-	dispersed	147.0	-29.3
A	4.30	24.11	precipitated	-	-
B	8.27	12.54	precipitated	-	-
C	12.39	8.37	dispersed	178.6	-41.9
D	16.52	6.28	dispersed	165.3	-38.0
E	20.65	5.01	dispersed	160.0	-37.3

In general, a stable homogeneous dispersion of Fe_3O_4-SiO_2 MNPs was achieved by controlling the TEOS:Fe_3O_4 molar ratio. Under the present experimental conditions, MNP-SiO_2 prepared at a TEOS:Fe_3O_4 molar ratio of < 12.5 gave a stable MNP-SiO_2 dispersion. Increasing the ratio of TEOS:Fe_3O_4 to above this threshold generally resulted in the precipitation of nanoparticles. This observation highlighted the critical ratio to make stable dispersion. **Table 2-4** shows the list of samples that exhibited a homogeneous dispersion. In comparison to uncoated Fe_3O_4, the D_h of the most samples were increased by *ca.* 20 nm after reaction with TEOS, suggesting a successful silica coating on the MNP. The zeta potential was used to measure the dispersion stability of the silica coated MNP [135, 151] because colloidal stability is important for biomedical applications. A high zeta potential (> 30 mV, either positive or negative) characterises a stable system due to strong electrostatic repulsion, while a low zeta potential value is typical of unstable ones. The zeta potentials for SiO_2 coated and uncoated Fe_3O_4 MNPs

were all negative due to the ionized silica hydroxyl groups at pH 7.0 as shown in **Table 2-4**. In comparison to the uncoated Fe_3O_4 nanoparticles, the silica coated Fe_3O_4 MNPs exhibited higher negative zeta potentials, suggesting that silica coating may render the MNPs better colloidal stability to than the uncoated ones.

2.4.2 Synthesis of amine modified Fe_3O_4-SiO_2 MNPs

3-(aminopropyl)triethoxysilane (APTES) was used to introduce functional amine groups to the Fe_3O_4-SiO_2 MNPs as shown in the schematic diagram in **Figure 2-13**. The driving force here was the *in situ* formation of polysiloxane, which bond the MNP surface silanol groups (Si-OH) through the formation of Si–O–Si bonds [149]. The synthesis was done in ethanol which provided an appropriate polarity to reduce the attractive force between APTES and the surface of Fe_3O_4-SiO_2 [147].

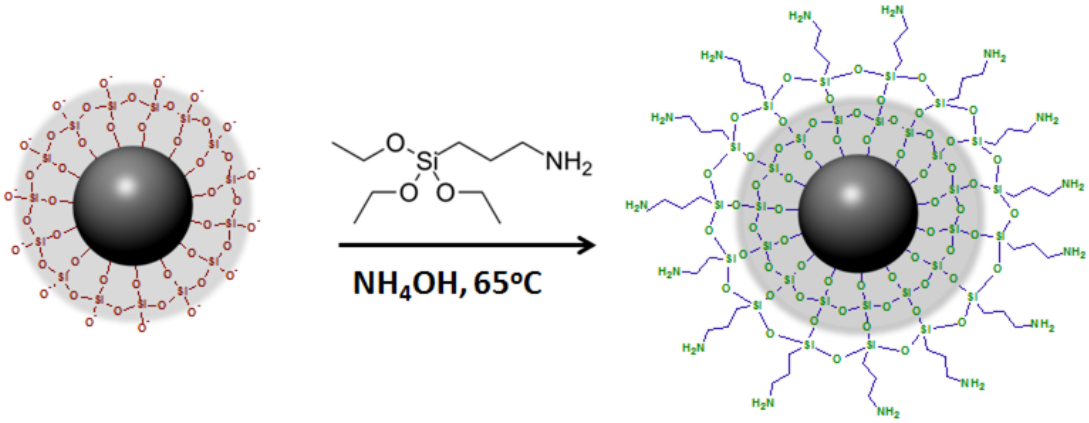

Figure 2-13. Schematic diagram for the synthesis of MNP-NH_2 nanoparticles

Several trials were done to modify the Fe_3O_4-SiO_2 surface silica at room temperature, but all attempts gave negative results in the qualitative test for amines. The low concentration of ammonia used in the experiment might lead to a slow hydrolysis of APTES, leading to the very low quantity of amines to deposite on the MNP-SiO_2 surface. Increasing temperature (to *i.e.* 65 °C) would accelerate the hydrolysis and condensation of APTES on the MNP-SiO_2 particle surfaces.[147]. However, aggregation was observed upon treatment of the Fe_3O_4-SiO_2 particles with large amounts (> 2.137 x 10^{-3} mol) of

APTES, possibly due to that the negatively charged MNPs were attracted to the positive charge of the amine on APTES or its hydrolysed aggregates. The D_hs of the amine modified Fe_3O_4-SiO_2 core-shell nanoparticles were determined by DLS and shown in **Table 2-5**. Amine modification led to a large increase in the D_h, possibly due to aggregation or cluster formation during amine coating. This behaviour was also observed in another study wherein the introduction of a greater amount of aminosilane increased the tendency of agglomeration [147]. Moreover, the irregular shapes of the Fe_3O_4 MNPs synthesized by the co-precipitation method might also have contributed to its large D_h. Zeta potential of the MNP-NH_2 dispersions in water at pH 7.0 was shown in **Table 2-5**. The Fe_3O_4-SiO_2 MNPs showed a more negative zeta potential than the earlier examples, suggesting that the citrate treatment increased the MNP stability via adsorption of negatively charged citrates on the MNP surface, strengthening the electrostatic repulsions among the MNPs.

Table 2-5 Chemical and physical parameters of the prepared MNP-NH_2. The Fe_3O_4-SiO_2 nanoparticles treated with 350 µL , 500 µL, 750 µL, and 1000 µL APTES were labelled as NH_2-350, NH_2-500, NH_2-750, NH_2-1000 respectively.

Sample	APTES amount (mmol)	D_h (nm)	Zeta potential (ξ, mV)
Fe_3O_4-SiO_2	none	188.6	-36.4
NH_2-1000	4.3	3747	+ 0.134
NH_2-750	3.2	5212	-2.50
NH_2-500	2.1	1869	-11.2
NH_2-350	1.5	2854	-14.4

In general, the high negative zeta potential of Fe_3O_4-SiO_2 was significantly reduced or turned into slightly positive after amine modification, suggesting poor colloidal stability of the MNPs-NH_2 dispersions. The positive charge of the amine groups at pH 7 reduced the overall negative charge of the SiO_2 coated MNP, thereby decreasing their electrostatic stabilization. The samples treated with high amounts of APTES (*i.e.* NH_2-1000 and NH_2-750) had very low zeta potential values, suggesting easy particle aggregation to form large particles. The results clearly demonstrated that the amount of APTES directly affected the colloidal stability of MNP-NH_2. Several attempts were carried out to improve the water stability and to reduce the size of the MNP-NH_2. **Figure**

2-14 shows a facile approach to functionalise the Fe_3O_4-SiO_2 MNPs with a cationic surfactant, poly (diallyldimethyl) ammonium chloride (PDDA), prior to amine modification.

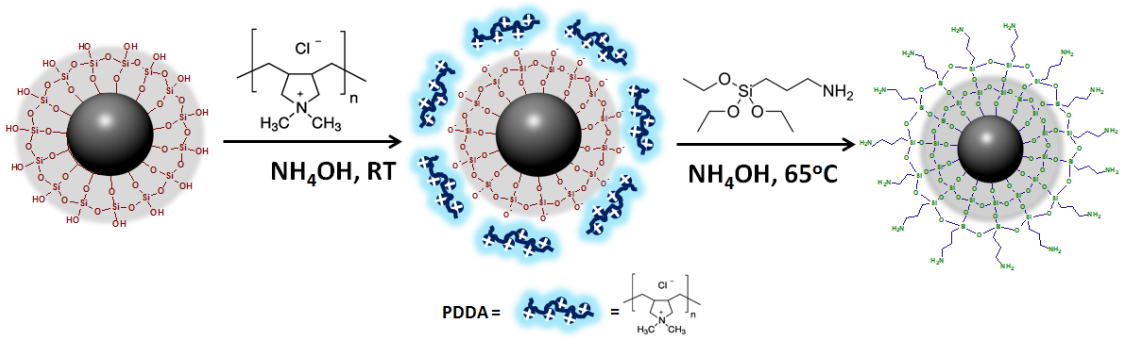

Figure 2-14. Schematic diagram for the synthesis of MNP-NH_2 with a PDDA pretreatment of Fe_3O_4-SiO_2 nanoparticles.

PDDA contains quaternary ammonium functional groups which adsorb strongly to the negatively charged silica surface *via* electrostatic attraction, reducing the possibility of charge reversal induced particle aggregation upon APTES coating. It was mentioned that increasing the MNP-SiO_2 with APTES temperature (*i.e.* 65 ºC) accelerated the condensation of APTES on the surface of silica particles and effectively modifies the MNPs surface with the desired amine functionality. However, one consequence of heat treatment was that it led to agglomerated particles, due to the electrostatic attraction between the APTES (hydrolyzed and aggregated) and the surface silanolate. We hypothesized that a PDDA coating would block the negatively charged silanolate (-Si-O^-), reducing the interaction between the hydrolysed APTES and silica surface thereby giving to smaller amine-modified nanoparticles. The D_h and zeta potentials of MNP-NH_2 prepared with a PDDA pretreatment were determined and compared to those without a PDDA pretreatment and shown in **Figure 2-15** .

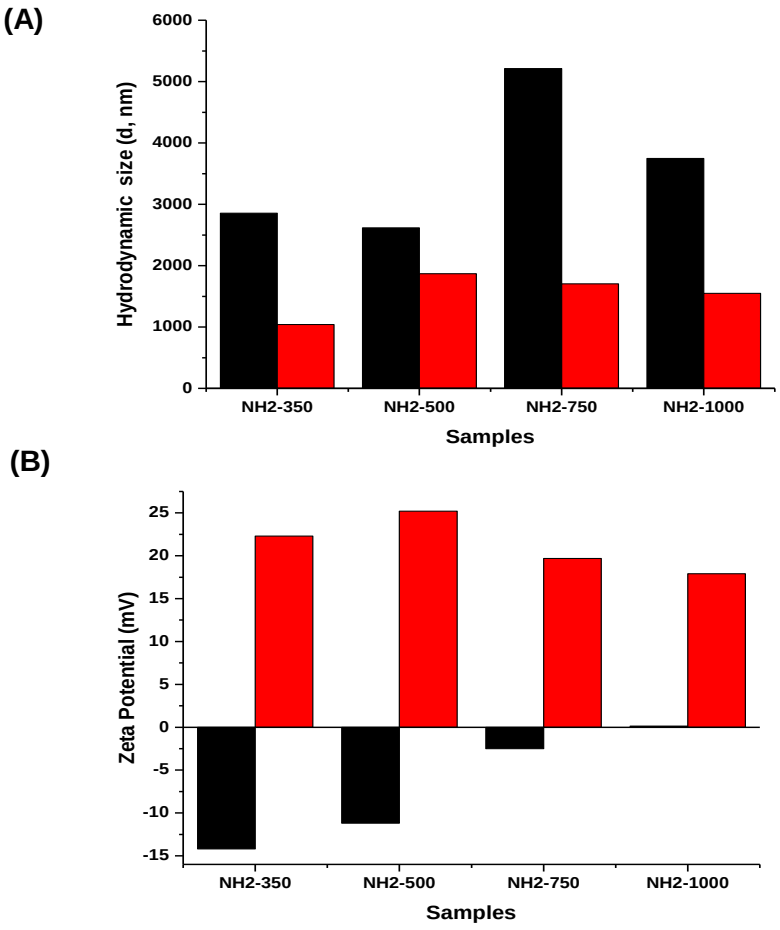

Figure 2-15. (A) Hydrodynamic size and (B) Zeta potential with (red) and without (black) PDDA treatment prior to amine modification.

The PDDA treatment reduced the particle size of MNP-NH_2. However, the results also clearly indicated the particle aggregation even with the PDDA pretreatment judging from their large D_hs (*i.e.* > 1 μm). The zeta potentials of the PDDA treated MNP-NH_2 **(Figure 2-15 (B))** were all >15 mV, suggesting good water stability.

2.4.3 Amine Quantification using Ninhydrin Assay

Ninhydrin was used to quantify the MNP surface primary amines by forming Ruhemann's purple which absorbed at 560 nm as shown in Figure 2-16 **(A)**[135]. The absorbance *v.s.* concentration calibration plot gave a high linear correlation (R^2 =0.9805, Figure 2-16 **(B)**). The molar concentrations of the free amines on the amino-modified MNPs were determined and converted to the molar quantity of amine in $mol \cdot g^{-1}$ for comparison.

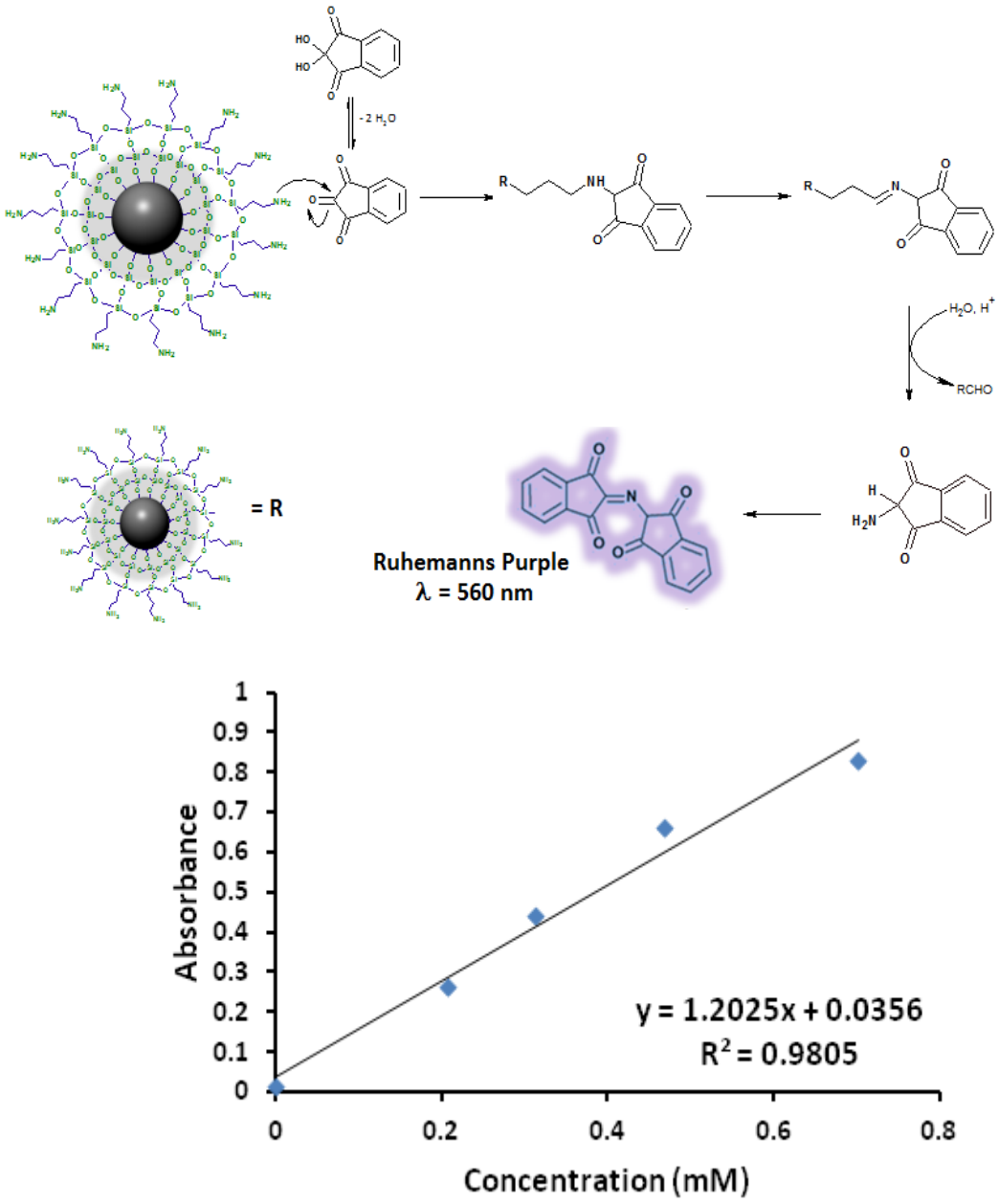

Figure 2-16. (A) Schematic Diagram for the reaction of NH_2-MNPs with ninhydrin, (B) absorbance versus APTES concentration calibration curve.

Using **Equation 2-1**, the amounts of the amine grafted on the surface of MNPs were calculated and shown in **Table** 2-6. The addition of 350 µL (1.50 $x10^{-3}$ mmol) and 500 µL (2.137 × 10^{-3} mmol) of APTES afforded a large amount of accessible (or reactive) amines on the MNP surface. Moreover, comparing the DLS sizes of the NH_2-MNPs, more accessible amines were grafted on the small MNPs such as those NH_2-500 and NH_2-350 samples.

Table 2-6 Molar quantity of amine (A_M) grafted on the surface of MNP-SiO_2

Sample	APTES (mmol)	A_M (mol/g)
NH_2-1000	4.52 $x10^{-3}$	5.27 $x10^{-4}$
NH_2-750	3.21 $x10^{-3}$	1.08 $x10^{-3}$
NH_2-500	2.14 $x10^{-3}$	2.61 $x10^{-3}$
NH_2-350	1.50 $x10^{-3}$	2.06 $x10^{-3}$

A possible explanation here is that the use of high concentration of APTES may form thicker shells where not all amines are exposed on the surface. Moreover, bigger particles have smaller surface-to-volume ratios and hence lower amount of exposed surface amines. In addition, aminosilanes can undergo self-catalysis, leading to the formation of polymerized products at high concentrations [148]. The electrostatic attraction between amine and silanolate groups on the MNP surface may lead to amino groups being oriented towards the silica surfaces as well as self-polymerization of aminosilane groups in the solvent. Both phenomena can adversely affect the efficiency of the surface functionalization by aminosilane molecules [150]. At low amounts of APTES, hydrolyzed APTES molecules tend to diffuse to the MNP surface to form a well ordered monolayer with amine head groups exposed on the silica surface as shown in **Figure 2-17 (A)**. However, at high amounts, some APTES molecules may be hydrolysed and polymerised in the solution before diffusion to the silica surfaces **Figure 2-17 (B)**), leading to poor surface functionalization and reduced surface reactive amines.

(A)

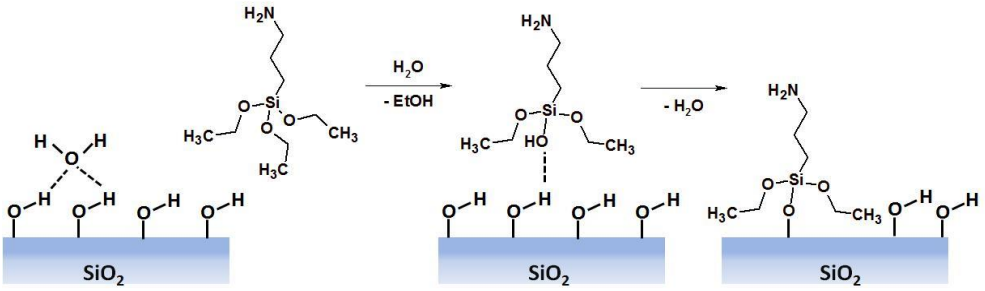

(B)

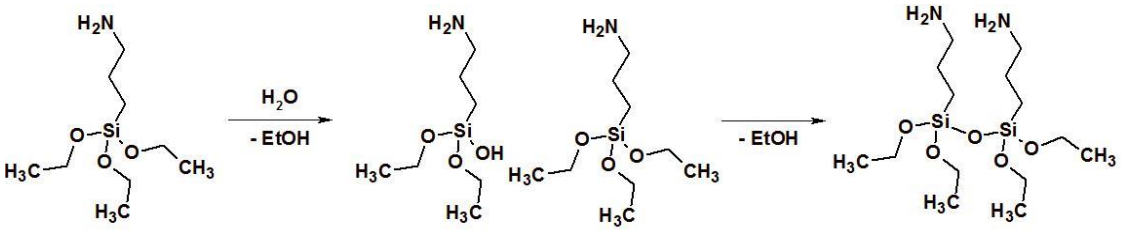

Figure 2-17. Schematic diagram of APTES hydrolysis and condensation under (A) low concentrations and (B) high concentrations of APTES. Reprinted from reference [33]

2.4.4 Characterization of Fe_3O_4 –SiO_2 nanoparticles.

Transmission electron microscopy (TEM) imaging was done to determine the size and morphology of the F_3O_4-SiO_2 core-shell nanoparticles. **Figure 2-18 (A-C)** revealed nearly spherical F_3O_4 particles of *ca.* 18 nm but with poor size and shape uniformity, and high degree of aggregation. The poor control of particle size distribution was due to the lack of robust surface protecting ligands that can prevent aggregation and limit growth speed. Moreover, the kinetic factors like nucleation and growth of crystals also affected shape homogeneity. When the concentration of the precursors reached supersaturation, the nucleation occurs instantly to form “seeds”. Then a slow process of crystal growth *via* diffusion of precursors on the surface of the “seeds” takes place. The key to produce nanoparticles with narrow size distribution is to separate nucleation from growth [152]. TEM

images (**Figure 2-18 (B)** and **(C)** inset) show that the nanoparticles poses core-shell structures with a high tendency of aggregation, consistent to their relatively large D_h measured by DLS. Moreover, silica coated samples showed an amorphous silica shell as shown in the Figure insets.

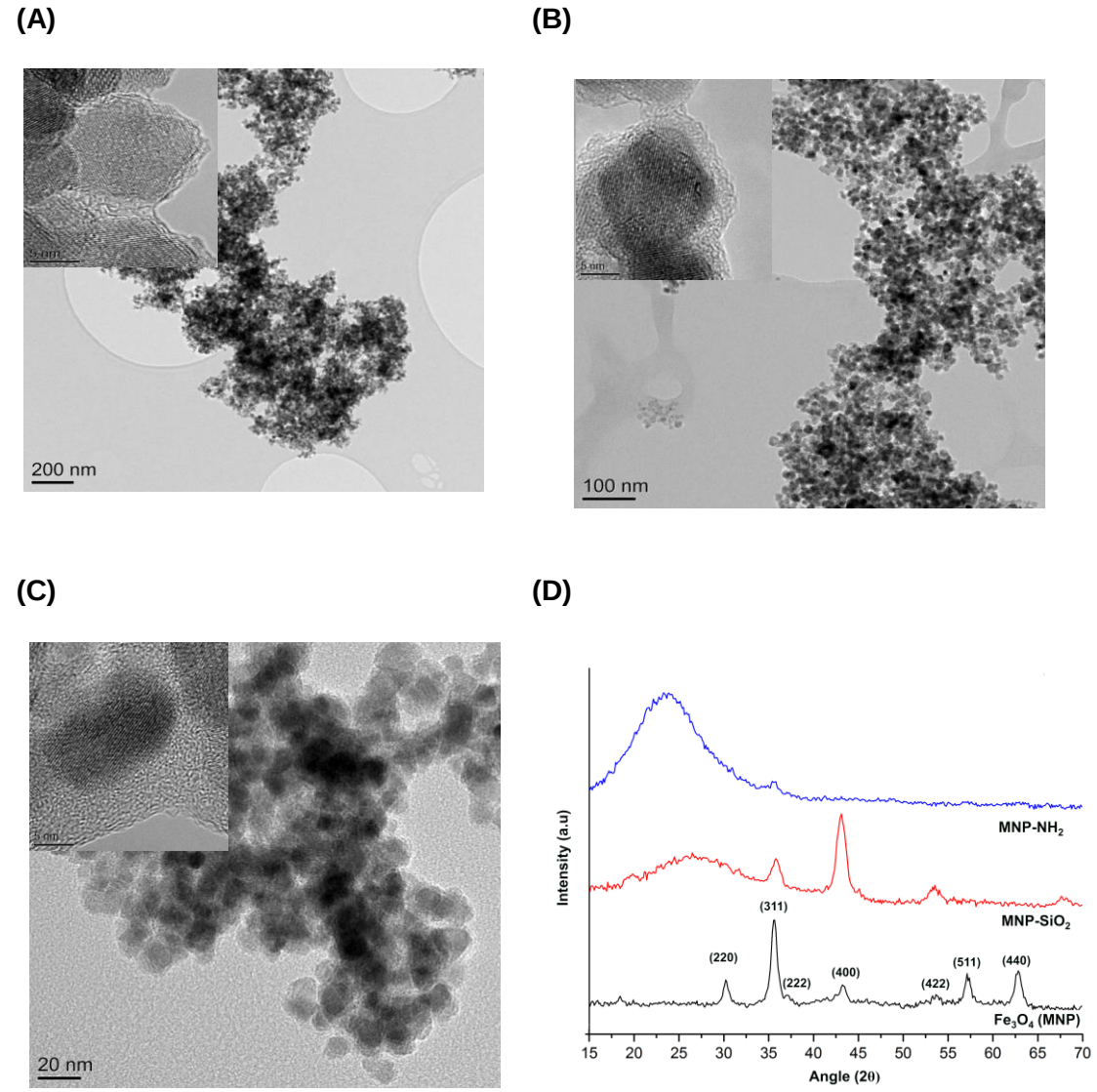

Figure 2-18. TEM images of (A) uncoated F_3O_4 nanoparticles, (B) Fe_3O_4-SiO_2 core-shell nanoparticles sample Cx, and (C) F_3O_4-SiO_2 core-shell nanoparticles sample Ez. The Figure insets show the magnified images of Fe_3O_4 and the silica coatings for B and C, and (D) X-ray diffractograms of MNPs prepared using co-precipitation method.

The structural information of the MNPs is collected by powder X-ray diffraction. **Figure 2-18 (D)** shows the XRD patterns of the coated and uncoated MNPs. All the major peaks were indexed to the standard pattern for Fe_3O_4 (JCPDS No. 19-0629). The Fe_3O_4

showed peaks at Bragg angles 2θ ~30.2°, 35.5°, 43.0°, 53.1°, 57.0°, 62.5° and 74.2° corresponding to Miller indices (220), (311), (400), (422), (511), and (440) respectively, suggesting that Fe_3O_4 MNPs were in inverse spinel structure [JCPDS card no. 19-0629].

The XRD pattern for MNP-SiO_2 showed weakening Fe_3O_4 peaks together with the occurrence of a broad peak 23° associated with amorphous silica [134]. This implied that a thin coating on the Fe_3O_4 MNPs was achieved. The peaks associated with Fe_3O_4 were not observed after the further treatment with APTES. For robust biomedical applications, every MNP, regardless of size, must be coated with a homogeneous silica shell - which the co-precipitation route appeared to be lacking even after several optimization steps. In view of this, thermal decomposition was seen as a more viable route to prepare more uniform MNPs for biosensing applications.

2.4.5 Synthesis of Fe_3O_4 nanoparticles using thermal decomposition method

Thermal decomposition route is known to yield nanoparticles with narrow size distribution, high crystallinity, and excellent shape control [118, 119, 132, 133]. In this study, an organic precursor ferric acetylacetonate [$Fe(acac)_3$] was decomposed at high temperature inside a high boiling point non-polar solvent phenyl ether (bpt. 290°C) in the presence of capping agent (oleic acid) and a reducing agent (1,2-hexadecanediol). This approach can achieve high monodispersity of the final nanoparticles because the nucleation and growth steps occur at different temperatures. The precursor was heated up to 200 °C to decompose the precursor and was kept at that temperature for 2 hrs to initiate the nucleation process. It was reported that increase the temperature directly to reflux could result in poor particle monodispersity [153]. The temperature was then increased to 300 °C for the growth process. The final nanoparticles were coated with oleic acid to impart hydrophobicity and solubility in non-polar solvents like hexane. Zhang and colleagues showed that that the oleic acid molecules were chemisorbed on the MNP surface and formed a single layer structure [154].

Figure 2-19 (A) showed a TEM image of Fe_3O_4 MNPs prepared by thermal decomposition. The MNPs were mostly monodisperse, non-aggregated and had an

average diameter of 6.4 ± 0.72 with a narrow size distribution (polydispersity ~ 11%, **Figure 2-19 (B)**, in good agreement with literature. The as-synthesized nanoparticles were subjected to one round of seed mediated growth to increase particle size. The Fe_3O_4 nanoparticles after seeded growth appeared to be spherical with an average size of 12.6 ± 2.0 nm (**Figure 2-19 (C)**).

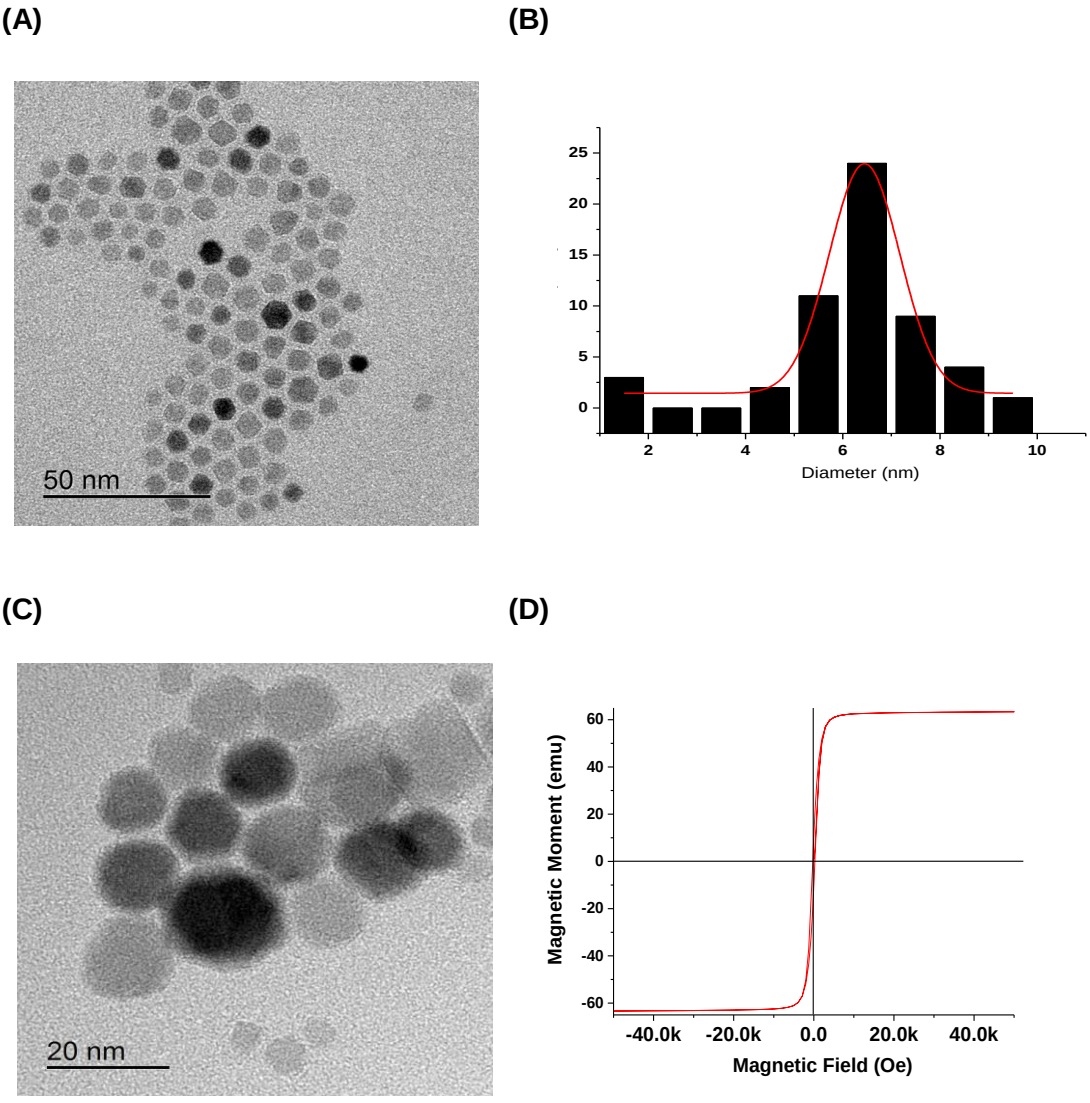

Figure 2-19. Representative TEM micrographs of (A) the Fe_3O_4 MNP seeds prepared by thermal decomposition (B) Corresponding particle size distribution histogram of MNPs, (C) Fe_3O_4 MNPs after one round of seed mediated growth, and (D) Magnetization of the Fe_3O_4 MNP in (C) as a function of magnetic field obtained by VSM.

The Fe_3O_4 MNPs obtained after 1 round of seed mediated growth were coated with silica and subsequently modified with APTES to impart amine functional groups. Silica coating

was carried out using reverse micro-emulsion method due to the ability of generating narrow size distribution and an ability to coat hydrophobic nanoparticles *via* ligand exchange mechanism. Reverse or water-in-oil micro-emulsion means that the water phase covered with a surfactant is dispersed in a non-polar media. In a sense, the "water droplets" act as constrained nanoreactors which are the key to attain narrow size distribution. The silica coating mechanism is illustrated in **Figure 2-20**.

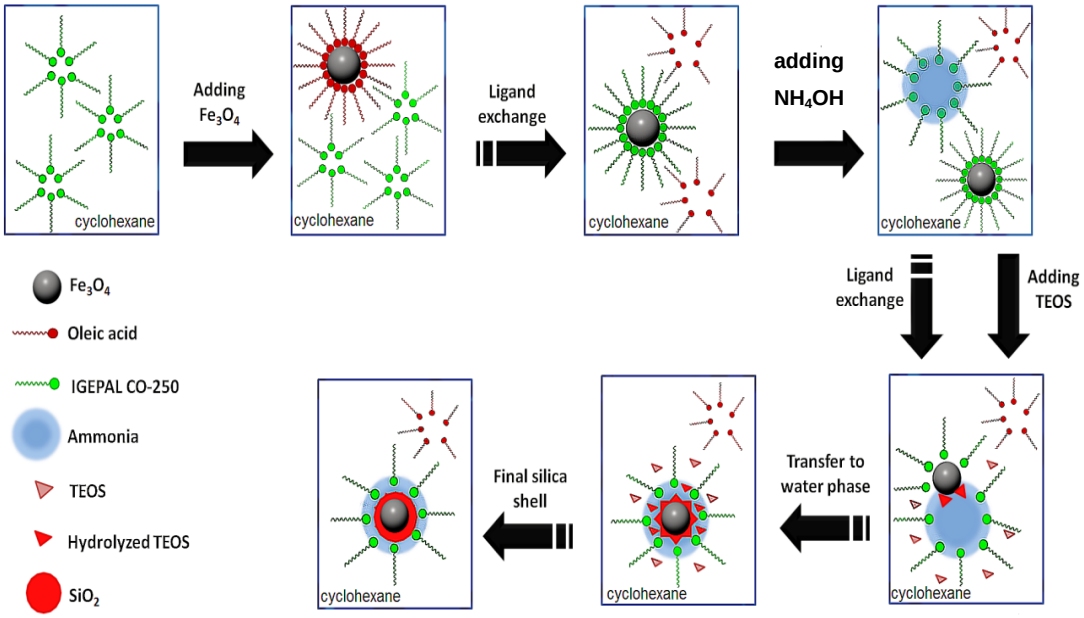

Figure 2-20. Schematic illustration of the mechanism of silica coating on Fe_3O_4 nanoparticles *via* the reverse emulsion method.

First, the IGEPAL CO-520 spontaneously forms micelles structures in cyclohexane because of its hydrophilic groups. As the Fe_3O_4 nanoparticles are added to the solution, a ligand exchange between oleic acid and IGEPAL CO-520 takes place. However, fractions of IGEPAL CO-520 molecules still adsorbs on the surface of the iron oxide nanoparticles with part of the IGEPAL CO-250 micelles still in the micelle form. Addition of ammonia fills and enlarges the size of IGEPAL CO-250 micelles and forms stable a reverse micro-emulsion system. Subsequently, the added TEOS hydrolyses at the oil/water interface and perform the ligand exchange with IGEPAL CO-520 adsorbed on the iron oxide surface and then transfer the nanoparticles to the water phase. Ultimately, the hydrolysed TEOS on the Fe_3O_4 surface undergoes a condensation process and forms a silica shell. The obtained MNP-SiO_2 core-shell nanoparticles display uniform dispersion and the thickness of SiO_2 shell can be tuned easily and precisely by changing the quantity of TEOS. Using this strategy I was able to obtain monodisperse and size-tuneable Fe_3O_4-SiO_2 core-shell nanoparticles with MNPs located at the centre. As shown in **Figure 2-21 (A)**, MNP-SiO_2 NPs were successfully synthesized through one-step TEOS addition (75 µL) using IGEPAL CO-520 as surfactant; more that 95 % of the SiO_2 beads contained only one MNP at the centre.

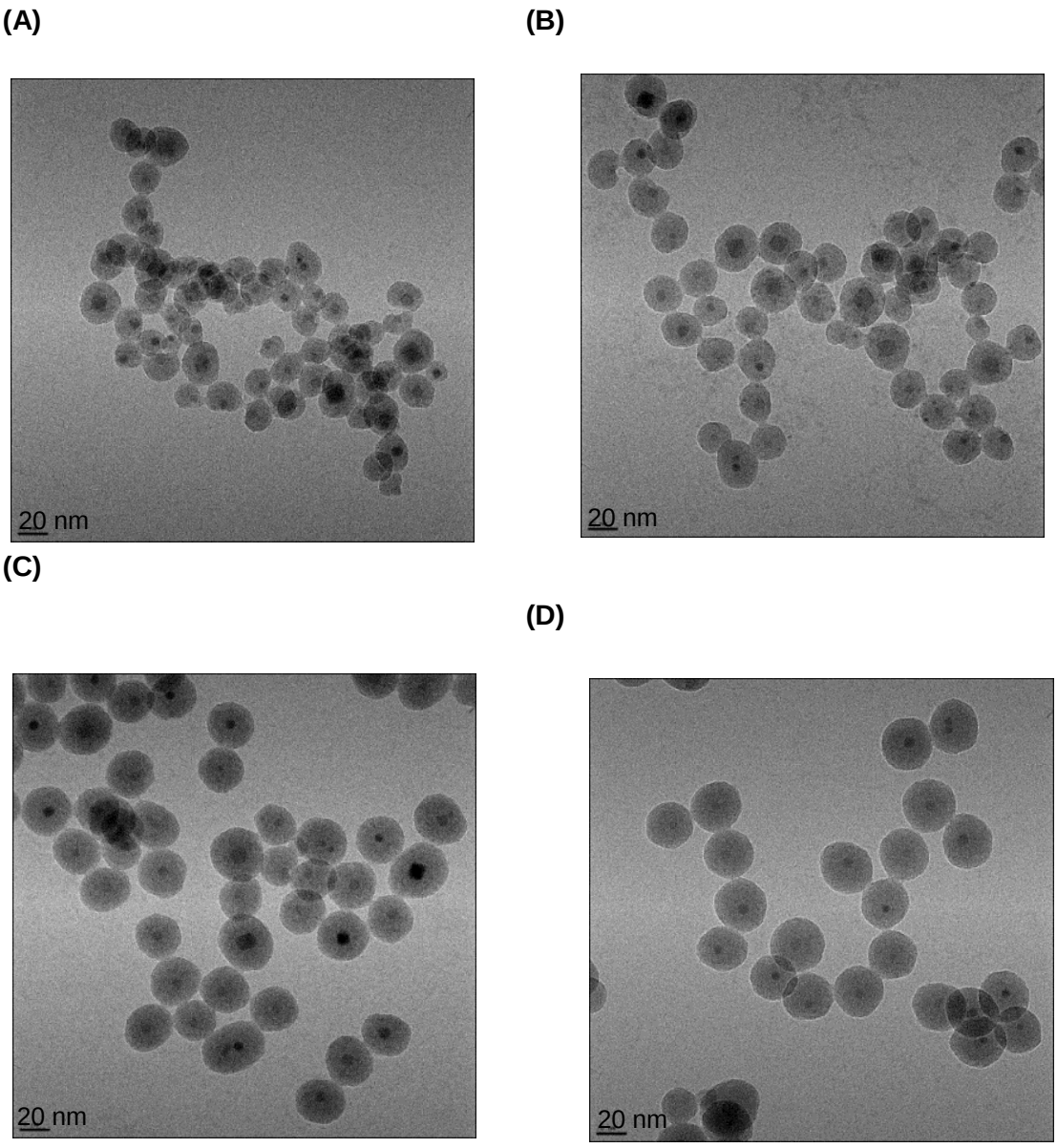

Figure 2-21. MNP-SiO_2 core-shell nanoparticles prepared using different amount of TEOS. (A) 75 µL, (B) 150 µL, (D) 300 µL, and (D) 450 µL TEOS. The scale bars are all 20 nm.

The particles were roughly spherical with some degrees of inhomogeneity and aggregation. Increasing the amount of TEOS (from 75 to 450 µL) allowed to obtain MNP with thicker SiO_2 shell (from 7 nm to 15 nm). **Figure 2-21 (A – D)** showed that the addition of more TEOS improved, in general, the particle morphology to more spherical with higher degree of particle homogeneity and less aggregation. A close examination of different TEM images showed the occurrence of single core, multi-core, and core-free silica NPs. **Table 2-7** showed the percentages of the different types of MNP-SiO_2 nanoparticles.

Table 2-7. Percentages of different types of MNP-SiO_2 nanoparticles

Weight MNP (mg)	Weight IGEPAL-CO 520 (g)	Volume TEOS (µL)	Volume NH_3 (µL)	Single core (%)	Multi-core (%)	Core-free (%)
1.3	0.50	75	100	96	1	3
1.3	0.50	150	100	92	6	2
1.3	0.50	300	100	89	4	8
1.3	0.50	450	100	84	5	10

The high (>84 %) occurrence of single-core MNP indicates that MNP acts as heterogeneous nucleation points for SiO_2 deposition, consistent with the mechanism elucidated by Meijerink and colleagues [155]. In general, a decrease of the single-core nanoparticles together with an increase of core-free silica was observed with the increasing TEOS amount. This observation highlights the role of TEOS in the stability of the microemulsion which is sensitive to the alcohol content generated in TEOS hydrolysis: a high concentration of TEOS will produce more ethanol, leading to increased MNP-SiO_2 polydispersity [156]. With all other experimental conditions held constant (*i.e.* weight of MNP, weight surfactant, volume NH_3), the increased concentration of TEOS may destabilise the micelle systems, leading to the formation of core-free SiO_2 NPs. Nevertheless, the MNP-SiO_2 particles prepared by micro-emulsion are more homogeneous than those prepared by co-precipitation and mostly single-cored. Although, a detailed analysis also reveals the existence multi-core nanoparticles albeit at relatively small proportions (< 6 %). The unequal core number and silica shell thickness can result in an irregular magnetic field causing uneven heating in hyperthermia and tissue distribution[108, 157]. However, for biosensing applications, multi-

cored nano-composites can be an advantage because it will allow easier and faster magnetic retrieval after target capture in solution.

To clarify the effect of the amount of MNP, different amounts of MNP (e.g. 1.4, 4.0 and 10 mg) were added to the reverse emulsion while the volume of TEOS was held constant. The corresponding TEM images were presented in **Figure 2-22 (A) – (C)**. The particles appeared as non-aggregated spherical core-shell nanoparticles when 1.4 mg of Fe_3O_4 MNPs was used (**Figure 2-22 (A))**. However, a gradual deviation from spherical core-shell nanoparticles was observed as the amount of Fe_3O_4 MNPs was increased to 4.0 mg (**Figure 2-22 (B)**). Increasing the weight of MNP to 10 mg destabilised the micelle system, resulting in serious particle aggregation (**Figure 2-22 (C)**). Thus, the preparation of multiple MNP cored particles cannot be achieved by simply increasing the MNP amount in the reverse micro-emulsion system.

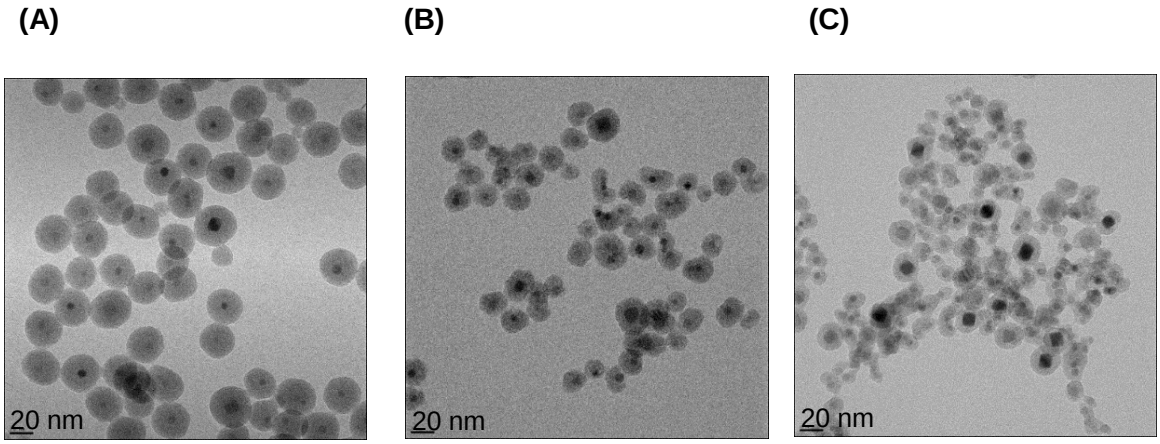

Figure 2-22. MNP-SiO_2 prepared using different amount of MNPs. The scale bars are all 20 nm.

The silica coated nanoparticles were treated with APTES to introduce amine groups for further conjugation as before. Initial attempts to modify the Fe_3O_4-SiO_2 with amine were done by addition of APTES on the same reaction flask containing the Fe_3O_4 and TEOS using the fractionated drop method. However, it was observed that the particles gradually settled down after the addition of APTES. With this observation, the amine modification was done using the same method used in the earlier part of the study. The silica coated Fe_3O_4 nanoparticles were washed three times by ethanol to remove excess

surfactant, dispersed in ethanol and was modified with APTES at 65 ^{o}C. Under these experimental conditions, the final amine-modified nanoparticles were stable in ethanol, but became flocculated when being transferred to water. The aggregation of the amine modified MNPs in water might be due to the formation of hydrogen bonds between amino groups of the MNPs [147]. Shown in **Figure 2-23**. is a TEM image of the amine modified Fe_3O_4 nanoparticle which clearly exhibits a distinct core-shell structure. The average size of the nanocomposite was determined to be 32 ± 4.2 nm (polydispersity = 13 %) and an average shell thickness of ~ 10 nm. The overall silica coating is composed of two shell layers, from hydrolysis and condensation of TEOS and APTES respectively, thus, giving a thick shell coating. Note that the ~10 nm shell thickness was not directly measured due to shell inhomogeneity, but was derived from the overall particle size increase compared with the seed mediated growth MNPs and MNPs coated with silica shell. Moreover, there was no crystallinity of the silica shell was observed.

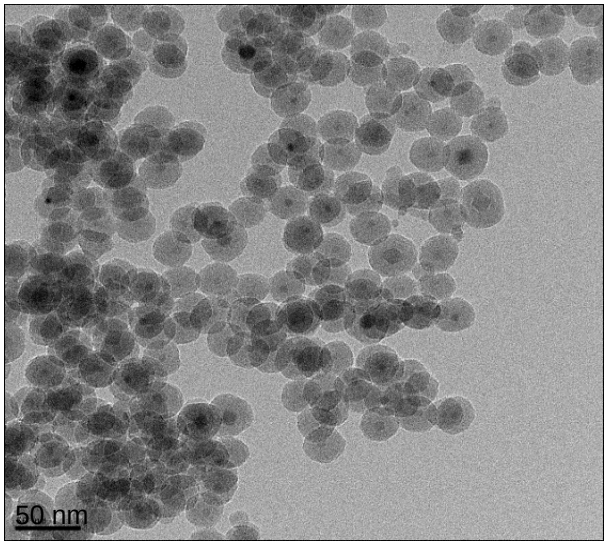

Figure 2-23. TEM images of amine-modified Fe_3O_4 core-shell nanoparticles synthesized at 65 ^{o}C using 350 µL of APTES.

2.4.6 Surface Functionalization of MNP-NH_2

The MNP-NH_2 were functionalized with by NHS-$PEG_{\sim 23}$-N_3 and NHS-$PEG_{\sim 17}$-OCH_3. The NHS ester moiety specifically reacted amino groups, thus, covalently linking the PEG linkers onto the surface of the MNP. The unreacted surface amines were further blocked

with NHS-PEG$_{\sim 17}$-OCH$_3$. The PEG group functioned to stabilize the MNP dispersion in aqueous solutions and provided a protective layer against non-specific adsorption of horse radish peroxidase in biosensing assays. The functionalization of the bifunctional PEG linker introduced surface azide groups for further conjugation to the DBCO modified DNA *via* click chemistry. The conjugation steps were monitored by zeta potential measurement as shown in **Figure 2-24** .

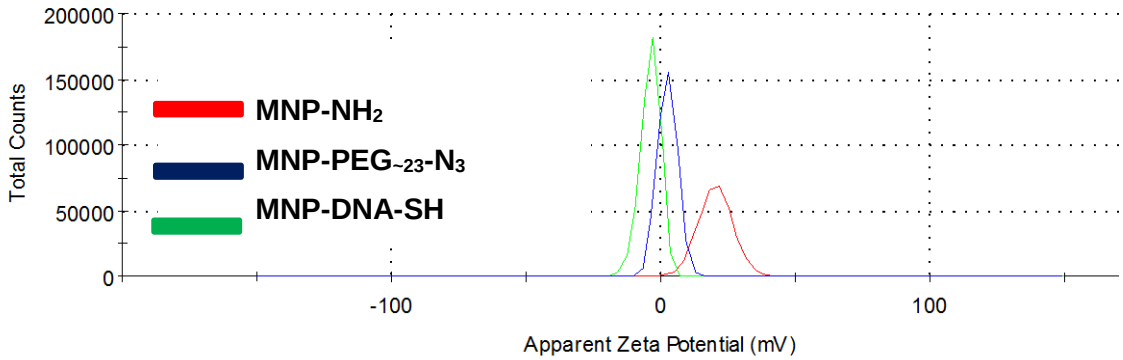

Figure 2-24. Zeta potential of the MNP-NH$_2$ and after functionalization of PEG linkers and capture DNA strands.

The MNP-NH$_2$ surface showed a positive zeta potential (+20.2 mV), implying that the silica coated MNPs were modified with amino groups. The introduction of the PEG linkers decreased the zeta potential to +2.63 mV, suggesting most amino groups have been converted to neutral PEGs. A negative zeta potential (-3.70 mV) was observed after conjugation of the DBCO-DNA-SH, due to the anionic nature of the DNA backbone. The changes in surface charge of the MNP after each surface functionalization step confirmed the attachment of the desired molecules.

2.4.7 Biosensing Principle

The general biosensing approach using MNP-DNA_{ds}-HRP probes is shown in **Figure 2-25.** HRP is conjugated to the MNP-capture DNA via biotin-neutravidin interaction (Design 1) or covalent linkage (Design 2). In both designs, the HRP enzyme that acts to amplify the signal produced. The capture DNA contains a sequence 5′-…G/AATTC…-3′ while the other (*i.e.* target DNA) contains a sequence 3′-…CTTAA/G…-5′. The capture DNA is complimentary to target DNA and forms a palindromic sequence that can be recognized by ECORI endonuclease. Incubation with ECORI cuts the specific double strand DNA sequence and releases the DNA-HRP fragments into the solution. The MNP can be conveniently retrieved by centrifugation and a magnet. The supernatant containing thousands of HRP molecules can catalyse the conversion of amplex red in the presence of H_2O_2 to a highly coloured product resorufin. The absorbance was determined spectrophotometrically at λ = 570 nm. The simple biosensing strategy is easy to carry out and does not require any rigorous washing steps, thus, shortening the assay time to ~ 4 hours.

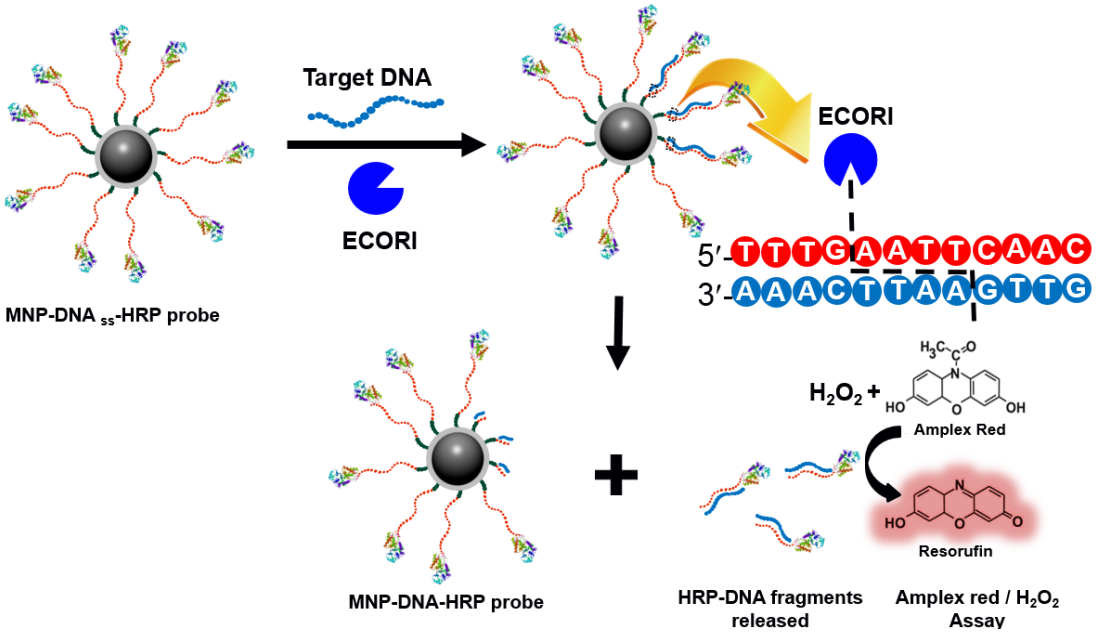

Figure 2-25. Schematic illustration for the MNP based colourimetric biosensor for detection of ECOR-I and DNA. The blocking of MNP with $PEG_{\sim 17}$-OCH_3 was omitted for simplicity. The MNP PEG and capture DNA strand are shown in green and red colours respectively.

2.4.8 ECOR-I Detection with MNP-DNA$_{ds}$-HRP Design-1

The MNP-DNA$_{ds}$-HRP Design-1 probes were incubated with different concentrations of ECOR-I from 10 to 0.01 U·mL^{-1} at 37 °C and 2 hrs. The production of resorufin was monitored by recording the time-dependent absorbance at 572 nm for 30 min (**Figure 2-26 (A)**). The samples were mixed using a pipette at several stages of the measurement because the formation of a non-homogeneous coloured solutions was observed. **Figure 2-26 (A)** showed an increase in the solution absorbance with time, suggesting that DNA-HRPs were released into the solution after ECOR-I incubation. Based from the slope shown in **Figure 2-26 (B)**, 10 U·mL^{-1} ECOR-I gave the highest signal, and the signal decreased with the decreasing ECOR-I concentration as expected. This observation suggested that ECOR-I was able to cut and release DNA-HRP from the MNPs as designed.

(A) **(B)**

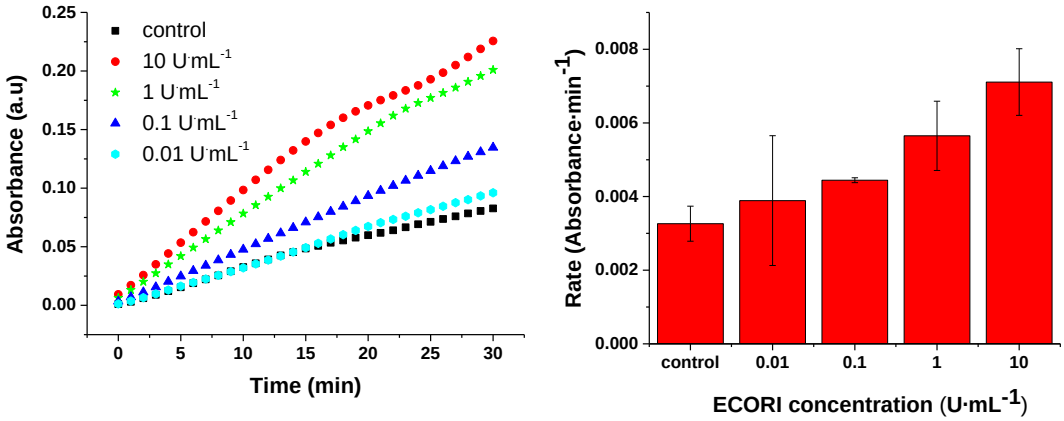

Figure 2-26. ECOR-I detection using MNP-DNA$_{ds}$-HRP Design-1 after incubation with ECOR-I at 37 °C for 2 hrs. (A) Time dependent absorbance of the samples at λ = 572 nm. (B) The corresponding slopes from the linear fit plots in (A).

Although a general trend of increasing absorbance of the samples with the increasing ECOR-I concentration was observed, the rate of resorufin production was slow. This could be due to the difficulty of the ECOR-I accessing the nicking site of the DNA. The control experiment (without target, WOT) also showed high background absorbance, possibly due to non-specifically adsorbed NAV-HRP detaching from the MNP probe surface or the dissociation of the biotin– NAV-HRP complex. Several experimental parameters were changed to improve the current design of the MNP probes and obtain

greater signal. Specifically, the capture DNA was re-designed to introduce a longer oligo thymine spacer at the 5' end and a covalent linkage between the HRP and the MNP-DNA probe, resulting in Design-2. We hypothesised that the use of a longer spacer would improve the accessibility of the ECOR-I to recognise and cleave the specific DNA sequence. A covalent linking of the enzyme should be able to lower the background signal by avoiding the biotin-NAV dissociation. The incubation temperature and time with ECOR-I were also optimised to get a more reliable biosensor.

2.4.9 ECOR-I and DNA detection with MNP-DNA$_{ds}$-HRP Design-2

2.4.9.1 Optimization of incubation temperature and time

The effect of incubation temperature and time of MNP-DNA$_{ds}$-HRP Design-2 probes with ECOR-I were investigated to determine the optimum condition for ECOR-I to cut the DNA strand and release DNA-HRP to the solution. Firstly, the MNP-DNA$_{ds}$-HRP Design-2 were incubated with ECOR-I from 4 to 40 ^{o}C for 1 hr. A high ECOR-I concentration of 10 U·mL^{-1} was used to ensure efficient cut all the DNA linkage and release DNA-HRP into the solution to generate a high signal. The amplex red-H_2O_2 amplification was carried out in 1 hr and stopped with addition of 100 μL of 1 M NaN_3. This method provided a better alternative to the real time monitoring of the solution absorbance because the colour was homogenously dispersed. **Figure 2-27 (A)** showed the average absorbance of assay solutions incubated at different temperatures.

A higher absorbance was observed at 37 °C than that obtained with Design-1 at the same ECOR-I concentration (10 U·mL^{-1}). Moreover, a lower background signal was also observed. Thus, the use of longer spacer length and the covalent linkage of the HRP to the DNA successfully improved the assay signal and also reduced the background. The sample incubated at 4 ^{o}C gave a low signal that was almost comparable to the control experiment. This observation implies that ECOR-I activity is almost negligible at this temperature. Increasing incubation temperature resulted to an increase in the signal and the highest signal was observed at 30 ^{o}C together with a low background. Further increasing temperature resulted in a decrease in signal, suggesting a reduced ECOR-I activity. Thus 10 U·mL^{-1} ECOR-I can effectively cut the specific DNA sequence and release a large amounts DNA-HRP fragments in solution. Moreover, the use of a high activity HRP is important because it can catalyse the fast conversion of amplex red to resorufin. Hence, all succeeding experiments were conducted at 30 ^{o}C.

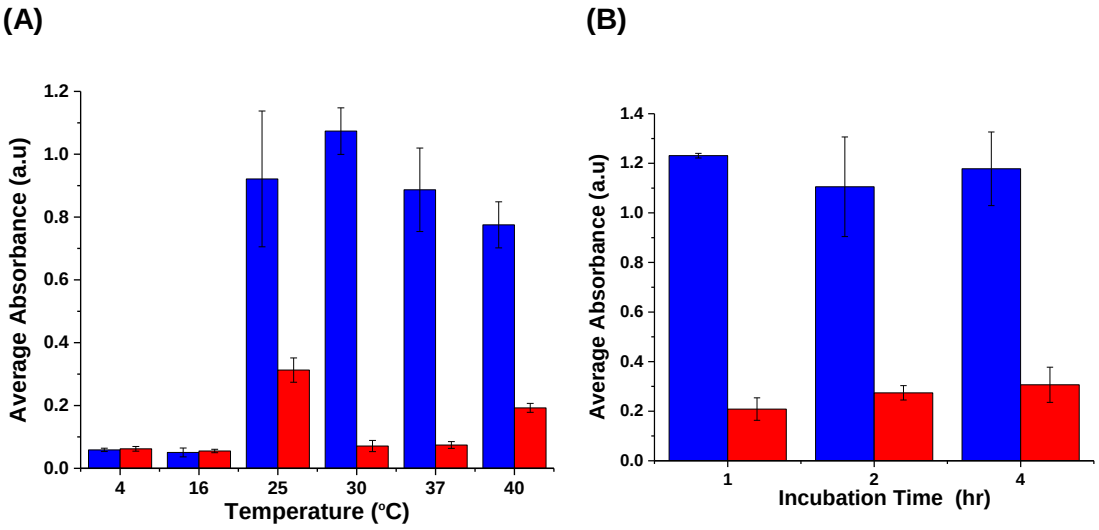

Figure 2-27. (A) Effect of incubation temperature (indicated underneath each bar) using Design 2 probes incubated with 10 U·mL^{-1} ECOR-I, (B) Effect of incubation time on assay performance using MNP-DNA$_{ds}$-HRP Design 2 and 10 U·mL^{-1} ECOR-I at 30 °C. The blue ■ and red ■ bar indicates the experiment containing the target DNA and control experiment (*i.e.* without the target DNA) respectively.

The effect of ECOR-I incubation time was also investigated. The MNP-DNA$_{ds}$-HRP Design-2 probes were incubated with 10 U·mL^{-1} ECOR-I at 30 °C for 1, 2 and 4 hours. It was expected that the longer the incubation, the more cutting and release of DNA-HRP fragments to the solution, leading to a higher signal generation. **Figure 2-27(B)** showed that the signal showed no significant difference for 1, 2 and 4 hr incubation, suggesting that 1 hr was enough for ECOR-I to cut most of the specific DNA sequence. Furthermore, the control sample (WOT) also showed a slight increase of the background signal with the prolonged incubation .

2.4.9.2 ECOR-I and DNA detection

Initial ECOR-I detection experiments were carried out by incubating the MNP-DNA_{ds}-HRP Design-2 probes at 30 ^{o}C for 1 hr with different concentration of the ECOR-I (10–$1x10^{-5}$ U·mL^{-1}). The enzymatic amplification with amplex red and H_2O_2 was carried out for 1 hr and were terminated with the addition of NaN_3. The absorbance of the solutions were recorded as shown in the **Figure 2-28** inset. Each sample were done in triplicates and the average absorbance was calculated and plotted in **Figure 2-28.** The incubated with 10 U·mL^{-1} showed the highest absorbance signal while those incubated with 1 U·mL^{-1} and lower concentrations ECOR-I showed very low signal and almost comparable to the controls.

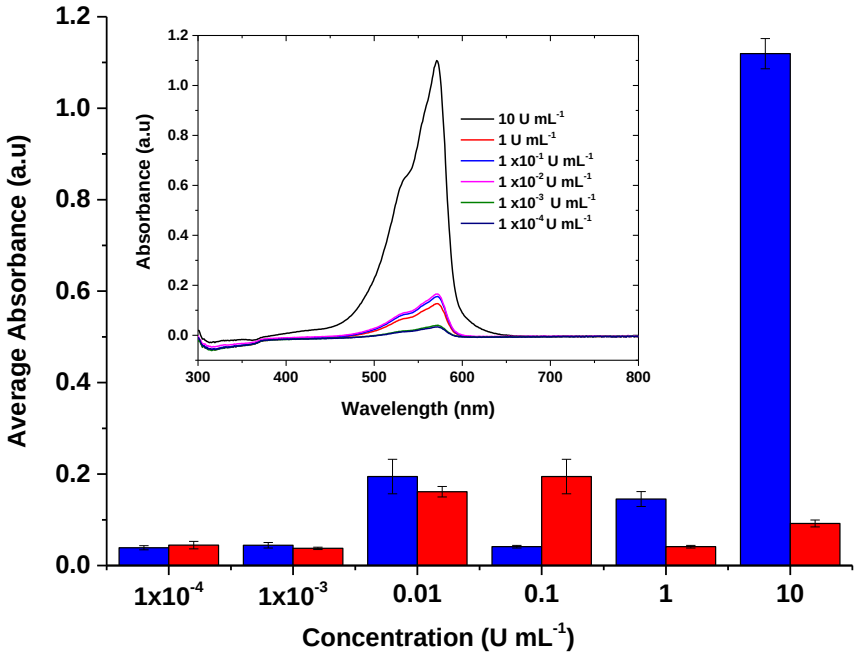

Figure 2-28. ECORI detection using MNP-DNAds-HRP Design-2. The MNP probe samples were incubated with different concentrations of ECORI for 1 hr at 30 °C. The term WOT refers to the control experiment without target DNA. Inset: absorbance wavelength scan of the test solutions. The blue ■ and red ■ bar indicates the experiment containing the target DNA and control experiment (*i.e.* without the target DNA) respectively.

The incubation time was prolonged to 2 hrs to allow low concentration ECOR-I to cut more dsDNA strands and release more HRPs hence to provide better signal to background ratio. Under this condition, the lower concentrations of ECORI can cleave

and release more of the DNA-HRP fragments in the solution. Prolonging the ECORI incubation will release enough DNA-HRP fragments and give appreciable difference in the absorbance of the solutions. The absorbance of the solutions were recorded after 1 hour reaction with amplex red and H_2O_2 and shown in **Figure 2-29**. A control experiment was carried out alongside with the MNP probes incubated with the target DNA. This was done to see whether the absorbance of solutions from MNP Design-2 probes incubated with the target DNA significantly differ than those MNP Design-2 probes without the target DNA.

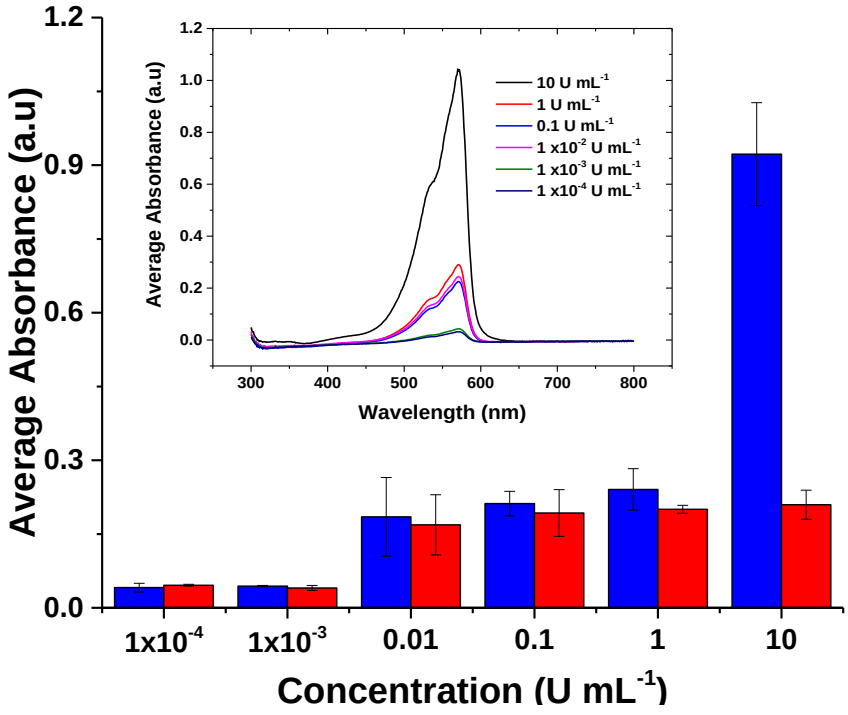

Figure 2-29. ECORI detection using MNP-DNA_{ds}-HRP Design-2. The MNP probe samples were incubated with different concentrations of ECORI for 2 hrs at 30 °C. The term WOT refers to the control experiment without target DNA. Inset: absorbance wavelength scan of the test solutions. The blue ■ and red ■ bar indicates the experiment containing the target DNA and control experiment (*i.e.* without the target DNA) respectively.

The signal was again the highest at 10 U·mL^{-1} ECOR-I as expected. However, those incubated with ECOR-I concentrations at ≤ 1 U·mL^{-1} still gave low signal and comparable with the negative controls, implying that most of MNP-dsDNA-enzyme probes were still

intact. Given the assay signal was slightly higher than the control at 10 $U \cdot mL^{-1}$, the MNP-DNA_{ds}-HRP Design-2 probe can detect ECOR-I down to ~1 $U \cdot mL^{-1}$.

The feasibility of the MNP-dsDNA-HRP Design-2 probe to detect target DNA was also investigated. The MNP probes were incubated with different concentrations of the target DNA with a fixed ECOR-I concentration of 10 $U \cdot mL^{-1}$.**Figure 2-30** showed the results after 1 hr of enzymatic amplification with amplex red and H_2O_2.

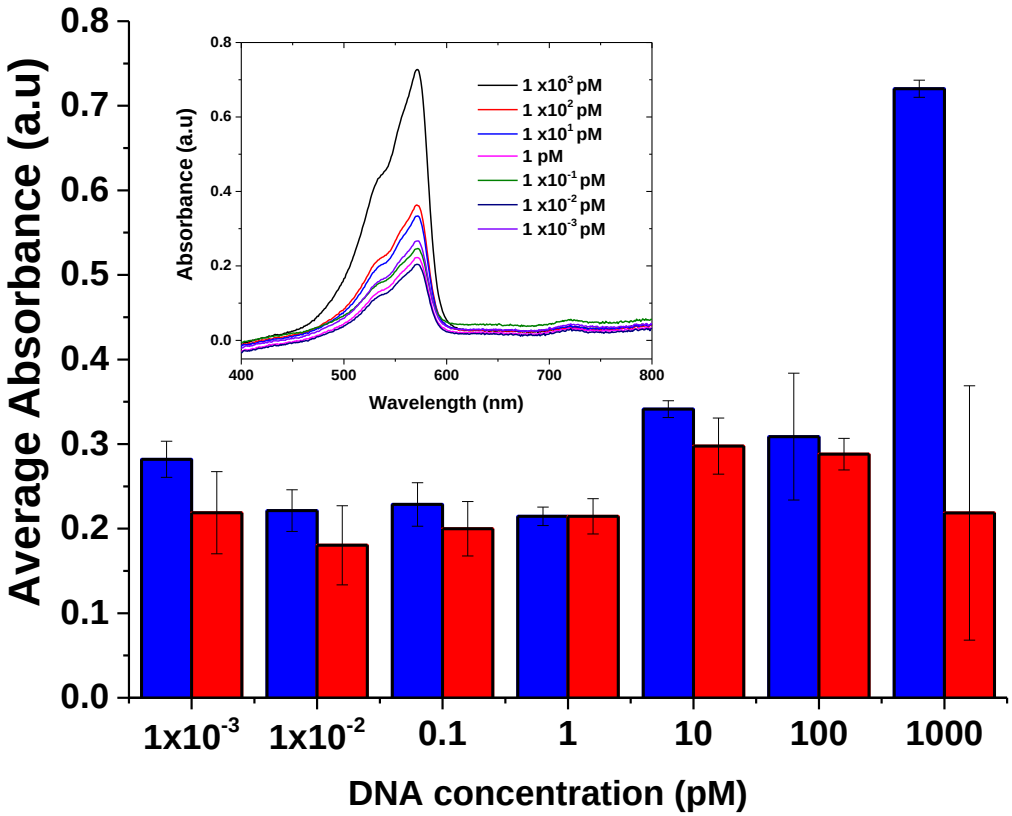

Figure 2-30 DNA detection using 10 $U \cdot mL^{-1}$ ECOR-I with 1 hr incubation at 30 °C. The term WOT refers to the experiment without target DNA. Inset: absorbance wavelength scan of the test solutions. The blue ■ and red ■ bar indicates the experiment containing the target DNA and control experiment (*i.e.* without the target DNA) respectively.

The assay with 1000 pM target DNA showed the highest signal with an appreciable difference form its control experiment. The MNP probes incubated with lower concentrations of the target DNA gave almost the same signal as the controls without

target DNA. Under this protocol, the MNP-DNA_{ds}-HRP Design-2 can positively detect 1000 pM of target DNA.

In summary, we have developed a MNP-SiO_2 core-shell nanoparticles for detection of ECOR-I and DNA. However, the current results for the biosensing is uncompetitive against several reported ECOR-I biosensors with similar detection strategy and DNA biosensors based on nicking endonuclease. These observations highlight an important aspect for the improvement of the biosensor, which is to control the surface chemistry of the MNP. Specifically, it is important to reduce non-specific adsorption of NAV-HRP in order to decrease the background signal. In this direction, a new MNP platform based on the polymer encapsulated MNP was carried out. Similarly, the PEG units will be used to graft to the polymer forming a thick brush like structure. This is expected to dramatically reduce background signal and contribute to a more sensitive biosensor. The details of the preparation of polymer encapsulated MNP and its application towards DNA biosensing is presented in Chapter 3.

2.5 Conclusion

Two different methods have been successfully employed to make Fe_3O_4 MNPs, 1) co-precipitation, and 2) thermal decomposition. Fe_3O_4 MNPs synthesised by co-precipitation generally yielded stable and water-dispersible MNPs. XRD analysis confirmed the identity of the MNPs being Fe_3O_4. However, TEM analysis revealed that the as-synthesized MNPs were ~18 nm in size but with poor size and shape uniformity. As a result, the thermal decomposition of Iron (III) acetylacetonate was used to synthesise aggregation-free MNPs with narrow size distribution and uniform spherical morphology. However, this synthesis process was more complicated and having lower yield than the former, and moreover the oleic acid capping ligands on the MNPs also rendered them hydrophobic and water in dispersible. Nonetheless, these negative features were easily outweighed by the formation of high quality MNPs, crucial for biomedical applications. The average particle size of the MNPs synthesised by thermal decomposition was 6.4 ± 0.72 nm and increased to 12.6 ± 2.0 nm after 1 cycle of seed mediated growth. Silica coating has been successfully applied to both types of MNPs, allowing for effective protection of the MNPs from oxidation, aggregation at physiological pH and also transfer the hydrophobic MNPs (prepared *via* thermal decomposition) to

the aqueous media. A sol-gel method was employed to coat the MNPs prepared by co-precipitation with a silica shell using base catalysed hydrolysis of TEOS in an aqueous solution. The successful silica coating was confirmed by XRD and TEM analysis. However, DLS measurements and TEM image analysis revealed significant agglomeration with poorly defined Fe_3O_4–SiO_2 core-shell nanostructures with co-precipitation prepared MNPs. For MNPs synthesised by thermal decomposition, the silica coating was achieved by a reverse micro-emulsion method. After several attempts, monodisperse core-shell hydrophilic nanoparticles were successfully synthesized as revealed by TEM imaging. The core-shell Fe_3O_4-SiO_2 nanoparticles were further functionalized with amine groups in a base catalysed hydrolysis and condensation of APTES on the silica surface at 65 ^oC. The overall silica shell thickness was estimated to be ~10 nm. The surface reactive amine groups were quantified using the ninhydrin assay.

The MNP were functionalised with PEGylated heterobifunctional linkers and passivation reagents (*i.e.* NHS-$PEG_{\sim 23}$-N_3 and NHS-$PEG_{\sim 17}$-OCH_3) to improve water stability and provide functional group for further conjugation with DBCO modified-DNAs. The results of each surface functionalization step were monitored by zeta potential measurement. The DNA modified MNPs were conjugated with HRP via biotin-Neutravidin interaction (with NAV-HRP) or covalent thiol-maleimide reaction to yield MNP-DNA_{ss}-HRP Design-1 and Design-2 probes respectively. The MNP probe Design-2 offered better signal to background ratio in ECOR-I detection than Design-1. A high ECOR-I activity was observed at 30 °C and incubation with the MNP probe Design-2 at 1 hr was enough to generate appreciable signal. The MNP-DNA_{ds}-HRP Design-2 can detect 10 $U{\cdot}mL^{-1}$ ECOR-I and 1 nM target DNA. Although this biosensing protocol is simple and easy to carry out, it can only offer limited sensitivity.

In general, the biosensor sensitivity can be improved by reducing the non-specific adsorption of the NAV-HRP on the MNP surface. This can be done by using a more effective surface passivation method such as coating the MNP with a PEGylated polymer. In addition, magnetic micro beads (typical size 0.5 – 500 µm) would be an ideal candidate to use for biosensing applications. Magnetic microbeads have inherent advantages over magnetic nanoparticles in biosensing protocol. The magnetic microbeads have the tendency to interact with each other in the presence of external magnetic field and this significantly reduces the timescale of separating the beads from

the rest of the solution. Moreover, magnetic microbeads have lower surface area to volume ratio as compared to their nanoparticle counterparts. This means that the surface have fewer adsorption sites for NAV-HRP, thus, leading to a reduction of background signals due to non-specific adsorption. These changes are expected to contribute to a better assay sensitivity and would lead to a more reliable biosensor.

Chapter 3

Ultrasensitive Detection of Cancer Related Single Nucleotide Polymorphisms by Combining Magnetic Nanoparticle Capture and Poly-enzyme Nanobead Amplification

3.1 Introduction

The development of sensitive DNA detection and quantification method has attracted significant research efforts due to importance in biomedical research [158-160] and clinical diagnosis [161-163]. In particular, ultrasensitive detection of single nucleotide polymorphisms (SNPs) in genetics has great potential to diagnose life-threatening illnesses (*i.e.* cancer, diabetes, vascular diseases, *etc.*), prediction of patient's response to treatments and risk of possible relapse, and therefore has been of great interest for both scientists and clinicians[164, 165]. However, disease related SNPs are often found in extremely low concentrations in an overwhelming background of wildtype gene, which can only be detected reliably after substantial amplification, making them challenging targets to detect reliably [166]. Among the many techniques that have been used for DNA amplification, polymerase chain reaction (PCR) remains the gold standard. However, PCR requires the use of multiple primers, DNA polymerases and high precision thermal cycling which can limit its use in resource poor countries. Moreover, PCR is also susceptible to contamination. Hence, considerable efforts have been focused to develop ultrasensitive DNA sensing methods that can provide rapid SNP detection without the need of target amplification. This is particularly important for the early non-invasive detection of tumours before they metastasize uncontrollably and become incurable. Over the past two decades, several methods capable of SNP detection and discrimination have been reported. These include high resolution DNA melting [167-169], single molecule fluorescence [170], molecular beacons [38, 171], hybridization chain reactions [85, 172], surface enhanced Raman scattering [173-176], and electrochemical detection [43, 177]. Despite well-designed strategies, most of these methods displayed either relatively low SNP discrimination ratio and/or insufficient sensitivity, limiting their potential in

real-world applications. While methods based on nicking endonucleases [47] or restriction enzymes [178] can offer high levels of SNP discrimination, these methods however, are not general and limited to targets containing the specific enzyme recognition site only. On the other hand, ligase-based approaches are general and can work with any target of interest and offer high SNP discrimination [75, 78]. Moreover, it can be coupled to various signal amplification strategies, *e.g.* rolling circle amplification [76, 179, 180], polymerase mediated target displacement, [181-183] as well as different nanomaterials to further improve the SNP detection sensitivity. In particular, coupling enzymes to magnetic nanoparticles (MNPs) are highly attractive because they form stable, homogenous dispersions in the absence of an external magnetic field, allowing for rapid target capture and high enzymatic activity [41]; yet they are readily retrieved from the media by applying an external magnetic field, allowing for efficient and rapid removal of contaminants and reducing background. Indeed, by combining target recycled ligation, MNP capture and enzymatic signal amplification, the Zhou group has previously developed a simple MNP-enzyme sandwich assay and demonstrated the successful detection of specific target-DNAs down to the sub-pM level with high SNP discrimination [52, 56], although their absolute sensitivities are still uncompetitive against some of the most recent ultrasensitive DNA detection methods [92, 184-186] . Building upon the previous MNP-enzyme sandwich assay developed in the Zhou group [52], herein we have further introduced a direct MNP-signal-DNA ligation strategy to increase the target-DNA to enzyme conversion efficiency. Moreover, we have developed a new poly-enzyme nanobead signal amplification strategy which can covert each captured target-DNA into thousands of copies of active enzymes for greatly enhanced signal amplification power, allowing us to realise ultrasensitivity and excellent SNP discrimination simultaneously. Using the KRAS somatic mutations (codons 12/13) which are widely found in human cancers, (*e.g.* colorectal, pancreas, ductal, and lung) as model examples [56], we show this new sensing strategy allows for rapid, ultrasensitive detection of cancer specific SNPs down to the low aM level.

3.2 Experimental

3.2.1 Reagents

Dry powders of manganese iron oxide magnetic nanoparticles ($MnFe_2O_4$ MNPs, nominal diameter ~50 nm), poly(ethylene glycol) (M_n ~1000), poly-(maleicanhydride-*alt*-1-octadecene) (PMAO, M_n = 30k-50k), dicyclohexylcarbodiimide (DCC),

dimethylaminopyridine (DMAP), NaN_3, and bovine serum albumin (BSA) were purchased from Sigma Aldrich (UK). Amine modified polystyrene nanobead aqueous dispersion (~180 nm diameter, containing 2.54% solid by weight) was purchased from Bangs Laboratories, Inc. (USA). HABA Biotin Quantitation kit was purchased from Cambridge Bioscience (UK). Sterilized ultra-pure water ($\geq$18.2 MΩ) generated by ELGA Purelab flex purification system was used throughout the experiments and to make buffer solutions (PBS: 20 mM phosphate, 150 mM NaCl, pH 7.4; PBS-tween: PBS containing 0.1% of tween 20).

3.2.2 DNA Probes and Reagents

All DNA probes used in this study were purchased from IBA GmbH (Germany). Their abbreviations and sequences are shown in **Table 3-1**. High activity neutravidin-HRP conjugate (NAV-HRP) and amplex red were purchased from Thermo Scientific (UK) and Invitrogen Life Technologies (UK), respectively. *Taq* DNA ligase (40,000 U/mL) and 10× ligation buffer were purchased from New England Biolabs (UK). Methoxy-polyethylene glycol amine (NH_2-PEG_n-OCH_3, MW ~1000, n = ~23) was purchased from Alfa Aesar (UK).

Table 3-1. The name and sequences of DNA oligonucleotides.

DNA Name	DNA Sequence
Capture-DNA	PO_4^- - 5'- TGGCGTAGGCAAGAG TT_8 - 3' – DBCO *
Signal-DNA	Biotin-5'-T_5GTGGTAGTTGGAGCTG<u>G</u>- 3'
Wild type DNA: (T1)	5'-ACTCTTGCCTACGCCA**<u>C</u>**CAGCTCCACCTACCAC-3'
Cancer SNP1: (T2)	5'-ACTCTTGCCTACGCCA**<u>T</u>**CAGCTCCACCTACCAC-3'
Cancer SNP2: (T3)	5'-ACTCTTGCCTACGCCA**<u>A</u>**CAGCTCCACCTACCAC-3'

3.2.3 Polymer Modification and Characterization

Figure 3-1 shows the steps for the modification of PMAO with amino-PEG linkers to yield an amphiphilic polymer.

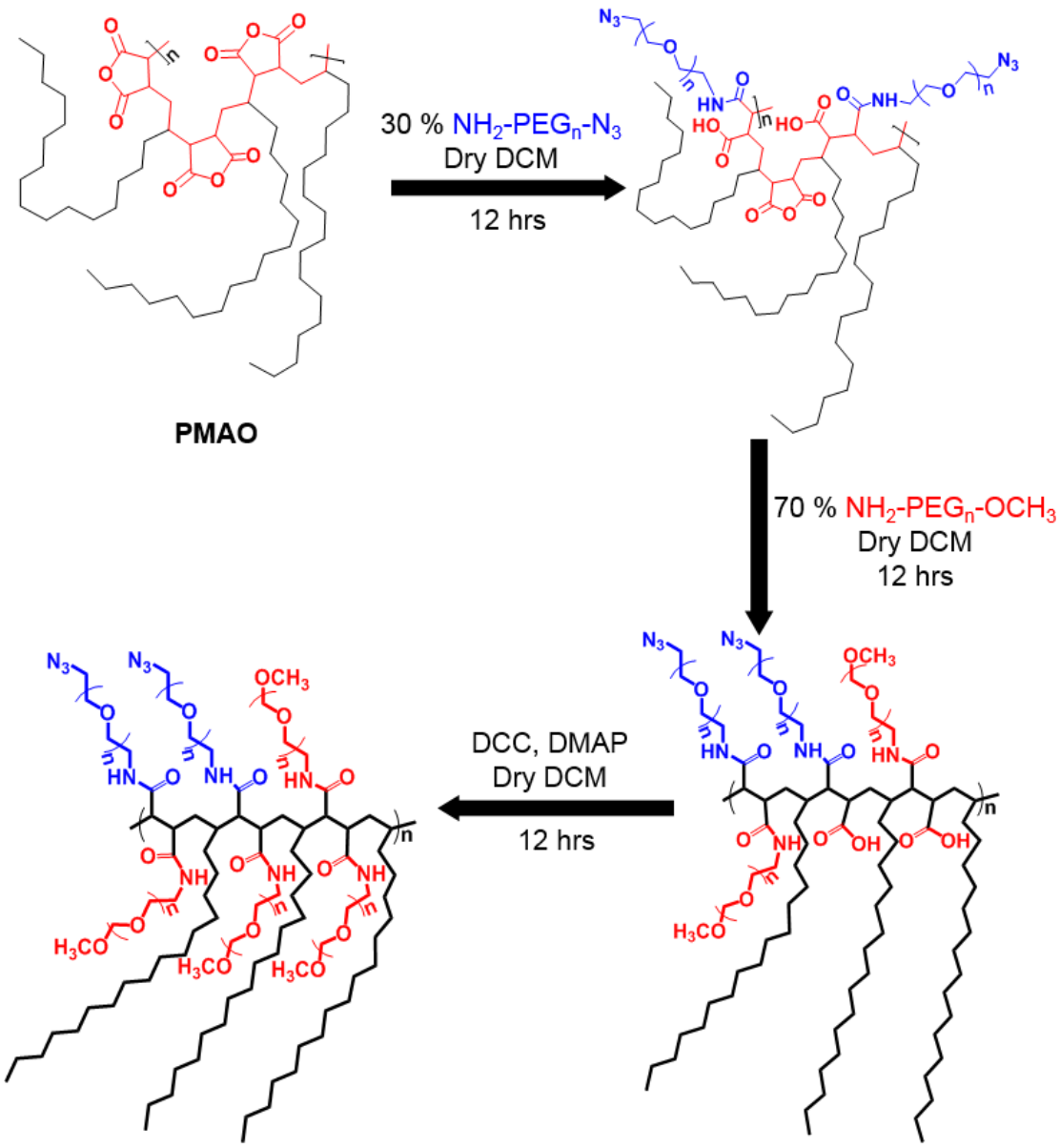

Figure 3-1. Synthetic route to PEG modified PMAO amphiphilic polymer. DCC: N,N'-dicyclohexylcarbodiimide, DMAP: 4 - dimethylaminopyridine

PMAO was modified with NH_2-PEG_n-N_3 (n = ~23) and NH_2-PEG_n-OCH_3 (n = ~23) in 30% and 70% grafting ratios (based on the PMAO monomer molar amount) respectively to form an amphiphilic PEG-PMAO polymer. This polymer grafting ratio was chosen primarily to control the amount of capture-DNA that will be further conjugated. The large amount of azide groups in the surface will lead to high capture-DNA loading and can eventually lead to high background signals as seen in our earlier studies. The long PEG chain (n= ~23) also confers the resulting grafted

polymer with good hydrophilicity and steric stabilisation. In the first step of the reaction, the lone pair of electrons from the amine group of NH_2-PEG_n-N_3 was utilized in the nucleophilic ring opening of succinic anhydride yielding the carboxylic acid-PEG-azide derivative. The remaining intact succinic anhydride rings were reacted with NH_2-PEG_n-OCH_3. The DCC/DMAP coupling step was used to convert the carboxylic acids formed during the anhydride ring opening to amide linked-PEGs to increase PEG grating density.

The number of moles of the amino-PEG reagents were twice that the PMAO monomer unit. First, PMAO (0.250 g, 0.66 mmol monomer unit) was reacted with NH_2-PEG_n-N_3 (0.396 g, 0.396 mmol) in dry $CHCl_3$ under a N_2 atmosphere for 12 h. The remaining unreacted anhydride groups were reacted with NH_2-PEG-OCH_3 (0.923 g, 0.923 mmol) for 24 h. The solvent was removed and the crude polymer was dried under vacuum. The reaction flask was then sealed, purged with N_2 and placed in an ice bath. Dry $CHCl_3$ (5 mL) was added to dissolve the polymer followed by DCC (0.164 g, 0.792 mmol) and DMAP (0.014g, 0.11 mmol) dissolved in dry $CHCl_3$ at 0 ºC. The reaction mixture was allowed to gradually warm up to RT and stirred for 72 h. The reaction mixture was filtered and concentrated under vacuum to give a yellowish oil (~1.5 g). It was dissolved in $CHCl_3$ to make a ~100 $mg{\cdot}mL^{-1}$ stock solution and was used directly to encapsulate hydrophobic $MnFe_2O_4$ MNPs without further purification, taking the full advantage of MNP's ease of magnetic retrieval for efficient removal of undesirable impurities. For NMR characterisation, a 5 mL of the crude polymer was transferred to a round bottom flask and the solvent was removed by rotary evaporation. The polymer was then dissolved in 10 mL of ultrapure water and was dialysed (MW cut-off 30,000 Da) versus water for 24 hours. The polymer solution was dried by rotary evaporation and further lyophilized for 48 hours, yielding a white solid. The purified polymer was characterized using ^{1}H-NMR spectroscopy as shown in **Figure 3-2**. The ^{1}H NMR (400 MHz, $CDCl_3$); δ ppm, 0.88 (t, 3 H, J = 6.7 Hz, -$(CH_2)_{15}C\underline{H}_3$, 1), 1.45-1.14, (18H, -$(C\underline{H}_2)_{14}$-$CH_2$-$CH_3$, 2,3), 1.50-1.70 (52H, -$C\underline{H}_2$-$C\underline{H}$-, *contains H_2O impurity), 3.41-3.33 (m, 2H, C(O)-$C\underline{H}$-$C\underline{H}$-, 6,7), 3.49-3.43 (-$C\underline{H}_2$-N_3,10), 3.72-3.55 (m, 57H -$(C\underline{H}_2$-O-$C\underline{H}_2)_n$ where n ~ 14 units), 3.80 (m, 2H, -NH-$C\underline{H}_2$). The presence of a broad singlet peak at ~1.60 ppm which corresponds to a water peak have obscured the correct integration of protons in the 1.50-1.70 ppm region.

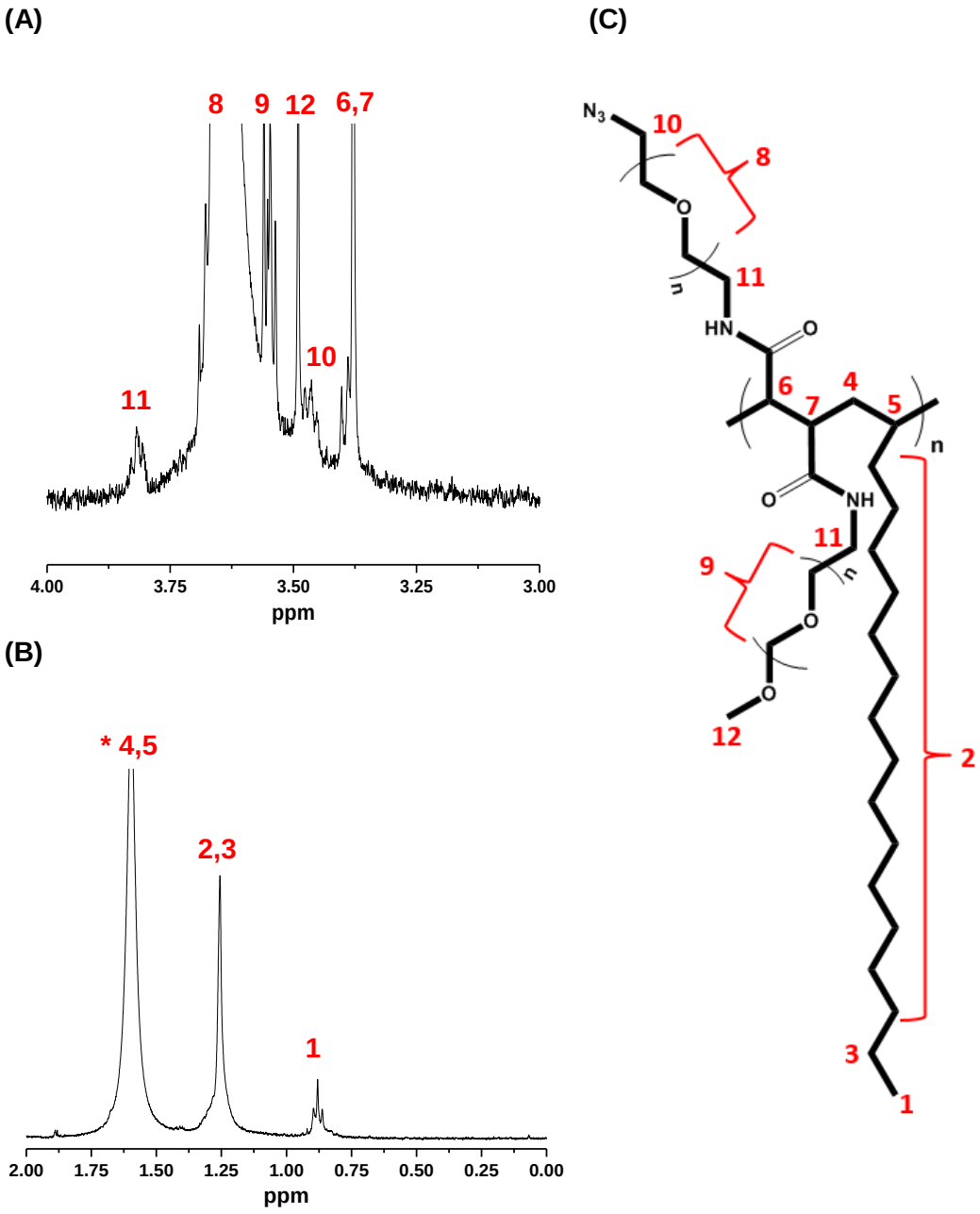

Figure 3-2. (A) Enlarged ^{1}H-NMR spectra from region 4.0-3.0 ppm (B) Enlarged ^{1}H-NMR spectra from region 2.0 – 0.0 ppm. The characteristic peaks of alkyl chains (C_{16}) in PMAO were observed at ~0.89 – 1.50 ppm, The peak of amide bond was weak due to low abundance as compared to the protons of the alkyl chain and the PMAO backbone, and (C) Proton assignment in the PEG-PMAO monomer unit.

3.2.4 MNP Encapsulation and Stability Evaluation

A 5.0 mg of dry $MnFe_2O_4$ MNPs were dispersed in 1.0 mL $CHCl_3$ through sonication, then different amount of the PEG-PMAO polymer was added (MNP:polymer weight ratio = 1:5, 1:10 and 1:15) and stirred overnight at RT. After that, ethanol was added to reach a 1:1 volume ratio with $CHCl_3$ and then $CHCl_3$ was slowly removed by rotary evaporation. The resulting MNP dispersion was transferred to a centrifugal filter (10000 MW cut-off) and water was added to a 1:1 v:v ratio and then centrifuged at 4000 rpm for 10 min. The MNPs were washed five times by centrifugation with water and finally dispersed in sterilized water to give a black solution. The solution was filtered through a 0.45 µm syringe filter to remove any large aggregated particles. The MNPs were further centrifuged (14000 rpm, 15 min) and washed with water 3 times to remove any unbound polymers and other contaminants, and finally dispersed in pure water. Combining several different batches, a final MNP stock solution of ~10 $mg \cdot mL^{-1}$ was obtained. The MNP colloidal stability and hydrodynamic sizes at different temperatures (25-75 ºC) and salt contents were determined by dynamic light scattering (DLS) [187].

3.2.5 MNP-capture-DNA Conjugation

The copper-free “click” reaction between the MNP surface azide and DBCO-modified capture-DNA was employed for the capture-DNA-MNP conjugation. **Figure 3-3** shows the mechanism for the copper- free click chemistry. This reaction does not use relies on the use of strained cyclooctynes that possess a decreased activation energy as compared to terminal alkynes, thus, do not require an exogenous catalyst such as copper (I) ions. The conjugation chemistry based on the strain promoted cycloaddition reaction between a dibenzocylcooctyne (DBCO) with an azide which readily occurs under normal conditions without the use of reagents such as copper or microwave heating. The resulting MNP-capture DNA conjugate are crosslinked via a stable triazole moiety highlighted in yellow in **Figure 3-3**. The PEG-PMAO encapsulated MNPs (10 mg) were mixed with the DBCO capture-DNA (100 µL, 100 µM) and incubated for 48 h at a constant 600 rpm vortex. After that, the MNPs were centrifuged and washed three times with pure water to remove any unbound capture-DNA. The clear supernatants were collected and used to determine the amount of unbound DNA. The capture-DNA loading was calculated from the difference between

the amount of DNA added and that remained in the clear supernatant as described previously [52].

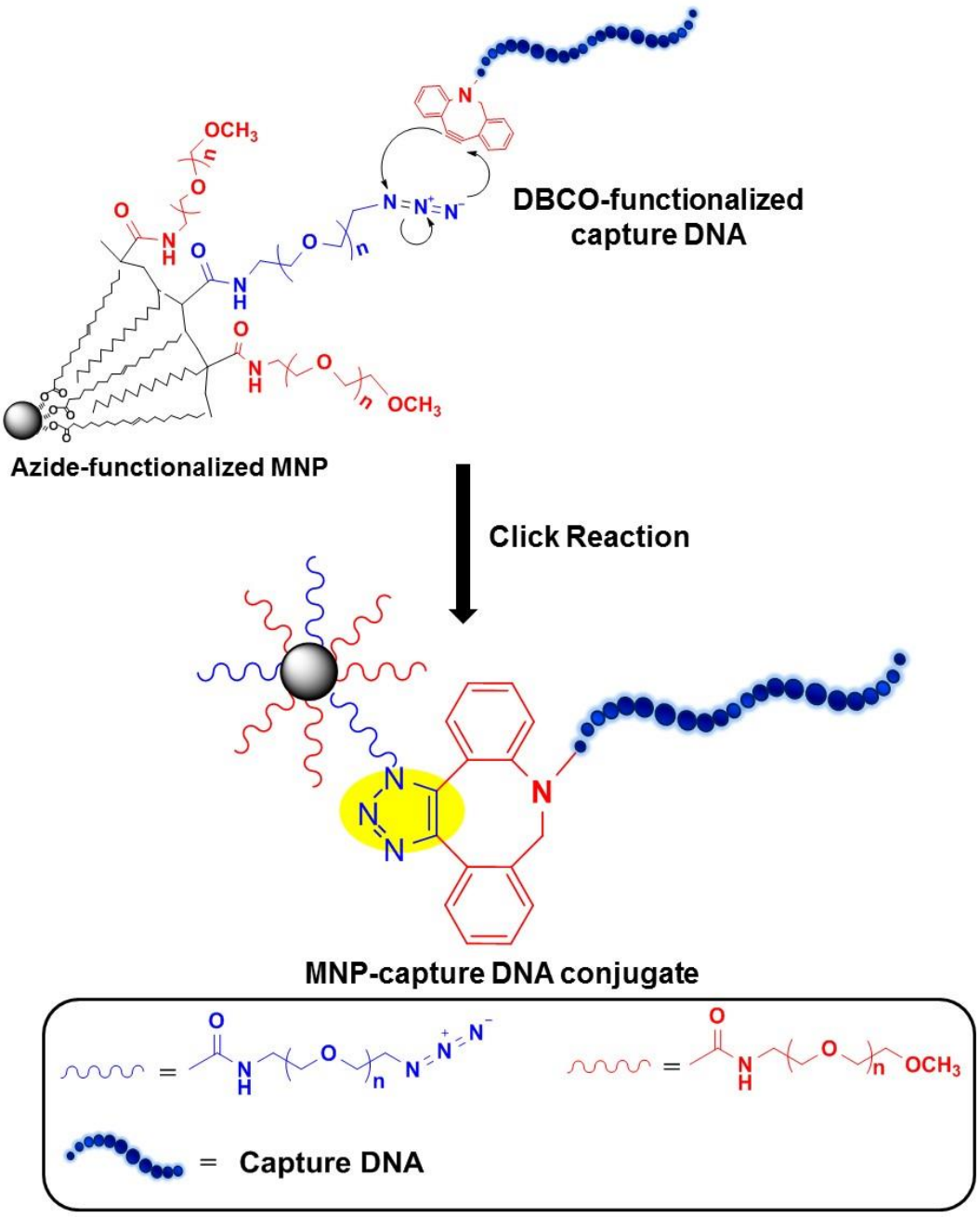

Figure 3-3 Mechanism for the copper free click chemistry between DBCO-capture DNA and the azide moiety of the polymer encapsulated MNP.

3.2.6 Target Ligation and Enzymatic Assay

All sample tubes were pre-treated with PBS containing 1.0 $mg \cdot mL^{-1}$ of BSA to minimise any possible non-specific adsorption. All ligation experiments were done with the MNP having a capture-DNA loading of ~0.35 $nmol.mg^{-1}$ (MNP). All ligation experiments were performed by dispersing 30 μg of the MNP-capture-DNA (10 μL) to a tube containing 15 μL ultrapure water, 5 μL ligase buffer (10×), 10 μL target-DNA (different concentration), 10 μL signal-DNA (500 pM), and 1 μL Taq DNA ligase (10 U/μL). The samples were incubated at 45 °C in a dry heating block for 60 min, after which they were cooled to RT naturally. The MNPs were centrifuged (3000 rpm) for 1 min and pulled to the tube wall *via* a permanent magnet. The clear supernatant was carefully removed, and the MNPs were washed twice with PBS-Tween. NAV-HRP (50 μL, 100 pM) was then added and incubated for 60 min, after which the samples were centrifuged to remove the clear supernatant. The MNPs were washed four times with PBS-Tween, once with PBS and finally dispersed in PBS (80 μL) and transferred to 96 microplate wells. Each well was added amplex red (300 μM, 10 μL) and H_2O_2 (300 μM, 10 μL) to initiate enzymatic assays which was monitored by fluorescence time traces on an Envision® plate reader using BODIPY TMR FP 531 excitation filter and Cy3 595 emission filter. Ligation assays for SNP discrimination were performed in the same way by changing the target-DNAs.

3.2.7 Preparation of polymer nanobead (PB)-EG_{12}-Biotin

Figure 3-4 shows the steps for the preparation of the polymer nanobead signal amplifier. The signal amplifier was prepared by tagging several thousand copies of Neutravidin-HRP on the surface of a polymer bead. This greatly improved the assay sensitivity by dramatically increasing the number of enzymes that could be converted from each ligated DNA sandwich. An aqueous suspension of amino-functionalized polymer nanobeads (100 μL, 2.54 % weight) was centrifuged for 1 min at 15,000 g and the clear supernatant was discarded. The beads were washed twice with sodium bicarbonate buffer (20 mM $NaHCO_3$, pH 8.3), and then dispersed in 1.0 mL of sodium bicarbonate buffer (pH 8.3). NHS-EG_{12}-Biotin (100 μL, 250 mM) was added to the nanobeads and the resulting suspension was incubated overnight at a rotor at 600 rpm at RT. The unreacted surface amino groups were further passivated by treatment with NHS-PEG_{17}-OMe (containing on average 17 PEG units, 100 μL, 100 mM) to minimize non-specific adsorption. The resulting biotinylated polymer nanoparticles

were centrifuged at 20,000 g and washed twice with PBS and finally dispersed in 5 mL of PBS.

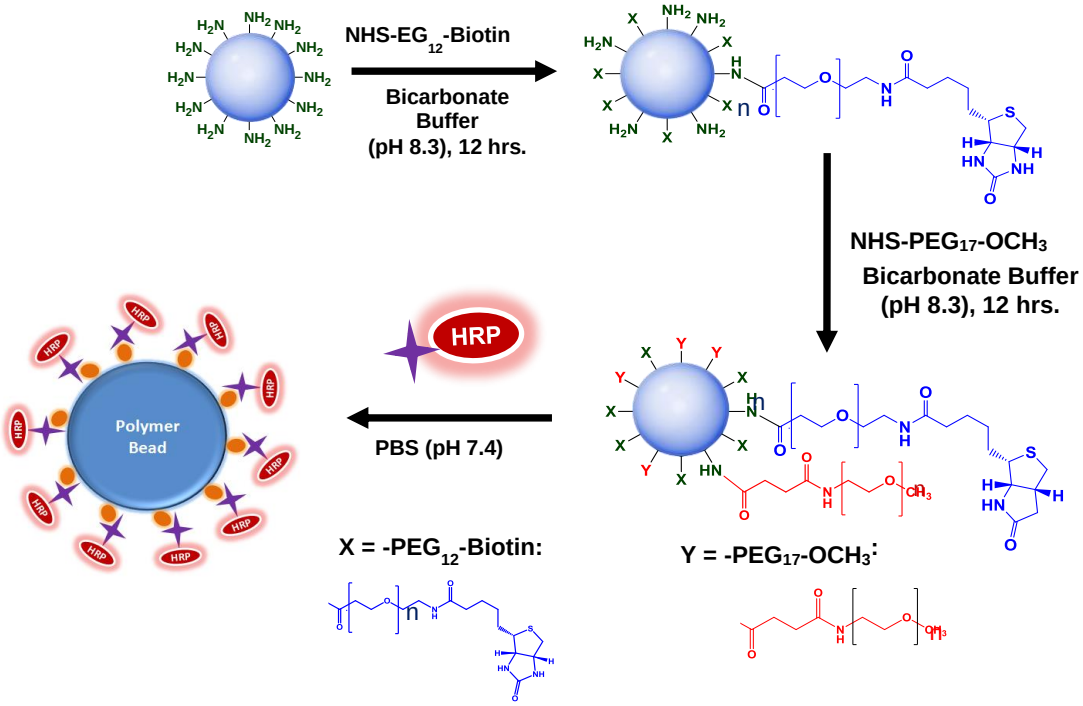

Figure 3-4. Schematic process used for the preparation of the poly-enzyme nanobead signal amplifier.

3.2.8 Determination of polymer nanobead biotin valency and tagging with NAV-HRP

The amount of biotin attached to the polymer beads was determined using HABA assay. An assay solution was prepared by adding avidin to HABA solution following the kit instruction and mixed for 5 min. 900 µL of the HABA/Avidin solution was added to a cuvette and its absorbance at 500 nm was measured. Then, a 100 µL biotin-modified polymer nanobeads was added and mixed by inversion. After centrifugation to remove the polymer beads, the absorbance of the supernatant at 500 nm was measured. The biotin valency was determined as ~10^4 per nanobead. An equimolar amount of NAV-HRP to the bead surface biotin was added to make the poly-enzyme nanobead signal amplifier with a stock concentration of 0.50 µM (based on the NA-HRP concentration, C_{HRP}).

3.2.9 Biosensing via poly-enzyme nanobead amplification

The MNP-capture-DNA and signal-DNA was ligated under the same procedures as above except with much lower target-DNA concentrations (e.g. 0.001, 0.02, 0.1, 1, 10, 100 and 1000 fM). After ligation, the samples were washed twice with PBS-Tween and then dispersed in 100 µL of the poly-enzyme nanobead signal amplifier in PBS (final C_{HRP} = 1.0 pM) and incubated for 60 min at RT. The samples were washed twice with PBS-tween and then transferred to a 96 well plate to initiate enzymatic assays as described above.

3.3 Results and Discussion

3.3.1 Biosensing Principle.

The sensing principle is illustrated schematically in **Figure 3-5**. It uses a pair of DNA probes, one covalently linked to a MNP for target capture (*i.e.* capture-DNA, 5' phosphorinated), and the other (*i.e.* signal-DNA) is biotinylated for NAV-HRP binding and signal amplification. The capture- and signal- DNA sequence are complimentary to each half of the target-DNA, allowing them to hybridize with a target-DNA to form nicked double-stranded DNA sandwich. The signal-DNA-Biotin was used to hybridize with half of the sequence of the target-DNA rather than an enzyme labelled signal-DNA (*i.e.* signal-DNA-HRP). The small biotin moiety in the signal-DNA would allow efficient hybridization with the target-DNA without complications that might arise if a bulky HRP group is at the terminal of the signal DNA. Moreover, a smaller biotin end group would allow the *Taq* ligase to reach the nick site during ligation step without being sterically restricted by HRP for a signal-DNA-HRP probe design.

A ligation step using *Taq* DNA ligase then covalently links the biotinylated signal-DNA to the capture-DNA (templated by a full-match, but not a SNP target-DNA), ensuring that it will not detach from the MNP surface in the subsequent washing steps, thereby increasing the target-DNA to enzyme conversion efficiency (the nicked double-stranded DNA sandwich may dissociate during the washing steps). It is important that a single-base mismatch in the target-DNA probe must be at the nick site to prevent ligation, thus, capture-DNA and target-DNA (*i.e.* SNP) remain unlinked. In

this manner, the biosensor can effectively discriminate a perfectly matched target and a SNP target DNA.

After washing to remove any unbound species, excess NAV-HRPs (Route a) are added to bind to the MNP surface biotin, converting each MNP-ligated signal-DNA into a MNP-linked HRP for enzymatic signal amplification by converting the non-fluorescent substrate, amplex red, into a strongly fluorescent product, resorufin [41]. The rate of fluorescence production is linear to the number of the HRPs bound to the MNP surface, which is directly correlated to the full-match target-DNA concentration. To further improve sensitivity, a more powerful signal amplification strategy using poly-enzyme nanobeads, each tagged with about ten thousand copies of NAV-HRP, is designed (Route b). It can convert each successfully ligated signal-DNA into thousands of copies of HRPs for greatly improved sensitivity, allowing us to detect ultralow levels of target-DNA directly without the need of PCR target amplification. Moreover, the strict requirement of perfect-match to produce successful ligation also enables our approach to effectively discriminate between wildtype and cancer specific SNPs: a single base mismatch at the nicking double-stranded site can prevent covalent ligation [56].

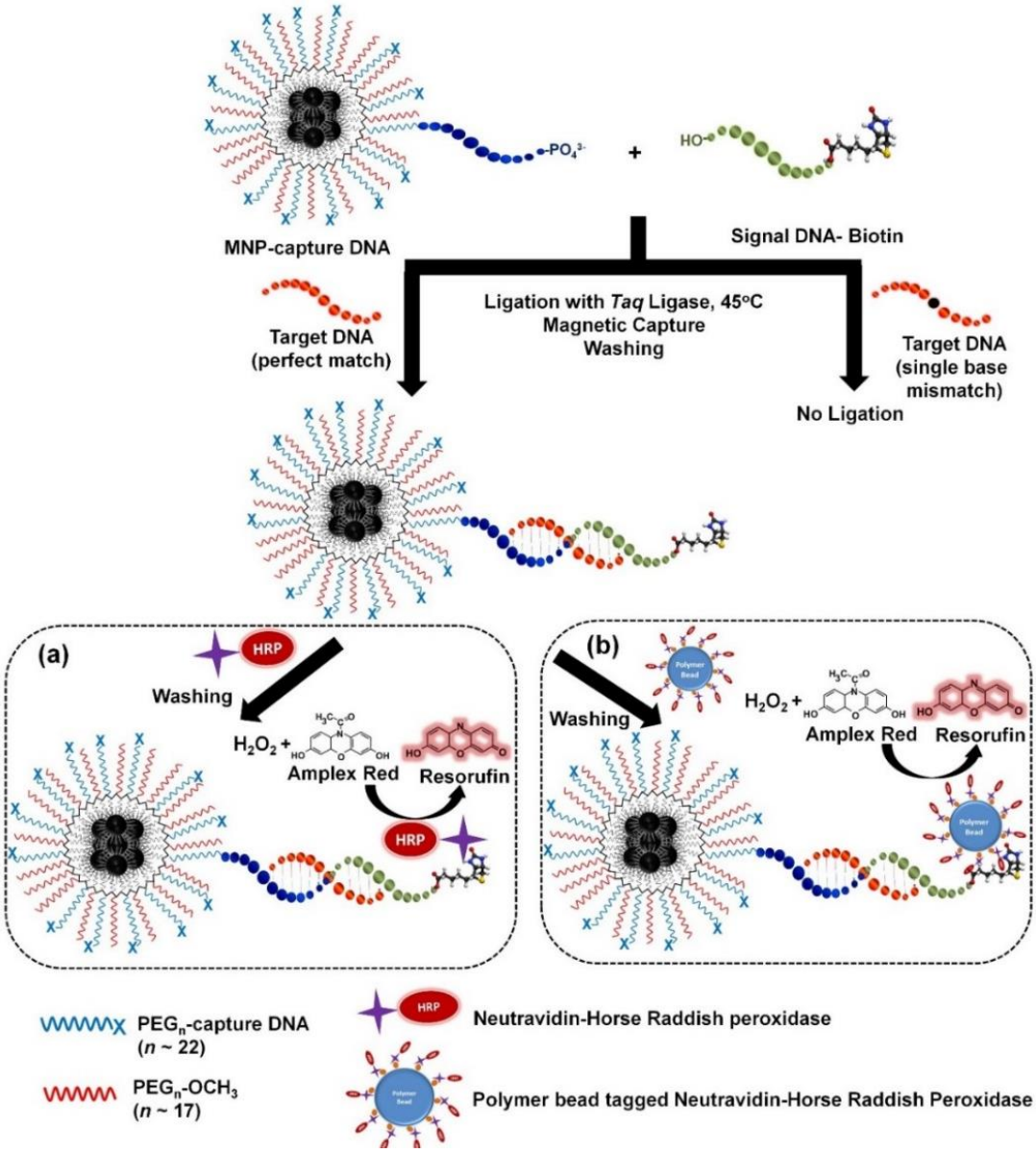

Figure 3-5. Schematic Illustration of our DNA sensing strategy. A MNP linked capture-DNA and a biotinylated signal-DNA are used to sandwich hybridize with the target-DNA followed by ligation. Only the perfect-match target-DNA, but not the SNP target, can template the covalent ligation of the MNP-capture-DNA and signal-DNA, producing a MNP-linked biotin for binding to NAV-HRP (Route a) or poly-NAV-HRP polymer nanobead (Route b) for HRP catalysed enzymatic assay.

3.3.2 MNP dispersion and stability

The dispersion of hydrophobic MNPs in water was achieved *via* PEG-PMAO-amphiphilic polymer encapsulation. PEG was used owing to its ability to resist the non-specific adsorption of biomolecules (*i.e.* proteins) and excellent biocompatibility.[188-190] Its flexible ether backbone utilizes hydrogen bonding and steric stabilization, and not electrostatic interactions, to achieve stable water dispersion. This confers PEG encapsulated or modified nanoparticles excellent colloidal stability in aqueous media over a wide range of pH and even with high salt contents. The maleic anhydride ring in PMAO was opened by reacting to an amino-PEG molecule (*i.e.* NH_2-PEG-N_3), forming a carboxylic acid and an amide linked-PEG-N_3. The generated free carboxylic acid group was further reacted with NH_2-PEG-OCH_3 *via* a DCC/DMAP mediated amide coupling to increase the PEG graft density, forming a dense, brush like PEG structure to offer excellent hydrophilicity and resistance against non-specific adsorption.

Figure 3-6 showed the FT-IR spectra of the unmodified PMAO and PMAO-PEG copolymers. The original PMAO gave a strong peak at 1775 cm^{-1}, assigning to the C=O stretching of the anhydride ring [191]. This peak was completely diminished after modification, indicating a complete reaction of the anhydride functional groups. The opening of the anhydride ring was also confirmed by the appearance of the amide C=O stretching peak at 1655 cm^{-1} and amide N-H bending peak at 1514 cm^{-1}. Moreover, the appearance of the azide stretching peak at 2100 cm^{-1} as well as the -C-O-C- absorption at 1060 cm^{-1} clearly demonstrated the successful grafting of the NH_2-PEG-N_3. The -C-H stretching peaks of the alkyl chains at 2882 and 2930 cm^{-1} remained unchanged. These alkyl chains can interact with the hydrophobic ligands on the MNP surface *via* van der Waals interactions, leaving the hydrophilic PEG moieties exposed to the aqueous media to confer particle water-dispersity.

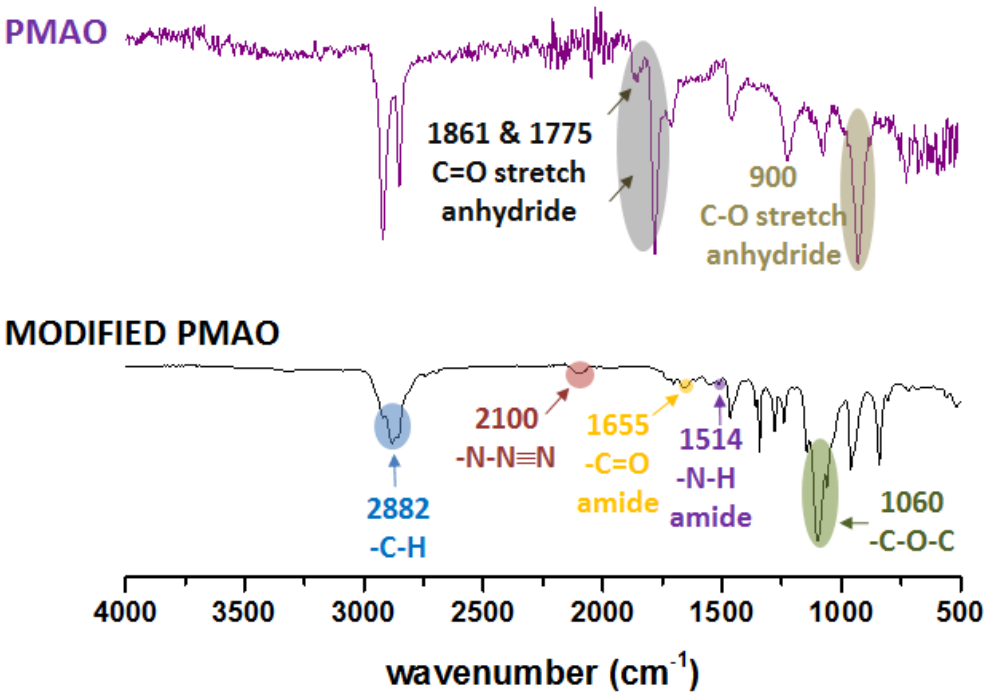

Figure 3-6. FT-IR spectra of the unmodified (top) and azide-PEG-modified (bottom) PMAO polymers.

The prepared PMAO-PEG copolymer was used directly to water-disperse hydrophobic $MnFe_2O_4$ MNPs using a modified solvent exchange method first reported by Bao and colleagues [192]. First, ethanol was added to a chloroform solution containing the MNP and PMAO-PEG polymer in 1:1 volume ratio. Then chloroform was selectively removed by rotary evaporation, and finally, ethanol was replaced by water using centrifugal filter tubes (10000 MW cut off). During this process, the solvent polarity was increased gradually from chloroform to water which has shown to improve the encapsulation efficiency. The amphiphilic PMAO-PEG encapsulates the hydrophobic MNPs *via* multiple hydrophobic-hydrophobic interactions between the polymer alkyl chains and the MNP surface hydrophobic ligands, leaving the hydrophilic PEG arms exposed to the aqueous environment to provide stable dispersion as shown in **Figure 3-7 (A)**.

(A)

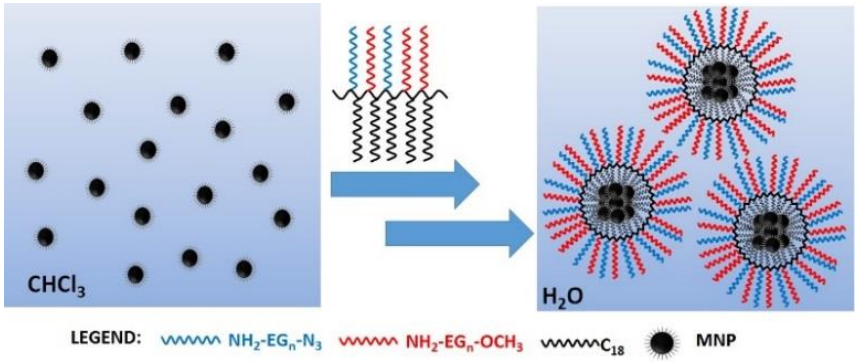

(B)

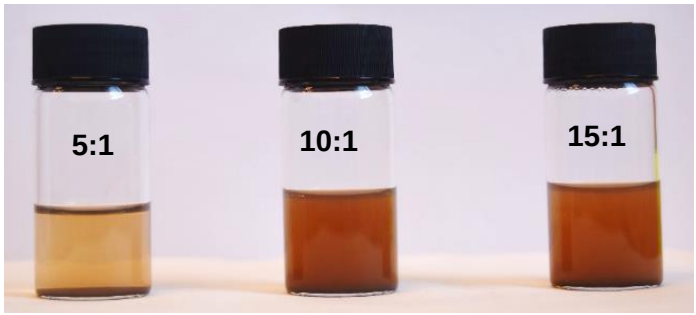

(C)

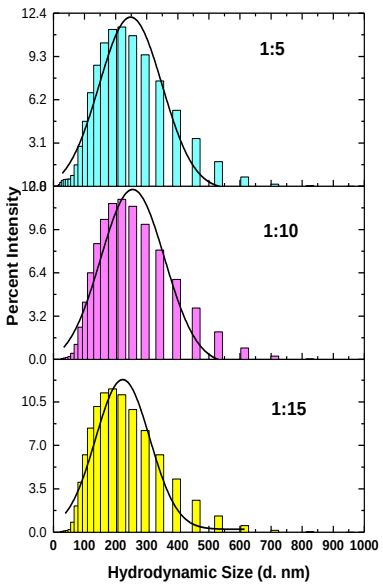

Figure 3-7. (A) Schematic diagram of polymer encapsulation and stabilization of MNPs in an aqueous solution. (B) Photographs of polymer encapsulated MNPs dispersed in water under different polymer:MNP weight ratios after standing for 24 h. The 5:1 sample is mostly precipitated but the 10:1 and 15:1 samples show good water-dispersability. (C) Hydrodynamic sizes of the MNP-polymer suspensions determined using dynamic light scattering method.

The amounts of the PMAO-PEG for MNP encapsulation was optimized by varying the polymer:MNP weight ratios from 5:1 to 15:1. MNP dispersed at 5:1 gave a much fainter colour as compared to those prepared at 10:1 or 15:1 as shown in **Figure 3-7 (B).** This indicates that 5:1 ratio was insufficient to promote high MNP water-dispersion. In contrast, those dispersed at 10:1 and 15:1 were similar in colour and both were much darker than that of 5:1, suggesting these ratios provided high MNP encapsulation efficiency. Furthermore, the percentage encapsulation efficiency for each polymer: MNP ratio was also determined. After removing the supernatant containing polymer encapsulated MNP, the precipitated MNPs were washed 3 times with water to remove excess polymer. The MNPs were dried in an oven for 3 days and their weights were determined. The weight difference between the initial MNP and that remained in the precipitate was considered as polymer encapsulated. Using this method, the polymer encapsulation efficiency was calculated as 39 , 56 and 53 % for the 5:1, 10:1, and 15:1 polymer: MNP ratio, respectively.

The polymer:MNP ratio of 5:1 gave the lowest encapsulation efficiency which was also visually confirmed by the faint brown colour of the supernatant. However, more than 50 percent of the MNPs were successfully encapsulated as the amount of the polymer was increased and an optimum coating efficiency was observed for a polymer:MNP ratio of 10:1. Further increase in the amount of polymer did not decrease in encapsulation efficiency. The primary goal here was to make stable MNP dispersions in high yields using the minimal amount of polymer possible, hence 10:1 was determined to be optimal. The <100% encapsulation efficiency was due to that the MNP powders were heavily aggregated prior to polymer encapsulation: they could not be fully dispersed in $CHCl_3$ even after extensive sonication. The hydrodynamic diameters (D_hs) of the polymer encapsulated MNPs were found to be ~230 nm by dynamic light scattering as shown in **Figure 3-7 (C)**. Such relatively large D_h sizes were likely due to MNP clustering as revealed by TEM imaging as shown in **Figure 3-8** and bilayer formation: the polymer alkyl chains interact with the hydrophobic ligands on the MNP surface *via* hydrophobic interactions [193].

(A)

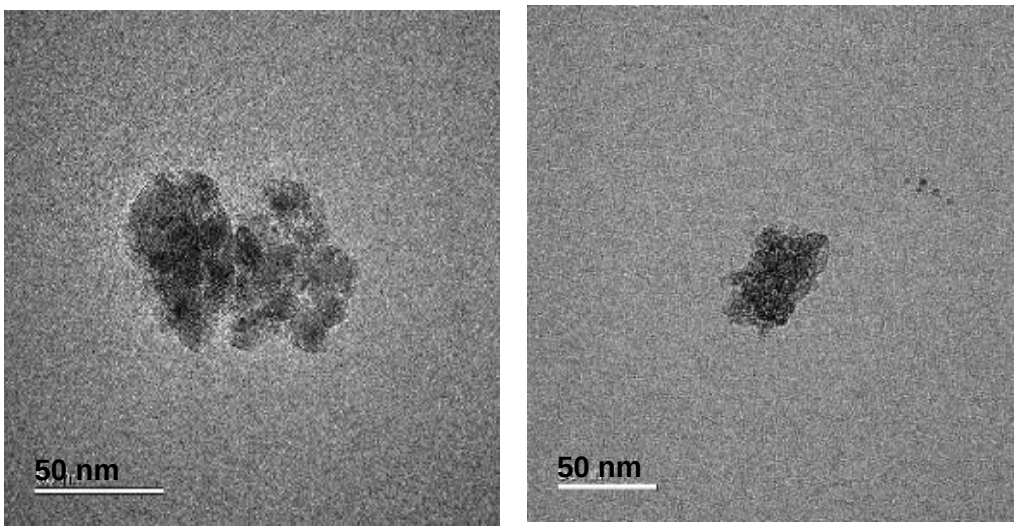

(B)

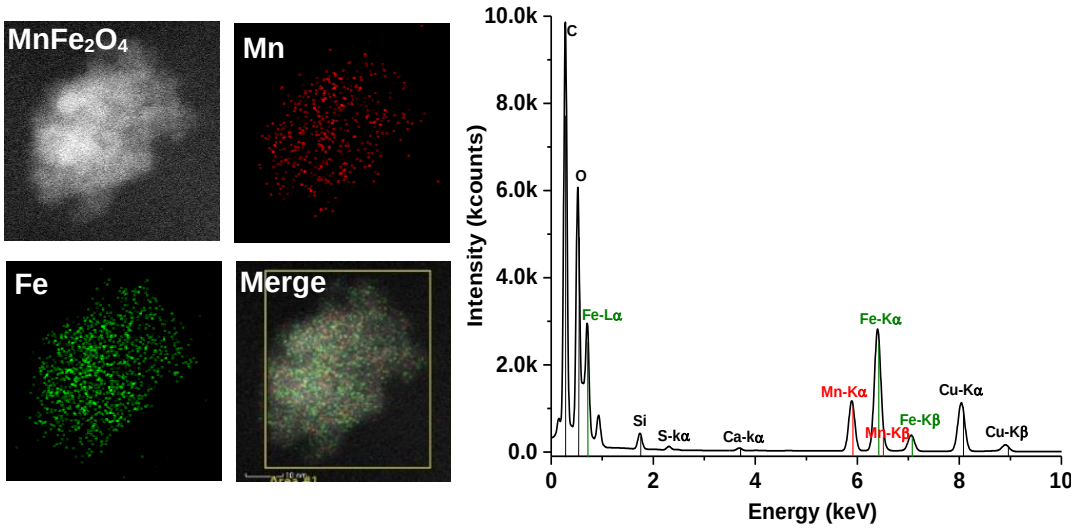

Figure 3-8. (A) TEM image of the polymer coated $MnFe_2O_4$ nanoparticles showing a clustered morphology of smaller MNPs with an overall magnetic core size of ~90 nm (scale bar 50 nm). (B) Elemental mapping of a MNP cluster (scale bar 50 nm) using high angle annular dark field (HAADF) for elemental analysis showing the presence of Mn (red dots) and Fe (green dots) atoms. The Energy Dispersive X-ray (EDX) spectrum of the same MNP cluster.

The colloidal stability of the MNPs under different pH, temperature, and salt content were further investigated. **Figure 3-9 (A)** showed that the MNPs did not display any significant D_h size variations over a wide pH range (*i.e.* 2-12). Since the ligation step will be carried out at 45 ^oC, the thermal stability of the MNPs was further tested. As shown in **Figure 3-9 (B)** no significant MNP size changes were found as temperature was increased from 25 to 70 ^oC, suggesting that the PMAO-PEG provided a stable coating on the MNP surface, presumably *via* multiple hydrophobic interactions between the polymer alkyl chains and MNP surface hydrophobic ligands [194].

Moreover, the polymer encapsulated MNPs were found to be stable under different salt contents (e.g. 100, 300 mM NaCl) with similar D_{hs} as those dispersed in pure water as shown in **Figure 3-9 (C)**. Together, these results suggested that the MNPs were not mainly stabilized by electrostatic repulsion, otherwise significant D_h increase would have been expected in high salt media which are efficiently in screening the electrostatic repulsion. The high MNP colloidal stability was attributed to effective steric stabilisation afforded by a thick amphiphilic polymer coating with extended PEG graphs which can prevent the MNPs from interaction with each other [195-197]. The stability of the polymer encapsulated MNPs was further confirmed by comparing the hydrodynamic size of the same batch of polymer encapsulated MNP after 6 months storage as shown in **Figure 3-9 (D)**. The D_{hS} of the freshly prepared MNP-polymer taken as 0 month is 204.9 nm and increased to 244.6 nm after 6 months of storage. The ~ 40 nm change in Dh suggests slight aggregation of polymer encapsulated MNP. However, visual inspection of the solution gave no signs of precipitation. The increase in size can be taken to have an insignificant effect for use of these polymer encapsulated MNP for biosensing applications. Overall, these results suggests that the attachment of the PMAO-PEG co-polymer to the MNP surface can be viewed as “irreversible” in an aqueous environment, making such MNPs capable of withstanding relatively harsh conditions.

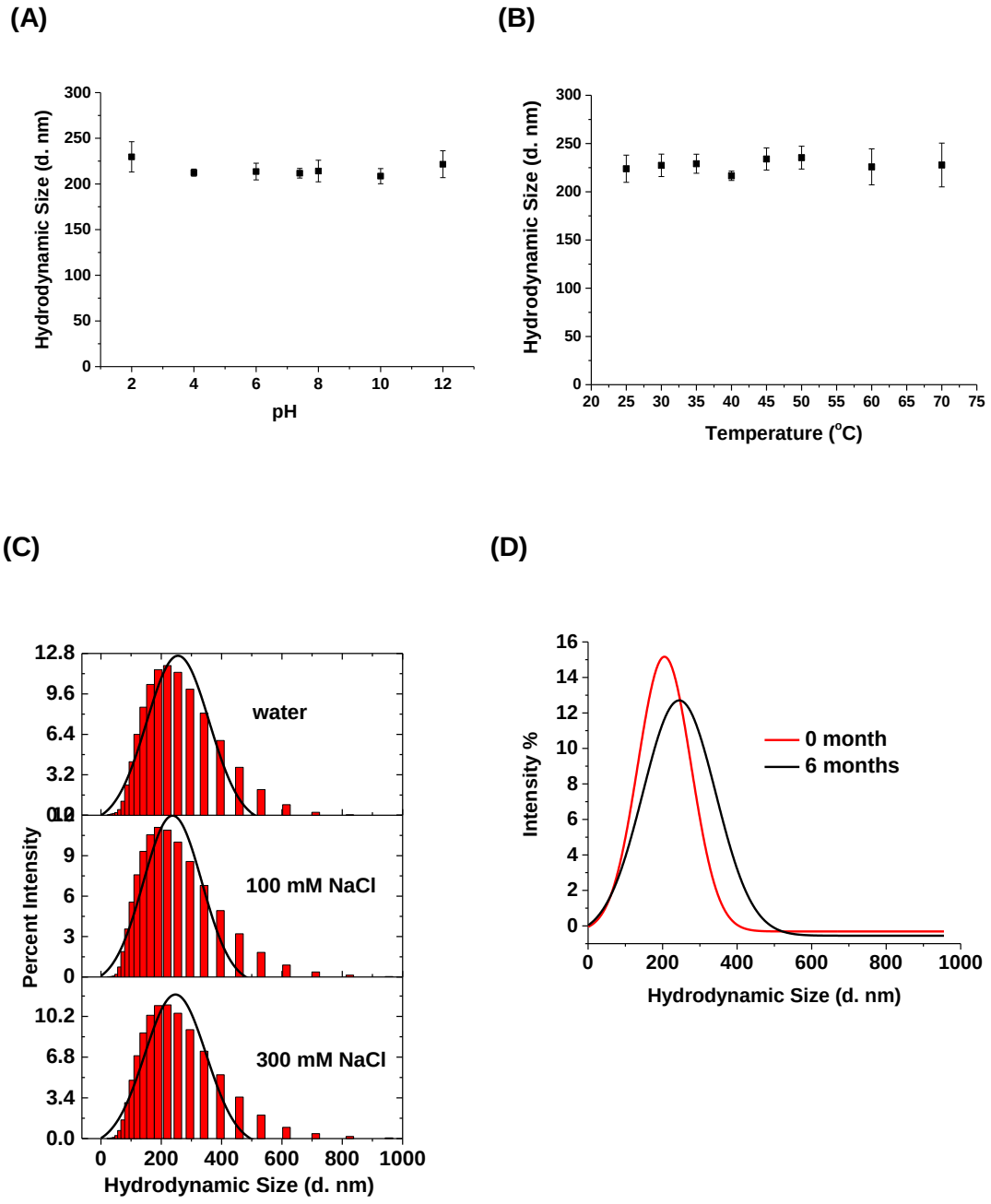

Figure 3-9. Comparison of the hydrodynamic diameters of the polymer encapsulated MNPs in water at different (A) pH, (B) temperature (C) different salt concentration, (D) Dynamic Light scattering measurements were performed on the sample at two time points after coating. Dh histograms of freshly prepared and after storage for 6 months.

3.3.3 Optimization of capture-DNA loading

The Zhou group has previously found that increasing capture-DNA loading on silica coated MNPs could increase the target-DNA capture efficiency, presumably *via* enhanced binding affinity.[52] However, too high a capture-DNA loading could also lead to high background signals, possibly due to non-specific interactions.[52] Therefore, the MNPs with different capture-DNA loading (e.g. 0.04, 0.10, 0.20, and 0.35 nmol·mg^{-1}) were prepared to investigate the optimal loading. The MNPs (30 µg each) were mixed with the signal-DNA and full-match target-DNA (10 pM each) followed by ligation and then NAV-HRP binding. A control without the target-DNA (WOT) was also prepared under identical conditions. The typical time-dependent fluorescence response curves and the corresponding slopes were shown in **Figure 3-10**.

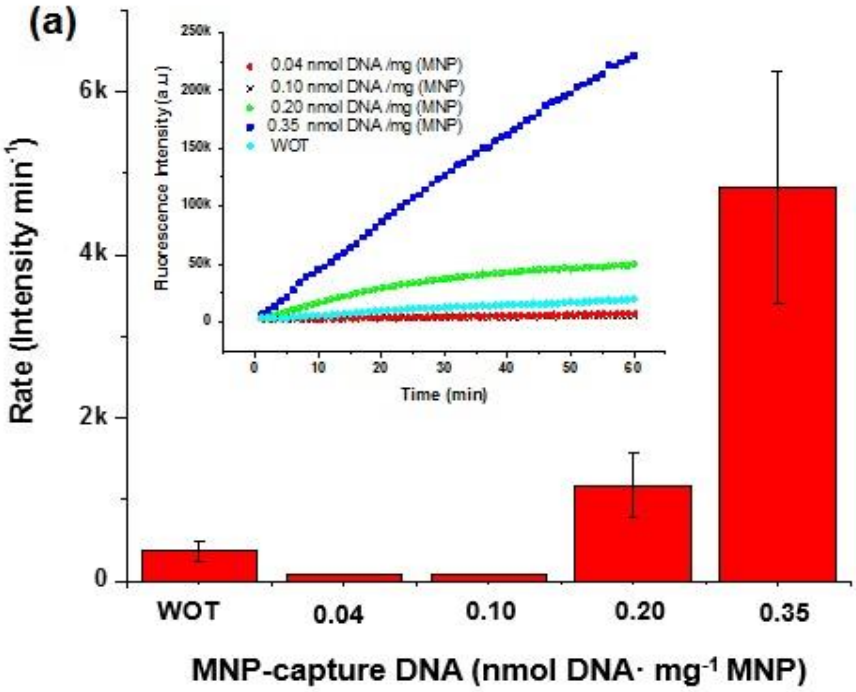

Figure 3-10. Comparison of fluorescence response (slopes of fluorescence response curves shown in figure inset) for MNP-DNA conjugates with different capture DNA loadings (n =3). Figure inset: typical time-dependent fluorescence intensity profiles for detecting perfect match T1 for MNP-capture DNA with different capture DNA loading.

The highest signal was obtained for the MNP having the highest capture-DNA loading (e.g. 0.35 nmol·mg^{-1}), while those having the capture-DNA loading of 0.04 and 0.10 nmol·mg^{-1} were rather low and comparable to the WOT control. Unfortunately, we were unable to prepare MNPs with the capture-DNA loadings higher than 0.35 nmol·mg^{-1} despite several tries, including the use of higher amounts of capture-DNA, possibly limited by the amount accessible PEG-azide on the MNP surface. Therefore MNPs with this capture-DNA loading was used in all subsequent sensing experiments.

All subsequent DNA sensing experiments *via* the Route (a) were carried out with a fixed 100 pM signal-DNA in PBS. The assay gave a steady increase of fluorescence with time **Figure 3-11 (A)**. The signal was highest for the highest target-DNA concentration (10 pM) and decreased with the decreasing target-DNA concentration with the control giving the lowest signal as expected. The slopes were determined and plotted versus the DNA target concentration as shown in **Figure 3-11(B).** The limit of detection (LOD) based on three times the standard deviation plus the negative control signal (*i.e.* LOD = $3\sigma_{WOT} + I_{WOT}$) [180, 198] was determined as 1.0 pM. This LOD was comparable to many previously reported DNA sensors which typically offered nM-pM sensitivity (see **Table 3-2**).

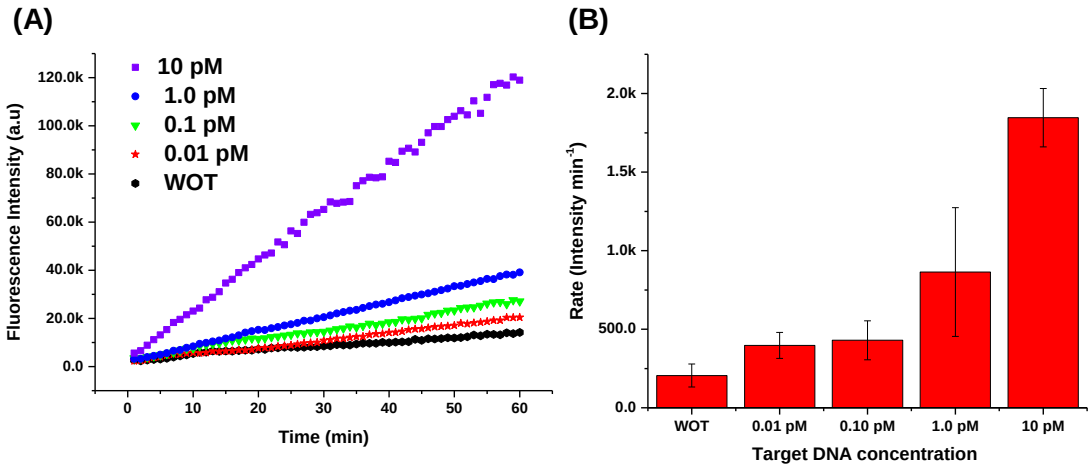

Figure 3-11. (A) Representative time-dependent fluorescence responses curves for detecting different concentrations (0.01 - 10 pM) of the full-match target-DNA (T1). (B) Typical fluorescence response rates for T1 detection (*n* =3).

Traditional DNA hybridization assays are usually performed using “sandwich-type” detection designs that is suitable for the detection of label-free target DNA. The unlabelled target DNA is bordered by a nanomaterial tagged with capture-DNA probes and a biotinylated signal-DNA reporter probe that can bind with NAV-HRP. Interestingly, our simple approach MNP based DNA sandwich assay is comparable in terms of its LOD to a more intricate electrochemical DNA sensing using a DNA tetrahedron structure [160] In general, one of the major drawback often encountered in surface –based (flat and spherical) biomolecular detection is the limited accessibility of target molecules to the probes immobilized on heterogeneous surface as compared to the probe-target binding events in solution phase which is often specific and fast. Thus, addition of inert linkers are often added to the surface to passivate vacant spaces and allow the capture-DNA probes to adopt an upright surface position that will favour hybridization with the target DNA. In this study, the long chain PEG backbones (n~23 ethylene glycol units) can be thought of stretching outward the nanoparticle surface. Moreover, the addition of the inert linker (-$PEG_{\sim 23}$-OCH_3) might have forced the PEG-capture-DNA strands to adopt a rod-like spatial orientation with the capture-DNA oriented toward the solutions in order to readily hybridize with the target-DNA. This requirement is imperative in order to increase probe-target affinity and increase DNA hybridization efficiency. In addition, the polyethylene glycol units imparted the nanoparticle surface with non-specific adsorption properties. In this manner, the target-DNA does not adsorbed on the nanoparticle surface and allows more target DNA to hybridize with the capture-DNA, thus, leading to more efficient hybridization. Interestingly, this simple design of polymer encapsulated MNP coupled to traditional DNA sandwich hybridization can achieve LOD comparable to many previously reported DNA sensors which typically offered nM-pM sensitivity without the need of several DNA primers or the use of more sophisticated instruments. However, this 1 pM level of sensitivity was still uncompetitive against some of the recent ultrasensitive DNA assays [63, 90, 94, 199]. Therefore a more powerful signal amplification strategy using poly-enzyme nanobead was designed to further improve sensitivity (see section 3.3.5).

Table 3-2 Comparison of the sensing performances of some sensitive DNA assays (LOD = limit of detection).

Sensing Method	LOD (pM)	Ref.
Photonic crystal hydrogel beads	0.66	[200]
Electrochemical detection based on bar-coded GNPs	~4	[161]
MNP-dye sandwich assay	100	[163]
Au particle-on-wire surface-enhanced Raman scattering (SERS)	10	[201]
Fluorescence based on Ag@poly(m-phenylenediamine) nanoparticles	250	[158]
Microcantilever array based nanomechanical sensing	10	[202]
Silver particle amplified dual-wavelength surface enhanced Raman scattering	1-33	[203]
Graphene quenched fluorescent DNA nanoprobes	~100	[204]
Graphene-based high-efficiency surface-enhanced Raman scattering	10	[173]
Zn(II)-porphyrin/G-quadruplex complex with Exo III-assisted target recycle	200	[205]
MNP-enzyme probes detected *via* a personal glucose sensor	40	[162]
Electrochemical DNA sensing using a DNA tetrahedron structure	1	[160]
Gold nanoparticle amplified surface Plasmon resonance sensing	10	[206]
Electrochemical sensing *via* a DNA Super-sandwich Assembly	0.1	[159]
Enzyme-Based Electrochemical DNA Sensing	0.01	[207]
MNP-sandwich + ligation with single-enzyme amplification	~1	**This work**
MNP-sandwich + ligation with poly-enzyme nanobead amplification	0.00001	**This work**

3.3.4 SNP discrimination

The sensor was further evaluated for its ability to detect specific SNPs in the KRAS gene associated with many human cancers (*e.g.* colorectal, pancreas, ductal and lung). Here three target-DNAs (all 10 pM) were employed: wild-type T1 (counting from 5', base 17 → C), two cancer mutants: T2 (17C → T) and T3 (17C → A). The sensing was done in PBS and PBS containing 10% human serum to mimic clinical assay conditions. **Figure 3-12 (A)** revealed that only the full-match target-DNA (T1) produced a high fluorescence response, the signals for both SNP targets (T2, T3) were practically the same as background, *i.e.* this sensor was highly specific.

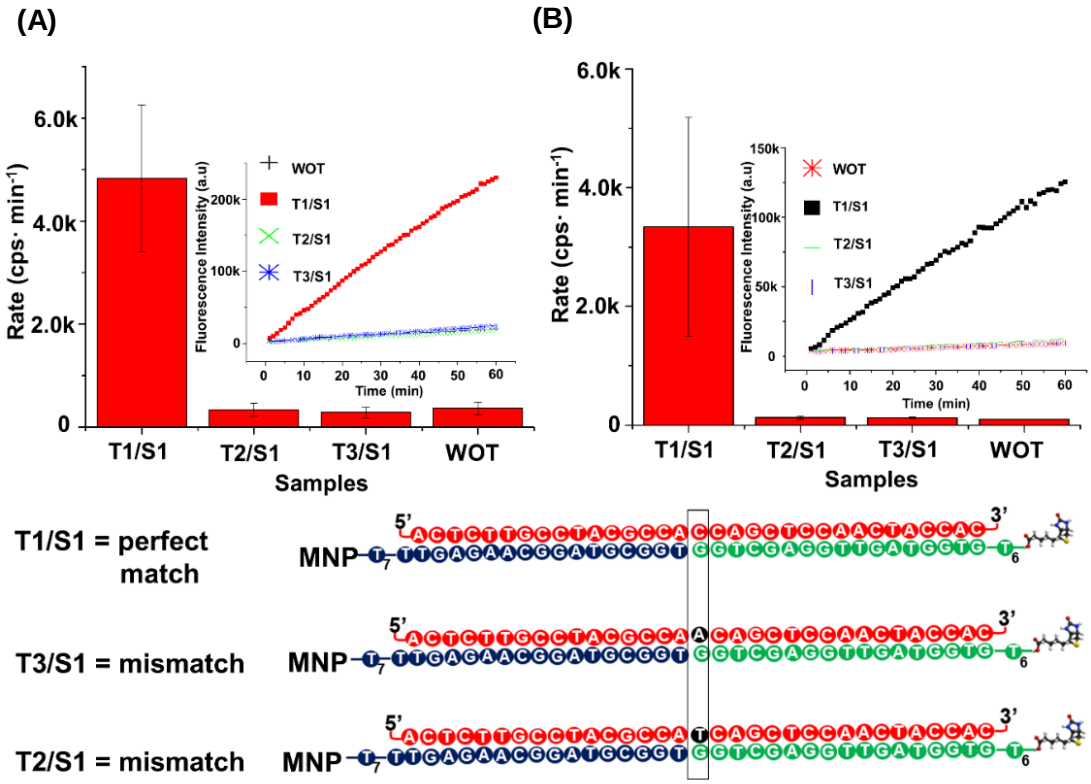

Figure 3-12. Discrimination of the perfect-match (T1) against other SNP targets (T2 and T3). (A) Comparison of average fluorescence production rates (slopes of fluorescence response curves shown in inset) for different DNA targets in PBS (A) or PBS containing 10% Human serum (B, *n* = 3).

The SNP discrimination ratio for T1 against the SNP targets before background correction was determined as ~14.3 and ~16.8 for T2 and T3, respectively. This level of SNP discrimination was comparable or better than many other assays reported in the literature [163-165, 208, 209]. More importantly, even higher SNP discrimination ratios (*ca.* 33) were obtained when the detection was carried out in clinically relevant media (e.g. PBS containing 10 % human serum, see **Figure 3-12 (B)**, demonstrating that our sensor was highly robust and could work effectively under clinical relevant conditions.

3.3.5 Poly-enzyme nanobead amplification

A more powerful signal amplification strategy using poly-enzyme nanobeads each tagged with ~10^4 copies of NAV-HRPs was designed to further improve sensitivity (Scheme 1, Route b). We first prepared NHS-PEG_{12}-biotin modified polymer nanobeads, determined its biotin valency as ~10^4 per bead, and then conjugated the nanobead with NAV-HRP by incubating with 1:1 mole ratio of NAV-HRP to the bead surface biotin. The MNP-capture-DNA, signal-DNA and different amounts of target-DNA were mixed, ligated as above and then treated with poly-enzyme nanobead. The resulting fluorescence response curves were shown **Figure 3-13 (A)** inset. Each sample was done in triplicates and the average of the slopes were calculated and plotted in **Figure 3-13**. The highest signal was observed for the 1 pM target-DNA sample as expected. Very low fluorescence signals were observed from the controls (no target-DNA), suggesting that the polymer encapsulated MNP was highly effective in resisting non-specific adsorption. Here a low background was critical to achieve high sensitivity, allowing for unambiguous detection of weak signals arising from ultralow levels of target molecules.

The fluorescence intensity was plotted against the logarithm of the target DNA because at lower concentration, the fluorescence intensity approaches a linear expression according to the equation:

$$F = k' I_o(log_{10} \varepsilon lc)$$

Equation 3-1

Where F refers to fluorescent intensity, k' is a rate constant that takes quantum yield into account, I_o intensity of the incident radiation, ln is the natural logarithm, ε is the extinction coefficient, l is the path length and c is the concentration. A linear dependence between the fluorescence intensity and the logarithm of the target DNA concentration was obtained in the range from 0.001 fM to 1000 fM. As shown in **Figure 3-13 (B)**, our sensing strategy provided a rather wide linear dynamic range of 6 orders of magnitude (*e.g.* 1 aM to 1 pM, $R^2 = 0.966$) with a LOD of as 1.6 aM based on the interception point between the linear fit and the background + 3σ level. Such levels of sensitivity place it among the most sensitive DNA biosensors reported in the literature as shown in **Table 3-2.** We attributed the ultrasensitivity here to the greatly increased signal amplification power of the poly-enzyme nanobead, each carrying ~10^4 copies of HRPs. As a result, it was able to covert each captured full-match target-DNA into ~10^4 copies of HRPs (*versus* 1 in the traditional sandwich assay) for greatly enhanced sensitivity.

In general, the use of MNP for efficient target capture and enzyme-tagged polymer beads were of great significance to this work. This study illustrates its novelty on the simple design and universality of signal amplification approach. The signal amplification mechanism only requires an enzyme (*i.e*. HRP) immobilized on polymer beads. The signal amplifier can be reliably and easily prepared by incubating NAV-HRP on a biotinylated polymer nanobeads and has the potential to be scaled up. Furthermore, the beauty of using such powerful signal amplification approach is that it only requires incubation step with MNP-DNA_{ds}- Biotin, thus, eliminating the use DNA primers and time consuming steps as in RCA or the use of sophisticated thermal cyclers in LCR-based signal amplification strategies. Moreover, the poly-NAV-HRP nanobead also offers a new and powerful signal amplification strategy that can be adopted in any bioassay formats because it only needs a free biotin for binding (e.g. ELISA). To the best of our knowledge this is the first report that utilized a poly-enzyme nanobead as signal amplifier for SNP detection.

(A)

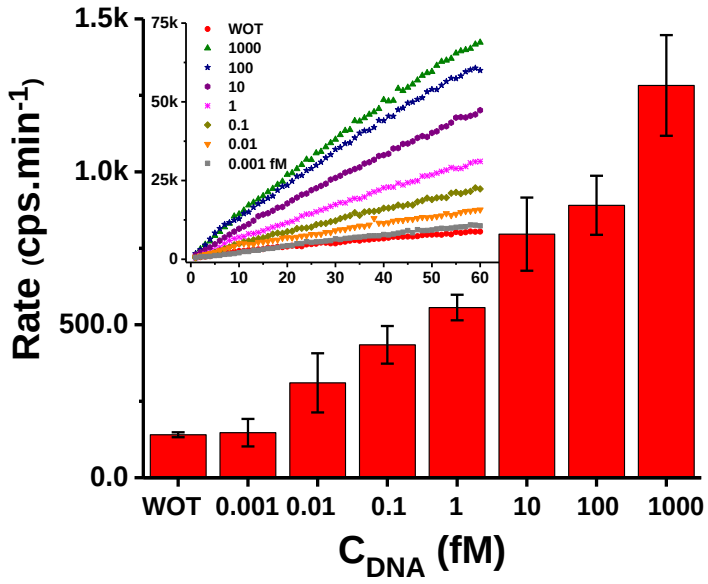

(B)

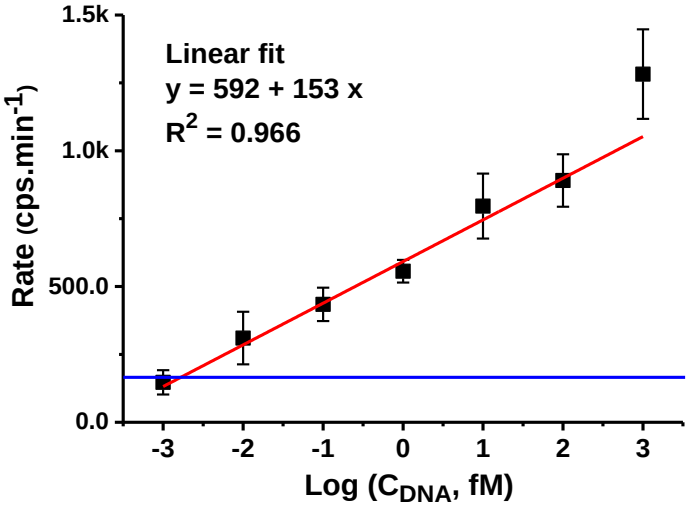

Figure 3-13. (A) Comparison of the average fluorescence increase rate (cps·min^{-1}) for assays containing 0-1000 fM of T1 (inset show the corresponding time-dependent fluorescence responses, n=3). (B) Relationship between the fluorescence increase rate and the log(C_{DNA}, in fM) fitted by a linear function (y = 153x + 592, r^2 = 0.966). The blue line shows the background + 3σ level which intercepts with the linear fit at x = -2.788, corresponding to C_{DNA} = 1.6 aM.

Besides high sensitivity, the ability of accurate and reliable detection of low abundant specific SNPs in a background of wildtype genes is of great importance for the non-invasive diagnosis of cancer and other diseases.[24] Therefore the ability to detect low abundance full-match target-DNA (T1) in large excess of SNP targets (T2 and T3) was also investigated. The final DNA concentrations were 1 fM for the full-match T1 and 10 fM (*i.e*.10-fold excess) or 100 fM (*i.e.* 100-fold excess) for each SNP target (T2 and T3). **Figure 3-14** revealed that, increasing the SNP:T1 ratio led to a decreased fluorescence signal, presumably because the large excess of SNP targets (T2 or T3) could compete with T1 to sandwich hybridize to the capture- and signal-DNAs, reducing the chances of a successful ligation templated by the full-match T1. Nevertheless, the signal of samples containing just 1 fM T1 (1% of the T2/T3 SNP target concentration) was clearly higher than those of the SNP targets only, suggesting that our sensor can specifically detect 1 fM T1 even in the presence of 100 fold excess of SNP targets. This level of specificity for the perfect-match target-DNA over its SNP targets is among the very best SNP sensors reported in literature [42, 63].

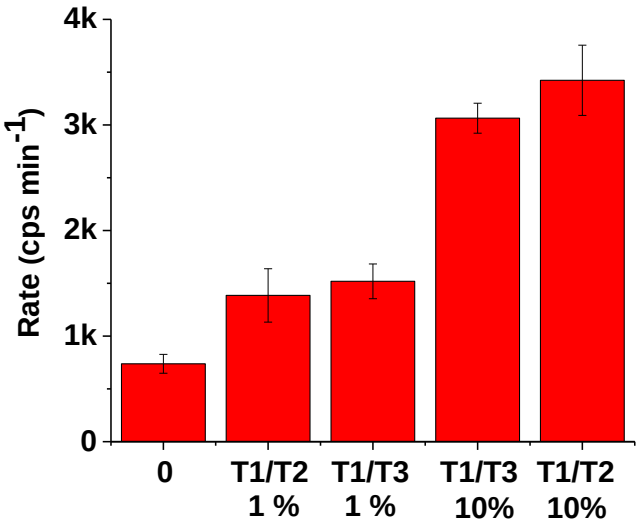

Figure 3-14. Detection of 1 fM perfect-match T1 in the presence of large excess (10 or 100 fold) of the SNP targets (T2, T3). A control with 100 fM of T2 and T3 each.

3.3.6 Conclusions

We have shown that encapsulation of hydrophobic MNPs with an azide-PEG functionalised amphiphilic polymer not only produces stable, well-dispersed MNPs that effectively resist non-specific adsorption, but also enables the convenient DNA conjugation *via* the Cu-free “click” chemistry. A new strategy based on sandwich hybridisation followed by ligation to introduce biotins on the MNP surface for enzymatic signal amplification has yielded excellent SNP discrimination. Moreover, a new powerful signal amplification strategy using poly-enzyme nanobead which can convert each captured target-DNA into thousands of copies of active enzymes has been developed, enabling the direct detection of target-DNA down to 1.6 aM with a linear dynamic range of 6 orders of magnitude, placing it among the most sensitive PCR-free DNA sensors. Furthermore, this sensor is highly robust (works effectively in clinical relevant media) and specific (can positively detect 1% of the full-match target in a background of 100 fold excess SNP targets), suggesting that it may have broad applications in biosensing and clinical diagnostics.

Chapter 4

Colloidal Silver Nanomaterials: Structure, Synthesis and Antimicrobial Properties

4.1 Introduction

Colloidal inorganic nanoparticles (NPs) are tiny objects sized between 1 to 100 nanometres (nm) and can form stable dispersions in a solvent [210]. The NPs can be made of a noble metal, metal or non-metallic oxides, semiconductors, magnetic compounds and a hybrid of them [210, 211]. Over the past years, scientists have developed new methodologies to synthesise colloidal NPs and unravelled their unique physical and chemical properties that are different or absent from their bulk counterparts. Colloidal NPs have been utilised in various biomedical and technological applications [210-212]. In terms of biomedical applications, the development of inorganic antimicrobial nanoparticles have a profound impact in the healthcare industry because of their ease in synthesis, stability, and nanoparticles tend to show a broad spectrum of bactericidal and fungicidal activities [213]. Furthermore, with emergence of antibiotic resistant bacterial strains, it is imperative to develop new antimicrobials that can offer better therapeutic property and less toxicity to mammalian cells [214]. In this regard silver nanoparticles (Ag NPs) are one of the most well studied nanomaterials that show outstanding antimicrobial activities over wide range of bacteria, viruses, and fungal strains [215, 216]. The antimicrobial properties of Ag NPs are dependent on its size, shape, and the presence of oxidizing agents such as molecular oxygen [217].

Recently, metallic nanoclusters (*e.g.* Pt, Au, Ag, Cu) with all three spatial dimensions below 2 nm have emerged as a new class of nanomaterials and have drawn research interests due to distinctive optical and chemical properties which differ significantly and unavailable from their nanoparticle counterparts [218-220]. In particular, water soluble silver nanoclusters (Ag NCs) have received considerable attention in the past

few years owing to the plethora of potential applications [221]. However, synthesis of water soluble Ag NCs is challenging because few-atom silver nanoclusters are highly reactive and tend to form large nanocrystals [221]. Hence, more research must be done to improve the stability of Ag NCs in aqueous solutions. Having luminescent properties, Ag NCs are being investigated for its applications in biological imaging [222, 223], catalysis [224, 225], and biological [226] and chemical [227, 228] sensing. It is surprising that only a few studies have reported the antibacterial properties of Ag NCs and more research has to be done to determine its antibacterial properties [229-232]. It is hypothesised that Ag NCs may have a stronger interaction with the bacterial cells than its larger NP counterpart due to their ultra-small sizes, leading to more effective antimicrobial potency.

This chapter will give an introduction on the electronic structure and optical properties that differentiate Ag NPs and Ag NCs. Moreover, the synthetic approaches to water-dispersible Ag NPs and Ag NCs will be discussed. This chapter will also highlight the current understanding of the antimicrobial mechanisms of Ag NPs against selected microbial strains.

4.2 Electronic Structures in Nanoparticles and Nanoclusters

Bulk metals are good electrical conductors and optical reflectors because of the free movement of delocalized electrons in the conduction band as shown in **Figure 4-1**. When the size is reduced to 2– 100 nm, metal nanoparticles display characteristic colours due to surface plasmon resonance (SPR) which is a result of the collective oscillation of conduction electrons at their surfaces upon interaction with light [233, 234]. When the size of these metals is further reduced to 2 nm or less (down to 300 atoms or less) [235, 236] , these particles are too small to support surface plasmon resonance. Moreover, at this sub-nanometre size scale, the band structure becomes discontinuous and is broken down into discrete energy levels [219]. This electronic structure is somewhat similar to the energy levels of molecules. Hence, metal nanoclusters are said to have “molecule-like” properties and do not exhibit plasmonic properties [219, 237]. Metallic nanoclusters are seen as materials that bridge the gap between plasmonic nanoparticles and individual atoms.

Nonetheless, metal nanoclusters can still interact with light *via* electronic transitions between energy levels, resulting in light absorption and emission. A prominent feature that makes metallic nanoclusters particularly attractive in biomedical applications is their strong photoluminescence, good quantum yields, tuneable fluorescence emission, large stokes shift and high photostability.[219, 237, 238]

.

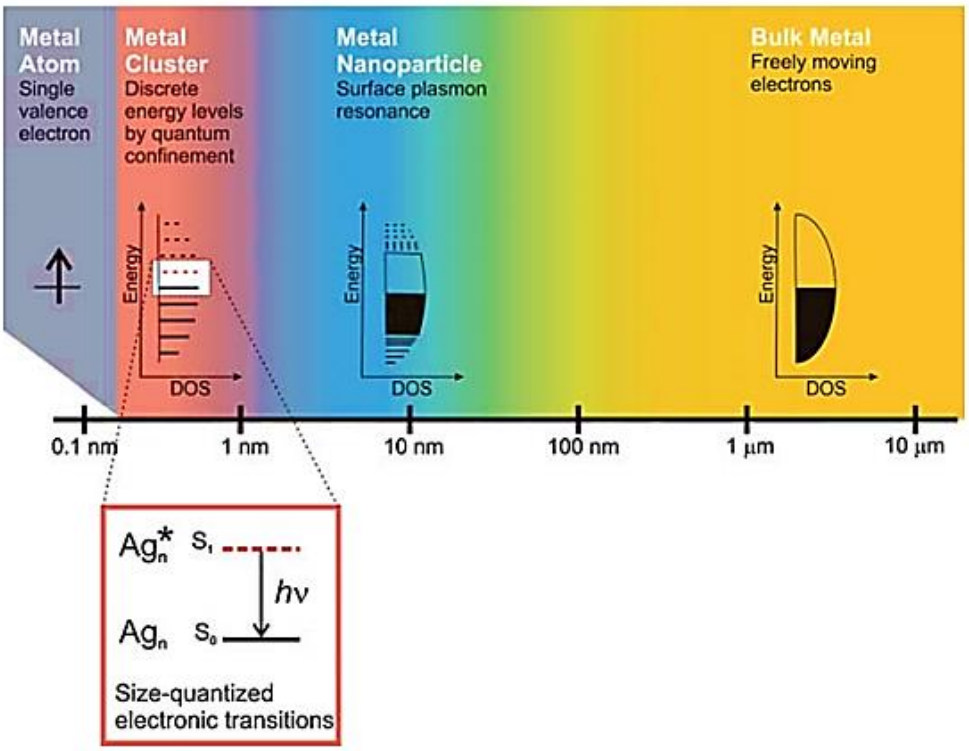

Figure 4-1. Whereas bulk metal and metal nanoparticles have a continuous band of energy levels, the limited number of atoms in metal nanoclusters results in discrete energy levels, allowing interaction with light by electronic transitions between energy levels. Metal nanoclusters bridge the gap between single atoms and nanoparticles. Reprinted from reference [239].

4.3 Optical Property of Metallic Nanoparticles

Noble metal NPs such as Gold (Au) and Silver (Ag) exhibit a unique optical property originating from their surface plasmon resonance (SPR) that can be conveniently detected by UV-Visible spectrophotometry. Au NPs typically display a strong the SPR band peaking in the range of 520 nm to 580 nm [240], depending on the particle size as demonstrated by El-Sayed and colleagues in 1999 [241]. Increasing the Au NP size resulted in a red shift of the SPR peak absorption in the UV-Vis spectrum [241]. Ag NP's SPR band appeared at the region of 420 nm to 450 nm [242, 243]. Moreover, a similar behaviour was observed for differently sized Ag nanoparticles, wherein the characteristic SPR peak position shifted to longer wavelengths with increasing particles size [244]. The SPR absorption is caused by the interaction between incident light and electrons on the surface of NPs as shown in **Figure 4-2**. The free electrons (s electrons) in the metal are free to move through the material. An incident light with wavelength greater than the diameter of the particle can lead to standing resonance conditions. As the wave front of incident light passes, the electron density in the nanoparticle is polarized to one surface and oscillates in resonance with the light's frequency causing a standing oscillation[234].

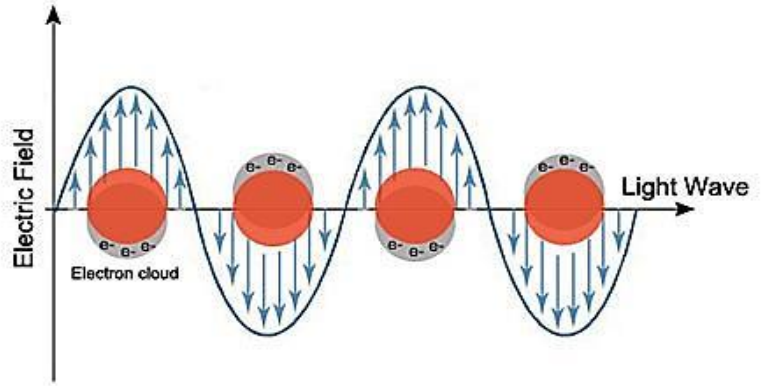

Figure 4-2. Basics of localized surface plasmon resonance (LSPR) of gold nanoparticles due to collective oscillation of surface electrons with incident light at a specific wavelength. Reprinted from www.cytogenetics.com

The Mie theory can be used to describe the response of spherical NPs whose diameter is smaller than the wavelength of incident light [245]. As shown in **Equation**

4-1, the extinction cross section of a single particle (C_{ext}) defines the energy loss in the direction of incident light due to both absorption and scattering. The C_{ext} is described in terms of dielectric function of the metal ($\varepsilon(\lambda) = \varepsilon'(\lambda) + i\varepsilon''(\lambda)$) and dielectric constant of the medium ε_m. From the equation, C_{ext} of the particle is dependent on the dielectric function of the metal of which the particle is composed. Hence, this give rise to the unique absorption and scattering profiles for different metal nanoparticles. For small nanoparticles compared to the wavelength of incident light (*e.g.* Au < 25 nm), only the dipole absorption of the Mie equation contributes to the extinction cross section C_{ext} of the nanoparticles [241]. The Mie theory then reduces to the following relationship:

$$C_{ext} = \frac{24\pi^2 R^3 \varepsilon_m^{3/2}}{\lambda} \frac{\varepsilon''(\lambda)}{(\varepsilon'(\lambda) + 2\varepsilon_m)^2 + \varepsilon''(\lambda)^2} \qquad \textbf{Equation 4-1}$$

where $\varepsilon(\lambda) = \varepsilon'(\lambda) + i\varepsilon''(\lambda)$ is the wavelength-dependent, complex dielectric function of the NP material, ε_m is the dielectric constant of the surrounding or embedding medium and R is the radius of the particle. The frequency of SPR is also dependent on the size and composition of NPs, as well as the dielectric constant of medium [241]. As the shape or size of the nanoparticle changes, the surface geometry changes causing a shift in the electric field density on the surface. This causes a change in the oscillation frequency of the electrons, generating different cross-sections for the optical properties including absorption and scattering [234]. The change in SPR frequency yields the change of NPs colour that can even be observed with bare eyes [234]. Zhong and colleagues [246] showed the size correlation with SPR properties and UV-vis absorption spectra for Au nanoparticle with diameters ranging from 10 to 100 nm as shown in **Figure 4-3**.

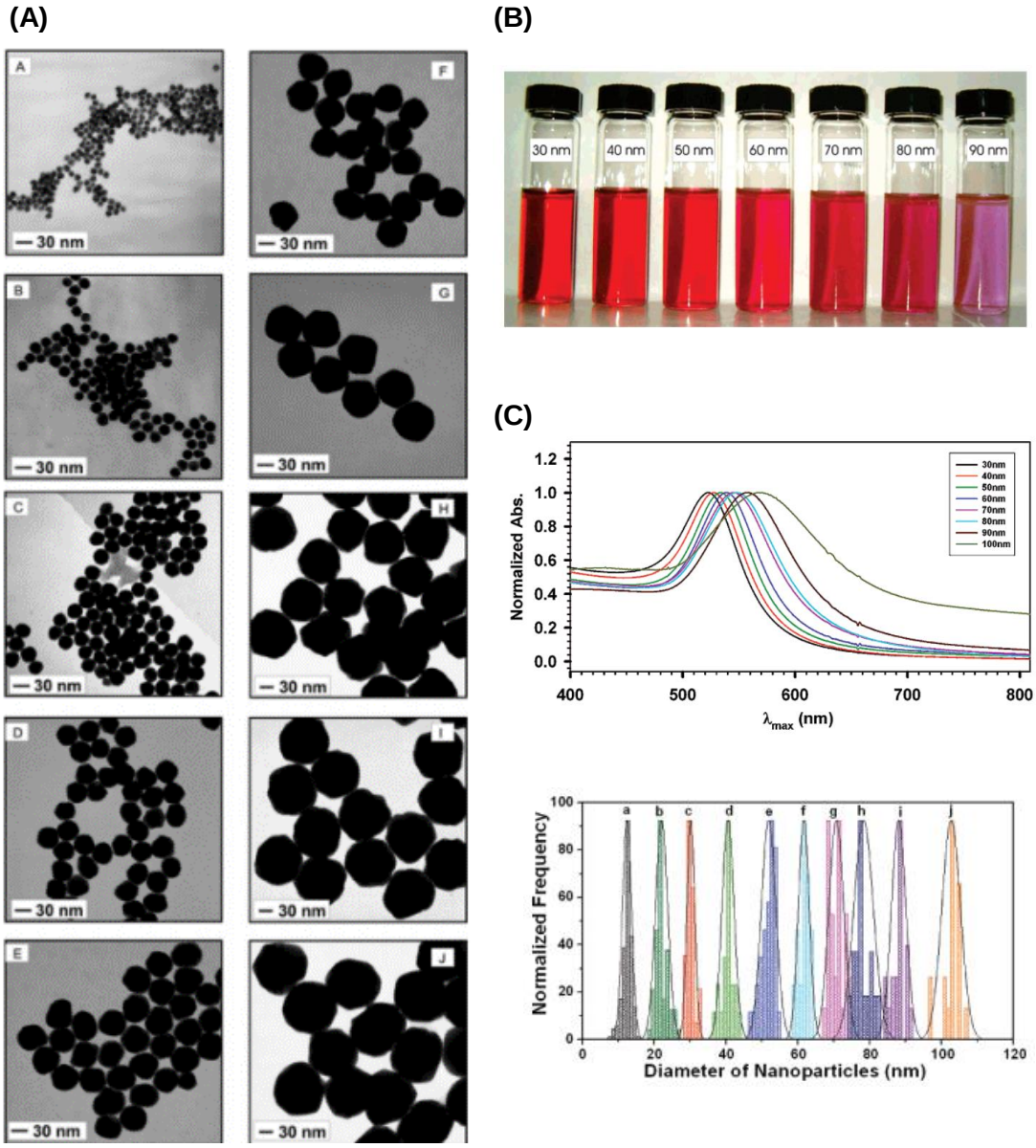

Figure 4-3. (A) TEM images of Au NPs of different sizes: 10 nm (A); 20 nm (B); 30 nm (C); 40 nm (D); 50 nm (E); 60 nm (F); 70 nm (G); 80 nm (H); 90 nm (I); and 100 nm (J). The size distributions of Au NPs: (a) 12.3±1.3 nm; (b) 20.6 ±1.5 nm; (c) 30.0±1.1 nm; (d) 40.3±1.7 nm; (e) 51.6±2.0 nm; (f) 61.3±1.5 nm; (g) 70.6±2.0 nm; (h) 78.3±2.7 nm;(i) 88.1± 2.0 nm; (j) 102.2 ± 2.6 nm. The y-axis represents normalized frequency. (B) Photo showing the colours of Au NPs with different particle sizes, and (C) The UV-vis spectra (normalized) for Au NPs with different particle sizes in aqueous solution. Reprinted from reference [246].

4.4 Optical Property of Metallic Nanoclusters

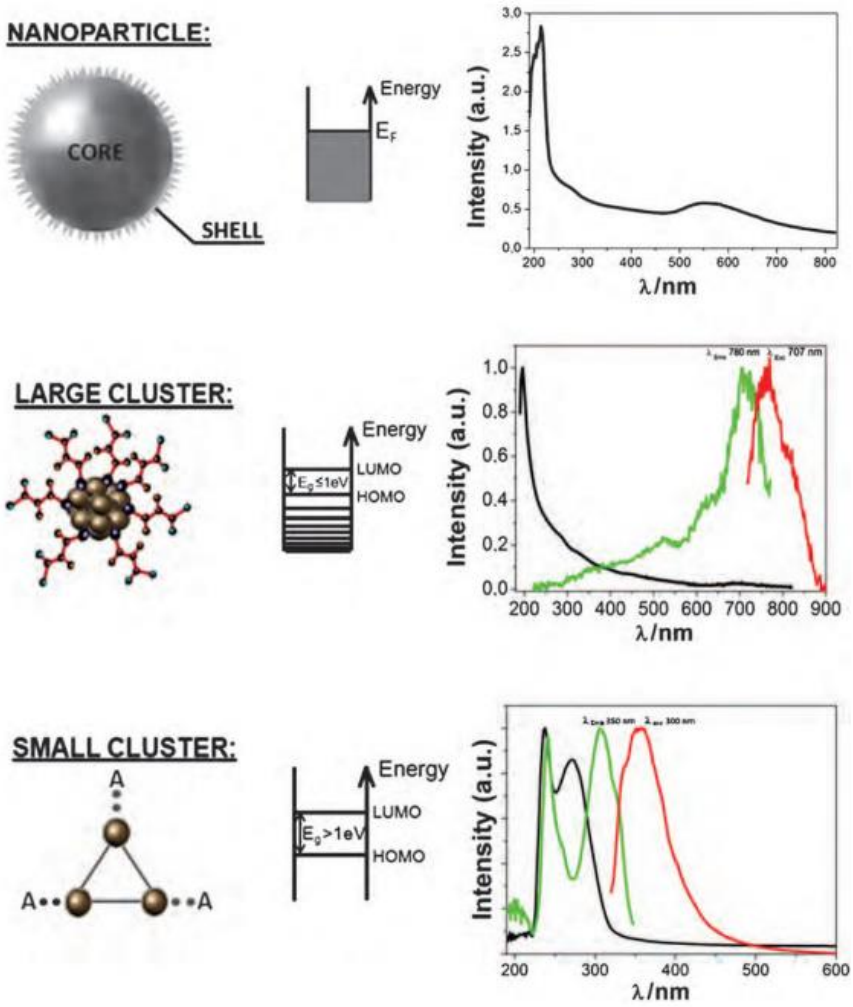

Figure 4-4. Schematic representation of the optical properties of nanoclusters and nanoparticles. Reprinted from reference [247].

The UV-Vis absorption spectra for nanoparticles and nanoclusters are shown in **Figure 4-4**. The absorption spectra of metallic nanoclusters do not show the typical surface plasmon resonance (SPR) feature of nanoparticles (**Figure 4-4 (A)**). Instead, NCs display a "molecule-like" optical characteristics due to their discrete electronic energy levels. This gives rise to size tuneable HOMO-LUMO gap that in turn can lead to size-dependent luminescence [248]. For larger NCs (those formed by a number of atoms N ≥ 10-15 atoms), the UV-Vis absorption spectra consists of a continuous increase of absorbance with decreasing wavelength (**Figure 4-4 (B)**). However, for

smaller metallic nanoclusters (those formed by a number of atoms N ≤ 10-15 atoms) display molecule bands (**Figure 4-4 (C)**) instead of collective plasmon excitations. As the size of the nanoclusters decreases, the spacing's between the discrete states in each band increases, leading to a blue shift in the absorption peaks. For example, Dickson and colleagues [249] reported Ag NC made of Ag_1–Ag_4 core showed absorption peaks at 440 nm and 357 nm [249]. Recently, the UV-Vis absorption spectra of DHLA-stabilized Ag_4 and Ag_5 NCs were found to exhibit peaks at 435 nm and 335 nm and a shoulder peak at 500 nm [227]. These observations clearly indicate that discrete electronic transitions in few atom metal NCs exhibit molecular like behaviour.

Luminescence of metals (*e.g.* bulk and nanoparticles) is extremely weak for any practical applications due to the efficient non-radiative decay channels and lack of energy gap [250]. Interestingly, metallic nanoclusters were reported to exhibit strong luminescence which can have ~ 9 orders of magnitude higher than bulk gold (QY = 10^{-10}). Unfortunately, there is no general mechanism that explains the emission from all metal NCs as compared to the well-established emission mechanism in quantum dots (QDs). Instead, several studies have shown that the luminescence mechanism of metal NCs may vary with sizes, coating ligands, and their synthesis routes. For instance, Huang and Murray suggested the visible light emission from monolayer-protected metal NCs is due to the interband transitions between the filled d band and the conduction band [238, 251]. Whetten and colleagues attributed the infrared luminesce of glutathione protected Au_{25} NCs to the relaxed radiative recombination across the HOMO-LUMO gap within the sp conduction band (intra-band transition) [252]. Zheng and colleagues proposed that luminescent nanoparticles synthesized by dissociation of polymeric Au(I) thiolates can actually be considered as intermediate between luminescent Au(I) complexes/clusters and non-luminescent gold nanoparticles [253]. Very recently, Wu and Jin [254] reported that the surface ligands have a profound effect on the fluorescence of thiol-protected Au NCs. In summary, these studies suggest that fluorescence emission from nanoclusters may originate from (a) the metal core

intrinsic quantization effects and (b) the property of nanocluster surface determined by the chemical interactions between the surface ligands and the metal core.

4.5 Synthesis of Ag NPs and Ag NCs

A variety of methods have been developed for the synthesis of water-soluble Ag NPs and Ag NCs since most applications their applications involve aqueous conditions (*e.g.* chemical and biological sensing, imaging, *etc.*). Various synthetic approaches involve the reduction of silver salts in the presence of suitable stabilizers which can be accomplished by physical methods (*e.g.* radiolytic [221, 255-259], photochemical [260-270], sonochemical [271-281], and microwave [281, 282]), and chemical methods.

The synthesis of water-soluble Ag NPs *via* chemical reduction typically involves the reduction of $AgNO_3$ solution in the presence of an appropriate stabilizer (*i.e.* capping agent) with an effective reducing agent. The stabilizer is necessary to avoid particle aggregation by shielding the growth of the particles [210, 211]. The final particle size and aggregation state of Ag NPs strongly depend on experimental parameters such as the initial $AgNO_3$ concentration, reducing agent, Ag:ligand, and Ag:reducing agent molar ratios, and stabilizer concentrations. Several reducing agents are suitable for the synthesis. As for any redox reactions, the standard reduction potential (E°) of the reaction determines a successful chemical conversion (*i.e.* $Ag^+ \rightarrow Ag^0$). Furthermore, the Gibbs free energy change ($\Delta G°$) in the reaction must be negative. Note that $\Delta G° = -nFE°_{cell}$, where n is the number of electrons involved, F = Faraday constant (96485 coulombs/mole) and E^0_{cell} is the standard potential of the redox reaction. If $E^0_{cell} > 0$, then $\Delta G°$ would be negative and hence reaction can happen. In case of Ag NP synthesis, the large reduction potential for $Ag^+ \rightarrow Ag^0$ in water ($E° = +0.799$ V, [283]) permits the use of several reducing agents such as sodium citrate ($E° = -0.180$ V, [284]), sodium borohydride ($E° = -0.481$ V, [283]), hydrazine ($E° = -0.230$ V, [285]) and hydroquinone ($E° = -0.699$ V, [286]). Strong reductants usually generate small and monodisperse Ag NPs but it is difficult to produce larger size Ag NPs. Weak reducing agents lead to slower reduction reactions and more polydisperse Ag NP sizes [287]. Size controlled Ag NP synthesis can be achieved in a two-step method involving two reducing agents, where nuclei particles are prepared using a strong

reducing agent and then enlarged by a weak reducing agent [288, 289]. Capping agents also play an important role in the final outcome Ag NP size and shape because they can constrain the growth of distinct crystal faces by preferential adsorption. Weak capping agents such as surfactants [290], ligands [291], polymers [290], and dendrimers [292] commonly produce spherical nanoparticles. However, capping ligands were also found to allow the formation of other nanoparticle shapes by controlling the growth rates for {111} and {100} crystallographic planes and thus determining the final shape of the nanoparticles [293]. A good example is the selective adsorption of both poly(vinyl pyrrolidone) (PVP) and bromide ions (Br^-) to {100} facets of Ag to slow down their growth rate resulting in the formation Ag nanocubes and nanobars [294, 295]. Furthermore, citrate has been shown to bind more strongly to {111} than {100} facets, favouring the formation of Ag nanoplates [296, 297].

The typical synthesis of Ag NCs also involves the reduction of an aqueous solution of $AgNO_3$ with $NaBH_4$ in the presence of stabilizing agents with high affinity for Ag^+. Common stabilizers reported include DNA [249], peptides [298, 299], proteins[300], and polythiol [301, 302] or polyethyleneimine appended molecules [303]. Dickson and colleagues first reported the synthesis of Ag NC using DNA as template and reported that silver ions have strong interactions with oligonucleotide bases (N3 in the pyrimidines and N7 in the purines) but not with the negatively charged phosphate backbone. Mass spectral analysis of the synthesized Ag NCs further revealed ~ 4 Ag atoms are contained in a single DNA template [249]. Single stranded DNA consisting mostly of 12 cytosine bases were found to generate near-IR emitting Ag NC with a high quantum yield ~ 17 %. The resulting Ag NCs exhibit excellent photostability and show no photoblinking at 0.1 to > 1000 ms time scales [304].

Lipoic acid and polyethylene glycol appended lipoic acid ligands were also used to synthesize water-soluble and stable Ag NCs. Usually, a strong reducing agent (*i.e.* $NaBH_4$), was used to reduce the lipoic acid to dihydrolipoic acid ligands, so they chemisorb on the Ag NC surface and make the Ag NCs water-dispersible. Banerjee and colleagues prepared Ag NCs with Ag:L ratio of 1:10 and high resolution mass spectral analysis revealed that Ag NC consisted of Ag_4 and Ag_5 [227]. Using the same synthesis method but with an Ag:L ratio 1:5, Meijerink and colleagues reported a larger Ag_{25} cluster. It is highly likely that the smaller cluster size (Ag_4 and Ag_5) resulted from the fragmentation of Ag_{25} clusters [305]. Interestingly, size control of Ag NCs can

be achieved using polyethylene glycol modified lipoic acid by simply varying the molar ratio of Ag^+ ions to the ligand [306]. Ag NPs were formed when Ag:L ratio is between 1:0.001 to 1:0.2, while Ag NCs were formed when Ag:L ratio were 1:1 and 1:10 as shown in **Figure 4-5** [306]. The use of PEG molecules with different terminal functional groups (-OCH_3, -NH_2, -COOH) gives the Ag NCs different surface property that can be used in various biological applications.

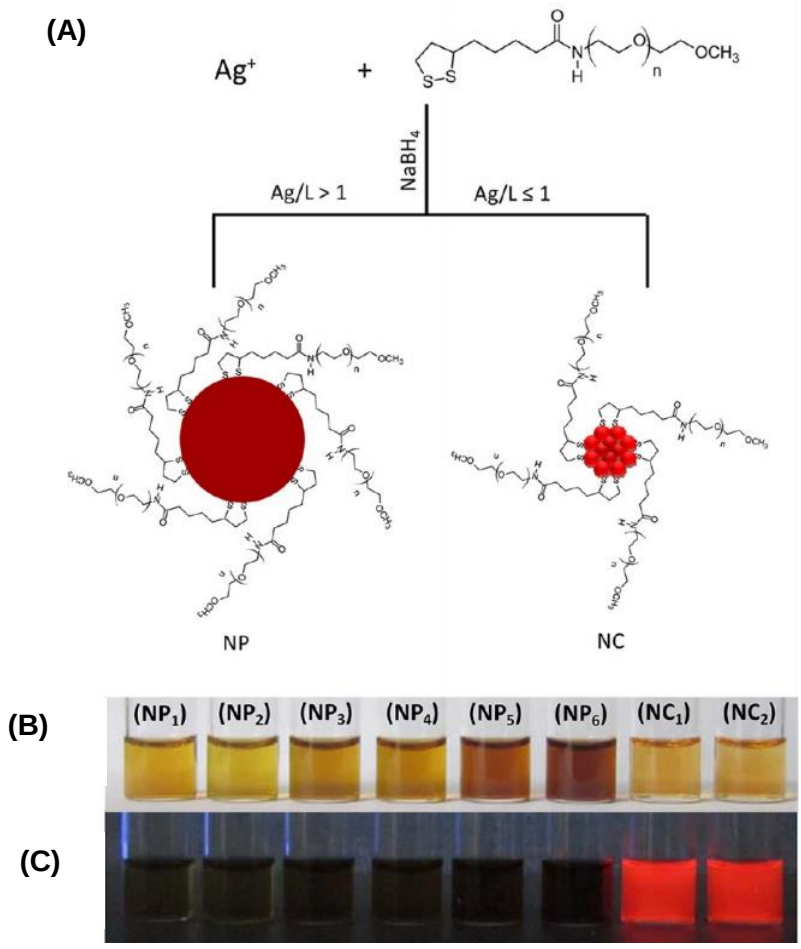

Figure 4-5. (A) synthetic strategy of NPs/NCs of various core sizes. (B) and (C) Photographs of aqueous dispersions of the particles synthesized at various Ag:L ratios under room light and UV light irradiation. The Ag:L ratio for NP_1, NP_2: NP_3, NP_4, NP_5, NP_6, NC_1 and NC_2 were 1:0.001,1:0.01, 1:0.02, 1:0.04, 1:0.1, 1:0.2, 1:1 and 1:10 respectively. Images were collected from a set of freshly prepared dispersions, without filtration or adjustment of the nanoparticle or cluster concentrations. Reprinted from reference [306].

4.6 Antimicrobial Mode of Action

A number of paper has studied the anti-bacterial properties of Ag NPs over the past years [217, 307, 308]. However, the exact mechanism of action remains a hot debating topic. Currently, there is a wealth of experimental evidence that supports the different antimicrobial mechanisms of Ag NPs. Ag NPs can cause cell lysis or inhibit bacterial growth through several mechanisms which include silver ion release from Ag NPs, cell membrane damage, DNA interactions and generation of reactive oxygen species (ROS).

Silver ions has been previously shown to cause considerable morphological changes in bacterial cell membrane and cause *S. aureus* and *E. coli* to reach an "active but non culturable" (ABNC) state and eventually die [309]. Hence, researchers have correlated the release of silver ions from Ag NPs as a possible mechanism for its antimicrobial property. Silver ($E°= +0.799$ V) as a noble metal, is not attacked by water or acid but Ag metal and Ag NPs continuously release small amounts of silver ions under aerobic conditions [310, 311]. These silver ions are biochemically active and can interact with thiol and nitrogen groups of many enzymes, thus, interfering in many biochemical process inside bacterial cells. The highest concentration of released silver ions was observed in the case of the highest surface area of Ag NPs (*e.g.* smallest NPs). While the lowest concentration of released silver ions was observed for the biggest Ag NPs with the lowest surface area, resulting in weak antimicrobial properties [312]. Interestingly, Alvarez and colleagues excluded the "particle-effect" as a mechanism for the antimicrobial effects of Ag NPs. They prepared and stored Ag NPs under anaerobic conditions and the effect on *E.coli* was studied under the exclusion of oxygen. The results showed a direct correlation with the amount of released silver ion to the toxicity of Ag NPs. Moreover, Ag NPs alone were found to be not toxic up to 200 $mg \cdot L^{-1}$ [313].

Another antimicrobial mechanism of Ag NPs involves the anchoring and penetration of Ag NPs to bacterial cell wall. Electron microscopy imaging of Ag NPs treated *E.coli* and *S. aureus* have revealed the formation of 'pits' in the cytoplasmic membrane and accumulation of Ag NPs on the cell surface [314]. The Ag NPs anchored on the bacterial surface can cause pronounced defects in the cell membrane which can lead to changes in the permeability of the cell membrane and eventually to death of the cell.

Silver can interact with the protein portion of the bacterial membrane to form complexes with electron donors that contain oxygen, phosphorus, nitrogen or sulphur atoms [215, 307, 315]. Several bacterial membrane proteins are known to contain sulphur which can interact with silver, leading to the inactivation of membrane-bound enzymes and proteins [242, 316]. Alternatively, Ag NPs can chemically interact with the lipid portion of the bacterial membrane[317, 318]. It has been reported that silver ions and Ag NPs are able to increase the trans/cis ratio of unsaturated membrane fatty acids [319]. Moreover, silver species were also observed to cause modifications in fatty acid composition in bacterial cell wall [320]. Taken together, these reactions (e.g., cis to trans isomerization and modifications in lipid composition) can affect membrane fluidity and hinder normal membrane function by inducing an increase in permeability and loss of membrane integrity [314, 321, 322].

The production of free radicals by the Ag NPs is another possible mechanism by which bacterial cells die. These highly reactive species have the ability to damage the cell membrane, making it porous which can ultimately lead to cell death. Electron spin resonance spectroscopy (ESR) was used to investigate if free radical generation from Ag NPs is related to the observed antimicrobial effect. The results showed that microbial growth inhibition may be caused by the formation of free radical species from the surface of Ag NPs, and led to radical-induced membrane damage [323]. In another study, Soo-Hwan and colleagues showed the antibacterial activities of Ag NPs against *S. aureus* and *E.coli* generate ROS that lead to protein breaks, increased cell membrane permeability and inactivation of lactate dehydrogenase [324]. The toxicity of Ag NPs was significantly higher in aerobic conditions than in anaerobic conditions [325]. Moreover, loss of Ag NP toxicity was observed upon addition of an antioxidant, N-acetylcysteine [325]. These results clearly suggests that ROS formation plays a key role on the toxicity of Ag NPs.

Several investigations have demonstrated the lethal DNA damage caused by interaction of silver ions with DNA. Experimental evidence based on a combination of FTIR spectroscopy and capillary electrophoresis revealed that Ag^+ ions have optimal binding sites at guanine N7 and adenine N7 [326]. Vishnupriya and colleagues [327] studied the interaction between *E. coli* and citrate-reduced Ag NPs (size 25 nm) through Raman spectroscopy in conjunction with plasmon resonance imaging of single bacterial cells. The technique of hyperspectral imaging showed Ag NPs inside the *E. coli* cells and Raman spectroscopy showed that the bacterial DNA was degraded

after 1 hour, causing a decrease in the nucleotide-specific Raman signals. This result suggested that Ag NPs interacted mainly with DNA. In another study, Ouda and colleagues [328] studied the antibacterial effect of Ag NPs (38 nm) against *Proteus sp.* and *Klebsiella sp.*. Growth in both bacterial strains were inhibited, cellular components became disorganized, and bacterial cell wall was ruptured. The reported an MIC value of 10 $\mu g \cdot mL^{-1}$ for both bacterial strains. Furthermore, agarose gel electrophoresis images showed the destruction of both pathogenic bacteria genomes. In effect, this resulted in a loss of DNA replication and promoted degradation, thereby inhibiting bacterial growth [328].

4.7 Overview of the Project

Ag NPs and NCs are interesting silver nanomaterials with unique optical properties. An increasingly common application of Ag NPs are their incorporation to consumer based products [329, 330] and as surface coatings to medical implants and equipment [331] primarily to provide protection against bacteria. On the other hand, Ag NCs are a new class of silver nanomaterials that are composed of several to a few hundred Ag atoms and exhibit a strong and tuneable photoluminescence[224, 236]. With their unique optical properties, it is also interesting investigate and compare the antibacterial activities of Ag NPs and Ag NCs. The ultra-small size of Ag NCs could have a “scaling effect” in biological systems over their larger NP counterparts. Thus, it is of paramount importance to clarify and gain a better understanding of the antimicrobial properties of Ag NPs and Ag NCs.

There is a large volume of work that demonstrated the antibacterial property of Ag NPs are dependent on shape and size, where smaller Ag NPs displayed better antimicrobial properties over bigger Ag NPs [215, 332]. In terms of shape, cubic Ag NPs exhibited greater antibacterial efficacy over nanospheres and nanowires due to the exposed (111) facet of the nanocubes having greater surface energy than facet of nanospheres [333]. The antibacterial properties of Ag NCs have also been recently investigated and showed potent antibacterial action against several bacterial strains [229] and even with the multi-drug resistant bacteria *P. Aeruginosa* [334]. Interestingly, Jin and colleagues (2017) [231] were able to show that Ag NCs can be internalized into *E. coli* DH 5α and *E.coli* DSM 4230 cells *via* different mechanisms and the silver ions inside the cells were assumed to contribute to the bacterial growth inhibition and

death [231]. It has been hypothesized that the ultra-small size of Ag NCs might have a better interaction with cellular components, thus, penetrated through cell membranes and exerted in their antibacterial action. This raises an important fundamental question whether “particle size effect” is a predominant factor that can differentiate the antimicrobial efficiency between Ag NPs and Ag NCs. Current literature provide sufficient but separate information about the antimicrobial properties of Ag NPs [287] and Ag NCs [237]. However, a direct comparison between the silver nanomaterial systems is difficult because of the difference in the preparation of silver nanomaterials and the different bacterial strains and growth medium used in these studies. To address these challenges, Ag NPs and Ag NCs were prepared in the same chemical synthesis protocol, thus, allowing direct comparison of their antimicrobial properties without any of the aforementioned complications.

A topic that deserves further investigation is the effect of the zeta potential of Ag NPs and Ag NCs on their antibacterial activities. Capping ligands which provide surface charge and stability to Ag NPs also play an important role in their use as antimicrobial agents [335]. This was exemplified in a study of *Enteroccocus faecalis* that were incubated with chlorhexidine (control), neutral, negative and positively charged Ag NPs (size 10 nm). The results showed that that positively charged Ag NPs were more toxic to *E. faecalis* (>10^6 fold) than negatively charged nanoparticles [336]. Unfortunately, experimental evidence regarding the effect of surface charge to the antibacterial properties of Ag NCs is still lacking in the literature. Furthermore, a direct comparison of surface charge between Ag NPs and Ag NCs with regard to their antimicrobial activities remains unknown. To address these issues, the project aims to prepare polyethylene glycol appended lipoic acid based ligands with different terminal functional groups (*e.g.* zwitterion, $–NH_2$, -OH, $-OCH_3$) and use them to prepare Ag NPs and Ag NCs.

Chapter 5

Ligand Synthesis and Preparation of Silver Nanomaterials as Antibacterial Agents

This chapter describes the synthesis of thioctic acid–PEG based (TA-PEG-X, X refers to the different functional groups) ligands, zwitterion–appended thioctic acid ligand, and the preparation of water-soluble silver nanoparticles (Ag NPs) and silver nanoclusters (Ag NCs). Each TA-PEG-X based ligand contains a thiotic acid head group that provides strong binding to the metallic silver surface by bidendate chelative binding; PEG moiety which provides good water dispersion stability and terminal functional group such as (-OCH_3 and NH_2). The chemical structures of these ligands are shown in **Figure 5-1.**

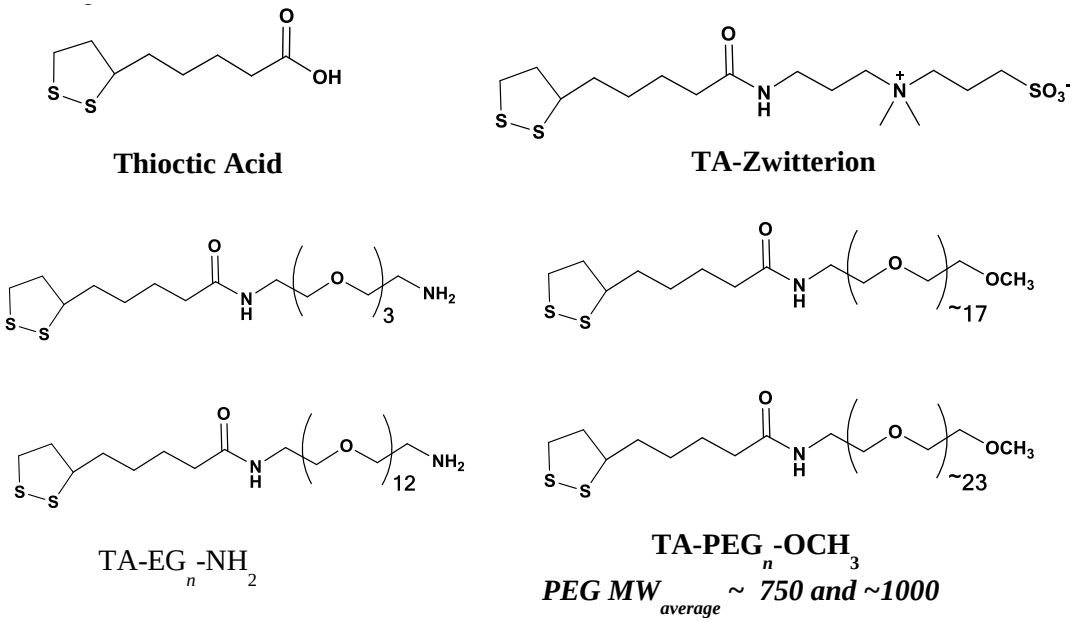

Figure 5-1. Chemical structures of thioctic acid and thioctic acid based ligands for the synthesis Ag nanomaterials. The EG and PEG refers to the uniform length and a mixture of ethylene glycol chain respectively.

These ligands were prepared and purified by following the literature procedures [337, 338] and the purity and structure of the products were confirmed by thin layer chromatography (TLC), proton nuclear magnetic resonance (^{1}H NMR) spectroscopy, and mass spectrometry (MS). The spectroscopic data of the ligands were found to be consistent with those reported in the literature.

Note: Undergraduate students Alexandra Gummer and Wei Ng in Dr. Dejian Zhou's group contributed to the results in this chapter. The author of this Thesis (L. Lapitan) contributed in the planning of the experiments, synthesis and purification of the ligands, preparation of the Ag nanomaterials and co-supervision of the students. The antibacterial properties (i.e. MIC experiments) of the Ag nanomaterials were carried out by Dr. Christopher Randall from Antimicrobial Research Centre, School of Molecular and Cellular Biology, University of Leeds. The silver concentration ion were determined using ICP-Ms analysis and conducted by Dr. Karen Arnes Thorne from the Faculty of Engineering, University of Leeds. The TEM imaging was carried out by Dr. Nicole Hondow and Dr. Michael Webb from the Faculty of Engineering, University of Leeds. The data presented in this chapter are taken from the undergraduate thesis of A. Gummer and W. Ng and were re-formatted by L. Lapitan to suite the explanations made in the text. The contributions of the students and collaborators were specified in the captions of relevant figures.

5.1 Materials and Methods

5.1.1 Equipment

Fluorescence and UV-Vis measurements were recorded using Cary Eclipse®Spectrofluorimeter and Varian Cary 50 Bio® Ultraviolet -Visible spectrophotometer respectively. The silver ion concentration were determined using Perkin Elmer ELAN DRC-e Inductively Coupled Plasma / Mass Spectrometry. Proton NMR (^{1}H NMR) and Mass spectrometry (MS) data were collected using BRUKER DPX400®, 400 MHz nuclear magnetic resonance spectrometer and high resolution BRUKER Maxis Impact® mass spectrometer respectively. Hydrodynamic size and zeta potential measurements of Ag nanomaterials were measured using Malvern® zetasizer-nano with BI-APD detector using a He-Ne laser at 633 nm (scattering angle: 90°, temperature, 25°C). Transmission electron microscopy (TEM) images were

taken using the FEI Titan Themis G2 300 Analytical transmission electron microscope. The specimen for TEM study was prepared by depositing a drop of the MNP solution onto a carbon-coated TEM grid. Ultrapure water (resistance >18.2 MΩ·cm) was purified by ELGA Purelab classic UVF system, was used for all experiments. Ultracentrifugation was carried out using Thermo Scientific Heraeus Fresco 21 and agarose gel electrophoresis was carried out using Bio-Rad HU6 Mini Horizontal Gel Unit.

5.1.2 Materials

Flash column chromatography using silica gel 60 A (Merck grade 9385) was used to purify the ligands. Thin layer chromatography was done on a silica gel-60 F254 on aluminium plates. Quartz cuvette was used for UV-Visible spectroscopy (1 mL, 10 mm optical path length) and fluorescence spectroscopy (0.7 mL, 10 mm optical path length). Centrifugal filtration (Amicon- Vivaspin® MW cut-off 5000 Da and 10 000 Da) was used to concentrate and purify the Ag nanomaterials.

5.1.3 Reagents

Thioctic acid (TA,>98+%), Triethylamine (>99%), Triphenylphosphine (>99%), Polyethylene glycol methyl ether (MW_{ave} ~ 750 g·mol^{-1}) and sodium hydrosulfide hydrate were purchased from Acros Organics. Silver nitrate, sodium borohydride, ammonium hydroxide, and agarose purchased from Fisher Scientific. Methanesulfonyl chloride (>99.7%), N,N-dimethyl-1,3-propanediamine (>99%), 1,3-propanesultone (>99%), sodium azide (>99.5%), dicyclohexylcarbodiimide (DCC,>99%), dimethylaminopyridine (DMAP, >99%), anhydrous magnesium sulphate (>99%), Methanol (>99.9%), potassium hydroxide, ethyl acetate (>99.0%), methylene chloride (>98%) sodium bicarbonate (>99.5%), Rhodamine 6G, chloroform-d (99.8%), and sodium carbonate (>99.5%) were purchased from Sigma-Aldrich. Hydrochloric acid, dichloromethane, chloroform and methanol are analytical grade and were purchased from VWR Chemicals. Amino polyethylene glycol methyl ether (H_3CO-$PEG_{\sim 23}$-NH_2) (MW ~1000 g·mol^{-1}) was purchased from Alfa Aesar and Azido dodcylethylene glycol amine (N_3-EG_{12}-NH_2) and triethylene glycol amine (N_3-EG_3-NH_2) were purchased from Polypure Inc.

5.2 Ligand Synthesis

5.2.1 Synthesis and Spectroscopic Analysis of TA-PEG$_{\sim 17}$-OCH$_3$

The chemical structures and synthetic route for the synthesis of TA-PEG$_{\sim 17}$-OCH$_3$ are shown in

Scheme 5-1. The starting material is a mixture of polyethylene glycol methyl ether with an average molecular weight of 750 g·mol^{-1}. This PEG molecular weight corresponds to ~ 17 ethylene glycol units.

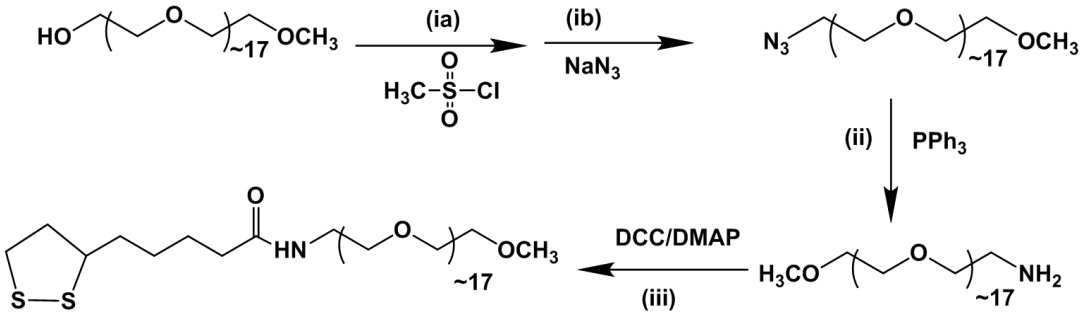

Scheme 5-1. The synthetic route to TA-PEG$_{17}$-OMe. The reaction conditions are: (ia) MsCl, Et$_3$N, THF; (ib) NaN$_3$, NaHCO$_3$, H$_2$O; (ii) PPh$_3$, EtOAc and 1 M HCl; (iii) thioctic acid, DCC/DMAP, CH$_2$Cl$_2$.

5.2.1.1 Synthesis of H$_3$CO-PEG$_n$-N$_3$ (n ~17)

Polyethylene glycol methyl ether (MW ~750 g·mol^{-1}) (37.5 g, 50 mmol), dry THF (150 mL) and methanesulfonyl chloride (11.45 g, 100 mmol) were added in a 500 mL two-necked round bottomed flask equipped with an addition funnel, septa and a magnetic stirring bar. The reaction mixture was purged with N_2 and cooled to 0 °C in an ice bath. Triethylamine (Et_3N, 15 mL, 111 mmol) was then added dropwise to the reaction mixture through the addition funnel (total addition time ~30 min). After that, the reaction mixture was allowed to warm up gradually to room temperature (~20 °C) and stirred for 12 hrs. The product was checked by TCL on silica gel with $CHCl_3$:MeOH = 10:1 (vol/vol) as elution solvent, $R_{f\,(MsO–PEG17–OMe)}$ = 0.65, $R_{f\,(HO–PEG\sim17–OMe)}$ = 0.35. The mixture was then diluted with H_2O (50 mL) and $NaHCO_3$ (3.125 g, 37 mmol) was added. The mixture was transferred to a separatory funnel and extracted with $CHCl_3$

(60 mL × 3). The combined organic layer was concentrated on a rotary evaporator, yielding slightly yellowish oil, 40 g (48.3 mmol) and 96.6% yield. The product (40 g), sodium azide (7.75 g, 120 mmol), THF (50 mL), H_2O (50 mL) and $NaHCO_3$ (3.125 g, 37 mmol) were then added to 500 mL two-necked round-bottomed flask equipped with a distilling head with a round-bottomed flask as a solvent trap. The solvent trap was cooled with an ice-bath. The biphasic reaction mixture was heated under N_2 to distill off the THF. The reaction mixture was then refluxed for ~12 hrs. After the reaction mixture was cooled to room temperature, it was transferred to a separation funnel and extracted with $CHCl_3$ (100 mL × 5). The product was checked with TCL using $CHCl_3$: MeOH =10:1 (vol/vol) as elution solvent, $R_{f\ (N3\text{-}PEG\sim17\text{-}OMe)}$ = 0.75. The combined organic layers were dried over $MgSO_4$ with stirring for 30 minutes. The $MgSO_4$ was filtered and the combined organic layer was concentrated on a rotary evaporator. A pale brown oil (24.93g, yield: 66.7%) was obtained and its ^1H NMR was shown in **Figure 5-2.** $H_3CO\text{-}PEG_n\text{-}N_3$: 1H NMR (400 MHz, δppm): 7.27 ($CDCl_3$ solvent peak); 3.65-3.60 (m, -C**H**$_2$- in repeated EG groups, 4), 3.56-3.52 (t, 2H, J = 4.8, -C**H**$_2$-OCH_3, 2), 3.38 (s, –OC**H**$_3$-, 3H, 1), 2.85-2.87 (t, 2H, J = 4.8 Hz,-C**H**$_2$-N_3,3).

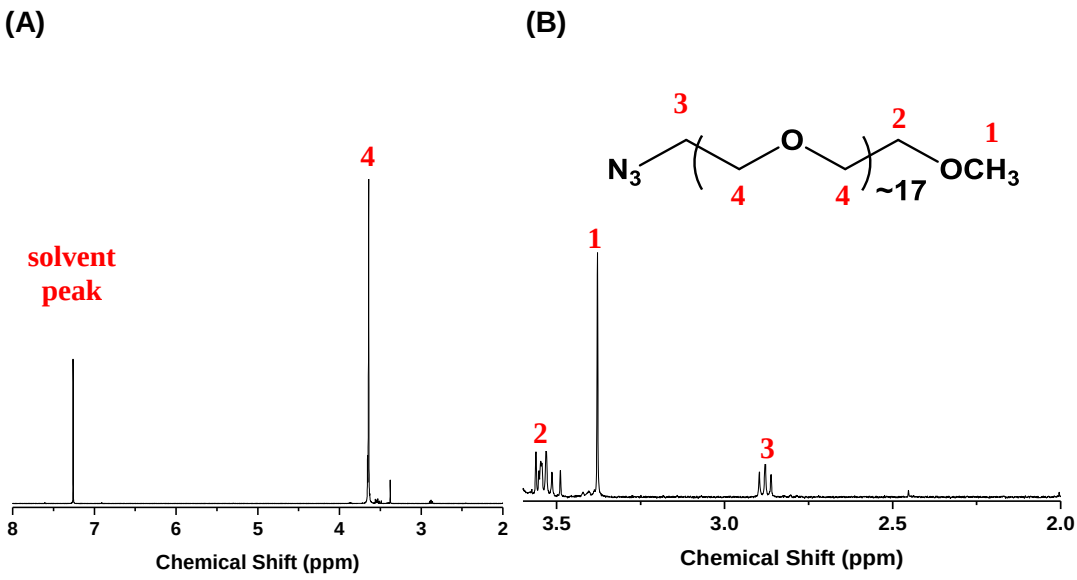

Figure 5-2. (A) The ^1H NMR spectrum of $H_3CO\text{-}PEG_n\text{-}N_3$ from 2.0-8.0 ppm. (B) Enlarged ^1H NMR spectrum from 2.0 to 3.70 ppm.

The chemical structure of $H_3CO\text{-}PEG_n\text{-}N_3$ was further characterized using high resolution mass spectrometry. The chromatogram of the purified compound is shown **Figure 5-3 (A)**. The general molecular formula used to calculate the MW peaks [MW+Na^+] of $H_3CO\text{-}PEG_n\text{-}N_3$ is shown in **Figure 5-3 (B)**. The mass spectra of $H_3CO\text{-}PEG_n\text{-}N_3$ and the assignment of the corresponding EG chain length for each molecular ion peak is shown in **Figure 5-3 (C).**

(A)

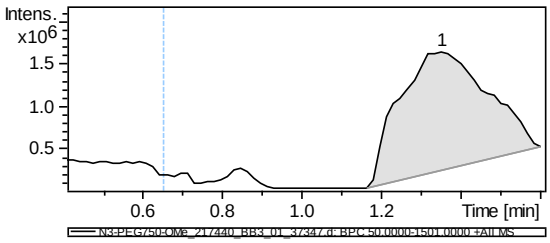

(B)

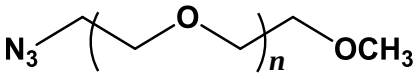

$$MW = 124 + 44n\ (M + Na^+)$$

(C)

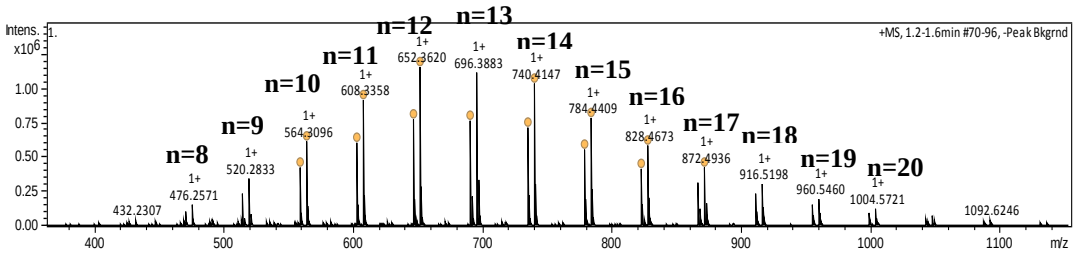

Figure 5-3 (A) Chromatogram of $N_3\text{-}PEG_n\text{-}OCH_3$ (PEG MW ~750 g·mol^{-1}). (B) The structural and molecular weight equation used to estimate for the ethylene glycol chain lengths. (C) Accurate mass spectra of $H_3CO\text{-}PEG_n\text{-}N_3$. The ion peaks are reported as (M+Na^+) abduction and the corresponding ethylene glycol chains (*n*) lengths were assigned to each molecular ion peak.

The mass error in ppm was calculated using the formula [339]:

$$error\ (ppm) = \frac{m_i - m_a}{m_a}\ x\ 10^6 \qquad \textbf{Equation 5-1}$$

Where m_i and m_a refers to the measured accurate mass (experimentally observed m/z) and monoisotopic calculated exact mass (theoretical m/z) respectively. The m_a was determined by summing the masses of the individual isotopes for a given ion. The molecular formula for $H_3CO\text{-}PEG_n\text{-}N_3$ with 13 PEG units and a sodium atom is $C_{29}H_{59}N_3O_{14}Na$. Therefore, the measured accurate mass (from the mass spectra) and monoisotopic calculated exact mass are 696.3833 and 696.3900 respectively. The mass error in ppm = -9.62. The same calculation can be carried out to calculate the mass error of an assignment with the other mass spectral peaks in **Figure 5-3 (C).**

5.2.1.2 Synthesis of $H_3CO\text{-}PEG_n\text{-}NH_2$ (n ~17)

N_3–$PEG_{\sim 17}$–OCH_3 (8.0 g, ~10 mmol), EtOAc (150 mL) and 1 M HCl (25 mL, 25 mmol) were added into a 500 mL two-necked round-bottomed flask equipped with an addition funnel, septa and a magnetic stirring bar. Triphenylphosphine (2.8 g, ~10 mmol) dissolved in 100 mL EtOAc was transferred to the addition funnel. The reaction vessel was purged with N_2 and cooled to 0 °C in an ice-bath while stirring. The triphenylphosphine solution was then added dropwise under N_2. The temperature was maintained to below 5 °C with an ice bath during the addition. Once the addition was complete, the reaction mixture was gradually warmed up to room temperature and stirred overnight under N_2. The reaction mixture was then transferred to a separatory funnel and the biphasic solution was separated. The aqueous layer was collected and washed with EtOAc (100 mL × 2) to remove the formed triphenyl-phosphine oxide byproduct. The aqueous layer was transferred to a round bottom flask and cooled in an ice bath. KOH (13.5 g) was added slowly to the aqueous solution under magnetic stirring to adjust its pH to basic (pH > 10). The aqueous solution was transferred into a separatory funnel and extracted with $CHCl_3$ (60 mL × 5). The combined organic layer was dried over $MgSO_4$ for 30 mins. The $MgSO_4$ was filtered and the solvent was removed on a rotary evaporator. A light yellow oil was obtained, 4.58 g, yield: 59.2%. R_fs ($CHCl_3$:MeOH = 10:1, vol/vol) for $R_{f\ (N3\text{-}PEG17\text{-}OMe)}$ =

0.75, $R_{f\ (NH2\text{-}PEG17\text{-}OMe)}$ = 0.25. The chemical structure of OCH_3-PEG_n-NH_2 was determined by ^{1}H NMR as shown in **Figure 5-4.** H_3CO-PEG_n-NH_2 : ^{1}H NMR (400 MHz, δppm): 7.27 ($CDCl_3$ solvent peak); 3.65-3.60 (m, -CH_2- in repeated EG groups, 4), 3.56-3.52 (t, 2H, *J* = 4.8, -C**H**$_2$-OCH_3, 2), 3.38 (s, –OC**H**$_3$-, 3H, 1), 3.10 (t, 2H, *J* = 4.8, -C**H**$_2$-NH_2,3), 1.61 (2H, broad s, -N**H**$_2$, 5).

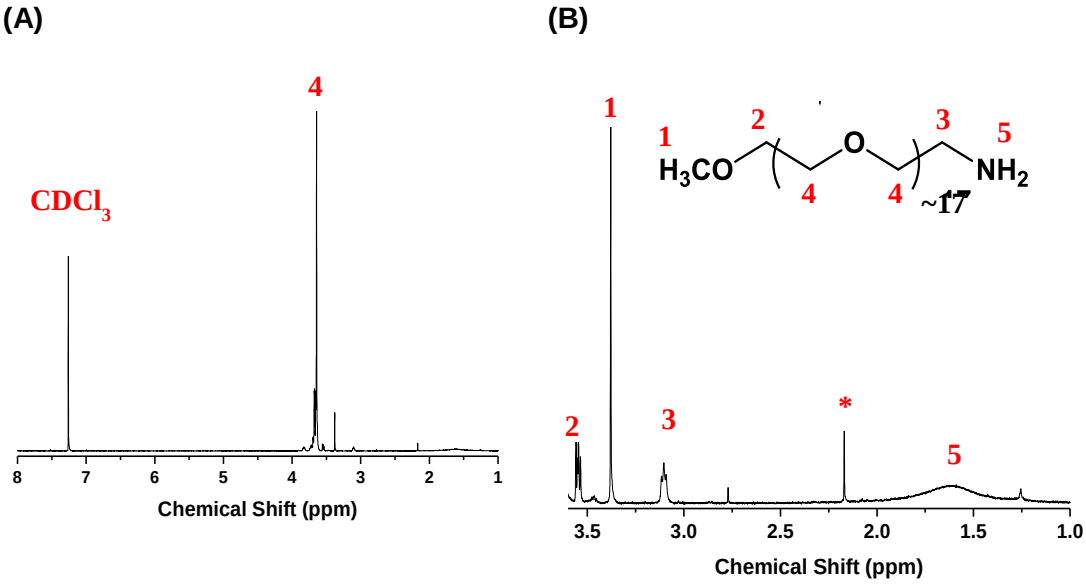

Figure 5-4. (A) The ^{1}H NMR spectrum of H_3CO-PEG_n-NH_2 from 1.0-8.0 ppm and (B) Enlarged ^{1}H NMR spectrum from 1.0 to 3.55 ppm. Impurity peak (*) at 2.17 ppm.

The chemical structure of H_3CO-PEG_n-NH_2 ligand was further characterized using mass spectrometry. The chromatogram of the purified compound is shown **Figure 5-5 (A)**. The general molecular formula used to calculate for the MW peaks [MW + Na^+] for H_3CO-PEG_n-NH_2 is shown in **Figure 5-5 (B)**. The mass spectra of H_3CO-PEG_n-NH_2 and the assignment of the corresponding EG chain length for each molecular ion peak is shown in **Figure 5-5 (C).**

The molecular formula for OCH_3-PEG_n-NH_2 with 17 EG units and proton is $C_{37}H_{78}N_1O_{18}$. Therefore, the measured accurate mass (from the mass spectra) and monoisotopic calculated exact mass are 824.5267 and 824.5224 respectively. The mass error in ppm = 5.22. The same calculation can be carried out to estimate the mass error of an assignment with the other mass spectral peaks in **Figure 5-5 (C).**

(A) **(B)**

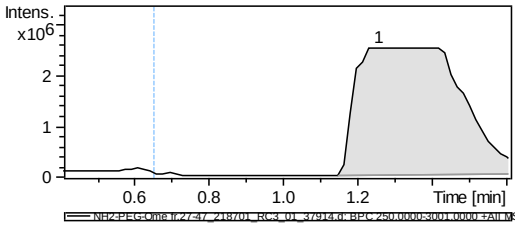

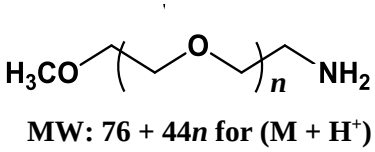

MW: 76 + 44*n* for (M + H$^+$)

(C)

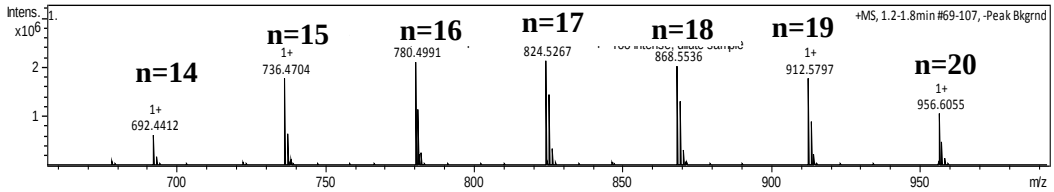

Figure 5-5. (A) Chromatogram of OCH_3-PEG_n-NH_2 (PEG MW ~750 g·mol^{-1}). (B) The structural and molecular weight equation used to compute for the ethylene glycol chain lengths. (C) Accurate mass spectra of H_3CO-PEG_n-NH_2. The ion peaks are reported as proton (M+H$^+$) abduction and the corresponding ethylene glycol chains (*n*) lengths were assigned to each molecular ion peak.

5.2.1.3 Synthesis of TA-PEG_n-OCH_3 (n = ~17)

NH_2-PEG~$_{17}$-OCH_3 (3.75 g, ~5.0 mmol), 4-(N,N-dimethylamino)pyridine (0.12 g, ~1.0 mmol), N,N'-dicyclohexylcarbodiimide (1.06 g, ~5.0 mmol) and CH_2Cl_2 (80 mL) were added into a 250 mL round-bottomed flask equipped with a magnetic stirring bar and an addition funnel. The mixture was kept at 0 °C in an ice bath. Thioctic acid (1.03 g, ~5.0 mmol) dissolved in 30 mL of CH_2Cl_2 was added dropwise using an addition funnel over 30 min under N_2 while stirring. The mixture was allowed to stir at 0 for 1 hr and was allowed to warm up to room temperature and stirred overnight. The mixture was then filtered off through celite and the celite plug was rinsed with $CHCl_3$. The solvent was then evaporated on a rotary evaporator, and the residue was added with saturated $NaHCO_3$, The aqueous mixture was extracted with ether (100 mL x 2). The aqueous layer was transferred to a separate funnel, and extracted with CH_2Cl_2 (100 mL x 2). The combined organic layer was dried over $MgSO_4$. The solvent was

evaporated on a rotary evaporator a yellow solid was obtained, weight 2.30 g, yield: 48.4%. TLC analysis ($CHCl_3$: MeOH=10: 1 (vol/vol) as elution) results, $R_{f\ (TA\text{-}PEG17\text{-}OMe)}$ = ~0.6, whereas $R_{f\ (NH2\text{-}PEG17\text{-}OMe)}$ = 0.25. The ^1H NMR spectra of TA-PEG_n-NH_2 is shown in **Figure 5-6.** H_3CO-PEG_n-TA: ^1H NMR (400 MHz, δppm): 7.27 ($CDCl_3$ solvent peak); 6.11 ppm (1H, broad s, amide N**H**, 6), 3.65-3.62 (m, -C**H**$_2$- in repeated EG groups, 4), 3.60 (m, 1H, -C**H**-in the ring, 11), 3.56-3.52 (m, 2H, -C**H**$_2$-OCH_3, 2), 3.45 (t, 2H, *J* = 5.0 Hz, -NH-C**H**$_2$-, 5), 3.38 (s, –OC**H**$_3$-, 3H, 1), 3.08 - 3.11 (m, 2H, 13), 2.47 (m, 1H,-C**H**$_2$- in the ring, 12), 2.18 (t, 2H, *J* = 7.4 Hz, -C**H**$_2$-C(O), 7), 1.91 (m, 1 H, -C**H**$_2$- in the ring, 12), 1.69-1.61 (m, 4H, -C**H**$_2$-CH_2-,8,9), 1.47 (m, 2H, -C**H**$_2$-, 10).

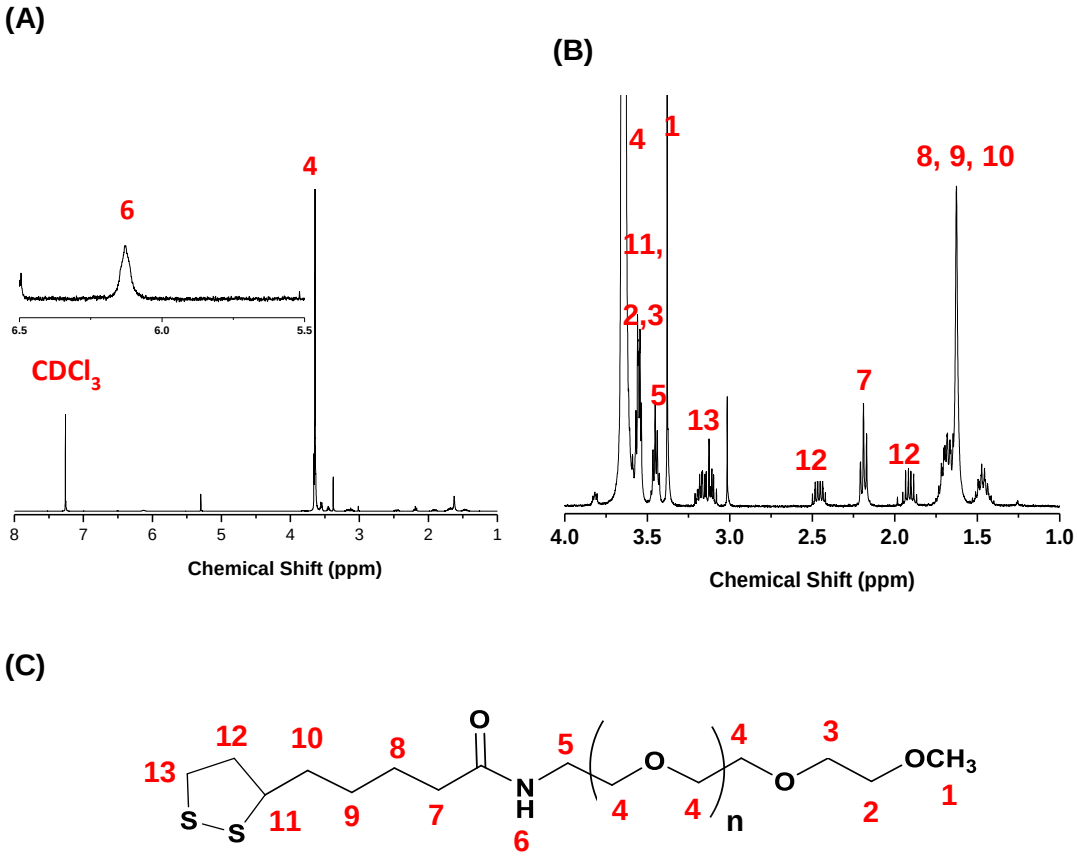

Figure 5-6. (A) The ^1H NMR spectrum of H_3CO-PEG_n-TA (n ~17) from 1.0-8.0 ppm and (B) Enlarged region from 1.0 to 4.0 ppm.

The chemical structure of TA-PEG_n-OCH_3 ligand was further confirmed by mass spectrometry. The chromatogram of the purified compound is shown Figure 5-7 **(A)**. The general molecular formula used to calculate for the MW peaks [MW + NH_4^+] for TA-PEG_n-OCH_3 in the mass spectra is shown in **Figure 5-7 (B)**. The mass spectra

of TA-PEG$_n$-OCH$_3$ and the assignment of the corresponding EG chain length for each molecular ion peak is shown in **Figure 5-7 (C).**

(A)

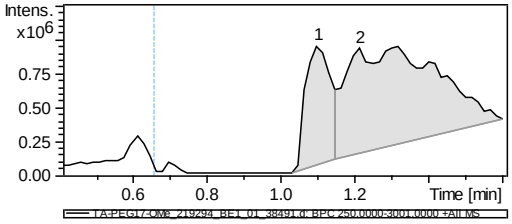

(B)

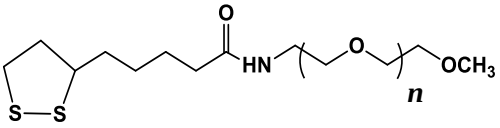

MW: 281 + 44*n* (M + NH_4^+)

250 + 44*n* (M + H^+)

(C)

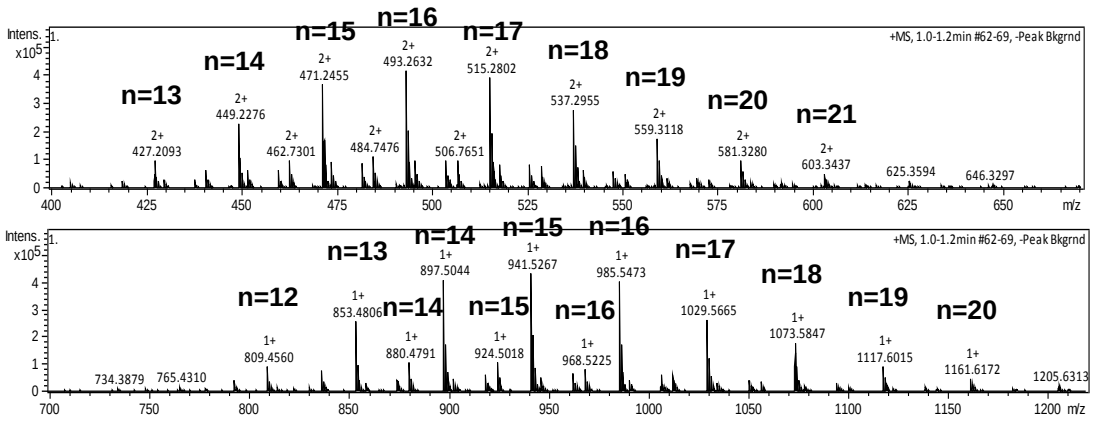

Figure 5-7. (A) Chromatogram of TA-PEG$_n$-OCH$_3$. (n~17, PEG MW ~750 g·mol^{-1}) (B) The structural and molecular weight equation used to compute for the ethylene glycol chain lengths. (C) Accurate mass spectra of TA-PEG$_n$-OCH$_3$. The ion peaks are reported as proton (M+H$^+$) and ammonium (M+NH$_4^+$) abductions and the corresponding ethylene glycol chains (*n*) lengths were assigned to each molecular ion peak.

The molecular formula for OCH_3-PEG_n-TA with 14 PEG units and a NH_4^+ ion is $C_{39}H_{81}N_2O_{16}S_2$. Therefore, the measured accurate mass (from the mass spectra) and monoisotopic calculated exact mass are 897.5044 and 897.5032 respectively. The mass error in ppm = 1.33. The same calculation can be carried out to estimate the mass error of an assignment with the other mass spectral peaks in **Figure 5-7 (C).**

5.2.2 Synthesis and Spectroscopic Analysis of TA-PEG_n-OCH_3 (n = ~22)

Monomethoxy polyethylene glycol amine (MW_{ave} ~ 1000 g·mol^{-1}) (2.43 g, 2.43 mmol), 4-N,N-dimethylaminopyridine (0.051g, 0.413 mmol), N,N'-dicyclohexylcarbodiimide (0.601 g, 2.92 mmol) were dissolved in 8 mL of dry CH_2Cl_2. The mixture was cooled to 0°C in an ice bath and under N_2 gas. Thioctic acid (0.500 g, 2.43 mmol) dissolved in 2 mL dry CH_2Cl_2 was slowly added over a 20 minute period. The reaction mixture was stirred at 0°C for 1 hour before being allowed to gradually warm up to room temperature (27°C in oil bath) and stirred for 24 hours. The reaction mixture was filtered and the solvent was evaporated in vacuum giving an oily yellow substance. The by-products were first eluted by using 1:15 (v/v) methanol/chloroform, then the desired products were eluted by using 1:10 (v/v) methanol/chloroform. The reaction yield was ~33%. **Figure 5-8** shows the ^{1}H NMR spectra for TA-PEG_n-OCH_3.

H_3CO-PEG_n-TA: ^{1}H NMR (400 MHz, δppm): 7.27 ($CDCl_3$ solvent peak); 6.11 ppm (1H, broad s, amide NH-, 6), 3.65-3.62 (m, -C**H**$_2$- in repeated EG groups, 4), 3.60 (m, 1H, -C**H**-in the ring, 11), 3.56-3.52 (m, 2**H**, -CH_2-OCH_3, 2), 3.45 (t, 2H, *J* = 5.0 Hz, -NH-C**H**$_2$-, 5), 3.38 (s, –OC**H**$_3$-, 3H, 1), 3.08 - 3.12 (m, 2H, 13), 2.47-2.50 (m, 1H,-C**H**$_2$- in ring, 12), 2.18 (t, 2H, *J* = 7.4 Hz, -C**H**$_2$-C(O), 7), 1.91 (m, 1 H, -C**H**$_2$- in ring, 12), 1.69-1.61 (m, 4H, -C**H**$_2$-C**H**$_2$- 8,9), 1.49 (m, 2H, -C**H**$_2$-, 10).

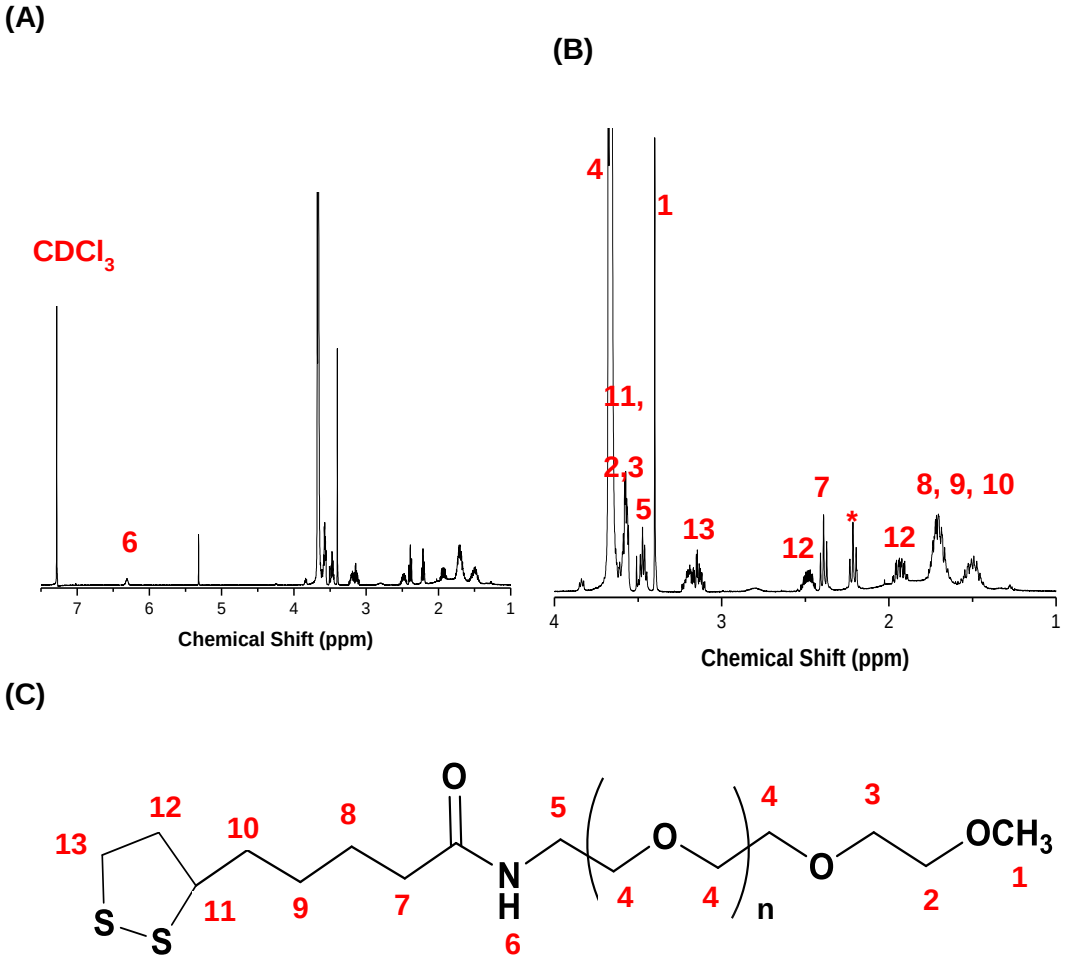

Figure 5-8. The ^{1}H NMR spectrum of H_3CO-PEG_n-TA from 1.0-7.5 ppm and (B) Enlarged region from 1.0 to 4.0 ppm. The data were collected by W. Ng in Dr. Zhou's group. Reproduced from W. Ng's BSc thesis (2015).

The chemical structure of TA-PEG_n-OCH_3 ligand was further characterized using mass spectrometry. The chromatogram of the purified compound is shown **Figure 5-9 (A)**. The general molecular formula used to calculate the MW peaks [MW + Na^+] for TA-PEG_n-OCH_3 is shown in **Figure 5-9 (B)**. The mass spectra and the assignment of the corresponding EG chain length for each molecular ion peak are shown in **Figure 5-9 (C).**

The molecular formula for OCH_3-PEG_n-TA with 17 PEG units and Na^+ ion is $C_{45}H_{89}N_1O_{19}S_2Na_1$. Therefore, the measured accurate mass (from the mass spectra) and monoisotopic calculated exact mass are 1034.5357 and 1034.5373 respectively.

The mass error in ppm = -1.54. The same calculation can be carried out to estimate the mass error of an assignment with the other mass spectral peaks in **Figure 5-9 (C).**

(A) **(B)**

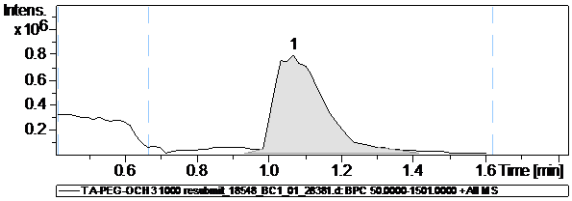

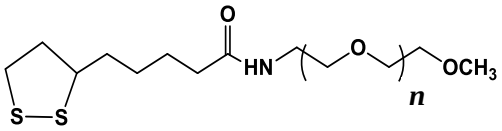

MW: 286 + 44*n* for (M + Na^+)

(C)

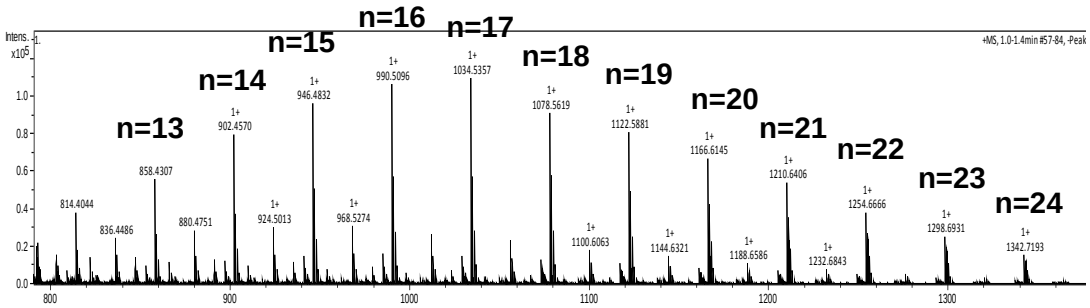

Figure 5-9. (A) Chromatogram of TA-PEG_n-OCH_3 (PEG MW ~1000 g·mol^{-1}). (B) The structural and molecular weight equation used to compute for the ethylene glycol chain lengths. (C) Accurate mass spectra of TA-PEG_n-OCH_3. The ion peaks are reported as sodium (M + Na^+) abductions and the corresponding ethylene glycol chains (*n*) lengths were assigned to each molecular ion peak. The data were collected by W. Ng in Dr. Zhou's group. Reproduced from W. Ng's BSc thesis (2015).

5.2.3 Synthesis and Spectroscopic Analysis of TA-EG_n-NH_2 (n = 3, 12)

The synthesis of TA-PEG_n-NH_2 (n=3,12) is a two-step reaction involving amide coupling of thioctic acid and amino-polyethylene glycol azide. The second reaction

involves the reduction of the azide to amine. The chemical structure and synthetic steps to TA-PEG$_n$-NH$_2$ is shown in **Scheme 5-2**.

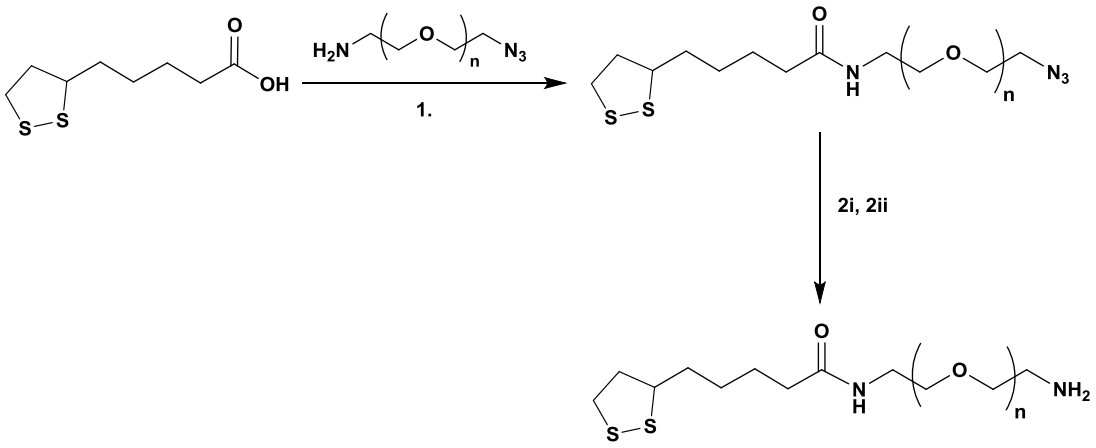

Scheme 5-2. The synthetic route TA-EG$_n$-NH$_2$. The reaction conditions are, (i) DCC/DMAP, CH$_2$Cl$_2$, (2i) PPh$_3$, dry THF, 27^{o}C, 3 hrs, and (2ii) H$_2$O work-up, 27^{o}C, 48 hrs.

5.2.3.1 Synthesis of TA-EG$_3$-N$_3$

Azido tri(ethylene glycol) amine (N$_3$-EG$_3$-NH$_2$) (1.00 g, 4.58 mmol), 4-N,N-dimethyl-aminopyridine (0.0895 g), N,N'-dicyclohexylcarbodiimide (1.0395 g, 5.04 mmol) were dissolved in 10 mL of dry CH$_2$Cl$_2$. The mixture was cooled to 0°C in an ice bath under dry conditions through purging N$_2$. Thioctic acid (0.950 g, 4.60 mmol), which was dissolved in 2 mL dry CH$_2$Cl$_2$ was slowly added over a 20 minutes under nitrogen gas atmosphere. The reaction mixture was then stirred at 0°C for 1 hour before being allowed to gradually warm up to room temperature (27^{o}C) and stirred for a further 24 hours. The reaction mixture was then filtered and the solvent was removed in vacuum yielding yellowish oil. This crude product was purified via silica gel column chromatography using CH$_2$Cl$_2$: CH$_3$OH (15:1 v/v) as eluting solvent. The product was a yellow oil, 1.48 g, yield ~ 80 %. ESI-MS (EI$^+$) calculated for C$_{16}$H$_{31}$N$_4$O$_4$S$_2$ (M+H$^+$) = 407.18; found *m/z* = 407.17 (M+H$^+$), mass error (ppm) = -24.5.

5.2.3.2 Synthesis of TA-EG$_3$-NH$_2$

TA-EG$_3$-N$_3$ (1.482 g, 3.65 mmol) and triphenylphosphine (1.91 g, 7.3 mmol) were dissolved in 20 mL of dry THF in a round bottom flask and stirred at room temperature for 1 hour under N_2. A 0.33 mL of de-gassed H_2O (36.4 mmol) was added and stirred at room temperature for 20 hrs. The solvent was removed by rotary evaporation and purified by column chromatography. The by-products were first eluted out of the column using 1:9 (v/v) MeOH: $CHCl_3$. The desired product was then eluted out of the column by using a 3:7 (v/v) MeOH: $CHCl_3$. The fractions were combined and the solvent was removed on a rotary evaporator. A yellow oil was obtained with 0. 91 g and yield ~ 66%. **Figure 5-10** shows the ^{1}H NMR of TA-PEG$_3$-NH$_2$.

TA-PEG$_3$-NH$_2$: ^{1}H NMR (400 MHz, δppm): 7.27 ($CDCl_3$ solvent peak); 6.78 (broad s, 1H, amide N**H**, 6), 3.69-3.60 (m, 14H, m, -C**H**$_2$- in repeated EG groups,4), 3.57-3.51 (m, 2H,-O-C**H**$_2$-, 3), 3.46-3.41 (m, 2H, -C**H**$_2$- next to amide NH, 5), 3.21-3.08 (m, 2H, -C**H**$_2$- in ring,13), 2.90-2.85 (m, 2H, -C**H**$_2$- next to NH_2, 2), 2.81 (br , 2H, N**H**$_2$, 1), 2.41 (m, 1H, -C**H**$_2$- in the ring, 12), 2.24-2.16 (m, 2H, -C**H**$_2$-C=O,7), 1.74-1.56 (m, 4H, -C**H**$_2$-C**H**$_2$-8,9), 1.51-1.39 (m,2H, -C**H**$_2$-, 10). ESI-MS (EI$^+$) calculated for $C_{16}H_{33}N_2O_4S_2$ (M+H$^+$) = 381.19; found *m/z* = 381.17 (M+H$^+$); mass error (ppm) = -52.4.

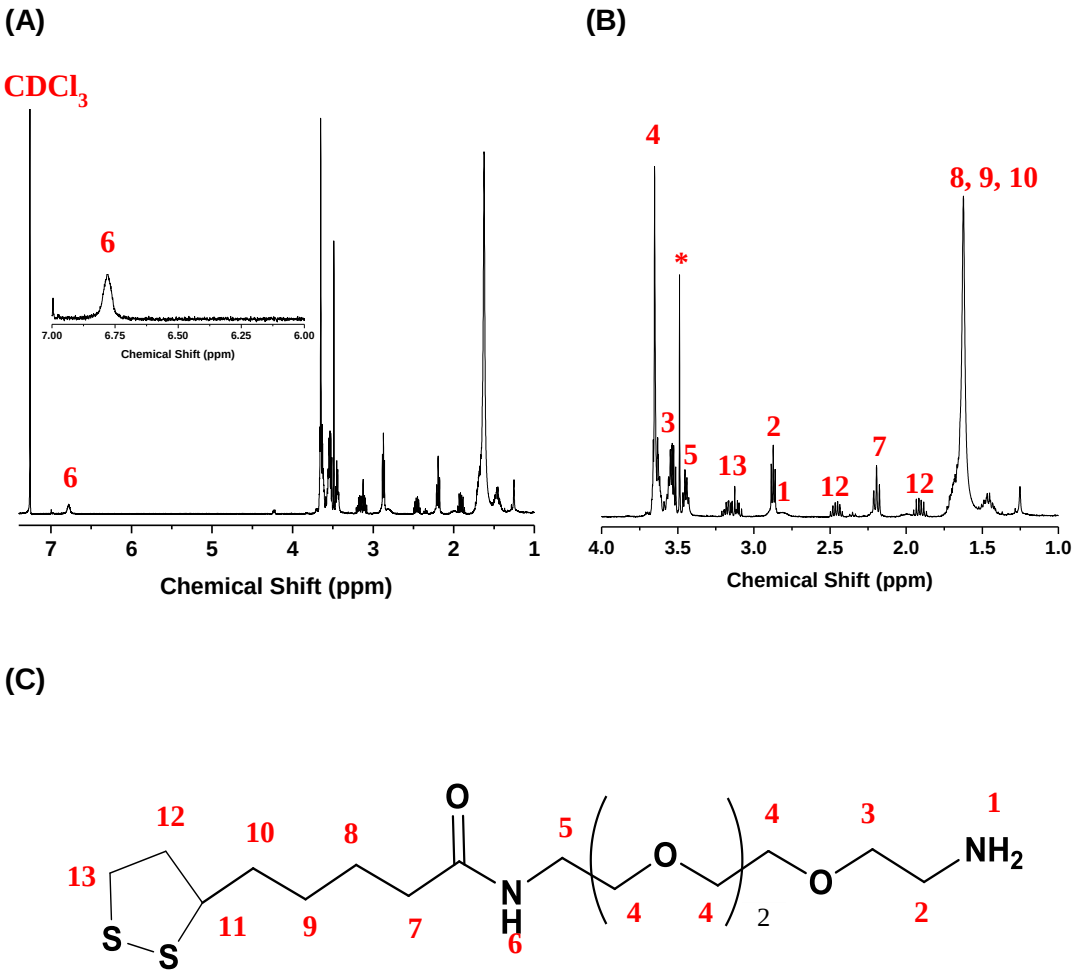

Figure 5-10 (A) The ^{1}H NMR spectrum of TA-PEG$_3$-NH$_2$ from 1.0-7.5 ppm. (B) Enlarged ^{1}H NMR spectrum from 1.0 to 4.0 ppm. The (*) denotes a MeOH impurity peak. The data were collected by A. Gummer in Dr. Zhou's group. Reproduced from A. Gummer's BSc thesis (2016).

5.2.3.3 Synthesis of TA-EG$_{12}$-N$_3$

Azido dodcylethylene glycol amine (N$_3$-EG$_{12}$-NH$_2$) (1.8 g, ~3 mmol), 4-N,N-dimethylaminopyridine (0.064 g, 0.5mmol), N,N'-dicyclohexylcarbodiimide (0.752 g, 3.65mmol) were mixed and dissolved with 10mL of dry DCM in a three-necked bottom flask. The mixture was left to stir in an ice bath under N$_2$ gas. Thioctic acid (0.65 g, ~3 mmol) dissolved in 2 mL of dry DCM was added slowly through a syringe over 20 minutes under N$_2$ gas. After the addition of thioctic acid, the mixture was left

to stir a further 1 hour at 0°C before warming up gradually to room temperature to be left to stir for 24 hours. The insoluble solid was washed with $CHCl_3$. The combined filtrate and washing solution was evaporated to dryness using a rotary evaporator, yielding the crude product as a yellow oil. The crude product was purified by using silica gel column chromatography using 1:10 (v/v) MeOH: $CHCl_3$ as eluting solvent. The solvent was removed in a rotary evaporator yielding yellow oil, 2.2878 g, yield ~ 93%. ESI-MS (EI^+) calculated for $C_{32}H_{62}N_4O_{12}S_2$ ($M+Na^+$) = 781.3708; found *m/z* = 781.3724 ($M+Na^+$); mass error (ppm) = 2.04.

5.2.3.4 Synthesis of TA-EG_{12}-NH_2

TA-EG_{12}-N_3 (2.3 g, ~3 mmol) and triphenylphosphine (1 g, ~4 mmol) was dissolved in 20 mL of anhydrous THF in a round bottom flask. The mixture was stirred at room temperature for 1 hour under N_2 gas. 1.410 mL of degassed H_2O was added to the mixture and stirred in room temperature for 24 hours. The by-products were first eluted out using 1:6 (v/v) MeOH: $CHCl_3$. Then, the desired product was eluted out using 10:10:1 (v/v) MeOH: $CHCl_3$:NH_4OH. The solvent was removed in a rotary evaporator yielding a yellow oil, 1.2455 g, yield ~56%. The chemical structure of TA-EG_{12}-NH_2 was determined using ^1H NMR spectra shown in **Figure 5-11**.

TA-EG_{12}-NH_2: ^1H NMR (400 MHz, δppm): 7.27 ($CDCl_3$ solvent peak); 6.11 ppm (broad s, 1H, amide NH-, 6), 3.70-3.64 (m, -C**H**$_2$- in repeated EG groups, 4), 3.61 (m, 1H, -C**H**- in the ring, 11), 3.51-3.49 (m, 2H, -O-C**H**$_2$-, 3), 3.45 (m, 2H, -C**H**$_2$- next to amide NH, 5), 3.08 - 3.12 (m, 2H, -C**H**$_2$- in ring,13), 2.90-2.87 (m, 2H,-C**H**$_2$- next to NH_2, 2), 2.70-2.65 (broad s, 2H, N**H**$_2$, 1), 2.49-2.42 (m, 1H, -C**H**$_2$- in the ring, 12), 2.18-2.27 (m, 2H, -C**H**$_2$-C=O, 7), 1.91-1.86 (m, 1 H, -C**H**$_2$- in the ring, 12), 1.80-1.61 (m, 4H, -C**H**$_2$-C**H**$_2$- 8,9), 1.49 (m, 2H, -C**H**$_2$-,10). ESI-MS (EI^+) calculated for $C_{32}H_{65}N_2O_{12}S_2$ ($M+H^+$) = 733.39; found *m/z* = 733.38 ($M+H^+$); mass error (ppm) = -13.63.

(A)

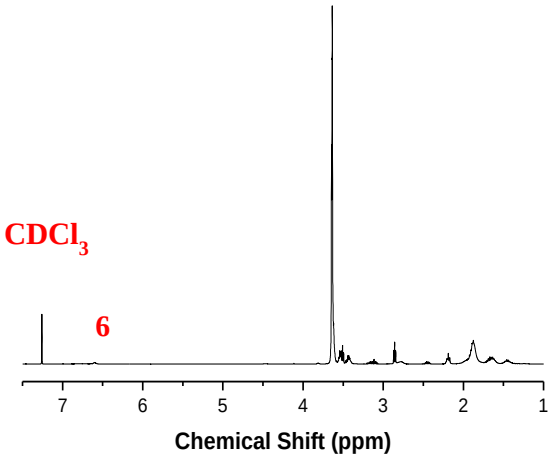

(B)

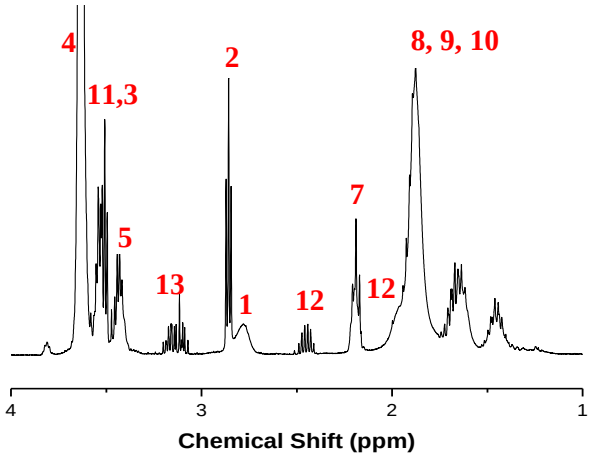

(C)

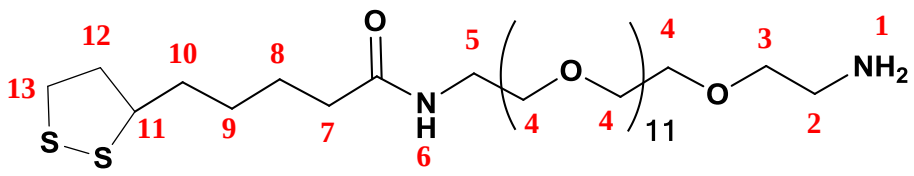

Figure 5-11. The ^{1}H NMR spectrum of NH_2-EG_{12}-TA from 1.0-7.5 ppm and (B) enlarged region from 1.0 to 4.0 ppm. The data were collected by W. Ng in Dr. Zhou's group. Reproduced from W. Ng's BSc thesis (2017).

5.2.4 Synthesis and Spectroscopic Analysis of TA-Zwitterion

Scheme 5-3 shows the chemical structures and synthetic strategies of the zwitterion appended thioctic acid.

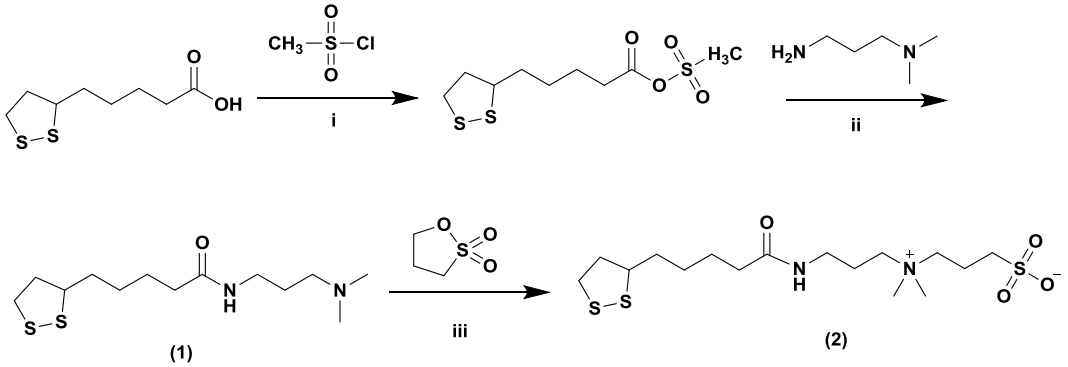

Scheme 5-3. The synthetic route to TA-Zwitterion. Reaction conditions are: i) Et_3N, dry CH_2Cl_2, MsCl, (ii) N,N-dimethyl-1,3-propanediamine, and (iii) $CHCl_3$, H_2O, 1,3-propanesultone.

5.2.4.1 Synthesis of Thioctic acid-N,N-Dimethyl-1, 3-propanediamine

Thioctic acid (3g, ~15 mmol), trimethylamine (1.47 g, ~15 mmol) and dichloro-methane (30 mL) were added in a three-necked round bottom flask. The mixture was cooled to 0°C with an ice bath and stirred under N_2 gas for 30 minutes. Methanesulfonyl chloride (1.67 g, ~15 mmol) was added dropwise by using a syringe. The mixture was stirred for a further 5 hours and then gradually warmed up to room temperature (25-27°C in oil bath). Triethylamine (0.61 g, ~6 mmol) and 20 mL of CH_2Cl_2 were added slowly into the mixture, which was left to stir overnight at room temperature under N_2 gas. The reaction mixture was washed twice with 30 mL of water in a separatory funnel followed by 100 mL of saturated Na_2CO_3 solution. The organic layer was dried using Na_2SO_4 and the solvent was removed in a rotary evaporator. The compound, N,N-dimethyl-1,3-propanediamine was obtained as a yellow oil, 1.83 g, yield ~43%. Its chemical structure was confirmed by ^{1}H NMR (**Figure 5-12).** N,N-dimethyl-1,3-propanediamine: ^{1}H NMR (400 MHz, δppm): 7.27 ($CDCl_3$ solvent peak); ^{1}H NMR assignment (400 MHz, $CDCl_3$): σ (ppm), ^{1}H NMR (400 MHz, $CDCl_3$): δ (ppm): 6.91 (broad s, 1H, amide N**H**, 5), 3.55 (m, 1H, -C**H**- in the ring, 10), 3.32 (m, 2H, -NH-C**H**$_2$- 4), 3.21 - 3.10 (m, 2H, -C**H**$_2$- in the ring,12), 2.49-2.45 (m, 1H, -C**H**$_2$- in the ring, 11), 2.37 (t, 2H, *J*=6 Hz, -C**H**$_2$-C(O), 6), 2.23 (s, 6H, -N-

($C\mathbf{H}_3)_2$,1), 2.17-2.13 (t, 2H, *J* = 6Hz, -$C\mathbf{H}_2$-N-,2), 1.90-1.83 (m, 1H, -$C\mathbf{H}_2$- in the ring, 11), 1.77 (m, 2H –$C\mathbf{H}_2$-,3), 1.72-1.62 (m, 4H,-$C\mathbf{H}_2$-$C\mathbf{H}_2$-, 7,8), 1.51-1.42 (m, 2H, -$C\mathbf{H}_2$-,9). ESI-MS (EI^+) calculated for $C_{13}H_{27}N_2OS_2$ ($M+H^+$) = 291.1564; found m/z = 291.1548 ($M+H^+$); mass error (ppm) = -5.49.

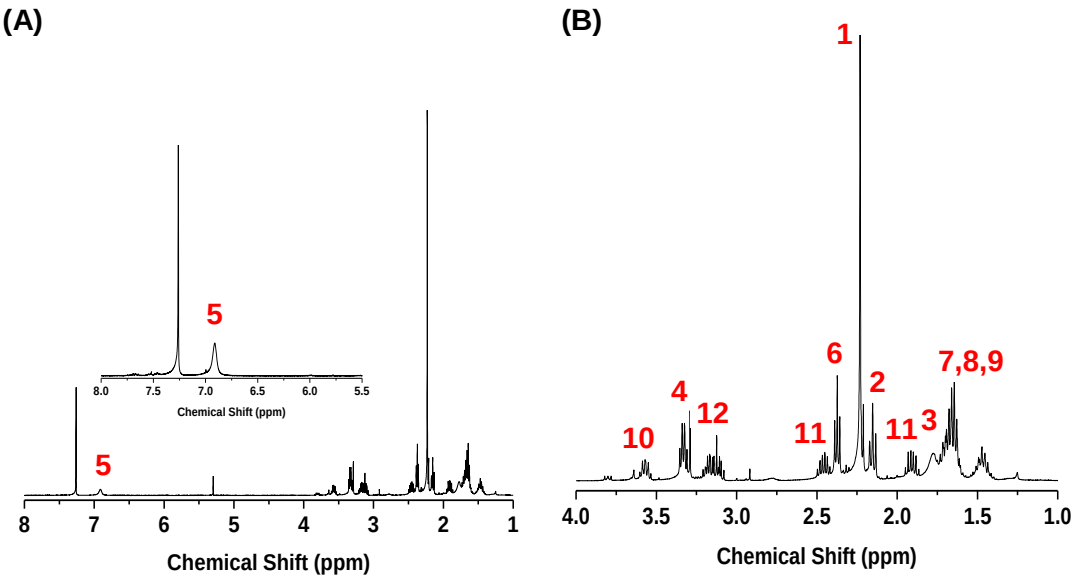

(C)

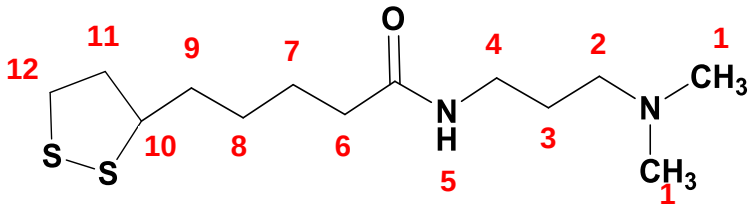

Figure 5-12. (A) The ^{1}H NMR spectrum of TA-N,N-dimethyl-1,3-propanediamine from 1.0-8.0 ppm and (B) enlarged region from 1.0 to 4.0 ppm. The data were collected by W. Ng in Dr. Zhou's group. Reproduced from W. Ng's BSc thesis (2017).

5.2.4.2 Synthesis of TA- Zwitterion

TA-N,N-dimethyl-1,3-propanediamine (1.8259 g, ~ 6.30 mmol) was dissolved in 20 mL of dry THF and purged under N_2 gas 30 minutes. 1,3-propanesultone (1.1488 g, ~9.40 mmol) dissolved in 4 mL of THF was added and stirred for 3 days. A gradual build-up of turbidity was observed as the reaction progressed due to the limited solubility of the TA-Zwitterion in THF. The solvent was evaporated in vacuum yielding a pale yellow solid. The crude product was washed with $CHCl_3$ three times to remove any impurities followed by dying in vacuum to yield TA-Zwitterion as yellow solid in ~48 % yield. Figure 5-13 shows the ^{1}H NMR spectra for TA-Zwitterion**.**

TA-Zwitterion: ^{1}H NMR (400 MHz, δppm): 4.620 (D_2O solvent peak); 3.79-3.70 (m, 1H, -CH- in the ring 13), 3.55−3.48 (m, 2H, -CH_2-SO_3, 1), 3.42−3.38 (m, 2H, -CH_2-$N(CH_3)_2$-, 3), 3.35 − 3.31 (m, 2H, -CH_2-$N(CH_3)$2-, 5), 3.28-3.20 (m, 2H, -NH-CH_2-, 7) 3.14 (s, 6H, -N-$(CH_3)_2$, 4), 3.03-2.99 (t, 2H, J = 6Hz -CH_2-C(O), 9), 2.57-2.49 (m, 1H, -CH_2- in the ring, 14) 2.34−2.30 (t, 2H, J = 9 Hz, 15), 2.27-2.23 (m, 2H, -CH_2-CH_2-CH_2-,6) 2.07-2.03 (m, 2H, -CH_2-CH_2-CH_2, 2), 2.03 −1.94 (m, 2H, -CH_2- in ring, 14), 1.72 − 1.62 (m, 2H, -CH_2-CH_2-CH_2-, 10,11), 1.56−1.43 (m, 2H, -CH-CH_2-, 12). ESI-MS (EI^+) calculated for $C_{16}H_{32}N_2O_4S_3$ ($M+H^+$) 413.16; found *m/z* = 413.15 ($M+H^+$), mass error (ppm) = -24.2.

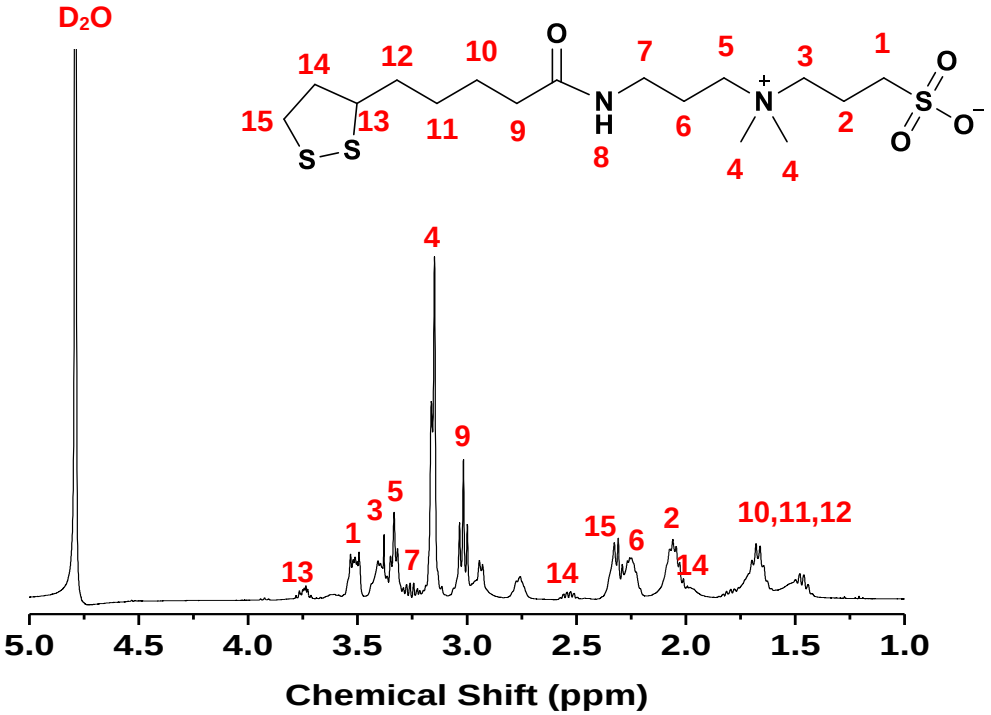

Figure 5-13. The 1H NMR spectrum TA-Zwitterion from 1.0-4.0 ppm. The data were collected by W. Ng in Dr. Zhou's group. Reproduced from W. Ng's BSc thesis (2017).

5.3 Synthesis of Ag NPs and Ag NCs

Silver nanoclusters (Ag NCs) and silver nanoparticles (Ag NPs) were prepared in a single step via reduction of Ag^+ ions by sodium borohydride in the presence of thioctic acid or zwitterion-/or PEG- appending thioctic acid ligands. The ligand:Ag^+ molar ratio was controlled to generate different Ag nanomaterials. Specifically, the ligand:Ag^+ molar ratio was varied from 1:1 – 5:1 to generate fluorescent Ag NCs and a lower ratio (e.g. 0.1-0.001:1) was used to obtain Ag NPs. **Scheme 5-4** shows the synthesis route to generate of Ag NPs and Ag NCs.

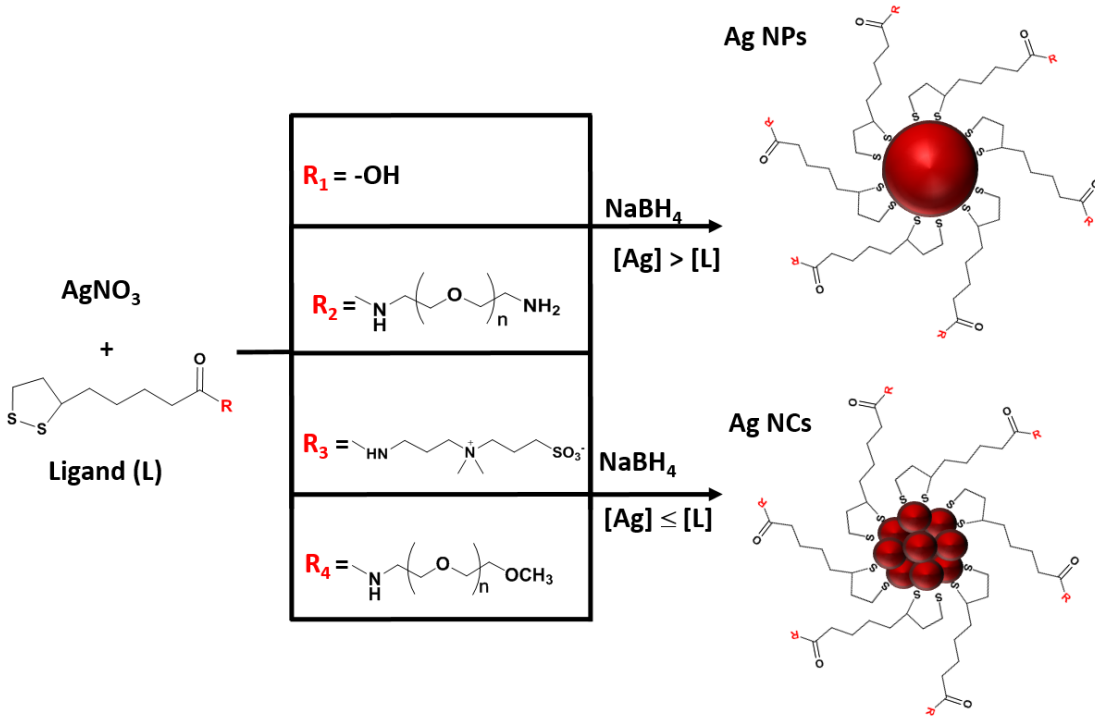

Scheme 5-4. Schematic representation of the synthetic route for the preparation of Ag NCs and Ag NPs stabilized by thioctic acid and thioctic acid based ligands.

5.3.1 Synthesis of Ag NC and Ag NP

Ag NCs were synthesized according to the method reported by the Mattoussi group [306] with several modifications. In detail, a 100 µL of 150 mM silver nitrate solution, water and the corresponding volume of 100 mM ligand were stirred for 60 minutes in the dark. A 1000 µL of 50 mM freshly prepared and ice-cold sodium borohydride was added to the solution and the reaction mixture was stirred overnight at room temperature (25°C). Ultrafiltration was conducted with a centrifugal filters (MW cut-off 5 000 Da membrane) to remove any unreacted silver ions and excess ligand and washed three times with water. The purified product was dried in vacuum, weighed and then re-suspended in deionized water to obtain the desired concentration (in $mg \cdot mL^{-1}$) for further experiments. **Table 5-1** showed the different volume of the reagents used in the Ag NC synthesis.

Table 5-1 Reagent volumes to synthesize Ag NCs. The ligand concentration was 100 mM.

Ag : L Ratio	$AgNO_3$ (µL)	Ligand (µL)	H_2O (µL)	$NaBH_4$ (µL)
1:1	100	150	1750	1000
1:2	100	300	1600	1000
1:3	100	450	1450	1000
1:4	100	600	1300	1000
1:5	100	750	1150	1000

Ag NPs were synthesized in a similar manner but with a lower Ligand:Ag ratio was used. **Table 5-2** shows the different volume of the reagents for the synthesis of Ag NPs.

Table 5-2 Reagent volumes to synthesize Ag NPs. The concentration of the ligand for Ag NPs at 1:0.1 is 100 mM. The concentration of the TA-Zwitterion ligand for the ratio 1:0.1 and 1:0.001 is 10 mM.

Ligand	Label	Ag : L Ratio	$AgNO_3$ (µL)	Ligand (µL)	H_2O (µL)	$NaBH_4$ (µL)
Thioctic acid (TA)	NP_1	1: 0.1	100	15	1885	1000
TA-Zwitterion	NP_2	1: 0.1	100	15	1885	1000
TA- EG_3-NH_2	NP_3	1: 0.1	100	15	1885	1000
TA-EG_{12}-NH_2	NP_4	1: 0.1	100	15	1885	1000
TA-$PEG_{\sim 17}$-OCH_3	NP_5	1: 0.1	100	15	1885	1000
TA-$PEG_{\sim 23}$-OCH_3	NP_6	1: 0.1	100	15	1885	1000
TA-Zwitterion	NP_7	1: 0.01	100	15	1885	1000
TA-Zwitterion	NP_8	1:0.001	100	1.5	1898.5	1000

5.3.2 Quantum Yield Calculations for Silver Nanoclusters

Quantum yield (QY) of the Ag NCs was determined using Rhodamine 6G in ethanol as the standard by the equation in **Equation 5-2**:

$$QY_{AgNCs} = QY_S \bullet (F_{AgNCs}/F_S) \bullet (A_S/A_{AgNCs}) \qquad \textbf{Equation 5-2}$$

Where $QY_{AgNCs,}$ F_{AgNCs} and A_{AgNCs} are the quantum yield, integrated fluorescent intensity and the absorbance at 480 nm of the Ag NC sample. $QY_{S,}$ F_S and A_S are the quantum yield, integrated fluorescent intensity and absorbance at 480 nm of the standard (Rhodamine 6G, which has a QY of 95% under 480 nm excitation). The silver nanoclusters and Rhodamine 6G were diluted and the solution with an absorbance of less than 0.1 (λ= 480 nm) was used as the first solution. Then, Beer Lambert Law (**Equation 5-3**) was used to calculate the absorbance of the other standard solution with lower concentrations.

$$A = \varepsilon l C \qquad \textbf{Equation 5-3}$$

Where A is the absorbance, ε is the molar extinction, l is the path length and C is the concentration of silver nanoclusters or Rhodamine 6.

5.3.3 Antimicrobial Test

To examine the antibacterial property of the Ag NPs and Ag NCs, *E. coli* BW25113, *S. aureus* SH1000 were used as standard strains in this study. The procedure was conducted in accordance with reference methods for the determination of minimal inhibitory concentrations (MICs) of aerobic bacteria by broth microdilution from the NCCLS consensus process (Methods for Dilution Antimicrobial Susceptibility Tests for Bacteria that Grow Aerobically – approved standard Sixth edition, January 2003).

5.4 Results and Discussion

5.4.1 Characterization of Ag NCs and Ag NPs

The synthesis of the Ag NC involved the mixing of the ligand to the silver nitrate solution followed by the addition of freshly prepared and ice-cold $NaBH_4$. The addition of the reducing agent immediately changed the colour of the solution to dark brown and finally to a yellow to reddish-orange colour after 12 hrs of mixing. These reddish-orange solutions emitted a red fluorescence under UV-light lamp excitation at λ = 365 nm as shown in **Figure 5-14 (A)**.

(A) **(B)**

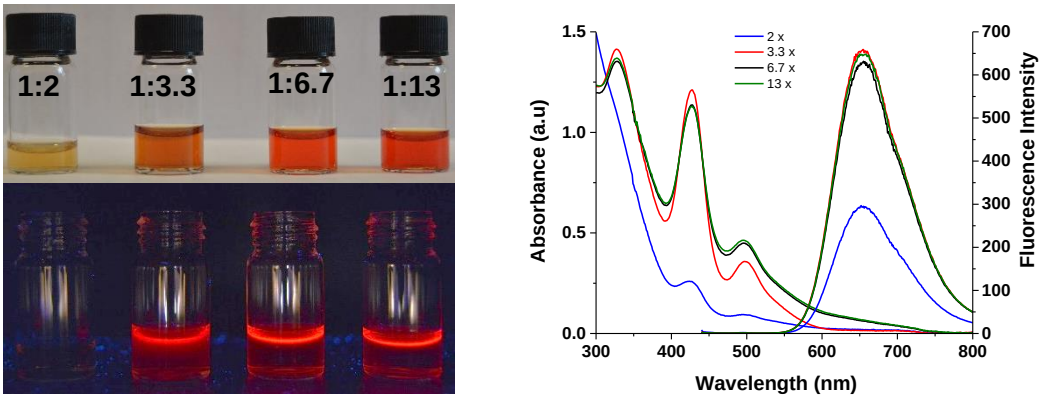

Figure 5-14. (A) Photos of Ag NC-DHLA in normal daylight (top panel) and under UV-light illumination (bottom panel), and (B) Spectroscopic characterization of the synthesized Ag Nanoclusters. The absorption spectrum and their corresponding fluorescence spectra (λ_{exc} = 480 nm) of Ag NCs dispersed in water. The Ag:L ratio was 1:3. The data were collected by A. Gummer in Dr. Zhou's group. Reproduced from A. Gummer's BSc thesis (2016).

Several synthesis parameters were investigated such as the amount of the reducing agent and ratio of silver ion to ligands. The amount of the $NaBH_4$ is critically important because it not only reduces silver ions to Ag NCs but also thioctic acid to dihydrolipoic acid (DHLA) based ligand for Ag NC stabilisation. The Ag NCs were prepared with different molar ratio of $NaBH_4$: Ag^+. The optical properties of the as-synthesized Ag NCs were characterized by UV-Vis and fluorescence spectroscopy as shown in **Figure 5-14 (B).** The Ag NC-DHLA exhibited well-defined absorption peaks at λ = 335 nm, 429 nm, and 500 nm regardless of the amount of the $NaBH_4$. The Ag NC showed a relatively broad emission peak centred at 660 nm (λ_{EX} = 425 nm). These observations were consistent with the results previously reported for DHLA protected Ag NC[305, 306]. Furthermore, relatively high fluorescence emission was observed at an Ag:$NaBH_4$ molar ratio of 1:3.33. Increasing the Ag:$NaBH_4$ ratio to 1:7 to 1:13 did not resulted in a higher florescence emission. Hence, a Ag:$NaBH_4$ ratio of 1:3.3 was chosen to synthesize Ag NCs. The same procedure was used to generate Ag NCs stabilized by different PEG-or zwitterion appending thioctic acid ligands. For simplicity, Ag NC will be denoted as Ag NC-PEG-X for PEG appended thioctic acid ligand and Ag NC-ZW for zwitterion appended thioctic acid ligand. The effect of concentration and nature of ligand on the spectral properties of the Ag NCs were investigated by varying the Ag:L molar ratio from 1:1 to 1:5. In general, Ag NC solutions exhibited dark brown colour when the Ag:L ratio was 1:1 but showed a yellow to reddish-orange colour at.higher ligand concentrations (*i.e.* 1:2 – 1:5) in normal day light conditions. Excitation under UV lamp (λ_{exc} = 365 nm) revealed that Ag NCs gave a red fluorescence emission in all Ag: L mole ratio (*i.e.* 1:1 – 1:5) tested as shown in **Figure 5-15 (A)-(F).**

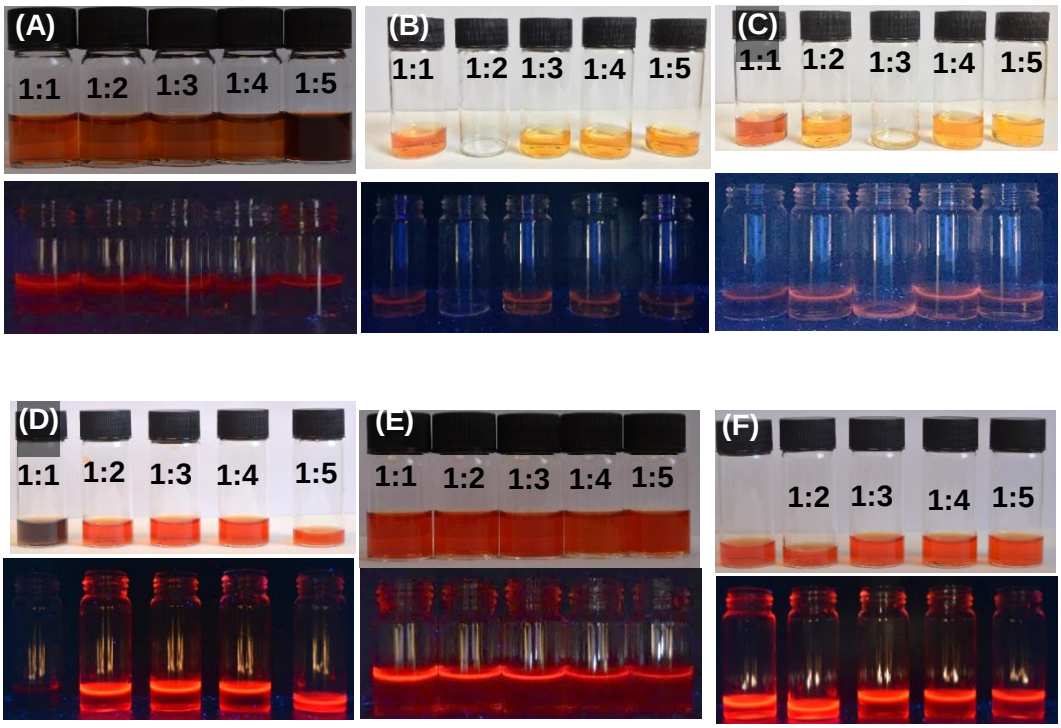

Figure 5-15. Photos of (A) Ag NC-DHLA, (B) Ag NC-ZW (C) Ag NC-PEG$_3$-NH$_2$, (D) Ag NC-PEG$_{12}$-NH$_2$, (E) Ag NC-PEG$_{17}$-OCH$_3$ and (F) Ag NC-PEG$_{23}$-OCH$_3$ under normal day light and UV–light illumination. The data were collected by W. Ng in Dr. Zhou's group. Reproduced from W. Ng's BSc thesis (2017).

The fluorescence emissions were generally brighter for Ag NC-PEG-X as compared to Ag NC-DHLA and Ag NC-ZW. This observations suggests that the nature of stabilizing ligand also affects the not only the surface properties but also the optical properties of Ag NCs. The UV-Visible absorption and fluorescence spectra of the different Ag NC were given in **Figure 5-16 (A) - (F)**.

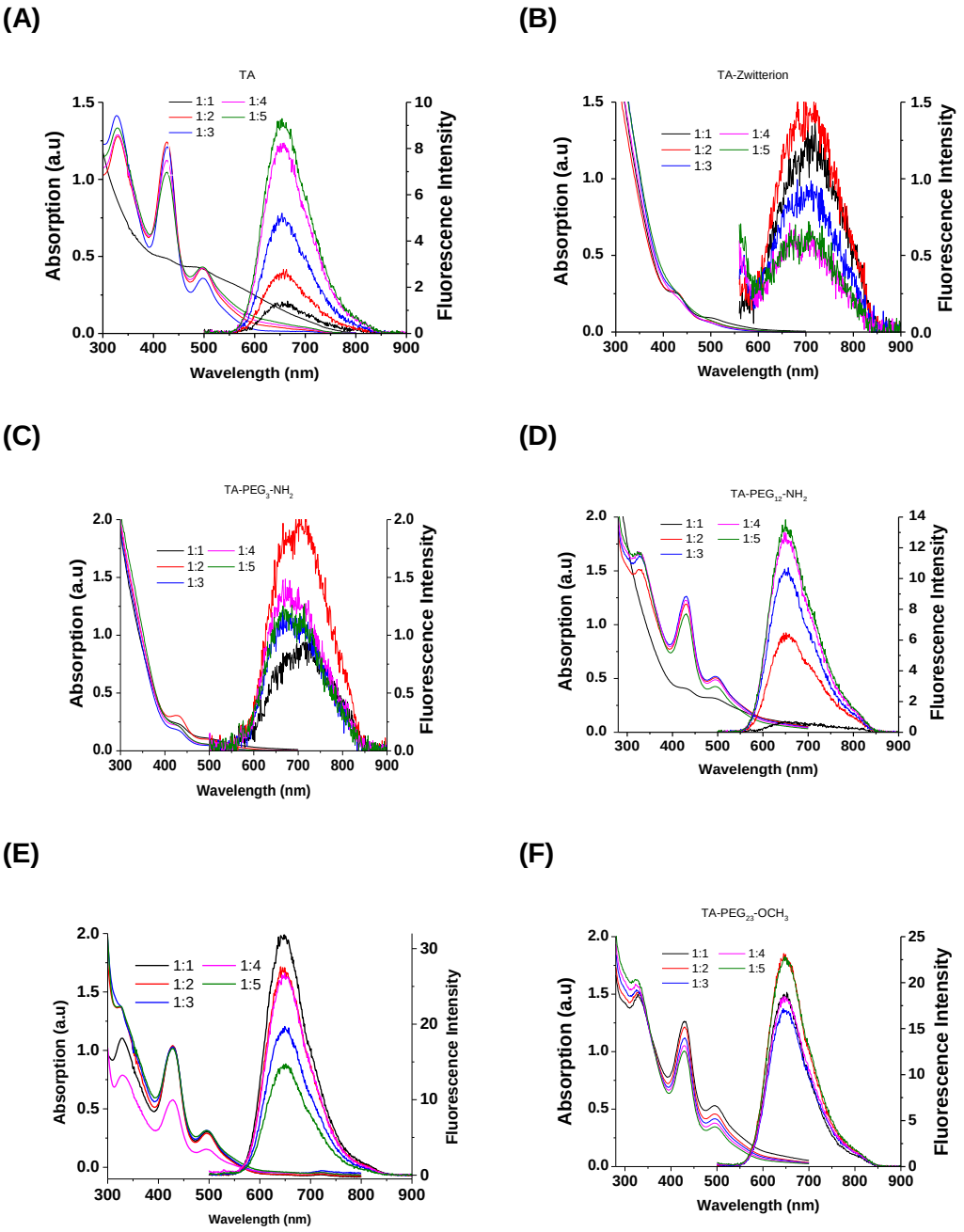

Figure 5-16. The UV-Vis absorption and Fluorescence (λ_{exc} = 425 nm) spectrum of (A) Ag NC-DHLA, (B) Ag NC-ZW, (C) Ag-PEG$_3$-NH$_2$, (D) Ag NC-PEG$_{12}$-NH$_2$, (E) Ag NC-PEG$_{\sim 17}$-OCH$_3$ and (F) Ag NC-PEG$_{\sim 23}$-OCH$_3$. The data were collected by W. Ng in Dr. Zhou's group. Reproduced from W. Ng's BSc thesis (2017).

The UV-Vis absorption spectra revealed similar absorption features Ag NC-DHLA (**Figure 5-16 (A)**), Ag NC-EG_{12}-NH_2 (**Figure 5-16 (D)**) AG NC-PEG_{17}-OCH_3 (**Figure 5-16 (E)**) and Ag NC- PEG_{23}-OCH_3 (**Figure 5-16 (F)**). The UV-Visible absorption spectra of Ag NCs stabilized by TA-Zwitterion (**Figure 5-16 (B)**), TA-EG_3-NH_2 (**Figure 5-16 (C)**) and revealed the absence of the peak at λ = 325 nm but the other main absorption peaks at λ = 429 nm and λ = 500 nm are present.

The Ag NCs excited at λ= 425 nm gave broad emissions peaked at λ= 660 - 680 nm region. The fluorescence emission peak for each Ag NC was unaffected by the molar excess of ligands, although it was slightly affected by the different ligand as shown in **Table 5-3**.

Table 5-3 Quantum Yield (η_F) of selected Ag NC. The data were collected by W. Ng in Dr. Zhou's group. Reproduced from W. Ng's BSc thesis (2017).

Ligand	Label	Ag: Ligand ratio	Emission Peak (nm)	Quantum Yield(η_F)
Ag NC-DHLA	NC_1	1:5	665	0.003
Ag NC-ZW	NC_2	1:2	615	0.42
Ag NC-PEG_3-NH_2	NC_3	1:2	665	0.28
Ag NC-PEG_{12}-NH_2	NC_4	1:5	656	2.5
Ag NC-$PEG_{\sim 17}$-OCH_3	NC_5	1:3	671	0.56
Ag NC-$PEG_{\sim 23}$-OCH_3	NC_6	1:2	644	2.6

The same procedure was used to generate Ag NPs stabilized by DHLA and DHLA – based ligands using lower ligand:Ag ratios which favoured the growth of larger nanoparticles as there were less ligands to passivate the nanoparticle. **Figure 5-17** showed the UV-visible spectra of Ag nanomaterials synthesized at Ag:L ratio of 1: 0.10. All the solutions exhibited an absorption spectra characteristic of SPR band for Ag NPs. The measured absorption maxima were λ = 391 nm for NP_1, 430 nm for NP_2, 403 nm for NP_3, 386 nm for NP_4, 404 nm for NP_6, and 400 nm for NP_5.

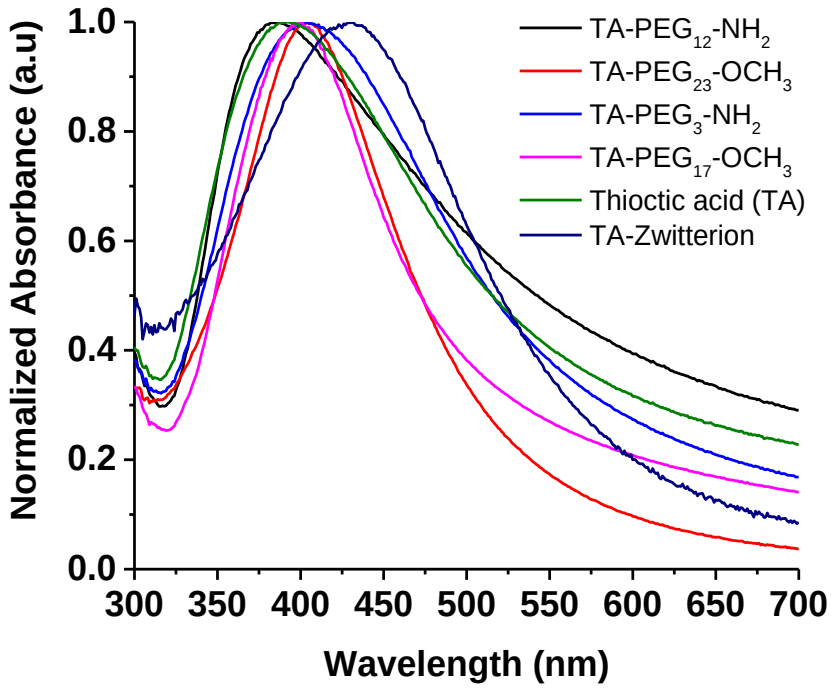

Figure 5-17. Normalized UV-Visible absorption spectra of the Ag NPs. The data were collected by W. Ng in Dr. Zhou's group. Reproduced from W. Ng's BSc thesis (2017).

5.4.1.1 Particle Size and Surface Charge Measurements

Table 5-4 showed the average hydrodynamic diameters (D_hs) with ± ½ full width at half height maximum (FWHM) of the purified Ag NCs. The D_h of Ag NC-DHLA was 2.5 ± 0.8 nm (average D_{hS} ± ½ FWHM), and comparable to the earlier reports [340, 341]. The D_hs of zwitterion stabilized Ag NCs were found to be 4.6 ± 1.4 nm, in close agreement to those prepared using a phosphatidylcholine zwitterion ligand (*i.e.* 4.9 ± 2.9 nm) [229]. The slightly bigger size as compared to Ag NC DHLA might be due to the longer length of the zwitterion ligand. In general, the D_hs of the Ag NCs prepared at Ag:L ratio of 1:1 were slightly bigger than those of prepared at higher Ligand:Ag ratios. This observation may suggest that larger clusters are likely to be synthesized at lower ligand ratio. Moreover, larger D_{hS} for Ag NC-EG_n-NH_2 (n =3, 12) were observed primarily due to the extended and longer ligand on the surface of the Ag NCs. The D_hs did not significantly differ for the Ag NCs synthesized at an Ag:L ratio of 1:2 and 1:5.

The Ag NC-PEG$_{\sim 17}$-OCH$_3$ and Ag NC PEG$_{\sim 23}$-OCH$_3$ gave interesting D_{hS} sizes for NCs. The nanocluster D_{hS} at Ag:L is 1:1 and 1:2 can be explained by the longer PEG units compared to the other ligands. However, the D_hs of 53 nm to 59 nm when Ag:L ratio is 1:3 and 1:5 is too big for a nanocluster system. Surprisingly, even larger hydrodynamic sizes were recorded for Ag NC PEG$_{\sim 23}$-OCH$_3$ when the Ag:L was > 1:2. Two different batches of the Ag NCs were prepared and several repeat DLS measurements were carried out and results showed similar large D_hs. A possible explanation to the observed large size could be due to the complexation of the PEG chains to Na^+ ions [342, 343] causing NCs to agglomerate.

Table 5-4 The average hydrodynamic diameters (D_h, in nm) of the Ag NCs ± ½ FWHM. The data were collected by W. Ng in Dr. Zhou's group. Reproduced from W. Ng's BSc thesis (2017).

Ag NC	1:1	1:2	1:3	1:4	1:5
Ag NC-DHLA	2.5±0.8	1.1±0.28	1.92±0.30	1.72±0.15	1.4±0.37
Ag NC-ZW	4.6±1.4	4.1±1.3	4.4±1.3	3.9±1.3	3.8±1.2
Ag NC-EG$_3$-NH$_2$	5.7±1.6	5.5±1.5	5.5±1.6	4.8±1.4	5.1±1.5
Ag NC-EG$_{12}$-NH$_2$	4.8±1.4	4.4±1.6	4.4±1.3	5.1±1.3	4.5±1.2
Ag NC-PEG$_{17}$-OCH$_3$	6.3±2.0	5.7±1.5	53±19	54±18	59.±22
Ag NC-PEG$_{23}$-OCH$_3$	5.2±1.4	136±57	143±66	152±72	146±68

Another probable reason for the large D_{hS} for the Ag NC-PEG$_n$-OCH$_3$ (n ~17, 18) system is due to the long PEG polymer. Although the size of a single Ag nanocluster unit is expected to be < 2 nm, it is possible that several Ag NCs can be embedded in the long PEG backbone making the movement of the nanoclusters in the surrounding medium slower, thereby increasing the hydrodynamic size.[344] Large D_{hS} sizes were also as previously reported using polymethylacrylic acid (PMAA) stabilized Ag NCs [345].

The D_hs of the Ag NPs were shown in **Table 5-5**. Surprisingly, the size of the Ag NP were smaller than expected > 5 nm diameter for NP_1, NP_3, and NP_4. The Ag NPs were synthesized in two batches and still showed almost the same D_hs. Considering that the Ag NPs were purified by centrifugal filtration, the DLS measurement should reveal the size of the nanoparticle without complication from the excess ligand. The D_hs for NP_2, NP_5, NP_6 showed expected sizes for nanoparticles and were larger than their corresponding nanocluster counterparts. It is important to validate the size Ag NPs with additional technique such as TEM imaging. Nonetheless, the UV-Vis spectra in **Figure 5-17** shows the characteristic SPR peak for Ag nanoparticles.

Table 5-5 Hydrodynamic diameters (D_h) of the Ag NPs. The data were collected by W. Ng in Dr. Zhou's group. Reproduced from W. Ng's BSc thesis (2017).

Ag NP	Label	D_h (nm)
Ag NP-DHLA	NP_1	1.20 ± 0.35
Ag NP-ZW	NP_2	7.96 ± 3.1
Ag NP-EG_3-NH_2	NP_3	2.18 ± 0.63
Ag NP-EG_{12}-NH_2	NP_4	1.90 ± 0.82
Ag NP-PEG_{17}-OCH_3	NP_5	9.32 ± 3.4
Ag NP-PEG_{23}-OCH_3	NP_6	6.40 ± 3.2

Surface charge is an important property that affects the stability and antimicrobial property of the Ag nanomaterials. This surface charge was determined using zeta potential measurements and shown in **Table 5-6**. The Ag NCs and Ag NPs were washed three times with ultrapure water and finally dispersed in 1.0 mL water before zeta potential measurements. This was done to eliminate the possible complication of the excess ligands during the measurement. The zeta potentials for Ag NC-DHLA and Ag NC-ZW were - 23.1 mV and – 21.8 mV respectively, due to the deprotonated carboxylic acid. The Ag NC-ZW was slightly negative charged, consistent to the near charge neutral of the zwitterionic ligand. The surface charge for Ag NP-DHLA and Ag NP-ZW were the same compared to their nanocluster counterparts but differ in magnitude. Zeta potential measurements also revealed that PEG appended Ag NCs also differed in their surface charge. The PEG backbone is expected to be neutral thus, the terminal group (*i.e.* $–NH_2$ and $–OCH_3$) are expected to dictate the over-all

charge of the Ag NC. The PEG-amine terminated Ag NCs and Ag NPs showed positive zeta potentials as expected from protonated amines. Surprisingly, the PEG methyl ether terminated Ag NCs exhibited a negative surface charge, a sharp contrast to their corresponding NPs which appeared to be positively charged. These results were unexpected because the methyl moiety cannot undergo protonation/deprotonation reactions and should render the entire ligand neutral. Again these experiments were repeated twice with two different batches of the methyl ether-PEG appended Ag NCs and Ag NPs which both gave the same surface charge. However, several reports have shown that PEGylated nanoparticles can indeed exhibit a negative zeta potential [346-349]

Table 5-6 Zeta potentials for the Ag NC and Ag NPs in pure water. The data were collected by W. Ng in Dr. Zhou's group. Reproduced from W. Ng's BSc thesis (2017).

Ligand	NC	Zeta Potential (ξ, mV)	NP	Zeta Potential (ξ, mV)
Thioctic acid (TA)	NC_1	-23.7	NP_1	-23.2
TA-zwitterion	NC_2	-2.47	NP_2	-10.4
TA-EG_3-NH_2	NC_3	+30.2	NP_3	+ 33.6
TA-EG_{11}-NH_2	NC_4	+7.69	NP_4	+ 34.6
TA-PEG_{17}-OCH_3	NC_5	-24.9	NP_5	+ 22.0
TA-PEG_{23}-OCH_3	NC_6	-23.1	NP_6	+ 16.3

Agarose gel electrophoresis was conducted to further confirm the surface charge of the silver nanomaterials. The Ag NCs and Ag NPs were loaded in each lane and the gel was run at 100 V for 30 minutes and the results were shown in **Figure 5-18.** The Ag NC bands were observed under UV light because of their fluorescence properties and also very weak absorption making them almost invisible under normal light. The NC_1 migrated towards the positive terminal, implying the ionized carboxylic acids imparted a negatively charged surface on the Ag NC-DHLA as expected for clusters with a negative zeta potential. Unfortunately, the very weak fluorescence of NC_2 made it difficult to see. The NC_3 moved towards the negative terminal which implies a positive surface charge on the Ag NC. This band migration agrees with the positive zeta potential for NC_3. The band movement NC_4 was difficult to observe due to its weak visible luminescence. The NC_5 and NC_6 showed slight movement towards the

positive terminal suggesting the negatively charged Ag NC surface which correlate to the observed negative zeta potential measured for NC_5 and NC_6.

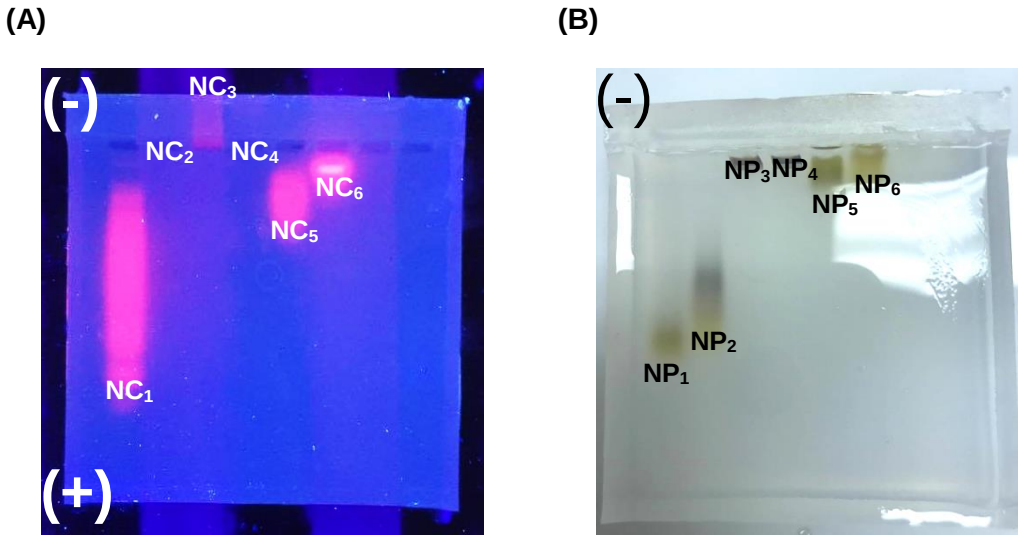

Figure 5-18. Agarose gels of (A) Ag NC (NC_{1-5}) and (B) Ag NP (NP_{1-5}). The data were collected by W. Ng in Dr. Zhou's group. Reproduced from W. Ng's BSc thesis (2017).

For the Ag NPs, band migrations were clearly observed due to their strong absorption. Both NP_1 and NP_2 migrated towards the positive terminal while NP_3 and NP_4 did not show any observable band movement. Moreover, both NP_5 and NP_6 showed a slight migration towards the positive terminal, implying a negative surface charge. This observation contradicted to what was expected from the positive zeta potentials for NP_5 and NP_6. The same ligands were used to prepare NP_5 and NP_6 with those of NC_5 and NC_6 which means they should exhibit similar negative surface charge. The agarose gel electrophoresis provided a more convincing evidence of the negative surface charge for NP_5 and NP_6. In general, the nature of the ligand influences the overall surface charge of the Ag NCs and Ag NPs. The zeta potential measurements and agarose gel electrophoresis results suggests that DHLA and zwitterion stabilized Ag NC and Ag NP exhibit a net negative surface charge and should migrate towards the positively charged electrodes as confirmed with the agarose electrophoresis gels. The amine-PEG stabilized Ag NC and Ag NP exhibit a positive zeta potential charge and were observed to migrate towards the negatively

charged electrode (*e.g.* NC_3). Finally, the agarose gel experiment provided and evidence of a negative surface charge for OCH_3-PEG stabilized Ag NCs and Ag NPs.

5.4.2 Antimicrobial Tests

Ag and Au NCs has recently been reported to exhibit potent antimicrobial properties and are considered as new generation of inorganic antimicrobials [308, 350]. In particular, Xie and colleagues (2017) first reported a comparison of the antibacterial activity of Au NCs and Au NPs [350]. The 6-mercaptophexanoic acid coated Au NCs were observed to possess superior growth inhibition of gram-positive *S. aureus* and gram negative *E.coli* as compared to Au NPs coated with the same ligand. The authors reasoned that the enhanced antibacterial action of Au NCs was due to its inherently small size which allowed it to have better interactions with the bacteria. Intriguingly, the study also observed that cellular internalization of Au NCs and Au NPs have no significant difference. It was later shown that ~15 fold higher concentration of Au NPs were needed to reach the same particle number dose for Au NC [350].

This study presents the antimicrobial properties of Ag NPs and Ag NCs bearing different terminal functional groups with two bacterial model species. The results gathered presents an interesting difference in the antibacterial properties between Ag NPs and Ag NCs. **Figure 5-19** shows the experimental principle to investigate the antibacterial properties of Ag nanomaterials. The Ag NPs and Ag NCs were prepared with the same synthesis protocol and stabilized by different types of ligands. The Ag nanomaterials were incubated with *S. aureus* and *E.coli*. The Ag nanomaterials can interact with the bacteria and exert its antimicrobial effect. It is known that the structural differences in bacterial cell walls may result in varied interactions between the bacteria and Ag nanomaterials. Therefore, knowledge regarding the bacterial cell wall in correlating the antibacterial properties of Ag nanomaterials is imperative because cell walls are the first point of contact of bacteria to the “external world”. The structure of bacterial cell wall can be categorized as either gram-negative or gram-positive. [351] The gram-negative bacteria cell wall are composed of two lipid membranes with a thin peptidoglycan layer in between (magnified in **Figure 5-19** for *E.coli*). [351] The outer membrane contains lipopolysaccharides (LPS), which have been suggested to protect bacteria from antibiotics [352] and surface proteins. The presence of phosphate groups as well as carboxylate groups present in sugar acids make the cell surface negatively

charged. In contrast, gram-positive bacterial cell walls feature a thick peptidoglycan layer (15-100 nm) [353]. This layers contains polymeric teichoic acids, surface proteins, and a cytoplasmic membrane underneath. The cell surface is also negatively charged due to the polymeric chains of teichoic acid which contain anionic phosphate groups in the glycerolphosphate repeat units. [354] The teichoic acid chains and peptidoglycan layer maintain cellular integrity and have been suggested to be binding sites for divalent cations in solution. [351]

The antibacterial activities of the Ag NPs and Ag NCs against *S. aureus* and *E.coli* strains were evaluated based on their Minimum Inhibitory Concentration (MIC). *E. coli,* the most characterized gram negative bacterium, has been used in various antimicrobial testing studies whereas *S. aureus,* a gram positive bacteria, is considered to be responsible for wide range of infectious diseases ranging from benign skin infection to life threatening endocarditis. Moreover, *S. aureus* is also one of the major cause of nosocomial infections because of its virulence and antibiotic resistance [355]. The MIC refers to the lowest concentration of an antimicrobial drug that prevents the visible growth of a microorganism after overnight of incubation with the media. The MIC vales reflect the potency of the antimicrobial drug, the lower the MIC value means the less drug is required for inhibiting of the microorganism [356].

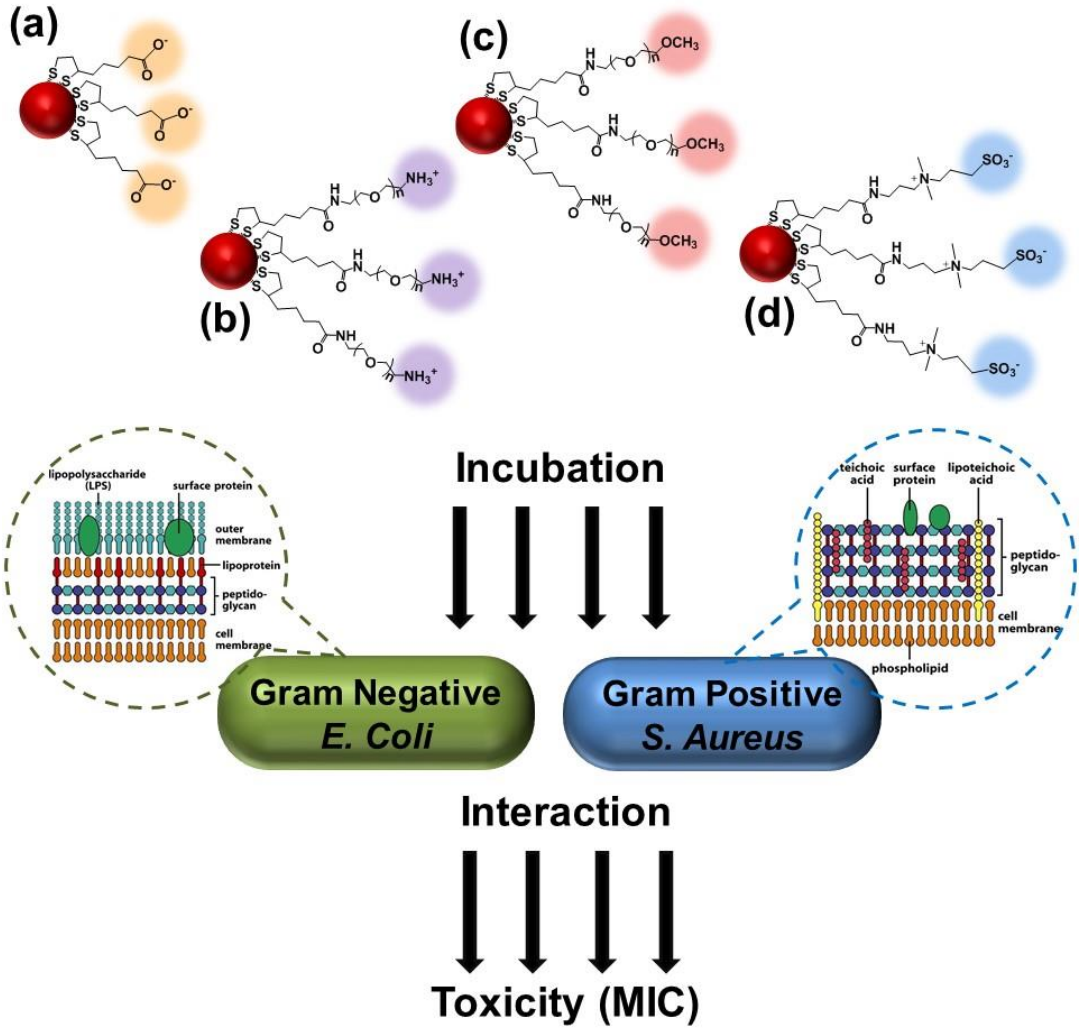

Figure 5-19 Schematic representation of overall experimental design. The Ag nanomaterial (Ag NP and Ag NC) core are denoted with a red sphere. The Ag nanomaterials were stabilized by (a) dihydrolipoic acid (DHLA) which is negatively charge, (b) DHLA-EG_n-NH_2 which is positively charge, (c) DHLA-PEGn-OCH_3 and (d) DHLA-Zwitterion. The Ag nanomaterials were incubated with *E. coli* and *S. Aureus* and their antimicrobial properties were determined by minimum inhibitory concentration (MIC) values.

The MIC values were determined for Ag NC and Ag NP are presented in **Table 5-7**. The Ag NCs revealed a different effectiveness in inhibiting the growth of the bacteria. The MIC values lower than 256 $\mu g \cdot mL^{-1}$ implies that bacterial strains are sensitive to the antimicrobial effect of the Ag NC. The Ag NC-DHLA (NC_1) and Ag NC-PEG_{23}-OCH_3 (NC_6) were able to inhibit bacterial growth for both *S. aureus* and *E. coli* . While NC_2, NC_3, and NC_4 showed a MIC of >256 $\mu g \cdot mL^{-1}$, suggesting these Ag NCs did not exert notable antimicrobial activity against these bacterial strains. Moreover, NC_5 inhibited the *E. coli* growth at 128 $\mu g \cdot mL^{-1}$ but was ineffective against *S. aureus*.

Table 5-7 Minimum inhibitory concentration (MIC) of Ag NC and Ag NP against *S. aureus* and *E.coli.* The data were collected by W. Ng in Dr. Zhou's group. Reproduced from W. Ng's BSc thesis (2017).

Nanoclusters - MIC ($\mu g \cdot mL^{-1}$)			**Nanoparticles - MIC ($\mu g \cdot mL^{-1}$)**		
Sample	***S. aureus***	***E. coli***	**Sample**	***S. aureus***	***E. coli***
NC_1	128	64	NP_1	64	32
NC_2	>256	>256	NP_2	8	8
NC_3	>256	>256	NP_3	>256	64
NC_4	>256	>256	NP_4	>256	64
NC_5	> 256	128	NP_5	32	32
NC_6	64	128	NP_6	16	16

The NC_1 inhibited bacterial growth for both *S. aureus* and *E.coli* with a MIC of 128 and 64 $\mu g \cdot mL^{-1}$ respectively. Thus NC1 was more effective in inhibiting the growth of *E.coli* than *S. aureus*. The antibacterial property of Ag NC-DHLA (NC1) has already been reported by Liu and colleagues (2017) *via* turbidity measurements. They reported that Ag NC-DHLA were able to inhibit the growth of *E.coli* DH 5α (MIC ~ 15 $\mu g \cdot mL^{-1}$) and *E. coli* DSM 4230 (MIC ~ 10 $\mu g \cdot mL^{-1}$) with 24 hr incubation but showed no inhibitory effects against *S. aureus* [231]. The authors attributed the observed antibacterial action through different membrane damage mechanisms in *E. coli* but no clear explanation was made for *S. aureus*. The Ag NC-DHLA damage the cell membrane and permeate to the cell as observed for *E.coli* DH 5α while Ag NC-DHLA

can enter into cells by diffusion as observed for *E. coli* DSM 4230 [231]. Bacterial death was attributed to the released Ag^+ ion from Ag NC cores which generated reactive oxygen species and damaging the respiratory chain leading to bacterial growth inhibition and death [231]. Interestingly, Xie and colleagues (2014) compared glutathione-Ag NC with the Ag core having different oxidation states. Specifically, the antibacterial activities of glutathione-Ag^+-NC (*i.e.* the dominant Ag species remained in Ag NCs are Ag^+ species) and glutathione-Ag^0-NC (*i.e.* all Ag atoms were at zero valence). The results obtained from disk diffusion assay showed that glutathione–Ag NC with Ag^+ ion rich cores exhibited better growth inhibition of gram positive bacteria such as *S. aureus* (MIC ~ 80 µM) and *B. subtilis* (MIC ~ 80 µM) than gram negative bacteria *P. aeruginosa* (MIC ~ 100 µM) and *E. coli* (MIC ~ 100 µM) [230]. In addition, Xie and colleagues (2013) have also reported the antibacterial effect of glutathione-Ag^+-NCs against a multi-drug resistant bacteria *P. aeruginosa* (MIC ~ 11.8 $\mu g \cdot mL^{-1}$) [334]. The comparison of antibacterial activities for Ag NC-DHLA and glutathione-Ag NCs is possible due to fact that both ligands contain carboxylate moieties which are assumed to provide negative charges and stabilize Ag NC by virtue of electrostatic repulsion. These two types of Ag NCs highlights the importance of the silver ions in achieving the desired antibacterial effect.

The silver ions released from the Ag NC and Ag NP cores were determined using inductively coupled plasma – mass spectrometry (ICP-MS). The Ag nanomaterials were concentrated in a centrifugal filter (MW 5000 Da) and were washed with 1.0 mL of water for 5 times to remove any free silver ions and ligands. They were dried in vacuum and weighed. The dried Ag nanomaterials were then re-dispersed in 1.0 mL of ultrapure water and normalized to the same weight concentration (1 $mg \cdot mL^{-1}$). The Ag nanomaterials were incubated for 24 hours and the supernatants were collected and diluted to a final volume of 15.0 mL for ICP-MS analysis. The free Ag ion concentrations obtained from the supernatants were shown in **Table 5-8**. Notably, NC_1 and NP_1 produced rather high free Ag^+ ion concentrations (273 and 248 ppb respectively) which appeared to be correlated well with their high antibacterial potencies.

Table 5-8 ICP-MS of silver ion concentration in parts per billion (ppb) from Ag NC and Ag NP. The ND refers to "not detected". Each sample supernatant were aspirated 10 times (n=10) to the sample injection valve. The average of 10 concertation readings ± standard deviation are reported.

Ag NC	Ag^+ (ppb)	Ag NP	Ag^+ (ppb)
NC_1	273 ± 18	NP_1	248 ± 9.8
NC_2	55 ± 1.6	NP_2	5.1 ± 2.9
NC_3	ND	NP_3	0.03 ± 0.01
NC_4	ND	NP_4	8.17 ± 7.1
NC_5	0.20 ± 0.11	NP_5	23.3 ± 5.4
NC_6	2.24 ± 0.30	NP_6	48.4 ± 4.8

Recent studies have shown that materials coated with zwitterionic ligands can reduce bacterial attachment and biofilm formation [357-360]. Zhang and colleagues (2013) [361] demonstrated that a silver-zwitterion nanocomposite surface provided an effective, reliable antimicrobial and anti-adhesive platform for the prevention of microbial growth [361]. Combining the zwitterion ligands with inorganic nanomaterials such as Ag NCs and Ag NPs may enhance the antibacterial activities of the Ag nanomaterials. Unfortunately, the Ag NC-ZW (NC_2) did not inhibit the growth of both bacterial strains even if it released considerable amount of Ag^+ ions (~55 ppb). This result is in stark contrast to recently reported antibacterial activity of phosphatidylcholine zwitterionic Ag NCs against *E. coli* (MIC ~100 $\mu g \cdot mL^{-1}$) and *S. aureus* (MIC ~100 $\mu g \cdot mL^{-1}$) [229]. It is noteworthy that the Ag NCs in this study were prepared in a similar manner to the ones reported. Hence, the difference in observed results might be due to the structural differences of the zwitterions (*i.e.* the orientation of charges). The NC_2 in this study contains the sulfobetaine zwitterion moiety wherein the terminal end contains the negative charge ($–N^{\oplus}(CH_3)_2\text{-}(CH_2)_2\text{-}SO_3^{\ominus}$) while the phosphatidylcholine zwitterion has the positive charge at the terminal end ($\text{-}PO_4^{\ominus}\text{-}(CH_2)_2\text{-}N^{\oplus}(CH_3)_3$). These results imply that the structure of the capping ligand on the Ag NCs may play an important role in dictating their antibacterial effect. Interestingly, Rotello and colleagues (2016) [362] also studied the effect of particle size and charge orientation in zwitterionic Au nanoparticles on their antibacterial properties. Two different zwitterionic ligands, a sulfobetaine zwitterion ($–N^{\oplus}(CH_3)_2\text{-}(CH_2)_2\text{-}SO_3^{\ominus}$) and an

acylsulfonamide zwitterion (-C(O)-$N^{\ominus}$-SO_2-$(CH_2)_3$-$N^{\oplus}(CH_3)_3$) were used to prepare Au NPs of 2, 4 and 6 nm in diameter. They found that the 6 nm Au NPs stabilized by acylsulfonamide zwitterionic exhibited superior antibacterial activities against *P. aeroguinosa* and *A. azurea* as compared to the sulfobetaine zwitterionic Au NPs. The results may imply that positive charge terminated zwitterionic ligands have higher affinity to the negatively charged bacterial membranes. Furthermore, the study also observed that increasing the Au NPs size from 2 nm to 6 nm increased their antimicrobial efficiency though bacterial membrane disruption. Surprisingly, the small 2 nm acylsulfonamide zwitterion coated Au NPs did not induce any membrane damage in the bacteria tested [362]. Overall, this study highlighted the importance of particle size and surface ligand structure (*i.e.* orientation of charges in the zwitterion ligand) in dictating the antimicrobial activity of the zwitterionic Au NPs.

Several reports also showed that cationic Ag NPs [336, 363] and Au NPs[364] exhibited a high level of effectiveness against the gram positive bacteria and gram-negative bacteria. These studies highlighted the importance of tuning the functional groups on the nanoparticle surface to achieve its desired antibacterial action. The negative charge in the bacterial cell wall can electrostatically attract the positive charge in NPs causing them to be more effective antibacterial NPs. Transmission electron microscopy imaging have revealed that positively charged Ag-polyethylenimine NPs tightly adhere to the bacterial surface and some of even fusing with cell wall. In contrast, no attachment was observed for the negatively charged citrate stabilized Ag-NPs. [365]

The ligands used to prepare NC_3 and NC_4 were designed to have a PEG moiety and a terminal amino group. The EG chain in NC_3 has 3 ethylene glycol (EG) repeat units whereas NC_4 has 12 EG repeat units. It was hypothesized that the protonated amino group will impart a positive charge on the Ag NC surface, allowing them to bind to the negatively charged components of the bacterial membrane such as the lipopolysacharride and lipoteichoic acid [366] by electrostatic interaction as shown in Error! Reference source not found.. Aside from imparting stability to the nanoclusters, the dual hydrophobic/hydrophilic character of PEG chains might allow to some extent enhance the permeation of the nanocluster through the cell membrane.

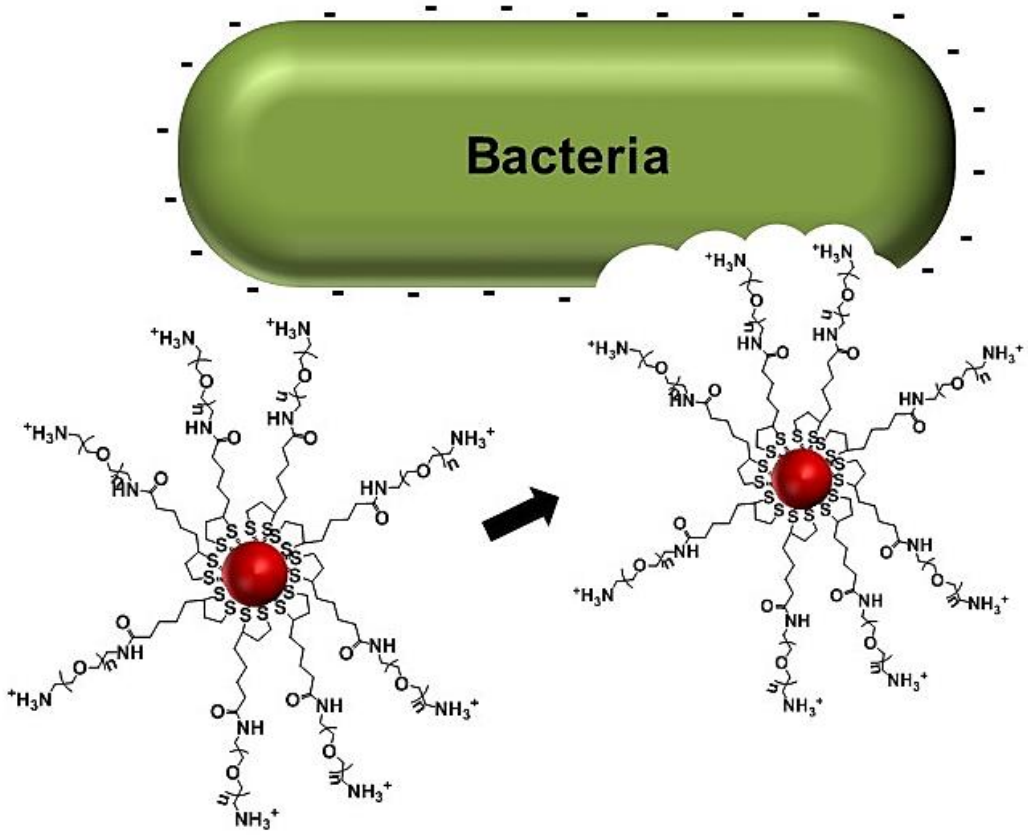

Figure 5-20 Schematic representation of a positively charged Ag NC interaction with the negatively charged bacterial cell wall. The Ag NC-EG$_n$-NH$_3^+$ is hypothesized to permeate the bacterial cell wall.

Surprisingly, the MIC results suggests that NC_3 and NC_4 were ineffective against *S. aureus* and *E. coli*. Moreover, the ICP – MS data revealed that Ag ion were too low to be detected in the supernatant for NC_3 and NC_4. In order to rationalize the MIC observation, a possible reason might be due to the total positive charge (*i.e.* charge density) on the surface of the Ag NCs. The total positive charge on the Ag NC surface might be low due to the small number of amine groups per ligand present. The effect of the number of cationic groups impacting their antibacterial activities was demonstrated by Cai and colleagues (2009) using poly(amidoamine) (PMAM) dendrimers [367]. Unmodified PMAM and other dendrimers with hundreds of peripheral amino groups were active against *P. aeruginosa* and *S. aureus* due to the polycationic nature of the protonated amines. The PEGylation of the terminal amines lead to drastic decrease in the antibacterial activities, and specially against *S. aureus*. The authors attributed the reduced potency to the decrease in the protonated amine

groups thus, decreasing the charge density and reducing the electrostatic interaction of the dendrimers to the negatively charged bacterial surface [367]. In a separate study, capping the amino groups of PMAM with acetyl groups led to a loss of ability to disrupt lipid bilayer membranes, an important mechanism in bacterial death [368]. These studies highlight the importance of having a high degree of protonated amino groups to achieve their antimicrobial effects. In another interesting study, multi-walled carbon nanotubes (MWCNTs) modified by cationic amino acids arginine (Arg) and lysine (lys) were also found effective against *E. coli* and *S. typhimurium* [369]. Radial diffusion assay and MIC data showed the antibacterial activity followed the sequence of MWCNTs-arginine > MWCNTs-lysine > pristine MWCNTs [369]. The difference in the activity is most likely due to the difference of pKa of Arginine (guanidinyl group, pKa ~ 12.5) and pKa of Lysine (primary amine group, pKa ~10.5). The higher pKa for the arginine simple means that guanidinyl proton are more tightly held and less easily are given up than in lysine. In turn, this could have provided a more positive charge for MWCNTs-arginine leading to a slightly higher antibacterial activities than MWCNTs-lysine. The current results obtained in this study implies that deprotonation of the amines had a detrimental effect on the antibacterial activity of NC_3 and NC_4. The deprotonated amines on the surface of Ag NC can no longer be electrostatically attracted to the negatively charged bacterial surface making them inactive against the test organisms as shown in **Figure 5-21**.

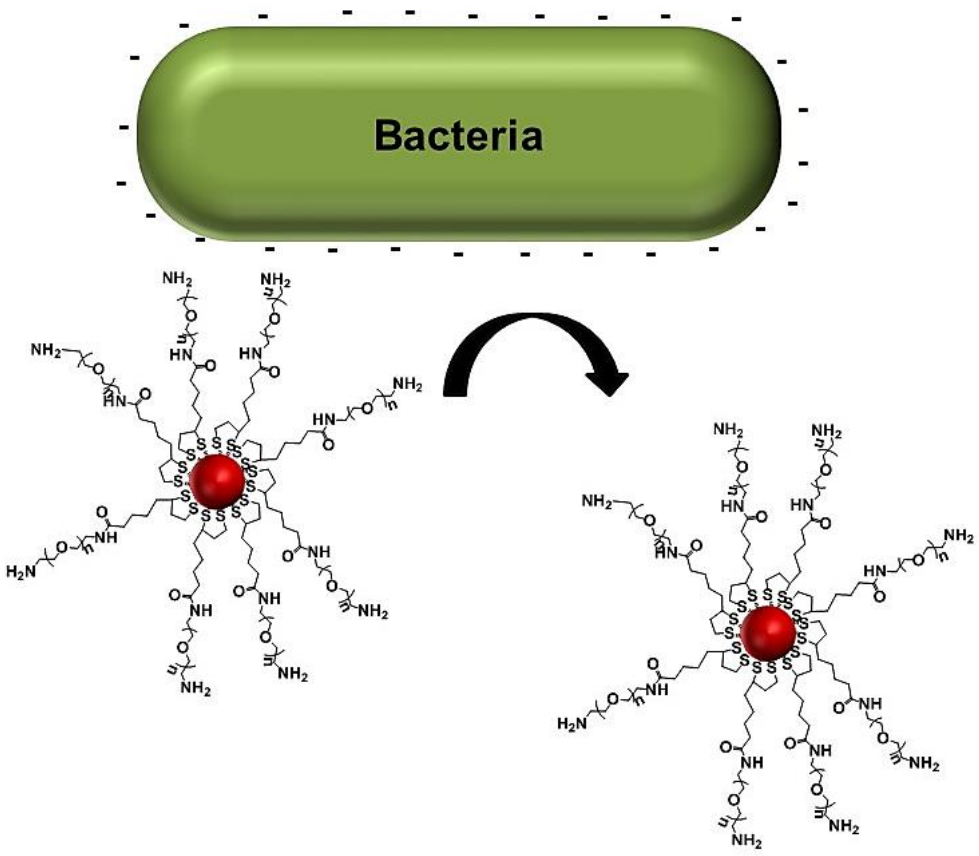

Figure 5-21 Schematic representation of Ag NC-EG$_n$-NH$_2$. The deprotonated amine are not electrostatically attracted to the negative bacterial cell wall leading to loss of antimicrobial activity.

In another study, Haynes and colleagues (2015) [370] shed light on the effect of different surface charge and charge densities Au NPs with *S. oneidensis* MR-1 and *B. subtilis* bacterial membranes as model organisms. The Au NPs were capped with anionic 3-mercaptopropionic acid (MPA), cationic 3-mercaptopropylamine (MPNH$_2$), and a cationic polyelectrolyte poly(allylamine hydrochloride) (PAH). The surface charge densities were determined using X-ray photoelectron spectroscopy (XPS) and were calculated to be 5.6, 4.6, and 2.8 for MPA, MPNH$_2$ and PAH modified AU NPs respectively. The results showed that anionic MPA–Au NPs had minimal toxic effect while both cationic Au NPs impacted the growth of both bacterial species to different extents. The data further demonstrated that cationic polyelectrolyte-wrapped Au NPs (PAH- Au NPs) were more toxic to both the gram negative and gram positive bacteria. These PAH-Au NPs induced the greatest membrane damage and toxicity to both bacterial models. The authors attributed superior antibacterial activity of cationic polyelectrolyte PAH-Au NPs to large

number of protonated amines leading to high positive surface charge density. Overall, the observed inactivity of NC_3 and NC_4 highlights importance of designing the structure of the ligands (*i.e.* charge and charge density) in order to achieve antibacterial effect [370].

The next design of ligand was to use longer PEG unit with a terminal methyl ether group to generate stable NC_5 and NC_6. The methyl ether group is considered neutral unlike the protonated amine group in NC_3 and NC. Historically, it was Cox (1966)[371] who first reported the antibacterial property of polyethylene glycol solutions against of *E. coli*. *S. marcesens* and *A. aerogenes*. The data suggests that longer PEG chains can inhibit bacterial growth even at lower solution concentration [371]. In a separate study, Kohn and colleagues (1983) also reported the antibacterial property of polyethylene glycol-400 (PEG 400) solutions[372]. Recent investigation also implicates the therapeutic PEGylated Ag nanoparticles as antibacterial agent [373]. In order to re-examine these previous observations, different PEG chain lengths (*i.e.* ~ 17 EG repeat units for NC_5 and ~23 EG repeat units for NC_6) were used to explore whether chain length has indeed a role in improving the antibacterial activity of the Ag NCs. The NC_5 and NC_6 showed different antimicrobial behaviours wherein NC_5 was able to inhibit *E. coli* but ineffective against *S. aureus*. The generally lower efficacy against *S. aureus* over *E. coli* could be due to the different membrane structures. The much thicker peptidoglycan of gram-positive bacteria (20-80 nm, e.g. *S. aureus*) over that of gram-negative bacteria (7-8 nm, *E. Coli*) [374, 375] might passivate the interactions between the NC and bacterial membrane. This may lead to less nanocluster penetration and hence infectivity of NC_5 as antibacterial agent towards *S. aureus*. Surprisingly, the NC_6 displayed high antimicrobial potency against both strains despite both of them released only minimal amount of free Ag^+ ions (i.e. 0.20 and 2.24 ppb for NC_5 and NC_6 respectively).

Considering that both NC_5 and NC_6 exhibited the same surface charge, the difference in antibacterial activity is tentatively attributed to the length of PEG chain. Comparing the MIC data of the PEGylated NC_3 and NC_4 (both ineffective) and those of NC_5 and NC_6, it appears that the PEG linker not only can provide the steric stabilization for the NCs but also more importantly the necessary hydrophobic/hydrophilic interactions with the bacterial membrane to exert its antibacterial potency. Indeed, a study conducted by Sogi and colleagues (2015)[376] compared the antibacterial vehicles propylene glycol, glycerine, PEG 400, and PEG 1000 (average MW ~1000 Da) for

endodontic therapy. Using broth dilution method, they determined the lowest concentration of the vehicles that can fully inhibit bacterial growth. Propylene glycol was effective against three organisms namely *S. mutans E. faecalis* and *E. coli* and its bactericidal activity was at 50%, 25% and 50% respectively. PEG 1000 was effective against *S. mutans* and *E. coli* at 25% solution concentration[376]. Using disk diffusion assay, the zone of inhibition for PEG-8000 stabilized Ag NPs after 24 incubation with *Bacillus* and *P. Aeruginosa* are 10.2 mm and 10 mm respectively, while for PEG-6000 stabilized Ag NPs are 7.5 mm and 9.5 mm respectively. The greater zone of inhibition for PEG-8000 Ag NPs implies a better antibacterial activity against both gram-positive and negative bacteria when compared to PEG-6000 stabilized Ag NPs [377]. Unfortunately, these studies did not present any explanation on how the PEG coating have impacted the antimicrobial properties of the Ag NPs. Nonetheless, these studies have confirmed experimental evidence on the antibacterial property of PEG stabilized NPs.

The antibacterial property of Ag NPs have been correlated with to the release Ag^+ ions. It is interesting to account the possible role of the PEG coating in the antimicrobial property of Ag NPs and Ag NCs. When bacterial cells are exposed to a solution of Ag ions, the ions are distributed and surrounds the bacterial cell with no specific localization. In contrast, NPs can interact with the bacterial cell wall and produce a localized source to continuously release ions, leading to higher toxicity to bacterial cells. [365] The Ag NP dissolution produces Ag ions that can be complexed by polyethylene glycol chains as shown in **Figure 5-22 (A)** [378]. The complexation of Ag^+ ions by polyethylene glycol can be analogous to the complexation of univalent ions (e.g. Na^+ and K^+) with cyclic ethers [137]. In order to achieve the desired antimicrobial effect, the Ag NPs should be in contact with the bacterial cell walls. The Ag NPs can be thought of like a “vehicle” containing large amounts of Ag^+ ions and delivers these Ag^+ ions into the bacterial cell walls as shown in **Figure 5-22 (B)**. The localized high Ag^+ ion concentration of further helps to penetrate the bacterial cell through different membrane channels present in the bacterial cell walls. As a consequence, the Ag NP dissolution is localized around the bacterial membrane leading to bacterial toxicity as confirmed by the low MIC values for NP_5 and NP_6.

(A)

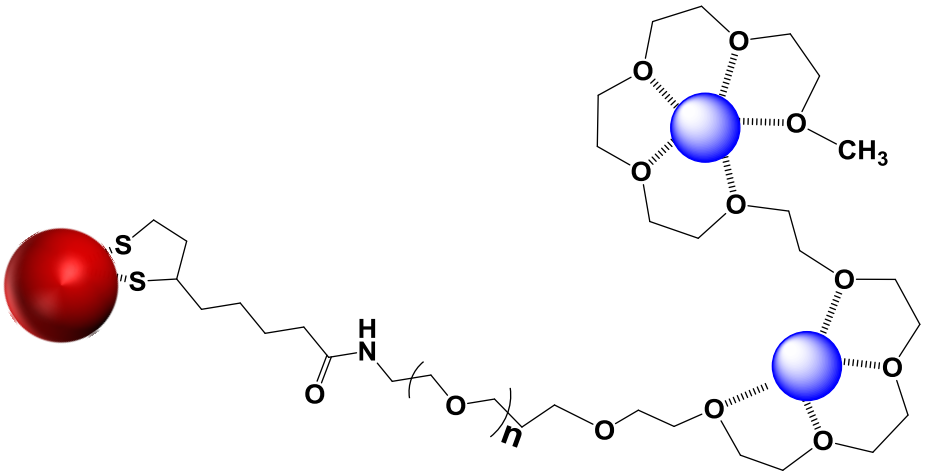

(B)

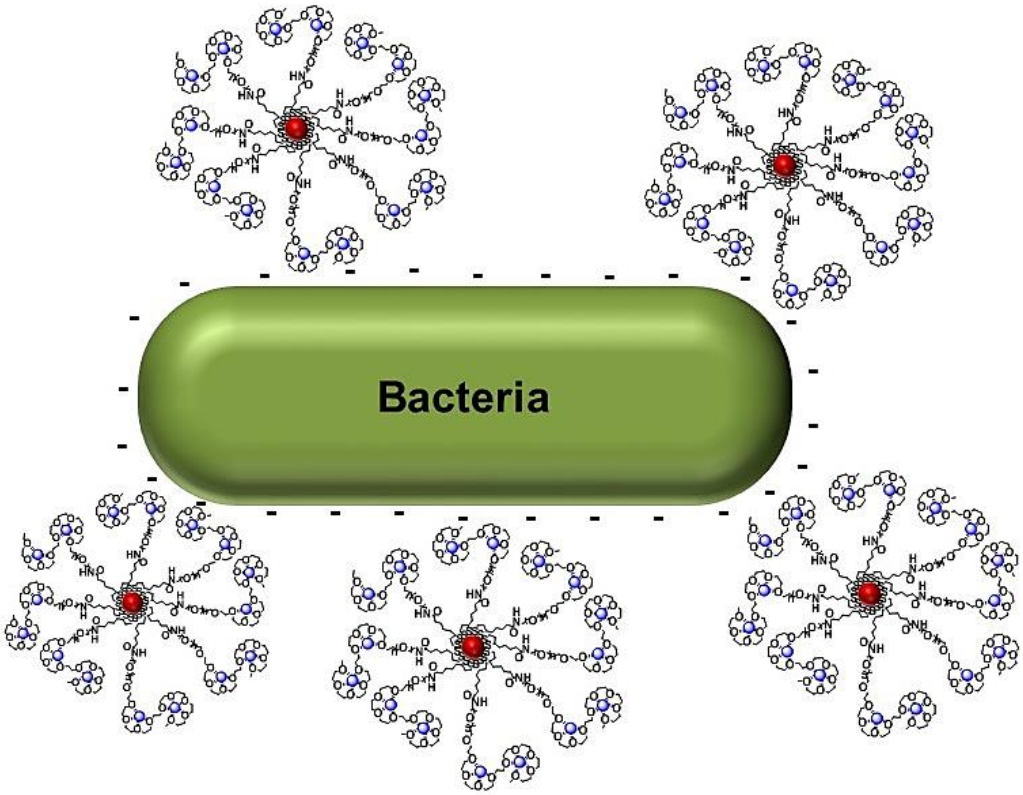

Figure 5-22 (A) Proposed complexation of silver ions (blue spheres) by PEG chains. The silver ions are stabilized by electrostatic interactions. The red sphere is the Ag NP core and only one PEG chain is shown for clarity. (B) The Ag NPs acts as vehicles to transport the Ag ions to the bacterial surface. The Ag NPs are localized sources that continuously release Ag ions to the bacterial membrane which a negative surface charge.

The MIC data obtained for the Ag NCs showed varied antibacterial activities against *S. aureus* and *E.coli*. Moreover, the ICP-MS analysis showed that the Ag^+ concertation released from Ag NPs was higher than the Ag NCs. The clear message here is that the antibacterial property of Ag NC is not solely governed by its size but more importantly to the structure of the ligand, charge of ligand and to the amount of released silver ions. The inherently small size of Ag NC means that most of the Ag atoms are present on surfaces and are capped with stable and functional ligands to ensure colloidal stability. Hence, it may be more difficult for Ag NCs to release Ag^+ ions as compared to Ag NPs. This basic structural difference might explain why the NPs gave better MIC values than the NCs. These results challenges the popular assumption that Ag NCs should possess superior antimicrobial activities over their larger size counterparts (*i.e.* NPs) solely because of their intrinsic ultra-small size[350]. It is assumed that the ultra-small NCs can easily permeate bacterial membranes, causing structural damage to the bacterial membrane and chemical damage by interacting with proteins and DNA and generating ROS inside the bacteria. If size were the primary factor that dictates their antimicrobial efficiency, then all Ag NCs of the same size, irrespective of surface charge and capping agents, would expect to exhibit similar levels of antimicrobial activities against *S. aureus* and *E. coli*. On the contrary, only a few Ag NCs inhibited bacterial growth. This study also confirms the antibacterial activity of Ag NC-DHLA (NC_1) against both gram positive and negative bacteria as reported previously. To the best of our knowledge, this study represents the first report of the antibacterial property of Ag NC-PEG_{23}-OCH_3 (NC_6) against both bacterial strains while Ag NC-PEG_{17}- OCH_3 (NC_5) can only to inhibit *E. coli* bacterial growth.

Ag NPs capped with the same ligands were synthesized in the same protocol and their antibacterial properties were compared to the smaller Ag NCs. Surprisingly, Ag NP system showed better inhibitory effect against *S. aureus* and *E.coli* with the lower MIC values. Interestingly, NP_2 showed a drastic decrease in MIC values from >256 (*i.e.* NC) to 8 $\mu g \cdot mL^{-1}$ (i.e. NP), suggesting that it was transformed from an ineffective to potent antibacterial agent (>~32 fold potency enhancement) by simply increasing the size to the nanoparticle regime. The ICP-MS data showed that the released Ag^+ ion concentration for NC_2 (*i.e* 55) was ~ 11 fold higher than that of NP_2 (*i.e* 5.1 ppb). Interestingly, the zwitterion - stabilized NPs gave the lowest MIC among all the Ag NCs and NP tested despite a rather low Ag^+ ion concentrations (5.09 ppb). The likely

explanation for the high antimicrobial activity of zwitterion-stabilized NP is the increase in monolayer organization of the ligand on the NP surface with the increasing particle size. For example, Murray and colleagues [379] showed that surface curvature decreased with the increasing NP size. The lower surface curvature for larger particles leads to a more densely packed ligand shell [379]. Thus the small size NCs may feature disorganized ligand shells, whereas, larger NPs would have highly organized monolayer surface. The more organized ligand monolayer on the larger NP surface may present more of terminal charged groups towards the bacterial surface, causing stronger membrane damage and bacterial death as shown in **Figure 5-23**. Another possible explanation is the zwitterionic capping agent might have acted synergistically by releasing the silver ions. Although the ICP-MS showed rather low released Ag^+ ion concentrations, but they can still contribute for the antibacterial action.

The NP_3, NP_4, NP_5, and NP_6 can all inhibit the growth of *E. coli*, but only NP_5 and NP_6 can inhibit *S. aureus*. A probable explanation here is the aforementioned differences in the structural makeup of the bacterial membranes which might entail the passage of the Ag^+ ions across the bacterial membranes. Moreover, ICP-MS data showed that NP_6 released higher concentrations of Ag^+ ions which might contribute to its better antibacterial efficacy than NP_5. These observations clearly indicates that the overall antibacterial action of Ag NPs is an interplay of several parameters such as the nature of ligand and release of silver ions. To date, there is still no literature reported on how different ligands regulate the release silver ion from silver nanoclusters and how this affects their antibacterial activities. Thus this study provides an additional understanding on why there is a difference in the antimicrobial activities between Ag NPs and Ag NCs.

(A)

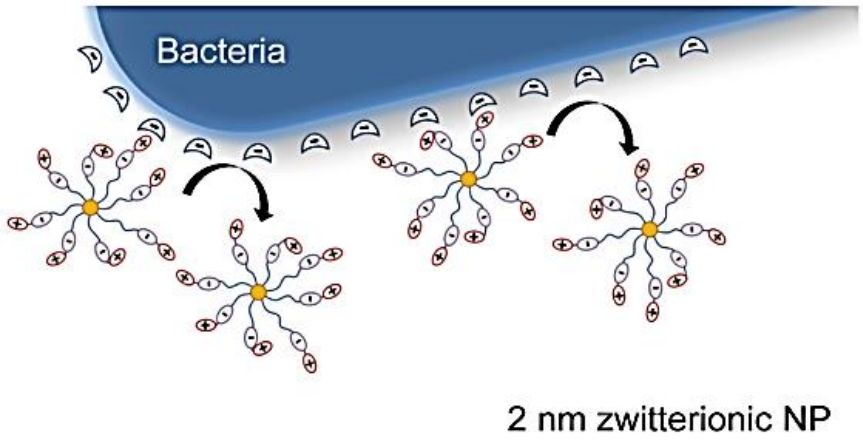

(B)

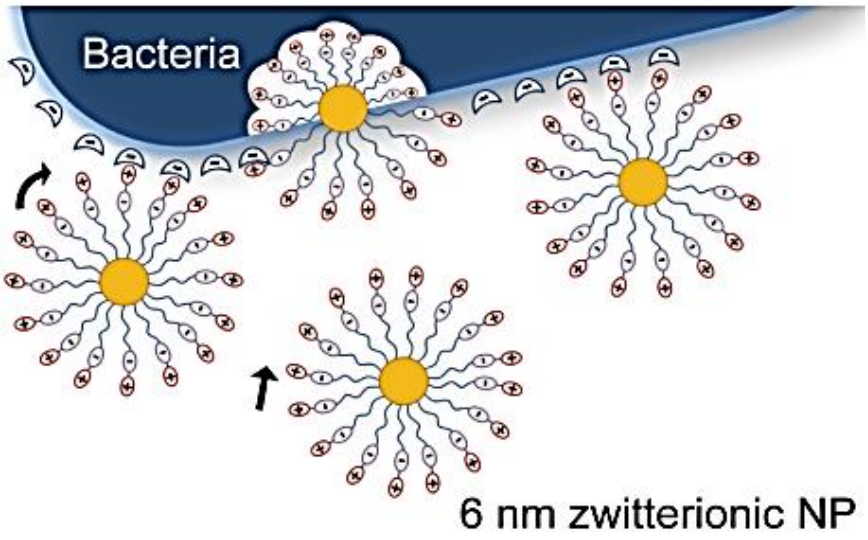

Figure 5-23 Schematic illustration of interaction mechanism between bacterial membrane with (A) 2 nm and (B) 6 nm core sized zwitterionic nanoparticles. Reprinted from reference [362]

To investigate the optimal size for high antibacterial potency, the most potent Ag NP among all investigated (e.g. coated with DHLA-ZW ligands) were synthesized with Ag:L ratio of 1:0.1 (referred to as NP_7) and 1:0.001 (referred to as NP_8). It was assumed that the lower L:Ag ratio should provide less ligands to passivate the Ag NP surface, leading to bigger Ag NPs. The size of the Ag NPs were characterized by and transmission electron microscopy (TEM) and dynamic light scattering technique (DLS). The UV-Vis absorption spectra of Ag NPs were found to be dependent to the

particle size as shown in **Figure 5-24 (A)**. All the DHLA-zwitterion stabilized Ag NPs showed a well-defined SPR band peaked 430 nm for NP_6, 390 nm for NP_7, and 392 nm for NP_8.

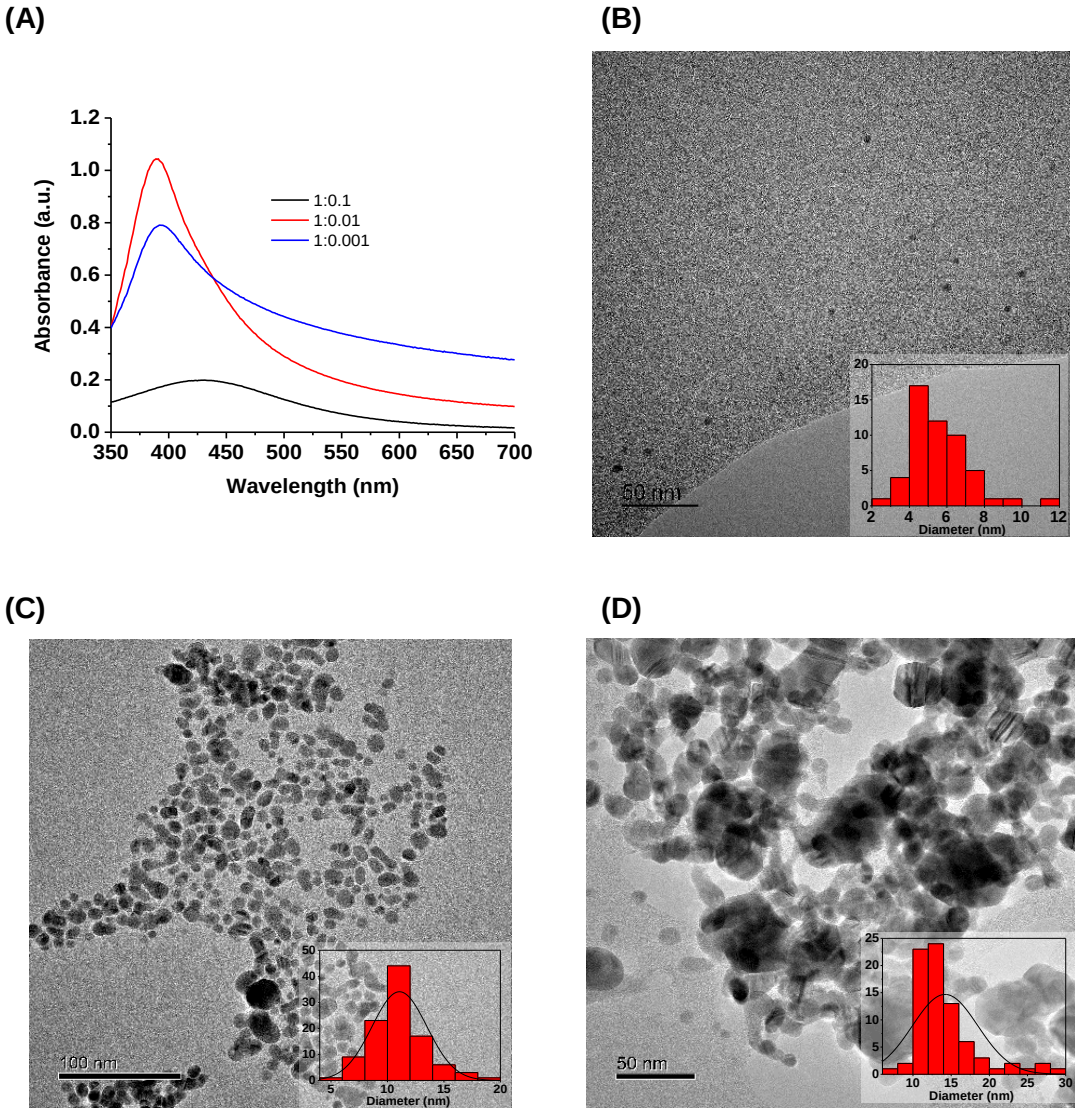

Figure 5-24. (A) UV-Visible absorption spectra of Ag NC-ZW synthesized at different Ag:L ratios. (B-D) TEM images and the corresponding particle size distribution histograms of Ag NC-ZW synthesised at an Ag:L ratio of (B) 1:0.1, (C) 1:0.01, and (D) 1:0.001. The data were collected by W. Ng in Dr. Zhou's group. Reproduced from W. Ng's BSc thesis (2017).

The Ag NPs synthesized at an Ag:L ratio of 1:0.1 appeared as non-aggregated, isolated small spheres as shown in **Figure 5-24 (B)**. The Ag NP (NP_7) synthesized at an Ag:L ratio of 1:0.01 appeared bigger than NP_6 (**Figure 5-24 (C))** A high degree of particle aggregation and large size were observed as the Ag:L ratio was further decreased to 1:0.001 as shown in **Figure 5-24 (D)**. The particle size were measured by *Image J* software of the TEM images and the corresponding particle size distribution histograms revealed a mean size of 5.7 nm for NP_6, 11.1 nm for NP_7 and 14.2 nm for NP_8. These results agreed well with the expectation that reducing the ligand:Ag ratio led to bigger and more aggregated Ag NPs which might have a profound impact in their antibacterial properties.

The Ag NPs were purified by centrifugal filtration to remove unreacted Ag^+ ion and ligand as above. Their D_hs were determined and their antibacterial activities were evaluated against *S. aureus* and *E. coli*. **Table** 5-9 summarised the particle sizes determined using DLS and TEM, the released Ag^+ ion concentration and the MIC data obtained from the Ag NP.

Table 5-9 Particle size, released Ag^+ ion concentration, and MIC values for zwitterion stabilized Ag NP. The data were collected by W. Ng in Dr. Zhou's group. Reproduced from W. Ng's BSc thesis (2017).

Label	D_h (nm)	TEM Diameter (nm)	Ag^+ concentration (ppb)	MIC (μg·mL^{-1})	
				S. aureus	***E. coli***
NP_2	7.5	5.7	5.1	8	8
NP_7	5.8	11.1	2.3	64	64
NP_8	9.9	14.2	13.4	128	128

The NP diameter measured by TEM increased with the reducing L:Ag ratio as expected. Surprisingly, NP_7 showed a lower D_h as compared to NP_6 and NP_8. The larger particle size measured by TEM is most likely due to the particle aggregation that makes accurate size determination difficult. All three Ag NPs inhibited the growth of *E.coli* and *S. aureus* but to different extents and NP_6 showed the highest potency. Considering that all three Ag NPs were coated with the same ligand, the most

possible reason for their different antibacterial activity were the size and morphology of the nanoparticles. The size of the Ag NP has been one of the most studied parameters impacting their antibacterial property [380-382]. A recent study on different size Ag NPs coated the same surface coating revealed that Ag NPs with diameters of < 10 nm exhibited potent antibacterial activities and those of 5 nm were optimal, showing the best antibacterial result and fastest bactericidal activity [332]. The MIC results obtained in this study also agreed well with the previous literature on size–dependent antibacterial potencies of Ag NPs towards *S. aureus* and *E. coli*. Furthermore, this is the first report of sulfobetaine based zwitterionic ligand capped Ag NPs as potent antimicrobial agents.

5.5 Conclusion

The synthesis of Ag NCs and Ag NPs bearing similar types of ligands by a common synthetic protocol provided a useful means of directly comparing their antibacterial properties. The MIC data revealed a varying degree of antibacterial effectiveness of the silver nanomaterials wherein only a few Ag NCs tested gave significant inhibitory effect against *E. coli* and *S. aureus*. On the contrary, most of the Ag NPs tend to be more effective antimicrobial agents. Interestingly, this study found that the ultra-small size does not primarily dictate the antibacterial efficiency of the nanoclusters. Instead, the antibacterial actions are governed by an interplay of parameters such as surface ligand structures and the amount of released silver ions. The Ag NP stabilized with zwitterionic ligands bearing the sulfobetaine group is the most potent antibacterial agent among all the ligands tested. Furthermore, their antibacterial potency decreases with the increasing particle size, with 5.7 nm giving the highest inhibition potency. While this study has successfully demonstrated, for the first time, that the antibacterial properties of silver nanomaterials differ significantly when coated with different ligands, more studies will be required to investigate the mechanisms of their anti-bacterial actions. Considering the superior antibacterial activity of the zwitterionic Ag NPs, these nanoparticles may be utilized effectively as coating for various surgical instruments and medical equipment.

Chapter 6

General Conclusions and Future Work Suggestions

6.1 General Conclusions

The first part of the thesis reports the development of a magnetic nanoparticle (MNP)-based DNA sensing technology that is suitable for rapid and sensitive detection of disease biomarkers such as cancer related single nucleotide polymorphisms (SNPs). In Chapter 2, a PEGylated amphiphilic polymer encapsulated MNP-DNA probe has been successfully developed for ultrasensitive DNA detection. The amphiphilic polymer was prepared by grafting amino-PEG_n-azide and amino-PEG_n-OCH_3 onto the hydrophobic PMAO polymer. This successfully introduced not only hydrophilic PEG segments but also functional azide groups for further conjugation with a capture DNA. The polymer encapsulated MNPs were stable over a wide pH range (pH 2-12), temperature (25 ^oC-70^oC), and in aqueous media containing high salt contents and over prolonged storage of 6 months. The capture DNA was successfully conjugated to the MNP by copper-free “click” reaction between the MNP surface azide moiety and the DBCO-group of the capture DNA. Using a DNA sandwich strategy coupled with a ligation step to convert each ligated target-DNA into an active HRP enzyme, the MNP-DNA sensor could offer a limit of detection (LOD) of ~1.0 pM for the perfect-match target-DNA. This sensor also offered excellent SNP discrimination between the full-match wild type target-DNA (T1) and cancer related SPNs with a discrimination ratio of ~14.3 and ~16.8 for T2 (cancer SNP-1) and T3 (cancer SNP-2), respectively before background correction. Moreover, a more powerful signal amplification strategy was developed by tagging a polymer nanobead (PB) with thousands of copies of NAV-HRP. By coupling the MNP-based DNA sandwich assay with the poly-enzyme PB amplification, I have demonstrated the successful quantification of the unlabelled target-DNA down to 10 attomolar with a large linear dynamic range of 5 orders of magnitude. Furthermore, the biosensor was highly specific and could specifically detect 1 fM full-match target-DNA (T1) even in the presence of 100 fold excess of SNP targets (T2 or T3).

In Chapter 3, a new MNP-DNA-enzyme based nanoprobe was designed for detection of nuclease (*e.g.* ECOR-I) and target-DNA. Firstly, amino modified Fe_3O_4-SiO_2 core-shell MNPs were prepared, characterised and modified by reacting with NHS-PEG_{22}-Azide ligand and further blocked with NHS-PEG_{17}-OCH_3. The introduction of the azide moiety provided means for DNA bioconjugation though copper free click chemistry approach. Two different designs of the MNP-DNA-HRP probes were prepared. Specifically, Design-1 probe used the non-covalent neutravidin – biotin interaction to link NAV- HRP to the MNP-DNA-Biotin. Design-2 probe, the maleimide labelled HRP was linked to the MNP-DNA-SH through the thiol-maleimide Michael addition. The hybridization of the target-DNA to the MNP-DNA-HRP formed a specific double-stranded DNA sequence that could be recognized and cleaved specifically by the endo-nuclease ECOR-I. This step released the HRP label into the solution for target quantification via an HRP catalysed colorimetric reaction. The Incubation temperature and time with ECOR-I was optimized. Using Design-2, the developed biosensor can detect ECOR-I at 10 $U \cdot mL^{-1}$ and can detect a perfectly matched target-DNA at ~1 nM concentration.

The second part of thesis presented the preliminary findings on the antimicrobial properties of Ag nanoparticles (NPs) and nanoclusters (NCs). First, a series of thioctic acid (TA)- based ligands with different terminal hydrophilic groups were synthesized and characterized in Chapter 5. These ligands were used to prepare the Ag nanomaterials by $NaBH_4$ reduction of $AgNO_3$ and the particle size could be controlled via the Ag:Ligand (Ag:L) ratio. The low Ag:L ratios (e.g. ≤ 1) resulted in the formation of Ag NCs and while Ag NPs were obtained at higher Ag:L ratios (e.g. >10). The optical properties (*i.e.* absorption and fluorescence), particle size, and surface charge of the Ag NCs and NPs were determined by UV-Vis and fluorescence spectroscopy, dynamic light scattering, zeta potential and agarose gel electrophoresis, respectively. The antibacterial efficacy of the Ag nanomaterials was determined by the minimum inhibitory concertation (MIC) assay. The Ag NC surface ligand was found to have a profound effect on its antibacterial potency: only those capped DHLA and DHLA-PEG_{-23}-OCH_3 could effectively inhibit the growth of *S. aureus* and *E.coli*. Interestingly, the Ag NPs exhibited significantly lower MIC values over their Ag NC counterparts, implying that the former posed better antibacterial properties. Among these, Ag NP-Zwitterion displayed the lowest MIC, suggesting

strong antimicrobial potency against the test organisms. Moreover, different sized Ag NP-Zwitterions were prepared and their antibacterial properties tested, revealing that Ag NP-Zwitterion of ~ 6 nm exhibited the most potent antimicrobial effect. This study provided a detailed investigation on how surface capping ligands affect the antimicrobial potency of both Ag NCs and Ag NPs and provided the fundamental evidence of the difference in antimicrobial activities between Ag NCs and Ag NPs.

6.2 Future Work Suggestions

1. In Chapter 2, a nanoparticle-DNA sensing technology suitable for fast and sensitive detection of a disease biomarker such as cancer related single nucleotide polymorphisms (SNPs) was developed. The biosensor demonstrated excellent sensitivity and selectivity in detecting cancer specific SNPs (KRAS codon 12/13) against wild-type non-cancerous target that makes it very attractive and potential useful for early cancer diagnosis. However, it still remained at the proof-of-principle stage where all sensing experiments were carried out using synthetic DNA samples rather than real clinical targets. Therefore, further efforts should be directed on the clinical validation of the developed biosensor.

2. In Chapter 3, two MNP-DNA_{ss}-HRP probes were designed. Future research should focus on improving the biosensor performance of the MNP-DNA_{ds}-HRP Design-2 probe. One possible solution is to use azide modified silica coated magnetic microparticle (MMP) to improve the magnetic retrieval for easier sample retrieval (e.g. removal of any uncut MMP-HRPs). In this study, the ECOR-I can cut any of the double stranded DNA which may or may not be linked with HRP. Thus, an alternative way of covalently linking the HRP to the MNP beads can also be taken into consideration. The proposed method involve the labelling of HRP with NHS-PEG_{12}-Maleimide followed by incubation with the DBCO-DNA-SH. The HRP-DNA-DBCO conjugates can be purified by gel electrophoresis before conjugation to the azide modified MMPs. In this manner, all of the DNA strands linked to the MMP will contain an HRP moiety, ensuring that all ECOR-I cutting events will release an HRP to the solution for signal amplification. As a result, this would improve the sensitivity in both ECOR-I and DNA detection.

Once the DNA strands are covalently linked with HRP is ensured, work can also be carried out to detect cancer related microRNAs via a similar detection strategy. The target miRNA hybridizes with complementary DNA to form a DNA/RNA hetero-duplex, which can be specifically cleaved by duplex-specific nuclease (DSN), leading to the release of NAV-HRP in the solution. The supernatant can be collected to detect the target miRNA using the same HRP catalysed Amplex red- H_2O_2 assay.

3. Chapter 5 presented some preliminary results on the antimicrobial properties of Ag NPs and Ag NCs coated with different DHLA-based functional ligands. Despite some encouraging results, more repeat measurements on the release of silver ions from the Ag nanomaterials is needed to ensure that the measured data are accurate. Further work on antibacterial characterizations are necessary to fully evaluate the antibacterial efficiency of the Ag nanomaterials. Work should also be carried out in the direction of elucidating the mechanisms of bacterial death. For example, TEM imaging can be employed to provide evidences about the integrity of the bacterial membrane after incubation with the Ag nanomaterials. Moreover, fluorescence microscopy could be carried out to assess Ag NC uptake in bacterial cells, taking the full advantage of their fluorescence properties. The information gathered from these experiments will deepen our understanding on the difference of antibacterial activities between Ag NPs and Ag NCs.

   Vancomycin is considered the “antibiotic of last resort”[383] due to its effectiveness in treating severe infections caused by gram positive bacteria. Vancomycin acts as inhibitor for the cell-wall biosynthesis by binding to the bacterial cell wall D-*Ala*-D-*Ala* terminal by forming five hydrogen bonds[384] as shown in **Figure 6-1 (A)**. The vancomycin binding effectively prevents the incorporation of N-acetylmuramic acid (NAM) and N-acetylglucoasmine (NAG)-peptide subunits from binding into the peptidoglycan (PG) layer [385]. The peptidoglycan matrix is essential for the bacteria to survive because it acts as an exoskeleton that prevents the bacteria from rupturing due to internal pressure[385]. The emergence of vancomycin-resistant Enterococci (VRE) and methicillin-resistant Staphylococcus aureus (MRSA) has caused a major global health issue. The ineffectiveness of vancomycin against VRE and MRSA is due to the D-*Ala*-D-*Lac* bacterial cell wall terminal[384] as shown in **Figure 6-1 (B)**. The change of the D-Alanine to D-Lactate results in a deletion

of one hydrogen bond and leads to lower binding affinity for Vancomycin by ~1000 fold making it therapeutically useless.[386]

(A)

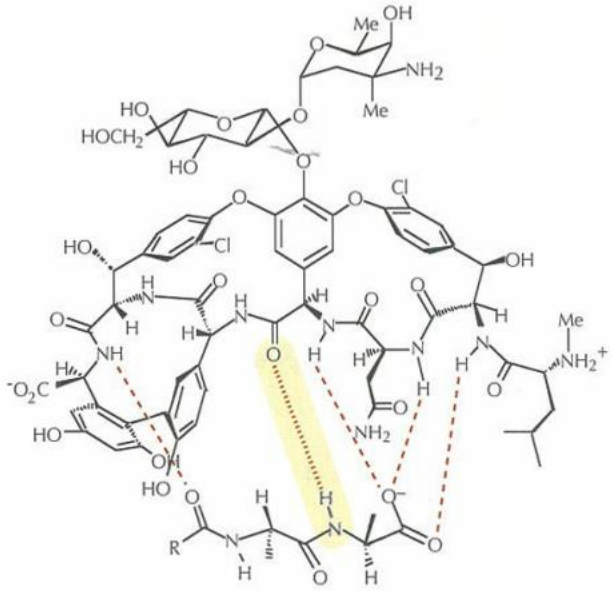

(B)

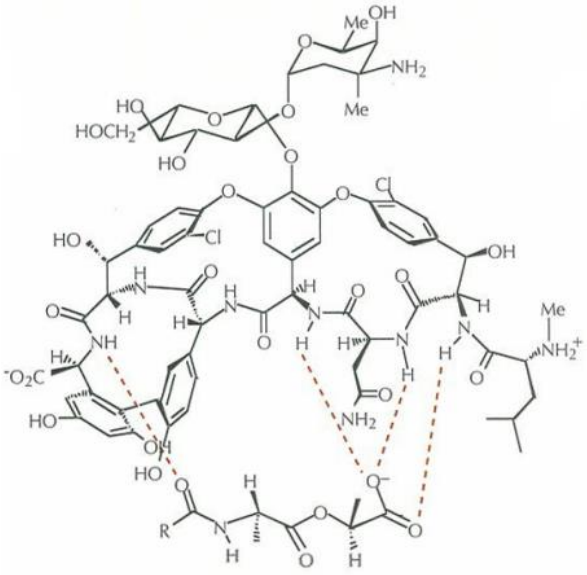

Figure 6-1 (A) Vancomycin complex with N-Acyl-D-*Ala*-D-*Ala* and (B) Vancomycin complex with N-Acyl-D-*Ala*-D-*Lactate*. The hydrogen bond highlighted in yellow is lost in the D-*Ala*-D-*Lactate* complex resulting in less than one hydrogen bond which lead to a lower binding affinity. Reprinted from reference[384]

Improving the antibacterial efficiency of vancomycin can further be achieved developing novel polyvalent multifunctional nanoparticle (PMN) strategy to exploit multivalency and unique properties of silver nanoparticles to overcome multi-drug resistance in bacteria. This can be done by modifying existing antibiotics (e.g. vancomycin) with a thiotic acid-PEG-linker and conjugate multiple such ligands onto the Ag NP as shown in **Figure 6-2**. The multivalent binding could greatly enhance the binding affinity of the Ag NP-(Vancomycin)$_n$ to the bacterial surface, thus, allowing it to overcome the vancomycin resistance in microorganisms[386].

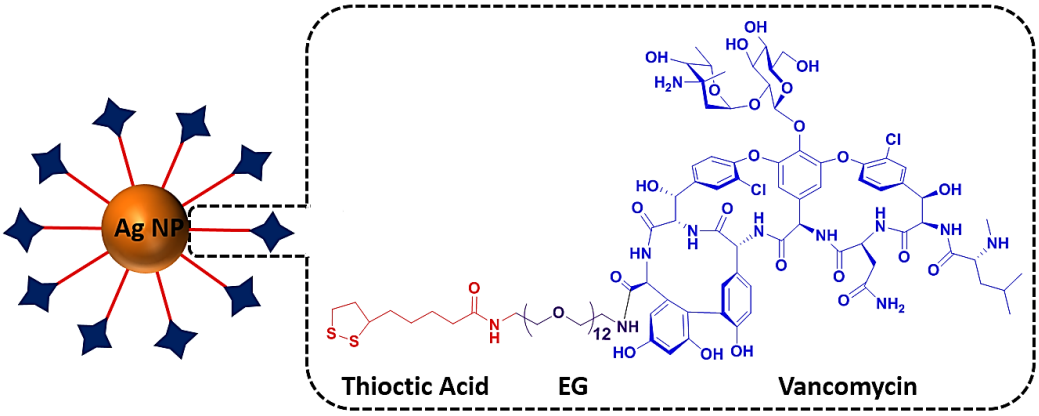

Figure 6-2. Schematic illustration of Ag NP coated with vancomycin ligand. The ligand contains a thioctic acid group for binding to the Ag NP surface, ethylene glycol (EG) spacer group, and the vancomycin molecule. Multi- and polyvalent ligands are expected to exhibit more effective in interaction bacterial cells.

References

1. I. S. M. W. Group, *Nature*, 2001, **409**, 928.
2. D. G. Wang, J.-B. Fan, C.-J. Siao, A. Berno, P. Young, R. Sapolsky, G. Ghandour, N. Perkins, E. Winchester and J. Spencer, *Science*, 1998, **280**, 1077-1082.
3. H. Erichsen and S. Chanock, *British Journal of Cancer*, 2004, **90**, 747-751.
4. D. Botstein and N. Risch, *Nature Genetics*, 2003, **33**, 228.
5. C. S. Carlson, M. A. Eberle, M. J. Rieder, J. D. Smith, L. Kruglyak and D. A. Nickerson, *Nature Genetics*, 2003, **33**, 518-521.
6. M. Monot, N. Honoré, T. Garnier, R. Araoz, J.-Y. Coppée, C. Lacroix, S. Sow, J. S. Spencer, R. W. Truman and D. L. Williams, *Science*, 2005, **308**, 1040-1042.
7. D. Zhang, J. Ma, K. Brismar, S. Efendic and H. F. Gu, *Journal of Diabetes and its Complications*, 2009, **23**, 265-272.
8. Y. Suh and J. Vijg, *Mutation Research/Fundamental and Molecular Mechanisms of Mutagenesis*, 2005, **573**, 41-53.
9. B. N. Chorley, X. Wang, M. R. Campbell, G. S. Pittman, M. A. Noureddine and D. A. Bell, *Mutation Research/Reviews in Mutation Research*, 2008, **659**, 147-157.
10. J. Robert, V. Le Morvan, D. Smith, P. Pourquier and J. Bonnet, *Critical Reviews in Oncology/Hematology*, 2005, **54**, 171-196.
11. B. Rahim-Williams, J. L. Riley, A. K. Williams and R. B. Fillingim, *Pain Medicine*, 2012, **13**, 522-540.
12. J. Liu, C. He, C. Xing and Y. Yuan, *Mutation Research/Fundamental and Molecular Mechanisms of Mutagenesis*, 2014, **765**, 11-21.
13. A. Figl, D. Scherer, E. Nagore, J. L. Bermejo, E. Dickes, R. K. Thirumaran, A. Gast, K. Hemminki, R. Kumar and D. Schadendorf, *Mutation Research/Fundamental and Molecular Mechanisms of Mutagenesis*, 2009, **661**, 78-84.
14. M. Oliveira-Cunha, K. D. Hadfield, A. K. Siriwardena and W. Newman, *Pancreas*, 2012, **41**, 428-434.
15. J. M. Ostrem, U. Peters, M. L. Sos, J. A. Wells and K. M. Shokat, *Nature*, 2013, **503**, 548-551.

16. O. I. Stenina, T. V. Byzova, J. C. Adams, J. J. McCarthy, E. J. Topol and E. F. Plow, *The International Journal of Biochemistry and Cell Biology*, 2004, **36**, 1013-1030.
17. F. Coppedè, C. Armani, D. Della Bidia, L. Petrozzi, U. Bonuccelli and L. Migliore, *Mutation Research/Fundamental and Molecular Mechanisms of Mutagenesis Mutation*, 2005, **579**, 107-114.
18. B. Roy, N. Maksemous, R. A. Smith, S. Menon, G. Davies and L. R. Griffiths, *Mutation Research/Fundamental and Molecular Mechanisms of Mutagenesis Mutation*, 2012, **732**, 3-8.
19. Z. Hu, J. Chen, T. Tian, X. Zhou, H. Gu, L. Xu, Y. Zeng, R. Miao, G. Jin and H. Ma, *The Journal of Clinical Investigation*, 2008, **118**, 2600.
20. B. M. Ryan, A. I. Robles and C. C. Harris, *Nature Reviews Cancer*, 2010, **10**, 389-402.
21. M. M. Mhlanga and L. Malmberg, *Methods*, 2001, **25**, 463-471.
22. Y. V. Gerasimova and D. M. Kolpashchikov, *Chemical Society Reviews*, 2014, **43**, 6405-6438.
23. L. J. Chin, E. Ratner, S. Leng, R. Zhai, S. Nallur, I. Babar, R.-U. Muller, E. Straka, L. Su and E. A. Burki, *Cancer Research*, 2008, **68**, 8535-8540.
24. D. Dressman, H. Yan, G. Traverso, K. W. Kinzler and B. Vogelstein, *Proceedings of the National Academy of Sciences*, 2003, **100**, 8817-8822.
25. S. Kim, H. D. Ruparel, T. C. Gilliam and J. Ju, *Nature Reviews Genetics*, 2003, **4**, 1001.
26. J. M. Butler, *Advanced Topics in Forensic DNA Typing: Methodology: Methodology*, Academic Press, 2011.
27. R. Twyman, *Encyclopedia of Neuroscience*, 2009, **8**, 881-885.
28. M. L. Ermini, S. Mariani, S. Scarano and M. Minunni, *Biosensors and Bioelectronics*, 2014, **61**, 28-37.
29. P. D. Howes, S. Rana and M. M. Stevens, *Chemical Society Reviews*, 2014, **43**, 3835-3853.
30. W. Shen, C. Le Lim and Z. Gao, *Chemical Communications*, 2013, **49**, 8114-8116.
31. X. Chen, A. Ying and Z. Gao, *Biosensors and Bioelectronics*, 2012, **36**, 89-94.
32. C. Bui, E. Nicolas, G. Sallmann, M. Chiotis, A. Lambrinakos, K. Rees, I. Trounce, R. G. Cotton, L. Blakesley and A. K. Godwin, *Molecular Diagnostics*, 2009, 29.

33. H. Zhang, X. Fu, L. Liu, Z. Zhu and K. Yang, *Analytical Biochemistry*, 2012, **426**, 30-39.
34. F. Kakihara, Y. Kurebayashi, Y. Tojo, H. Tajima, S. Hasegawa and M. Yohda, *Analytical Biochemistry*, 2005, **341**, 77-82.
35. H. A. Ho, K. Doré, M. Boissinot, M. G. Bergeron, R. M. Tanguay, D. Boudreau and M. Leclerc, *Journal of the American Chemical Society*, 2005, **127**, 12673-12676.
36. H. A. Ho, M. Boissinot, M. G. Bergeron, G. Corbeil, K. Doré, D. Boudreau and M. Leclerc, *Angewandte Chemie*, 2002, **114**, 1618-1621.
37. S. Wang and G. C. Bazan, *Advanced Materials*, 2003, **15**, 1425-1428.
38. B. Liu, S. Baudrey, L. Jaeger and G. C. Bazan, *Journal of American Chemical Society*, 2004, **126**, 4076-4077.
39. B. Liu and G. C. Bazan, *Chemistry of Materials*, 2004, **16**, 4467-4476.
40. S. W. Thomas, G. D. Joly and T. M. Swager, *Chemical Reviews*, 2007, **107**, 1339-1386.
41. J. Garcia, Y. Zhang, H. Taylor, O. Cespedes, M. E. Webb and D. Zhou, *Nanoscale*, 2011, **3**, 3721-3730.
42. W. Shen, H. Deng and Z. Gao, *Journal of American Chemical Society*, 2012, **134**, 14678-14681.
43. L. Qiu, L. Qiu, H. Zhou, Z. Wu, G. Shen and R. Yu, *New Journal of Chemistry*, 2014, **38**, 4711-4715.
44. W. Xu, X. Xie, D. Li, Z. Yang, T. Li and X. Liu, *Small*, 2012, **8**, 1846-1850.
45. L. Tang, I. S. Chun, Z. Wang, J. Li, X. Li and Y. Lu, *Analytical Chemistry*, 2013, **85**, 9522-9527.
46. C.-H. Liu, Z.-P. Li, B.-A. Du, X.-R. Duan and Y.-C. Wang, *Analytical Chemistry*, 2006, **78**, 3738-3744.
47. W. Xu, X. Xue, T. Li, H. Zeng and X. Liu, *Angewandnte Chemie International Edition*, 2009, **48**, 6849-6852.
48. C.-Y. Zhang, H.-C. Yeh, M. T. Kuroki and T.-H. Wang, *Nature Materials*, 2005, **4**, 826-831.
49. H. Ji, F. Yan, J. Lei and H. Ju, *Analytical Chemistry*, 2012, **84**, 7166-7171.
50. G. Liu, T. M. Lee and J. Wang, *Journal of the American Chemical Society*, 2005, **127**, 38-39.
51. G. Liu and Y. Lin, *Journal of the American Chemical Society*, 2007, **129**, 10394-10401.

52. Y. Zhang, C. Pilapong, Y. Guo, Z. Ling, O. Cespedes, P. Quirke and D. Zhou, *Analytical Chemistry*, 2013, **85**, 9238-9244.
53. S. Bi, L. Li and S. Zhang, *Analytical Chemistry*, 2010, **82**, 9447-9454.
54. F. Patolsky, Y. Weizmann, E. Katz and I. Willner, *Angewandnte Chemie International Edition*, 2003, **42**, 2372-2376.
55. S. Bi, Z. Zhang, Y. Dong and Z. Wang, *Biosensors and Bioelectronics*, 2014, **65C**, 139-144.
56. Y. Zhang, Y. Guo, P. Quirke and D. Zhou, *Nanoscale*, 2013, **5**, 5027-5035.
57. M. Luo, X. Chen, G. Zhou, X. Xiang, L. Chen, X. Ji and Z. He, *Chemical Communications*, 2012, **48**, 1126-1128.
58. D. Brouard, M. L. Viger, A. G. Bracamonte and D. Boudreau, *ACS Nano*, 2011, **5**, 1888-1896.
59. D. Brouard, O. Ratelle, A. G. Bracamonte, M. St-Louis and D. Boudreau, *Analytical Methods*, 2013, **5**, 6896.
60. D. Brouard, O. Ratelle, J. Perreault, D. Boudreau and M. St-Louis, *Vox Sanguinis*, 2015, **108**, 197-204.
61. N. Li, J. Zhang, Y. Liang, J. Shao, F. Peng, M. Sun, N. Xu, X. Li, R. Wang and S. Liu, *Journal of Proteome Research*, 2007, **6**, 3304-3312.
62. Y. Zhao, L. Xu, W. Ma, L. Wang, H. Kuang, C. Xu and N. A. Kotov, *Nano Letters*, 2014, **14**, 3908-3913.
63. D. Kato and M. Oishi, *ACS Nano*, 2014, **8**, 9988-9997.
64. Y.-p. Zeng, G. Zhu, X.-y. Yang, J. Cao, Z.-l. Jing and C.-y. Zhang, *Chemical Communications*, 2014, **50**, 7160-7162.
65. J.-M. Nam, S. I. Stoeva and C. A. Mirkin, *Journal of the American Chemical Society*, 2004, **126**, 5932-5933.
66. J. Hu, X. Hou and P. Wu, *Journal of Analytical Atomic Spectrometry*, 2015, **30**, 888-894.
67. C. Ding, Z. Wang, H. Zhong and S. Zhang, *Biosensors and Bioelectronics*, 2010, **25**, 1082-1087.
68. R. D'Agata, G. Breveglieri, L. M. Zanoli, M. Borgatti, G. Spoto and R. Gambari, *Analytical Chemistry*, 2011, **83**, 8711-8717.
69. J. Zhou, Q.-x. Wang and C.-y. Zhang, *Journal of the American Chemical Society*, 2013, **135**, 2056-2059.
70. L. Yan, J. Zhou, Y. Zheng, A. S. Gamson, B. T. Roembke, S. Nakayama and H. O. Sintim, *Molecular BioSystems*, 2014, **10**, 970-1003.
71. J. Kim and C. J. Easley, *Bioanalysis*, 2011, **3**, 227-239.

72. X. Duan, L. Liu and S. Wang, *Biosensors and Bioelectronics*, 2009, **24**, 2095-2099.
73. X. Wu, L. Xu, L. Liu, W. Ma, H. Yin, H. Kuang, L. Wang, C. Xu and N. A. Kotov, *Journal of the American Chemical Society*, 2013, **135**, 18629-18636.
74. W. Ma, H. Kuang, L. Xu, L. Ding, C. Xu, L. Wang and N. A. Kotov, *Nature Communications*, 2013, **4**.
75. Z. Zou, Z. Qing, X. He, K. Wang, D. He, H. Shi, X. Yang, T. Qing and X. Yang, *Talanta*, 2014, **125**, 306-312.
76. S. Zhang, Z. Wu, G. Shen and R. Yu, *Biosensors and Bioelectronics*, 2009, **24**, 3201-3207.
77. Y. Cheng, Z. Li, X. Zhang, B. Du and Y. Fan, *Analytical Biochemistry*, 2008, **378**, 123-126.
78. Y. Chen, M. Yang, Y. Xiang, R. Yuan and Y. Chai, *Analytica Chimica Acta*, 2013, **796**, 1-6.
79. C. Cheng, J. Wang, C. Yang, Y. Zhou, J. Chen, J. Zhang, N. Jia, H. Cao and G. Zhao, *Analytical Biochemistry*, 2013, **434**, 34-38.
80. A. V. Demchinskaya, I. A. Shilov, A. S. Karyagina, V. G. Lunin, O. V. Sergienko, O. L. Voronina, M. Leiser and L. Plobner, *Journal of Biochemical and Biophysical Methods*, 2001, **50**, 79-89.
81. Y. Cheng, J. Zhao, H. Jia, Z. Yuan and Z. Li, *The Analyst*, 2013, **138**, 2958-2963.
82. D. Giljohann, D. Seferos, W. Daniel, M. Massich, P. Patel and C. Mirkin, *Angewandte Chemie International Edition*, 2010, **49**, 3280-3294.
83. Y. Sato, K. Sato, K. Hosokawa and M. Maeda, *Analytical Biochemistry*, 2006, **355**, 125-131.
84. R. M. Dirks and N. A. Pierce, *Proceedings of the National Academy of Sciences of the United States of America*, 2004, **101**, 15275-15278.
85. P. Liu, X. Yang, S. Sun, Q. Wang, K. Wang, J. Huang, J. Liu and L. He, *Analytical Chemistry*, 2013, **85**, 7689-7695.
86. J. Ikbal, G. S. Lim and Z. Gao, *TrAC Trends in Analytical Chemistry*, 2015, **64**, 86-99.
87. F. Xuan and I.-M. Hsing, *Journal of the American Chemical Society*, 2014, **136**, 9810-9813.
88. L. Jia, S. Shi, R. Ma, W. Jia and H. Wang, *Biosensors and Bioelectronics*, 2016, **80**, 392-397.

89. S. Bi, M. Chen, X. Jia, Y. Dong and Z. Wang, *Angewandte Chemie International Edition*, 2015, **54**, 8144-8148.
90. H.-L. Shuai, K.-J. Huang and Y.-X. Chen, *Journal Materials Chemistry B*, 2016, **4**, 1186-1196.
91. D. Wu, B.-C. Yin and B.-C. Ye, *Biosensors and Bioelectronics*, 2011, **28**, 232-238.
92. J. Lei and H. Ju, *Chemical Society Reviews*, 2012, **41**, 2122-2134.
93. T. A. Taton, *Science*, 2000, **289**, 1757-1760.
94. H. T. Ngo, N. Gandra, A. M. Fales, S. M. Taylor and T. Vo-Dinh, *Biosensors and Bioelectronics*, 2016, **81**, 8-14.
95. C. Zhang, J. Lou, W. Tu, J. Bao and Z. Dai, *Analyst*, 2015, **140**, 506-511.
96. X. Li, J. Song, Q. Xue, H. Zhao, M. Liu, B. Chen, Y. Liu, W. Jiang and C.-z. Li, *Analyst*, 2017, **142**, 3598-3604.
97. R. De La Rica and M. M. Stevens, *Nature Nanotechnology*, 2012, **7**, 821-824.
98. L. Rodríguez-Lorenzo, R. de La Rica, R. A. Álvarez-Puebla, L. M. Liz-Marzán and M. M. Stevens, *Nature Materials*, 2012, **11**, 604-607.
99. L. Rodriguez-Lorenzo, R. de la Rica, R. A. Alvarez-Puebla, L. M. Liz-Marzan and M. M. Stevens, *Nature Materials*, 2012, **11**, 604-607.
100. C. Zhang and D. Xing, *Chemical Reviews*, 2010, **110**, 4910-4947.
101. J. Zhu, C. Qiu, M. Palla, T. Nguyen, J. J. Russo, J. Ju and Q. Lin, *RSC Advances*, 2014, **4**, 4269-4277.
102. P. S. Heeger and A. J. Heeger, *Proceedings of the National Academy of Sciences*, 1999, **96**, 12219-12221.
103. N. Green, *Biochemical Journal*, 1963, **89**, 585.
104. E. A. Bayer, H. Ben-Hur, Y. Hiller and M. Wilchek, *Biochemical Journal*, 1989, **259**, 369.
105. M. Wilchek, E. A. Bayer and O. Livnah, *Immunology Letters*, 2006, **103**, 27-32.
106. T. Sano and C. R. Cantor, *Proceedings of the National Academy of Sciences*, 1995, **92**, 3180-3184.
107. P. Vermette, T. Gengenbach, U. Divisekera, P. A. Kambouris, H. J. Griesser and L. Meagher, *Journal of Colloid and Interface Science*, 2003, **259**, 13-26.
108. A. K. Gupta and M. Gupta, *Biomaterials*, 2005, **26**, 3995-4021.
109. N. Lee and T. Hyeon, *Chemical Society Reviews*, 2012, **41**, 2575-2589.
110. A. Akbarzadeh, M. Samiei and S. Davaran, *Nanoscale Research Letters*, 2012, **7**, 144.

111. H. Gu, P.-L. Ho, K. W. Tsang, L. Wang and B. Xu, *Journal of the American Chemical Society*, 2003, **125**, 15702-15703.
112. H.-Y. Xie, R. Zhen, B. Wang, Y.-J. Feng, P. Chen and J. Hao, *The Journal of Physical Chemistry C*, 2010, **114**, 4825-4830.
113. J.-C. Leroux, *Nature Nanotechnology*, 2007, **2**, 679-684.
114. H. B. Na, I. C. Song and T. Hyeon, *Advanced Materials*, 2009, **21**, 2133-2148.
115. J.-H. Lee, J.-t. Jang, J.-s. Choi, S. H. Moon, S.-h. Noh, J.-w. Kim, J.-G. Kim, I.-S. Kim, K. I. Park and J. Cheon, *Nature Nanotechnology*, 2011, **6**, 418-422.
116. J. Gao, H. Gu and B. Xu, *Accounts of Chemical Research*, 2009, **42**, 1097-1107.
117. S. Singamaneni, V. N. Bliznyuk, C. Binek and E. Y. Tsymbal, *Journal of Materials Chemistry*, 2011, **21**, 16819-16845.
118. C. Yang, J. Wu and Y. Hou, *Chemical Communications*, 2011, **47**, 5130-5141.
119. L. Zhou, J. Yuan and Y. Wei, *Journal of Materials Chemistry*, 2011, **21**, 2823-2840.
120. T. Hyeon, *Chemical Communications*, 2003, 927-934.
121. V. Iacovacci, G. Lucarini, L. Ricotti and A. Menciassi, in *Lab-on-a-Chip Fabrication and Application*, InTech, Editon edn., 2016.
122. J. M. Drijvers, I. M. Awan, C. A. Perugino, I. M. Rosenberg and S. Pillai, in *Basic Science Methods for Clinical Researchers*, Elsevier, Editon edn., 2016, pp. 119-133.
123. R. H. Yolken, *The Yale Journal of Biology and Medicine*, 1980, **53**, 85.
124. M.-P. Zhao, Y.-Z. Li, Z.-Q. Guo, X.-X. Zhang and W.-B. Chang, *Talanta*, 2002, **57**, 1205-1210.
125. G. Song, C. Chen, J. Ren and X. Qu, *ACS Nano*, 2009, **3**, 1183-1189.
126. X. Xu, M. S. Han and C. A. Mirkin, *Angewandte Chemie*, 2007, **119**, 3538-3540.
127. R. M. DuBois, P. J. Slavish, B. M. Baughman, M.-K. Yun, J. Bao, R. J. Webby, T. R. Webb and S. W. White, *PLoS Pathogens*, 2012, **8**, e1002830.
128. B. Polisky, P. Greene, D. E. Garfin, B. J. McCarthy, H. M. Goodman and H. W. Boyer, *Proceedings of the National Academy of Sciences*, 1975, **72**, 3310-3314.
129. Y. Li, Y. Li, Y. Wu, F. Lu, Y. Chen and W. Gao, *Biosensors and Bioelectronics*, 2017, **89**, 585-591.
130. M. C. Mascolo, Y. Pei and T. A. Ring, *Materials*, 2013, **6**, 5549-5567.

131. Y.-F. Huang, Y.-F. Wang and X.-P. Yan, *Environmental Science & Technology*, 2010, **44**, 7908-7913.
132. S. Sun, H. Zeng, D. B. Robinson, S. Raoux, P. M. Rice, S. X. Wang and G. Li, *Journal of the American Chemical Society*, 2004, **126**, 273-279.
133. J. Park, K. An, Y. Hwang, J. G. Park, H. J. Noh, J. Y. Kim, J. H. Park, N. M. Hwang and T. Hyeon, *Nature Materials*, 2004, **3**, 891-895.
134. H. Ding, Y. Zhang, S. Wang, J. Xu, S. Xu and G. Li, *Chemistry of Materials*, 2012, **24**, 4572-4580.
135. H.-T. Lu, *Colloid Journal*, 2013, **75**, 311-318.
136. K. Susumu, B. C. Mei and H. Mattoussi, *Nature Protocols*, 2009, **4**, 424-436.
137. A. Bouzide and G. Sauvé, *Tetrahedron Letters*, 1997, **38**, 5945-5948.
138. Y. Zhang, S. Tsitkov and H. Hess, *Nature Communications*, 2016, **7**, 13982.
139. Z. Yuanbi, Q. Zumin and J. Huang, *Chinese Journal of Chemical Engineering*, 2008, **16**, 451-455.
140. U. S. Patil, H. Qu, D. Caruntu, C. J. O'Connor, A. Sharma, Y. Cai and M. A. Tarr, *Bioconjugate Chemistry*, 2013, **24**, 1562-1569.
141. Q. Liu, Z. Xu, J. Finch and R. Egerton, *Chemistry of Materials*, 1998, **10**, 3936-3940.
142. N. R. Jana, C. Earhart and J. Y. Ying, *Chemistry of Materials*, 2007, **19**, 5074-5082.
143. G. Bogush and C. Zukoski, *Journal of Colloid and Interface Science*, 1991, **142**, 1-18.
144. K. Lee, J.-L. Look, M. T. Harris and A. V. McCormick, *Journal of Colloid and Interface Science*, 1997, **194**, 78-88.
145. W. Stöber, A. Fink and E. Bohn, *Journal of Colloid and Interface Science*, 1968, **26**, 62-69.
146. Z. Lu, J. Dai, X. Song, G. Wang and W. Yang, *Colloids and Surfaces A: Physicochemical and Engineering Aspects*, 2008, **317**, 450-456.
147. T. Jesionowski, F. Ciesielczyk and A. Krysztafkiewicz, *Materials Chemistry and Physics*, 2010, **119**, 65-74.
148. E. T. Vandenberg, L. Bertilsson, B. Liedberg, K. Uvdal, R. Erlandsson, H. Elwing and I. Lundström, *Journal of Colloid and Interface Science*, 1991, **147**, 103-118.
149. A. Ulman, *Chemical Reviews*, 1996, **96**, 1533-1554.
150. M. Ma, Y. Zhang, W. Yu, H.-y. Shen, H.-q. Zhang and N. Gu, *Colloids and Surfaces A: Physicochemical and Engineering Aspects*, 2003, **212**, 219-226.

151. T. Horr and P. Arora, *Colloids and Surfaces A: Physicochemical and Engineering Aspects*, 1997, **126**, 113-121.
152. C. Destrée and J. Nagy, *Advances in Colloid and Interface Science*, 2006, **123**, 353-367.
153. S. Sun and H. Zeng, *Journal of the American Chemical Society*, 2002, **124**, 8204-8205.
154. L. Zhang, R. He and H.-C. Gu, *Applied Surface Science*, 2006, **253**, 2611-2617.
155. R. Koole, M. M. van Schooneveld, J. Hilhorst, C. de Mello Donegá, D. C. '. Hart, A. van Blaaderen, D. Vanmaekelbergh and A. Meijerink, *Chemistry of Materials*, 2008, **20**, 2503-2512.
156. S.-y. Chang, L. Liu and S. A. Asher, *Journal of the American Chemical Society*, 1994, **116**, 6739-6744.
157. C. C. Berry and A. S. Curtis, *Journal of Physics D: Applied Physics*, 2003, **36**, R198.
158. Y. Zhang, L. Wang, J. Tian, H. Li, Y. Luo and X. Sun, *Langmuir*, 2011, **27**, 2170-2175.
159. F. Xia, R. J. White, X. Zuo, A. Patterson, Y. Xiao, D. Kang, X. Gong, K. W. Plaxco and A. J. Heeger, *Journal of American Chemical Society*, **2010**, **132**, 14346-14348.
160. H. Pei, N. Lu, Y. Wen, S. Song, Y. Liu, H. Yan and C. Fan, *Advanced Materials*, 2010, **22**, 4754-4758.
161. D. Zhang, M. C. Huarng and E. C. Alocilja, *Biosenors and Bioelectronics*, 2010, **26**, 1736-1742.
162. Y. Xiang and Y. Lu, *Analytical Chemistry*, **2012**, **84**, 1975-1980.
163. H. Liu, S. Li, L. Liu, L. Tian and N. He, *Biosensors and Bioelectronics*, 2010, **26**, 1442-1448.
164. X. Duan, Z. Li, F. He and S. Wang, *Journal of American Chemical Society*, **2007**, **129**, 4154-4155.
165. X. Xiao, C. Zhang, X. Su, C. Song and M. Zhao, *Chemical Science*, 2012, **3**, 2257-2261.
166. F. Diehl, M. Li, D. Dressman, Y. He, D. Shen, S. Szabo, L. A. Diaz, S. N. Goodman, K. A. David and H. Juhl, *Proceedings of the National Academy of Sciences of the United States of America*, 2005, **102**, 16368-16373.
167. G. H. Reed, J. O. Kent and C. T. Wittwer, *Pharmacogenomics*, 2007, **8**, 597-608.

168. U. Malapelle, C. Carlomagno, M. Salatiello, A. De Stefano, C. De Luca, R. Bianco, R. Marciano, C. Cimminiello, C. Bellevicine and S. De Placido, *British Journal of Cancer*, 2012, **107**, 626-631.

169. S. Sorgenfrei, C.-y. Chiu, R. L. Gonzalez Jr, Y.-J. Yu, P. Kim, C. Nuckolls and K. L. Shepard, *Nature Nanotechnology*, 2011, **6**, 126-132.

170. I. I. Cisse, H. Kim and T. Ha, *Nature Structural and Molecular Biology*, 2012, **19**, 623-627.

171. J. Grimes, Y. V. Gerasimova and D. M. Kolpashchikov, *Angewandte Chemie International Edition*, 2010, **49**, 8950-8953.

172. J. Huang, Y. Wu, Y. Chen, Z. Zhu, X. Yang, C. J. Yang, K. Wang and W. Tan, *Angewandte Chemie International Edition*, 2011, **50**, 401-404.

173. S. He, K.-K. Liu, S. Su, J. Yan, X. Mao, D. Wang, Y. He, L.-J. Li, S. Song and C. Fan, *Analytical Chemistry*, **2012**, **84**, 4622-4627.

174. M. Li, S. K. Cushing, H. Liang, S. Suri, D. Ma and N. Wu, *Analytical Chemistry*, 2013, **85**, 2072-2078.

175. L. B. Sagle, L. K. Ruvuna, J. A. Ruemmele and R. P. Van Duyne, *Nanomedicine*, 2011, **6**, 1447-1462.

176. E. Papadopoulou and S. E. Bell, *Angewandnte Chemie International Edition*, 2011, **50**, 9058-9061.

177. L. Qiu, L. Qiu, Z. S. Wu, G. Shen and R. Q. Yu, *Analytical Chemistry*, 2013, **85**, 8225-8231.

178. W. Li, P. Wu, H. Zhang and C. Cai, *Analytical Chemistry*, 2012, **84**, 7583-7590.

179. M. M. Ali, F. Li, Z. Zhang, K. Zhang, D. K. Kang, J. A. Ankrum, X. C. Le and W. Zhao, *Chemical Society Reviews*, 2014, **43**, 3324-3341.

180. Y. Long, X. Zhou and D. Xing, *Biosensors and Bioelectronics*, 2013, **46**, 102-107.

181. Z. Zhang, D. Zeng, H. Ma, G. Feng, J. Hu, L. He, C. Li and C. Fan, *Small*, 2010, **6**, 1854-1858.

182. D. Wang, W. Tang, X. Wu, X. Wang, G. Chen, Q. Chen, N. Li and F. Liu, *Analytical Chemistry*, 2012, **84**, 7008-7014.

183. A. Chen, G.-F. Gui, Y. Zhuo, Y.-Q. Chai, Y. Xiang and R. Yuan, *Analytical Chemistry*, 2015, **87**, 6328-6334.

184. J. Wang, *Small*, 2005, **1**, 1036-1043.

185. Y. Chai, D. Tian, W. Wang and H. Cui, *Chemical Communications*, 2010, **46**, 7560-7562.

186. J. Li, S. Song, D. Li, Y. Su, Q. Huang, Y. Zhao and C. Fan, *Biosensors and Bioelectronics*, 2009, **24**, 3311-3315.

187. L. Song, V. H. Ho, C. Chen, Z. Yang, D. Liu, R. Chen and D. Zhou, *Advanced Healthcare Materials*, 2013, **2**, 275-280.

188. K. Knop, R. Hoogenboom, D. Fischer and U. S. Schubert, *Angewandnte Chemie International Edition*, 2010, **49**, 6288-6308.

189. D. Zhou, A. Bruckbauer, L. Ying, C. Abell and D. Klenerman, *Nano Letters*, 2003, **3**, 1517-1520.

190. L. Song, Y. Guo, D. Roebuck, C. Chen, M. Yang, Z. Yang, S. Sreedharan, C. Glover, J. A. Thomas and D. Liu, *ACS Applied Materials and Interfaces*, 2015, **7**, 18707-18716.

191. E. Peng, E. S. G. Choo, Y. Sheng and J. M. Xue, *New Journal of Chemistry*, 2013, **37**, 2051-2060.

192. S. Tong, S. Hou, B. Ren, Z. Zheng and G. Bao, *Nano Letters*, 2011, **11**, 3720.

193. E. E. Lees, T.-L. Nguyen, A. H. Clayton and P. Mulvaney, *ACS Nano*, 2009, **3**, 1121-1128.

194. M. Moros, B. Pelaz, P. López-Larrubia, M. L. García-Martin, V. Grazú and M. Jesus, *Nanoscale*, 2010, **2**, 1746-1755.

195. M. M. Yallapu, S. P. Foy, T. K. Jain and V. Labhasetwar, *Pharmaceutical Research*, 2010, **27**, 2283-2295.

196. W. S. Seo, J. H. Lee, X. Sun, Y. Suzuki, D. Mann, Z. Liu, M. Terashima, P. C. Yang, M. V. McConnell and D. G. Nishimura, *Nature Materials*, 2006, **5**, 971.

197. J. Shin, R. M. Anisur, M. K. Ko, G. H. Im, J. H. Lee and I. S. Lee, *Angewandnte Chemie International Edition*, 2009, **48**, 321-324.

198. D. M. Rissin, C. W. Kan, T. G. Campbell, S. C. Howes, D. R. Fournier, L. Song, T. Piech, P. P. Patel, L. Chang and A. J. Rivnak, *Nature Biotechnology*, 2010, **28**, 595-599.

199. F. Zhou, B. Li and J. Ma, *RSC Advances*, 2015, **5**, 4019-4025.

200. J. Hu, X.-W. Zhao, Y.-J. Zhao, J. Li, W.-Y. Xu, Z.-Y. Wen, M. Xu and Z.-Z. Gu, *Journal of Materials Chemistry*, 2009, **19**, 5730-5736.

201. T. Kang, S. M. Yoo, I. Yoon, S. Y. Lee and B. Kim, *Nano Letters*, 2010, **10**, 1189-1193.

202. J. Zhang, H.-P. Lang, F. Huber, A. Bietsch, W. Grange, U. Certa, R. McKendry, H.-J. Güntherodt, M. Hegner and C. Gerber, *Nature Nanotechnology*, **2006**, **1**, 214-220.

203. K. Faulds, F. McKenzie, W. E. Smith and D. Graham, *Angewandte Chemie International Edition*, **2007**, **119**, 1861-1863.
204. M. Zhang, B.-C. Yin, W. Tan and B.-C. Ye, *Biosensors and Bioelectronics*, **2011**, **26**, 3260-3265.
205. Z. Zhang, E. Sharon, R. Freeman, X. Liu and I. Willner, *Analytical Chemistry*, **2012**, **84**, 4789-4797.
206. L. He, M. D. Musick, S. R. Nicewarner, F. G. Salinas, S. J. Benkovic, M. J. Natan and C. D. Keating, *Journal of American Chemical Society*, **2000**, **122**, 9071-9077.
207. C. Fan, K. W. Plaxco and A. J. Heeger, *Proceedings of the National Academy of Sciences*, 2003, **100**, 9134-9137.
208. Y. Song, W. Zhang, Y. An, L. Cui, C. Yu, Z. Zhu and C. J. Yang, *Chemical Communications*, 2012, **48**, 576-578.
209. Y. Cheng, Q. Du, L. Wang, H. Jia and Z. Li, *Analytical Chemistry*, **2012**, **84**, 3739-3744.
210. G. Cao, *Nanostructures & Nanomaterials: Synthesis, Properties & Applications*, Imperial college press, 2004.
211. C. N. R. Rao, A. Müller and A. K. Cheetham, *The Chemistry of Nanomaterials: Synthesis, Properties and Applications*, John Wiley & Sons, 2006.
212. P. K. Jain, X. Huang, I. H. El-Sayed and M. A. El-Sayed, *Accounts of Chemical Research*, 2008, **41**, 1578-1586.
213. A. J. Huh and Y. J. Kwon, *Journal of Controlled Release*, 2011, **156**, 128-145.
214. M. Moritz and M. Geszke-Moritz, *Chemical Engineering Journal*, 2013, **228**, 596-613.
215. S. Chernousova and M. Epple, *Angewandte Chemie International Edition*, 2013, **52**, 1636-1653.
216. J. T. Seil and T. J. Webster, *International Journal of Nanomedicine*, 2012, **7**, 2767.
217. N. Durán, M. Durán, M. B. de Jesus, A. B. Seabra, W. J. Fávaro and G. Nakazato, *Nanomedicine: Nanotechnology, Biology and Medicine*, 2016, **12**, 789-799.
218. C.-A. J. Lin, C.-H. Lee, J.-T. Hsieh, H.-H. Wang, J. K. Li, J.-L. Shen, W.-H. Chan, H.-I. Yeh and W. H. Chang, *Journal of Medical and Biological Engineering*, 2009, **29**, 276-283.
219. Y. Tao, M. Li, J. Ren and X. Qu, *Chemical Society Reviews*, 2015, **44**, 8636-8663.

220. L. Zhang and E. Wang, *Nano Today*, 2014, **9**, 132-157.
221. H. Xu and K. S. Suslick, *Advanced Materials*, 2010, **22**, 1078-1082.
222. X. Le Guével, C. Spies, N. Daum, G. Jung and M. Schneider, *Nano Research*, 2012, 1-9.
223. J. Li, X. Zhong, F. Cheng, J.-R. Zhang, L.-P. Jiang and J.-J. Zhu, *Analytical Chemistry*, 2012, **84**, 4140-4146.
224. I. Díez and R. H. Ras, *Nanoscale*, 2011, **3**, 1963-1970.
225. Y. Lu and W. Chen, *Journal of Power Sources*, 2012, **197**, 107-110.
226. S. W. Yang and T. Vosch, *Analytical Chemistry*, 2011, **83**, 6935-6939.
227. B. Adhikari and A. Banerjee, *Chemistry of Materials*, 2010, **22**, 4364-4371.
228. G.-Y. Lan, C.-C. Huang and H.-T. Chang, *Chemical Communications*, 2010, **46**, 1257-1259.
229. A. Sangsuwan, H. Kawasaki, Y. Matsumura and Y. Iwasaki, *Bioconjugate Chemistry*, 2016, **27**, 2527-2533.
230. X. Yuan, M. I. Setyawati, D. T. Leong and J. Xie, *Nano Research*, 2014, **7**, 301-307.
231. J.-C. Jin, X.-J. Wu, J. Xu, B.-B. Wang, F.-L. Jiang and Y. Liu, *Biomaterials Science*, 2017, **5**, 247-257.
232. X. Wang, W. Gao, W. Xu and S. Xu, *Materials Science and Engineering: C*, 2013, **33**, 656-662.
233. S. Eustis and M. A. El-Sayed, *Chemical Society Reviews*, 2006, **35**, 209-217.
234. P. K. Jain, X. Huang, I. H. El-Sayed and M. A. El-Sayed, *Plasmonics*, 2007, **2**, 107-118.
235. R. Jin, *Nanoscale*, 2010, **2**, 343-362.
236. R. Jin, S.-K. Eah and Y. Pei, *Nanoscale*, 2012, **4**, 4026-4026.
237. Z. Luo, K. Zheng and J. Xie, *Chemical Communications*, 2014, **50**, 5143-5155.
238. T. Huang and R. W. Murray, *The Journal of Physical Chemistry B*, 2003, **107**, 7434-7440.
239. I. Díez and R. H. Ras, in *Advanced Fluorescence Reporters in Chemistry and Biology II*, Springer, Editon edn., 2010, pp. 307-332.
240. W. Haiss, N. T. Thanh, J. Aveyard and D. G. Fernig, *Analytical Chemistry*, 2007, **79**, 4215-4221.
241. S. Link and M. A. El-Sayed, *The Journal of Physical Chemistry B*, 1999, **103**, 4212-4217.

242. S. Pal, Y. K. Tak and J. M. Song, *Applied and Environmental Microbiology*, 2007, **73**, 1712-1720.
243. N. R. Jana, T. K. Sau and T. Pal, *The Journal of Physical Chemistry B*, 1999, **103**, 115-121.
244. K.-C. Lee, S.-J. Lin, C.-H. Lin, C.-S. Tsai and Y.-J. Lu, *Surface and Coatings Technology*, 2008, **202**, 5339-5342.
245. K. L. Kelly, E. Coronado, L. L. Zhao and G. C. Schatz, ACS Publications, Editon edn., 2003.
246. P. N. Njoki, I.-I. S. Lim, D. Mott, H.-Y. Park, B. Khan, S. Mishra, R. Sujakumar, J. Luo and C.-J. Zhong, *The Journal of Physical Chemistry C*, 2007, **111**, 14664-14669.
247. J. Calvo Fuentes, J. Rivas and M. A. López-Quintela, *Encyclopedia of Nanotechnology*, 2012, 2639-2648.
248. C. M. Aikens, *The Journal of Physical Chemistry C*, 2008, **112**, 19797-19800.
249. J. T. Petty, J. Zheng, N. V. Hud and R. M. Dickson, *Journal of the American Chemical Society*, 2004, **126**, 5207-5212.
250. A. Mooradian, *Physical Review Letters*, 1969, **22**, 185.
251. T. Huang and R. W. Murray, *The Journal of Physical Chemistry B*, 2001, **105**, 12498-12502.
252. S. Link, A. Beeby, S. FitzGerald, M. A. El-Sayed, T. G. Schaaff and R. L. Whetten, *The Journal of Physical Chemistry B*, 2002, **106**, 3410-3415.
253. C. Zhou, C. Sun, M. Yu, Y. Qin, J. Wang, M. Kim and J. Zheng, *The Journal of Physical Chemistry C*, 2010, **114**, 7727-7732.
254. Z. Wu and R. Jin, *Nano Letters*, 2010, **10**, 2568-2573.
255. M. Grzelczak and L. M. Liz-Marzán, *Chemical Society Reviews*, 2014, **43**, 2089-2097.
256. P. Chen, L. Song, Y. Liu and Y.-e. Fang, *Radiation Physics and Chemistry*, 2007, **76**, 1165-1168.
257. A. Henglein and R. Tausch-Treml, *Journal of Colloid and Interface Science*, 1981, **80**, 84-93.
258. A. Henglein, *Chemical Physics Letters*, 1989, **154**, 473-476.
259. M. Treguer, F. Rocco, G. Lelong, A. Le Nestour, T. Cardinal, A. Maali and B. Lounis, *Solid State Sciences*, 2005, **7**, 812-818.
260. J. C. Scaiano, P. Billone, C. M. Gonzalez, L. Marett, M. L. Marin, K. L. McGilvray and N. Yuan, *Pure and Applied Chemistry*, 2009, **81**, 635-647.

261. M. Zaarour, M. El Roz, B. Dong, R. Retoux, R. Aad, J. Cardin, C. Dufour, F. Gourbilleau, J.-P. Gilson and S. Mintova, *Langmuir*, 2014, **30**, 6250-6256.
262. V. K. Sharma, R. A. Yngard and Y. Lin, *Advances in Colloid and Interface Science*, 2009, **145**, 83-96.
263. A. R. Poda, A. J. Kennedy, M. F. Cuddy and A. J. Bednar, *Journal of Nanoparticle Research*, 2013, **15**, 1673.
264. Y. Lu, Y. Mei, M. Schrinner, M. Ballauff, M. W. Möller and J. Breu, *The Journal of Physical Chemistry C*, 2007, **111**, 7676-7681.
265. L. Huang, M. L. Zhai, D. W. Long, J. Peng, L. Xu, G. Z. Wu, J. Q. Li and G. S. Wei, *Journal of Nanoparticle Research*, 2008, **10**, 1193-1202.
266. Y. Zhou, S. H. Yu, C. Y. Wang, X. G. Li, Y. R. Zhu and Z. Y. Chen, *Advanced Materials*, 1999, **11**, 850-852.
267. J. Zheng and R. M. Dickson, *Journal of the American Chemical Society*, 2002, **124**, 13982-13983.
268. L. A. Peyser, A. E. Vinson, A. P. Bartko and R. M. Dickson, *Science*, 2001, **291**, 103-106.
269. L. Shang and S. Dong, *Chemical Communications*, 2008, 1088-1090.
270. I. Díez, M. Pusa, S. Kulmala, H. Jiang, A. Walther, A. S. Goldmann, A. H. Müller, O. Ikkala and R. H. Ras, *Angewandte Chemie International Edition*, 2009, **48**, 2122-2125.
271. H. Xu, B. W. Zeiger and K. S. Suslick, *Chemical Society Reviews*, 2013, **42**, 2555-2567.
272. J. Kis-Csitári, Z. Kónya and I. Kiricsi, in *Functionalized Nanoscale Materials, Devices and Systems*, Springer, Editon edn., 2008, pp. 369-372.
273. R. Salkar, P. Jeevanandam, S. Aruna, Y. Koltypin and A. Gedanken, *Journal of Materials Chemistry*, 1999, **9**, 1333-1335.
274. R. A. Caruso, M. Ashokkumar and F. Grieser, *Langmuir*, 2002, **18**, 7831-7836.
275. L.-P. Jiang, S. Xu, J.-M. Zhu, J.-R. Zhang, J.-J. Zhu and H.-Y. Chen, *Inorganic Chemistry*, 2004, **43**, 5877-5883.
276. M. M. Rahman, S. B. Khan, A. Jamal, M. Faisal and A. M. Asiri, *Chemical Engineering Journal*, 2012, **192**, 122-128.
277. Y.-p. Zhu, X.-k. Wang, W.-l. Guo, J.-g. Wang and C. Wang, *Ultrasonics Sonochemistry*, 2010, **17**, 675-679.
278. H. Xu and K. S. Suslick, *ACS Nano*, 2010, **4**, 3209-3214.

279. T. Zhou, M. Rong, Z. Cai, C. J. Yang and X. Chen, *Nanoscale*, 2012, **4**, 4103-4106.
280. C. Vollmer, E. Redel, K. Abu-Shandi, R. Thomann, H. Manyar, C. Hardacre and C. Janiak, *Chemistry-A European Journal*, 2010, **16**, 3849-3858.
281. H. Yin, T. Yamamoto, Y. Wada and S. Yanagida, *Materials Chemistry and Physics*, 2004, **83**, 66-70.
282. S. Liu, F. Lu and J.-J. Zhu, *Chemical Communications*, 2011, **47**, 2661-2663.
283. E. Series and P. Vanýsek, CRC Press, Cleveland, D-141, Editon edn., 1977.
284. A. Van Hoonacker and P. Englebienne, *Current Nanoscience*, 2006, **2**, 359-371.
285. B. L. Cushing, V. L. Kolesnichenko and C. J. O'Connor, *Chemical Reviews*, 2004, **104**, 3893-3946.
286. P. M. Hudnall, *Ullmann's Encyclopedia of Industrial Chemistry*, 2000.
287. C. Marambio-Jones and E. M. Hoek, *Journal of Nanoparticle Research*, 2010, **12**, 1531-1551.
288. S. Schneider, P. Halbig, H. Grau and U. Nickel, *Photochemistry and Photobiology*, 1994, **60**, 605-610.
289. N. Shirtcliffe, U. Nickel and S. Schneider, *Journal of Colloid and Interface Science*, 1999, **211**, 122-129.
290. L. Kvitek, A. Panáček, J. Soukupova, M. Kolář, R. Večeřová, R. Prucek, M. Holecova and R. Zbořil, *The Journal of Physical Chemistry C*, 2008, **112**, 5825-5834.
291. A. Taglietti, Y. A. Diaz Fernandez, E. Amato, L. Cucca, G. Dacarro, P. Grisoli, V. Necchi, P. Pallavicini, L. Pasotti and M. Patrini, *Langmuir*, 2012, **28**, 8140-8148.
292. X. Sun, S. Dong and E. Wang, *Macromolecules*, 2004, **37**, 7105-7108.
293. J. Zeng, Y. Zheng, M. Rycenga, J. Tao, Z.-Y. Li, Q. Zhang, Y. Zhu and Y. Xia, *Journal of the American Chemical Society*, 2010, **132**, 8552-8553.
294. Y. Sun, B. Mayers, T. Herricks and Y. Xia, *Nano Letters*, 2003, **3**, 955-960.
295. B. J. Wiley, Y. Chen, J. M. McLellan, Y. Xiong, Z.-Y. Li, D. Ginger and Y. Xia, *Nano Letters*, 2007, **7**, 1032-1036.
296. R. Jin, Y. Cao, C. A. Mirkin, K. Kelly, G. C. Schatz and J. Zheng, *Science*, 2001, **294**, 1901-1903.
297. R. Jin, Y. C. Cao, E. Hao, G. S. Métraux, G. C. Schatz and C. A. Mirkin, *Nature*, 2003, **425**, 487.

298. B. Adhikari and A. Banerjee, *Chemistry-A European Journal*, 2010, **16**, 13698-13705.

299. Y.-C. Shiang, C.-C. Huang, W.-Y. Chen, P.-C. Chen and H.-T. Chang, *Journal of Materials Chemistry*, 2012, **22**, 12972-12982.

300. J. Yu, S. A. Patel and R. M. Dickson, *Angewandte Chemie*, 2007, **119**, 2074-2076.

301. N. Cathcart, P. Mistry, C. Makra, B. Pietrobon, N. Coombs, M. Jelokhani-Niaraki and V. Kitaev, *Langmuir*, 2009, **25**, 5840-5846.

302. H. Yang, Y. Wang, H. Huang, L. Gell, L. Lehtovaara, S. Malola, H. Häkkinen and N. Zheng, *Nature Communications*, 2013, **4**, 2422.

303. Z. Yuan, N. Cai, Y. Du, Y. He and E. S. Yeung, *Analytical Chemistry*, 2013, **86**, 419-426.

304. T. Vosch, Y. Antoku, J.-C. Hsiang, C. I. Richards, J. I. Gonzalez and R. M. Dickson, *Proceedings of the National Academy of Sciences*, 2007, **104**, 12616-12621.

305. P. T. Chin, M. van der Linden, E. J. van Harten, A. Barendregt, M. T. Rood, A. J. Koster, F. W. van Leeuwen, C. de Mello Donega, A. J. Heck and A. Meijerink, *Nanotechnology*, 2013, **24**, 075703.

306. M. A. H. Muhammed, F. Aldeek, G. Palui, L. Trapiella-Alfonso and H. Mattoussi, *ACS Nano*, 2012, **6**, 8950-8961.

307. L. Rizzello and P. P. Pompa, *Chemical Society Reviews*, 2014, **43**, 1501-1518.

308. K. Zheng, M. I. Setyawati, D. T. Leong and J. Xie, *Coordination Chemistry Reviews*, 2018, **357**, 1-17.

309. W. K. Jung, H. C. Koo, K. W. Kim, S. Shin, S. H. Kim and Y. H. Park, *Applied and Environmental Microbiology*, 2008, **74**, 2171-2178.

310. S. Kittler, C. Greulich, J. Diendorf, M. Koller and M. Epple, *Chemistry of Materials*, 2010, **22**, 4548-4554.

311. W. Zhang, Y. Yao, N. Sullivan and Y. Chen, *Environmental Science & Technology*, 2011, **45**, 4422-4428.

312. G. A. Sotiriou and S. E. Pratsinis, *Environmental Science & Technology*, 2010, **44**, 5649-5654.

313. Z.-m. Xiu, Q.-b. Zhang, H. L. Puppala, V. L. Colvin and P. J. Alvarez, *Nano Letters*, 2012, **12**, 4271-4275.

314. W.-R. Li, X.-B. Xie, Q.-S. Shi, H.-Y. Zeng, O.-Y. You-Sheng and Y.-B. Chen, *Applied Microbiology and Biotechnology*, 2010, **85**, 1115-1122.

315. J. A. Lemire, J. J. Harrison and R. J. Turner, *Nature Reviews Microbiology*, 2013, **11**, 371.

316. K. B. Holt and A. J. Bard, *Biochemistry*, 2005, **44**, 13214-13223.

317. C.-N. Lok, C.-M. Ho, R. Chen, Q.-Y. He, W.-Y. Yu, H. Sun, P. K.-H. Tam, J.-F. Chiu and C.-M. Che, *Journal of Proteome Research*, 2006, **5**, 916-924.

318. P. Dibrov, J. Dzioba, K. K. Gosink and C. C. Häse, *Antimicrobial Agents and Chemotherapy*, 2002, **46**, 2668-2670.

319. N. Hachicho, P. Hoffmann, K. Ahlert and H. J. Heipieper, *FEMS Microbiology Letters*, 2014, **355**, 71-77.

320. A. Anas, J. Jiya, M. Rameez, P. Anand, M. Anantharaman and S. Nair, *Letters in Applied Microbiology*, 2013, **56**, 57-62.

321. J. R. Morones, J. L. Elechiguerra, A. Camacho, K. Holt, J. B. Kouri, J. T. Ramírez and M. J. Yacaman, *Nanotechnology*, 2005, **16**, 2346.

322. M. A. Ansari, H. M. Khan, A. A. Khan, M. K. Ahmad, A. A. Mahdi, R. Pal and S. S. Cameotra, *Journal of Basic Microbiology*, 2014, **54**, 905-915.

323. J. S. Kim, E. Kuk, K. N. Yu, J.-H. Kim, S. J. Park, H. J. Lee, S. H. Kim, Y. K. Park, Y. H. Park and C.-Y. Hwang, *Nanomedicine: Nanotechnology, Biology and Medicine*, 2007, **3**, 95-101.

324. S.-H. Kim, H.-S. Lee, D.-S. Ryu, S.-J. Choi and D.-S. Lee, *Korean Journal of Microbiology and Biotechnology*, 2011, **39**, 77-85.

325. H. Xu, F. Qu, H. Xu, W. Lai, Y. A. Wang, Z. P. Aguilar and H. Wei, *Biometals*, 2012, **25**, 45-53.

326. H. Arakawa, J. Neault and H. Tajmir-Riahi, *Biophysical Journal*, 2001, **81**, 1580-1587.

327. S. Vishnupriya, K. Chaudhari, R. Jagannathan and T. Pradeep, *Particle & Particle Systems Characterization*, 2013, **30**, 1056-1062.

328. S. M. Ouda, *American Journal of Infectious Diseases Microbiology*, 2014, **2**, 4-10.

329. T. M. Tolaymat, A. M. El Badawy, A. Genaidy, K. G. Scheckel, T. P. Luxton and M. Suidan, *Science of the Total Environment*, 2010, **408**, 999-1006.

330. M. E. Quadros, R. Pierson IV, N. S. Tulve, R. Willis, K. Rogers, T. A. Thomas and L. C. Marr, *Environmental Science & Technology*, 2013, **47**, 8894-8901.

331. F. Furno, K. S. Morley, B. Wong, B. L. Sharp, P. L. Arnold, S. M. Howdle, R. Bayston, P. D. Brown, P. D. Winship and H. J. Reid, *Journal of Antimicrobial Chemotherapy*, 2004, **54**, 1019-1024.

332. S. Agnihotri, S. Mukherji and S. Mukherji, *RSC Advances*, 2014, **4**, 3974-3983.

333. X. Hong, J. Wen, X. Xiong and Y. Hu, *Environmental Science and Pollution Research*, 2016, **23**, 4489-4497.

334. X. Yuan, M. I. Setyawati, A. S. Tan, C. N. Ong, D. T. Leong and J. Xie, *NPG Asia Materials*, 2013, **5**, e39.

335. A. M. El Badawy, R. G. Silva, B. Morris, K. G. Scheckel, M. T. Suidan and T. M. Tolaymat, *Environmental Science & Technology*, 2010, **45**, 283-287.

336. A. Abbaszadegan, M. Nabavizadeh, A. Gholami, Z. Aleyasin, S. Dorostkar, M. Saliminasab, Y. Ghasemi, B. Hemmateenejad and H. Sharghi, *International Endodontic Journal*, 2015, **48**, 790-800.

337. K. Susumu, B. C. Mei and H. Mattoussi, *Nature Protocols*, 2009, **4**, 424.

338. N. Zhan, G. Palui, H. Grise, H. Tang, I. Alabugin and H. Mattoussi, *ACS Applied Materials & Interfaces*, 2013, **5**, 2861-2869.

339. A. G. Brenton and A. R. Godfrey, *Journal of the American Society for Mass Spectrometry*, 2010, **21**, 1821-1835.

340. L. Shang, R. M. Dörlich, V. Trouillet, M. Bruns and G. U. Nienhaus, *Nano Research*, 2012, **5**, 531-542.

341. S. Huang, C. Pfeiffer, J. Hollmann, S. Friede, J. J.-C. Chen, A. Beyer, B. Haas, K. Volz, W. Heimbrodt and J. M. Montenegro Martos, *Langmuir*, 2012, **28**, 8915-8919.

342. M. J. Bogan and G. R. Agnes, *Journal of the American Society for Mass Spectrometry*, 2002, **13**, 177-186.

343. K. Shameli, M. Bin Ahmad, S. D. Jazayeri, S. Sedaghat, P. Shabanzadeh, H. Jahangirian, M. Mahdavi and Y. Abdollahi, *International Journal of Molecular Sciences*, 2012, **13**, 6639-6650.

344. M. de Kanter, J. Meyer-Kirschner, J. Viell, A. Mitsos, M. Kather, A. Pich and C. Janzen, *Measurement*, 2016, **80**, 92-98.

345. S. Raut, R. Rich, I. Akopova, E. Thyrhaug, T. Shtoyko, D. Shumilov, Z. Gryczynski and I. Gryczynski, *Chemical Physics Letters*, 2012, **549**, 72-76.

346. K. Yoncheva, E. Lizarraga and J. M. Irache, *European Journal of Pharmaceutical Sciences*, 2005, **24**, 411-419.

347. K. Rahme, L. Chen, R. G. Hobbs, M. A. Morris, C. O'Driscoll and J. D. Holmes, *RSC Advances*, 2013, **3**, 6085-6094.

348. O. Ogunwuyi, N. Kumari, K. A. Smith, O. Bolshakov, S. Adesina, A. Gugssa, W. A. Anderson, S. Nekhai and E. O. Akala, *Infectious Diseases: Research and Treatment*, 2016, **9**, IDRT. S38108.

349. A. Mandal, V. Meda, W. Zhang, K. Farhan and A. Gnanamani, *Colloids and Surfaces B: Biointerfaces*, 2012, **90**, 191-196.

350. K. Zheng, M. I. Setyawati, D. T. Leong and J. Xie, *ACS Nano*, 2017, **11**, 6904-6910.

351. T. J. Silhavy, D. Kahne and S. Walker, *Cold Spring Harbor Perspectives in Biology*, 2010, a000414.

352. N. Papo and Y. Shai, *Journal of Biological Chemistry*, 2005, **280**, 10378-10387.

353. W. Vollmer, D. Blanot and M. A. De Pedro, *FEMS Microbiology Reviews*, 2008, **32**, 149-167.

354. S. Brown, J. P. Santa Maria Jr and S. Walker, *Annual Review of Microbiology*, 2013, **67**, 313-336.

355. M. B. Edmond, S. E. Wallace, D. K. McClish, M. A. Pfaller, R. N. Jones and R. P. Wenzel, *Clinical Infectious Diseases*, 1999, **29**, 239-244.

356. R. Lambert and J. Pearson, *Journal of Applied Microbiology*, 2000, **88**, 784-790.

357. S. Jiang and Z. Cao, *Advanced Materials*, 2010, **22**, 920-932.

358. G. Cheng, Z. Zhang, S. Chen, J. D. Bryers and S. Jiang, *Biomaterials*, 2007, **28**, 4192-4199.

359. G. Cheng, G. Li, H. Xue, S. Chen, J. D. Bryers and S. Jiang, *Biomaterials*, 2009, **30**, 5234-5240.

360. Z. Cao, L. Mi, J. Mendiola, J. R. Ella-Menye, L. Zhang, H. Xue and S. Jiang, *Angewandte Chemie International Edition*, 2012, **51**, 2602-2605.

361. R. Hu, G. Li, Y. Jiang, Y. Zhang, J.-J. Zou, L. Wang and X. Zhang, *Langmuir*, 2013, **29**, 3773-3779.

362. S. Huo, Y. Jiang, A. Gupta, Z. Jiang, R. F. Landis, S. Hou, X.-J. Liang and V. M. Rotello, *ACS Nano*, 2016, **10**, 8732-8737.

363. A. Abbaszadegan, Y. Ghahramani, A. Gholami, B. Hemmateenejad, S. Dorostkar, M. Nabavizadeh and H. Sharghi, *Journal of Nanomaterials*, 2015, **16**, 53.

364. X. Li, S. M. Robinson, A. Gupta, K. Saha, Z. Jiang, D. F. Moyano, A. Sahar, M. A. Riley and V. M. Rotello, *ACS Nano*, 2014, **8**, 10682-10686.

365. A. Ivask, A. ElBadawy, C. Kaweeteerawat, D. Boren, H. Fischer, Z. Ji, C. H. Chang, R. Liu, T. Tolaymat and D. Telesca, *ACS Nano*, 2013, **8**, 374-386.

366. M. Zasloff, *Nature*, 2002, **415**, 389.

367. A. I. Lopez, R. Y. Reins, A. M. McDermott, B. W. Trautner and C. Cai, *Molecular BioSystems*, 2009, **5**, 1148-1156.

368. A. Mecke, I. J. Majoros, A. K. Patri, J. R. Baker, M. M. Banaszak Holl and B. G. Orr, *Langmuir*, 2005, **21**, 10348-10354.

369. H. Z. Zardini, A. Amiri, M. Shanbedi, M. Maghrebi and M. Baniadam, *Colloids and Surfaces B: Biointerfaces*, 2012, **92**, 196-202.

370. Z. V. Feng, I. L. Gunsolus, T. A. Qiu, K. R. Hurley, L. H. Nyberg, H. Frew, K. P. Johnson, A. M. Vartanian, L. M. Jacob and S. E. Lohse, *Chemical Science*, 2015, **6**, 5186-5196.

371. C. Cox, *Microbiology*, 1966, **45**, 275-281.

372. J. Chirife, L. Herszage, A. Joseph, J. Bozzini, N. Leardini and E. Kohn, *Antimicrobial Agents and Chemotherapy*, 1983, **24**, 409-412.

373. D. Bhattacharya, S. Samanta, A. Mukherjee, C. R. Santra, A. N. Ghosh, S. K. Niyogi and P. Karmakar, *Journal of Nanoscience and Nanotechnology*, 2012, **12**, 2513-2521.

374. T. J. Beveridge, *Journal of Bacteriology*, 1999, **181**, 4725-4733.

375. M. Madigan, J. Martinko and J. Parker, Inc, Editon edn., 2005.

376. T. M. Nalawade, K. Bhat and S. H. Sogi, *Journal of International Society of Preventive & Community Dentistry*, 2015, **5**, 114.

377. T. Jayaramudu, G. M. Raghavendra, K. Varaprasad, G. V. S. Reddy, A. B. Reddy, K. Sudhakar and E. R. Sadiku, *Journal of Applied Polymer Science*, 2016, **133**.

378. Y. S. Park, J. Won and Y. S. Kang, *Langmuir*, 2000, **16**, 9662-9665.

379. M. J. Hostetler, J. E. Wingate, C.-J. Zhong, J. E. Harris, R. W. Vachet, M. R. Clark, J. D. Londono, S. J. Green, J. J. Stokes and G. D. Wignall, *Langmuir*, 1998, **14**, 17-30.

380. Z. Lu, K. Rong, J. Li, H. Yang and R. Chen, *Journal of Materials Science: Materials in Medicine*, 2013, **24**, 1465-1471.

381. G. Martinez-Castanon, N. Nino-Martinez, F. Martinez-Gutierrez, J. Martinez-Mendoza and F. Ruiz, *Journal of Nanoparticle Research*, 2008, **10**, 1343-1348.

382. L. Shang, K. Nienhaus and G. U. Nienhaus, *Journal of Nanobiotechnology*, 2014, **12**, b26.

383. R. Novak, B. Henriques, E. Charpentier, S. Normark and E. Tuomanen, *Nature*, 1999, **399**, 590.

384. C. T. Walsh, S. L. Fisher, I.-S. Park, M. Prahalad and Z. Wu, *Chemistry & Biology*, 1996, **3**, 21-28.

385. P. E. Reynolds, *European Journal of Clinical Microbiology and Infectious Diseases*, 1989, **8**, 943-950.

386. S. K. Choi, A. Myc, J. E. Silpe, M. Sumit, P. T. Wong, K. McCarthy, A. M. Desai, T. P. Thomas, A. Kotlyar and M. M. B. Holl, *ACS Nano*, 2012, **7**, 214-228.